TU WIEN
DEPARTMENT OF GEODESY AND GEOINFORMATION
RESEARCH UNIT GEOPHYSICS

DISSERTATION

Rethinking field-scale geophysics: Quantifying hydraulic conductivity with electrical conductivity

Ausgeführt zum Zwecke der Erlangung des akademischen Grades eines Doktors der technischen Wissenschaften unter der Leitung von

Prof. Dr.rer.nat. Adrián Flores Orozco
Department für Geodäsie und Geoinformation
Forschungsbereich Geophysik

eingereicht an der Technischen Universität Wien
Fakultät für Mathematik und Geoinformation

von

Jakob Gallistl
Mat. Nr.: 1027940
Waldstraße 72, 3100 St. Pölten

Wien, Januar 2025

Jakob Gallistl (Verfasser) | Adrián Flores Orozco (Betreuer)

TU WIEN
DEPARTMENT OF GEODESY AND GEOINFORMATION
RESEARCH UNIT GEOPHYSICS

Dissertation

Rethinking field-scale geophysics: Quantifying hydraulic conductivity with electrical conductivity

Carried out for the purpose of obtaining the degree of Doctor technicae (Dr. techn.)
under the supervision of

Prof. Dr.rer.nat. Adrián Flores Orozco
Department of Geodesy and Geoinformation
Research Unit of Geophysics

submitted at TU Wien
Faculty of Mathematics and Geoinformation

by

Jakob Gallistl
Mat. Nr.: 1027940
Waldstraße 72, 3100 St. Pölten

Vienna, January 2025

Jakob Gallistl (Author)	Adrián Flores Orozco (Supervisor)

Examination commitee:

Prof. Dr. Adrián Flores Orozco
TU Wien
Department of Geodesy and Geoinformation
Research Unit of Geophysics

Prof. Dr. Dimitrios Ntarlagiannis
Rutgers University - School of Arts and Sciences
Department of Earth and Environmental Sciences
Near-Surface Geophysics

Prof. Dr. Matthias Bücker
Kiel University
Institute of Geosciences
Applied Geophysics

Affidavit

I declare in lieu of oath, that I wrote this thesis and performed the associated research myself, using only literature cited in this volume. If text passages from sources are used literally, they are marked as such.

I confirm that this work is original and has not been submitted elsewhere for any examination, nor is it currently under consideration for a thesis elsewhere.

Vienna, January 2025

Jakob Gallistl

This work was supported through the Austrian Science Fund (FWF) – Agence Nationale de la Recherche (ANR) research project I 2619-N29 and ANR-15-CE04-0009-01 "HYDRO-SLIDE: Hydro-geophysical observations for an advanced understanding of clayey landslides".

Abstract

This thesis investigates the application of geophysical methods, particularly (spectral) induced polarization (SIP) and electromagnetic induction (EMI), for characterizing landslides and estimating soil and hydraulic properties at various scales. The research objectives include the development of robust field procedures for high-quality SIP data collection, the evaluation of field-scale SIP and EMI imaging for landslide characterization, and the assessment of various approaches to obtain hydraulic properties from geophysical data using petrophysical relationships and pedotransfer functions (PTFs), along with exploring deep learning techniques for geophysical data inversion.

The first part of this thesis deals with improvements in the procedures for the collection of SIP data at the field scale, along with an analysis of their uncertainty. It presents SIP data collected with standard multicore and novel coaxial cables, and examines how electromagnetic (EM) coupling interferes with the data. While commonly assumed to only affect higher frequencies, the analysis reveals that EM coupling cannot be neglected for frequencies below 10 Hz. It is demonstrated that it is essential to use cables with takeout lengths identical to the selected electrode separation. Moreover, the deployment of coaxial cables permits to collect significantly improved data across all observed frequencies while maintaining the identical simple field procedures.

The evaluation of an integrated approach combining field-scale SIP, EMI, and other geophysical methods for an effective characterization of landslides is presented in the second part of this thesis. A particular focus was laid on delineating subsurface water flow and infiltration pathways as well as possible sliding and stable units. Such knowledge is essential for understanding the internal processes within landslides associated with their mobilization mechanisms. The initial implementation of this approach at a well-equipped Austrian landslide site revealed significant qualitative correlations between geotechnical parameters, such as dynamic probing and inclinometer data, and frequency-dependent electrical properties obtained from field-scale SIP. Building on these findings and testing their transferability, a multi-methodical approach was developed to characterize 3D soil textural and hydraulic subsurface properties and applied to another hillslope affected by subsidence. This approach integrated dense induced polarization (IP) mapping with transient electromagnetic soundings (TEM), refraction seismic tomography (RST), borehole soil-textural information, and subsurface displacement rates obtained from inclinometer measurements. By incorporating TEM-derived structural information into the IP data inversion, quantitative correlations between the induced polarization response and soil volume fractions were established and validated. Subsequently, a pedotransfer function (PTF) was applied to the predicted soil-textural information, enabling the delineation of a three-dimensional hydrogeophysical model parameterized in terms of subsurface hydraulic conductivity, aquiclude geometry, and preferential flow paths.

The third part of this thesis investigates the application of deep learning in conjunction with EMI mapping to predict soil properties at the catchment scale, and presents a novel deep learning network for EMI data inversion. Soil textural information from an extensive soil survey enabled the development of petrophysical relationships linking inverted electrical conductivity at different depths to soil volume fractions. Moreover, the recalibration of a field-scale PTF with predicted soil-textural information allowed for catchment-scale subsurface hydraulic conductivity prediction for depths down to 1.5 m, essential for calibrating hydrological run-off models. This thesis further discusses and develops a hydrogeophysical representation of the research catchment using an extensive IP mapping dataset collected over a decade, extending soil-textural and hydraulic information to depths of 40 m. Potential conceptual hydrogeophysical models were examined based on borehole information, with one model parameterized using three-dimensional hydraulic conductivity distributions and confining layer topography based on the geophysical dataset.

The comprehensive approach presented in this thesis demonstrates the potential of integrating geophysical methods, deep learning, and pedotransfer functions for an enhanced characterization of subsurface properties at various scales and environments, including clay-rich landslides and catchments, with implications for enhancing hydrogeological modeling and understanding of surface-groundwater interactions.

Kurzfassung

Diese Dissertation untersucht die Anwendung geophysikalischer Methoden, insbesondere der Bildgebungsmethoden mittels (spektral) induzierter Polarisation (SIP) und elektromagnetischer Induktion (EMI), zur Charakterisierung von Erdrutschen sowie zur Abschätzung bodenphysikalischer und hydraulischer Untergrundeigenschaften auf verschiedenen Größenskalen. Die Forschungziele umfassen die Entwicklung robuster Feldverfahren zur Erfassung von qualitativ hochwertigen SIP-Daten, die Evaluierung von SIP- und EMI-Bildgebung auf der Feldskala zur Charakterisierung von Erdrutschen sowie die Analyse verschiedener Ansätze zur Ermittlung hydraulischer Eigenschaften aus geophysikalischen Daten unter Verwendung petrophysikalischer Beziehungen und Pedotransferfunktionen (PTFs). Zudem wird die Anwendung von Deep-Learning-Techniken zur Inversion geophysikalischer Daten untersucht.

Der erste Teil dieser Arbeit befasst sich mit der Verbesserung von Messverfahren zur Erfassung von feldskaligen SIP-Datensätzen und der Analyse ihrer Unsicherheiten. Durch den Vergleich von SIP-Daten, die mit Standard-Multicore- und neu konstruierten Koaxialkabeln gesammelt wurden, wird gezeigt, wie elektromagnetische (EM) Kopplungseffekte die Daten beeinflussen. Entgegen der weitläufigen Annahme, dass die EM Kopplungseffekte erst bei höheren Frequenzen einen signifikanten Einfluss haben, zeigt die Analyse, dass diese bereits bei niedrigen Frequenzen unter 10 Hz berücksichtigt werden müssen. Falls keine Koaxialkabel verfügbar sind, zeigt sich, dass es unerlässlich ist, Kabel mit einer Länge zwischen den Elektrodenbereichen zu verwenden, die dem gewählten Elektrodenabstand entspricht. Grundsätzlich konnte durch den Einsatz von Koaxialkabeln eine Verbesserung der Datenqualität im gesamten Frequenzbereich beobachtet werden, ohne den Aufwand für die Feldmessungen durch komplizierte Feldverfahren zu erschweren. Mit gleichem Aufwand können daher durch den Einsatz von Koaxialkabeln im Vergleich zu Standard-Multicore-Kabeln signifikant bessere Daten erfasst werden.

Der zweite Teil dieser Arbeit präsentiert die Evaluierung einer integrierten Anwendung von SIP, EMI und anderen geophysikalischen Methoden zur effektiven Charakterisierung von Erdrutschen auf der Feldskala. Dabei wurde besonderer Fokus auf die Bestimmung des unterirdischen Wasserflusses und Infiltrationswegen sowie die Bestimmung von stabilen/instabilen Einheiten und möglicher Rutschhorizonte gelegt. Diese

Information ist für das Verständnis von, in der Hangrutschung stattfindenden Wasserbewegungen, die ihrerseits zur einer möglichen Mobilisierung der Hangrutschung beitragen, essentiell. Erste Anwendungen feldskaliger SIP-Messungen an einer technisch gut ausgestatteten Hangrutschung ergaben eine signifikante qualitative Korrelation zwischen geotechnischen Parametern (Rammsondierungs- und Inklinometerdaten) und den frequenzabhängigen elektrischen Leitfähigkeiten. Aufbauend auf diesen Erkenntnissen wurde ein umfassender multimethodischer Ansatz zur Charakterisierung der 3D-Bodentextur und der hydraulischen Eigenschaften des Untergrunds entwickelt und auf einer zweiten Hangrutschung angewandt. Dieser Ansatz kombinierte die Kartierung der unterirdischen elektrischen Eigenschaften durch dicht gemessene Profile mittels induzierter Polarisation (IP), transienten elektromagnetischen Sondierungen (TEM), refraktionsseismischer Tomographie (RST), Bohrlochinformation (Korngrößen und Bodentyp) sowie aus Inklinometermessungen gewonnene Verschiebungsraten. Durch die Einbeziehung, der aus TEM abgeleiteten Strukturinformationen, in die Inversion der IP-Daten konnten quantitative Korrelationen zwischen den Polarisationseigenschaften und der Korngrößenverteilung im Boden hergestellt und validiert werden. Die dicht gemessenen IP-Profile ermöglichten die Abschätzung der Korngrößenverteilung im Untergrund. Durch die Anwendung einer Pedotransferfunktion (PTF) konnte ein dreidimensionales hydrogeophysikalisches Modell erstellt werden, das die hydraulische Leitfähigkeit des Untergrunds, die Oberkante des Grundwasserleiters und bevorzugte Fließwege parameterisiert.

Der dritte Teil dieser Arbeit untersucht die Anwendung von Deep Learning in Verbindung mit flächiger EMI-Kartierung zur Abschätzung bodenphysikalischer Eigenschaften in einem kleinen Einzugsgebiet. Hiefür wurde ein neuartiger Deep Learning-Ansatz entwickelt, der die Inversion von EMI-Daten erlaubt. Informationen zur Korngrößenverteilung im Boden, die im Rahmen einer umfassenden Kartierungskampagne erfasst wurden, bildeten die Grundlage für die Entwicklung petrophysikalischer Beziehungen, die die in verschiedenen Tiefen ermittelte elektrische Leitfähigkeit aus den EMI-Daten mit der Korngrößenverteilung verknüpfen. Darüber hinaus ermöglichte die Rekalibrierung einer feldskaligen PTF auf Basis der vorhergesagten Korngrößen die Abschätzung der hydraulischen Leitfähigkeit im gesamten Einzugsgebiet bis zu einer Tiefe von 1,5 m. Diese Information ist für die Kalibrierung hydrologischer Abflussmodelle unerlässlich und stellt eine deutliche Verbesserung gegenüber bestehenden Ansätzen zur Bestimmung der hydraulischen Leitfähigkeit im Untergrund dar. Zusätzlich wird in dieser Arbeit eine hydrogeophysikalische Modellierung des Einzugsgebiets, unter Verwendung eines umfangreichen IP-Kartierungsdatensatzes, vorgestellt. Dabei wurde die Abschätzung der Korngrößenverteilung sowie der hydraulischen Leitfähigkeit auf Tiefen von bis zu 40 m erweitert. Mögliche konzeptionelle hydrogeophysikalische Modelle wurden auf der Grundlage von Bohrlochinformationen entwickelt und untersucht. Schließlich wurde ein Modell erstellt, das auf den dreidimensionalen Verteilungen der hydraulischen Leitfähigkeit sowie der abgeschätzten Oberkante eines Grundwasserstauers basiert und dieses parameterisiert.

Der in dieser Arbeit vorgestellte umfassende Ansatz, der die Integration verschiedener geophysikalischer Methoden, Deep Learning und Pedotransferfunktionen umfasst, zeigt erhebliches Potenzial für die verbesserte Charakterisierung bodenphysikalischer und hydraulischer Untergrundeigenschaften in verschiedenen Maßstäben und Umgebungen. Dies schließt tonreiche Hangrutschungen und kleine Einzugsgebiete ein und trägt zur Verbesserung von hydrologischen und hydrogeologischen Modellierung sowie zum Verständnis der Wechselwirkungen zwischen Oberflächen- und Grundwasser bei.

Acknowledgment

I would like to express my deepest gratitude to my supervisor, Adrián Flores Orozco, for his invaluable guidance and insightful feedback throughout this dissertation journey. His expertise and encouragement have been instrumental in shaping both this research and my academic growth.

I am also grateful to my peers and colleagues at TU Wien and all the other impressive people I met along the way for their stimulating discussions, constructive criticism, and collaborative spirit. Their diverse perspectives and camaraderie have enriched my research experience and contributed significantly to this work. Many friendships have grown, for which I am truly grateful.

Finally, my heartfelt thanks go to my family and my partner for their unconditional love, patience, and understanding during the challenging times of my academic pursuit. Their constant encouragement and belief in my abilities have been a source of strength and motivation.

Contents

1 Introduction

1.1 Scientific background and state of research

Climate change is a pressing global issue with far-reaching consequences, causing a range of extreme weather events such as heatwaves, droughts, floods and wildfires that significantly impact communities and ecosystems worldwide (Jentsch and Beierkuhnlein, 2008; Cook et al., 2018; Dunn et al., 2020; Balting et al., 2021). Although its implications have been predicted decades ago, stakeholders, governments and companies are only now slowly starting to recognize its imminent consequences. Despite international efforts to reduce global CO_2 emissions, it is becoming increasingly clear that worldwide reduction goals are unlikely to be met (Lui et al., 2021; Boubaker et al., 2024). This reality necessitates a shift in focus towards mitigation strategies to manage the impacts of climate change (Beermann, 2011; Adekola and Lamond, 2022).

Among the before mentioned hazards, climate change is having a significant impact on landslide development and the challenges associated with it. The increasing frequency and severity of extreme weather events (Dunn et al., 2020), such as heavy rainfall and flooding (Ban et al., 2015; Papalexiou and Montanari, 2019), are leading to an increase in the number of landslides (Sobie, 2020; Picarelli et al., 2021; Lin et al., 2020; Lin et al., 2022). Additionally, rising temperatures and changes in precipitation patterns in conjunction with deforestation are causing changes in the stability of slopes, making them more susceptible to landslides (Ren et al., 2012; Lehmann et al., 2019; Manchado et al., 2022).

One of the main challenges associated with climate change and landslides is the difficulty in accurately predicting and mitigating the effects of these events. This is due to the complex nature of the internal landslide structure and their associated mobilization processes, as well as the limited understanding of the underlying geological and hydrological processes (Van Asch et al., 1999; Bogaard and Greco, 2016; Greco et al., 2023). In particular, Greco et al., 2023 argue that there is still a conceptual mismatch of soil mechanics and hydrological models that is poorly understood and underinvestigated. Additionally, the impact of landslides on communities and infrastructure can be severe, leading to loss of life, property damage, and economic disruption (Petley, 2010; Haque et al., 2019). This requires a multi-disciplinary approach that integrates knowledge from fields such as geology, hydrology, engineering, and social sciences for effective landslide management strategies (Federici et al., 2007; Ausilio and Zimmaro, 2017; Bhandari and Dhakal, 2021). Effective management strategies must also consider the needs and perspectives of local communities and stakeholders.

In this context, geophysics emerges as a crucial tool for providing detailed subsurface information, which is essential for understanding and addressing climate change-related challenges, in particular in the context of landslides and mass movements. Near-surface geophysics, focusing on the earth's subsurface up to depths of a few hundred meters, offers valuable insights into the physical properties of the ground (Everett, 2013). By providing subsurface properties such as electrical conductivity or seismic velocity, it permits to obtain detailed 2D and 3D models of the subsurface. Given adequate petrophysical relationships such geophysical models can be transformed to soil-physical and hydrological models (Binley et al., 2015). This information is particularly valuable in understanding landslides and mass movements, as it reveals crucial details about subsurface structure, moisture dynamics and mobilization mechanisms (Whiteley et al., 2019; Pazzi et al., 2019). Such landslide knowledge is instrumental in developing effective strategies to mitigate the risks associated with these climate change-induced geological hazards, ultimately contributing to more resilient and adaptive communities in the face of ongoing environmental challenges.

Traditionally, geophysical landslide investigations relied heavily on electrical resistivity tomography (ERT), which permits to solve for 2D and 3D models of the subsurface electrical resistivity, or its inverse electrical conductivity. Due to the sensitivity of the obtained electrical resistivity to soil moisture and lithological variations, both of which are crucial in understanding landslide dynamics, ERT has been extensively applied to characterize landslides (e.g., Perrone et al., 2014, and references therein). However, the limitations of using a single method, along with the impossibility of the ERT method to discriminate between clay-rich and water-saturated zones, both characterized by low electrical resistivity, have become apparent, leading to the recognition of the need for multidisciplinary approaches (Bichler et al., 2004; Jongmans and Garambois, 2007; Hibert et al., 2012). Consequently, most contemporary publications in this field employ a combination of geophysical techniques, such as electrical, seismic and electromagnetic methods, alongside geotechnical methods and ground-truthing through soil-physical sampling (e.g., Soto et al., 2017; Pazzi et al., 2019; Di Maio et al., 2020; Perrone et al., 2021; Marciniak et al., 2021). This integrated approach helps to constrain the uncertainty in landslide models and provides a more comprehensive understanding of the subsurface conditions.

In recent years, induced polarization (IP) has emerged as a promising technique for environmental applications (Kemna et al., 2012). Among more recent applications are the assessment of permafrost dynamics (Steiner et al., 2021; Maierhofer et al., 2022; Maierhofer et al., 2024), the monitoring of bioremediation processes and microscale particle injections (Flores Orozco et al., 2011; Flores Orozco et al., 2013; Flores Orozco et al., 2015; Flores Orozco et al., 2019c), the quantification of critical raw material contents (Katona et al., 2024) or the quantification of biogeochemical carbon turnover hotspots (Katona et al., 2021) just to name a few examples. As an extension of ERT, IP not only permits to delineate the electrical resistivity but also the quantification of the capacitive properties of subsurface materials. This additional information about the capacitive behavior of subsurface materials allows for better discrimination between different lithological, hydrological or even geochemical units within the subsurface (Kemna et al., 2012), potentially opening up new possibilities for characterizing clay-rich landslides. At the outset of this dissertation, the contribution of IP to landslide research was limited with only a handful of published manuscripts (Marescot et al., 2008; Taboga, 2011; Sastry et al., 2012; Dahlin et al., 2013; Sirles et al., 2013). Apparently, there was a notable lack of field-scale studies investigating the potential of IP in landslide characterization, particularly in the realm of spectral IP (SIP). SIP measurements are performed at different excitation frequencies to characterize the frequency-dependent behavior of the subsurface electrical properties, which has been linked to soil textural (Weller et al., 2010; Revil et al., 2012c) and subsequently soil hydraulic parameters (Slater, 2007; Weller et al., 2015). This gap in the literature highlighted the need for comprehensive field-scale investigations to explore the full potential of the IP method in enhancing our understanding of (1) the internal structure of landslides along with their soil textural and hydraulic parameters and (2) the processes associated with triggering mechanisms.

Among the less commonly used geophysical imaging techniques in landslide research is the electromagnetic induction (EMI) imaging method. EMI is a frequency-domain electromagnetic method that permits the mapping of variations in the apparent electrical conductivity (ECa), and, in the case of inverted data, can provide 3D information about the electrical conductivity in the subsurface. The application of EMI imaging in soil science has been manifold (Doolittle and Brevik, 2014a; Boaga, 2017), including the monitoring of soil moisture (Shanahan et al., 2015; Martini et al., 2017a) and soil salinity variations (Akramkhanov et al., 2014; Yao et al., 2016), delineation of soil compaction (Schmäck et al., 2022), texture variations (Abdu et al., 2008; Zhao et al., 2019), and prediction of hydraulic properties (Brosten et al., 2011; Uhlemann et al., 2022). Although apparent electrical conductivity (ECa) maps have been the traditional approach, with the advent of computationally efficient inversion algorithms

(Triantafilis and Monteiro Santos, 2013; McLachlan et al., 2021a; Klose et al., 2022) and multi-coil/multi- configuration sensor systems, the field has progressed to the use of inverted 2D and 3D electrical conductivity (EC) models, that provide valuable depth-specific information.

Given the simple field procedures and ease of implementation in challenging terrain conditions, the sensitivity of EC to soil textural and even hydraulic properties, along with the rapid acquisition times, the EMI method appears to be a well-suited to tool for investigating complex soil structures typically associated with landslide-prone or already landslide-affected areas. However, to date, the application of EMI in slope stability studies remains relatively unexplored (Mauritsch et al., 2000; Grandjean et al., 2011; Altdorff and Dietrich, 2014; Kušnirák et al., 2016), underscoring the need for further research to fully realize the potential of the EMI method for an enhanced characterization of landslides as well as the associated processes.

As previously implied, the understanding of infiltration and subsurface water flow patterns holds significant importance in addressing the complex hydrological processes within landslides (Greco et al., 2023). However, when considering a larger scale, the detailed characterization of subsurface water flow is also critical for the understanding of groundwater recharge and its availability, which, due to climate change is projected to undergo significant shifts with substantial regional variations (Amanambu et al., 2020; Al Atawneh et al., 2021; Reinecke et al., 2021). This highlights the urgent need for innovative approaches in hydrogeology, which has promoted extensive research into the application of geophysics for hydrological and hydrogeological purposes along with the development of the field of hydrogeophysics (e.g., Binley et al., 2015; Boaga, 2017; Lubczynski et al., 2024, and references therein). Several studies conducted on laboratory samples observed a link between the frequency-dependent characteristics of the induced polarization response and grain size related properties, such as a referential grain size, grain size distribution, and pore length (e.g., Titov et al., 2002; Koch et al., 2011; Revil et al., 2012c), and further experiments targeted the potential relationship between spectral parameters and soil hydraulic properties (Titov et al., 2010; Revil and Florsch, 2010; Weller et al., 2015; Weller and Slater, 2019), which promoted confidence in the SIP method as a suitable tool for field-scale hydrogeological applications. However, the upscaling of laboratory-derived relationships, measured in well-controlled conditions, to field-scale applications presents significant challenges (e.g., Kemna et al., 2012). In particular, in the case of multi-frequency data, electromagnetic interference occurring at higher frequencies often impedes meaningful interpretation of the observed induced polarization response (Zimmermann et al., 2008). Moreover, the controlled settings in laboratory experiments are difficult to replicate under field conditions, especially when considering the complexities introduced by frequency-dependent measurements. Factors such as subsurface heterogeneity, anisotropy, varying soil moisture, and scale-dependent processes introduce complexities that are not fully captured in laboratory studies or are intentionally excluded. As a result, the direct application of laboratory-derived relationships to field-scale scenarios often leads to inaccurate estimations of hydraulic parameters because specific fitting parameters in the relationships are unknown or need to be approximated using proxy solutions (Hördt et al., 2009; Flores Orozco et al., 2022).

While laboratory experiments provide valuable insights into the fundamental relationships between the frequency-dependent IP response and hydraulic properties, field-scale studies are crucial for refining these relationships and advancing the applicability of the method. Unfortunately, there is a notable lack of comprehensive field-scale studies in this area, particularly those addressing the challenges of interpreting SIP data (Hördt et al., 2009; Attwa and Günther, 2013; Revil et al., 2021; Flores Orozco et al., 2022). This research gap hinders the development of robust upscaling methodologies and limits the practical application of SIP for hydraulic parameter estimation in real-world scenarios. The complexity of interpreting frequency-dependent IP responses under heterogeneous field conditions further exacerbates this challenge. Hence, alternative approaches that permit the quantification of hydraulic properties without the need to upscale complex laboratory relationships are required.

Pedotransfer functions (PTFs) enable the prediction of complex soil-hydraulic properties, such as saturated hydraulic conductivity, utilizing readily measurable soil physical data including sand, silt, and clay fractions, bulk density, and soil organic matter content (e.g., Patil and Singh, 2016; Van Looy et al., 2017a) . PTF implementations range from relatively simple regression models to sophisticated artificial intelligence-assisted prediction models (Zhang and Schaap, 2019) and PTFs that predict hydraulic conductivity are commonly developed for extensive databases of point-scale infiltration measurements, aiming at generalized formulations that can provide predictions at the local scale for diverse soil-textural settings. Thus, the use of PTFs in conjunction with geophysical methods could bridge the gap between laboratory-derived relationships and field-scale applications, provided it is possible to establish a link between the geophysical properties, for instance electrical conductivity, and the soil-physical parameters necessary for PTF application. Therefore, the implementation of PTFs could be considered an intermediate solution as well as a tool to evaluate the prediction performance of upscaled laboratory relationships (Hadzick et al., 2011; van Leeuwen et al., 2024).

This thesis focuses on advancing beyond the measurement of geophysical properties to the quantification of parameters that can be directly utilized by other disciplines and stakeholders and investigates the use of PTFs in geophysical frameworks. By developing approaches that provide quantitative, actionable information at the field scale, geophysical techniques such as SIP and EMI can become increasingly valuable tools for understanding and characterizing subsurface properties.

1.2 Research hypotheses and objectives

The hypotheses and derived objectives presented here emerged from the evolving landscape of geophysical methods and its current state of research. They reflect the ongoing efforts to enhance the understanding of complex subsurface systems and improve the accuracy and reliability of field-scale predictions and focus on advancing geophysical methods for subsurface landslide and catchment characterization, with a particular emphasis on improving the prediction of hydraulic properties. Specifically, the key research hypotheses and derived objectives are:

Hypothesis 1: *EM coupling affects frequency-dependent IP data at frequencies as low as 1 Hz and the use of optimized field procedures and cables can improve the quality of field-scale IP data.*

Objective: Development of robust field procedures for the collection of high-quality frequency-dependent IP data with a particular focus on data collected at the higher frequencies, subject to EM coupling.

Hypothesis 2: *SIP can provide a more detailed characterization of clay-rich landslides compared to traditional ERT alone, such that it permits to distinguish between water-saturated and clay-rich zones. In conjunction with EMI imaging, the understanding of the internal landslide structure and processes can be significantly improved.*

Objective: Application and evaluation of field-scale (S)IP and EMI imaging in the scope of landslide characterization, particularly for clay-rich sites.

Hypothesis 3: *PTFs used in conjunction with geophysical measurements can improve field-scale predictions of hydraulic properties compared to direct upscaling of laboratory relationships.*

Objective: Evaluation of approaches that permit to obtain hydraulic properties from geophysical data: using experimental petrophysical relationships and pedotransfer functions or through upscaling of laboratory-derived relationships.

Hypothesis 4: *Deep learning techniques can provide an effective alternative to deterministic inversion for processing and interpreting of EMI imaging data.*

Objective: Investigation of using deep learning techniques as an alternative to deterministic inversion of geophysical data.

1.3 Structure of the thesis

This thesis consists of eight chapters, with Chapters 3-6 drawing from material submitted to or published in peer-reviewed journals. The structure is as follows:

Chapter 2 provides a commentary on the predominating relationships of the electrical subsurface properties to soil-physical, chemical and hydraulic parameters. This is followed by an introduction and discussion of PTFs that permit to predict hydraulic parameters from easy-to-measure soil-physical properties such as the soil volume fractions or bulk density.

Chapter 3 addresses the implementation of adequate and robust field procedures for the collection of high-quality SIP data. Specifically, it presents a comparison of data collected with standard multicore and novel coaxial cables and examines how EM coupling interferes with the data. It is demonstrated that, contrary to the common assumption of EM coupling only arising at higher frequencies, EM coupling can be observed at frequencies below 10 Hz. Furthermore, this chapter emphasizes the necessity of using cables with takeout lengths (i.e., the length between each electrode connection) identical, or preferably not significantly larger than, to the chosen electrode separation, if the objective is to minimize the effects of EM coupling. Overall, this chapter clearly demonstrates that the use of coaxial cables provides superior data over the entire frequency range observed when compared to standard multicore cables, while maintaining the same simple field procedures.

Chapter 4 presents the first publication that implemented field-scale SIP and EMI imaging for a small, well-equipped landslide in Austria. The application of multiple mapping IP profiles and SIP along one profile, in conjunction with an extensive geotechnical and soil-physical database, facilitated a comprehensive evaluation of the SIP method's potential in landslide research. A significant qualitative correlation between geotechnical parameters and the frequency dependent behavior of the subsurface electrical properties was observed, which permitted an enhanced interpretation of subsurface water flow and infiltration pathways within the landslide.

Chapter 5 builds upon the findings of Chapter 4 and presents a multi-methodical approach to characterized 3D soil textural and hydraulic subsurface properties of a hillslope affected by mass movements. The approach integrates dense IP mapping in conjunction with TEM, RST, and soil-textural information collected from five boreholes. Following the integration of structural information regarding the distribution of subsurface electrical conductivity provided by TEM into the inversion of the IP data, a quantitative correlation of the complex conductivity response with the soil volume fractions of sand, silt and clay was established and these relationships were evaluated using borehole information not used in the correlation process. Subsequently, the application of a PTF using the predicted soil-textural information permitted the delineation of a 3D hydrogeophysical model, parameterized in terms of the subsurface hydraulic conductivity, and the geometry of an aquiclude along with preferential flow paths.

Chapter 6 investigates emerging techniques and presents a multi-step framework that combines deep learning and EMI mapping to predict soil-textural and hydraulic properties at the catchment scale (66 ha). A novel deep learning network to "invert" EMI data is outlined and its performance is evaluated through comparison with the standard deterministic inversion approach. Soil textural information, obtained from an extensive soil survey conducted in the catchment, permitted the development of experimental petrophysical relationships linking the inverted electrical conductivity to the soil volume fraction of sand, silt and clay. Recalibrating a field-scale PTF available for the catchment using the predicted soil-textural information enabled the prediction of subsurface hydraulic conductivity at the catchment scale, the knowledge of which is essential to calibrate hydrogeological models to enhance the understanding of surface-groundwater interactions and runoff processes.

Chapter 7 extends the research presented in Chapter 6 towards developing a hydrogeophysical representation of the research catchment by using an extensive dataset of IP mapping profiles collected throughout the catchment over the past decade. Such dataset, in conjunction with ground-truth information from boreholes, permitted to extend the soil-textural and hydraulic information to depths of up to 40 m. Based on the available borehole information, the chapter examines potential conceptual hydrogeophysical models, with one model subsequently being parameterized by means of three-dimensional hydraulic conductivity distributions and the topography of confining layers.

Chapter 8 concludes this dissertation and summarizes the key findings from all previous chapters. Moreover, this chapter provides an outlook for future research that could extend on the results presented herein.

2 Material and methods

2.1 Electrical properties and their relation to soil-physical, chemical, and hydraulic properties

2.1.1 Conduction and polarization mechanisms in porous media

Three processes govern the conduction in earth materials (Figure 2.1): ionic transportation of charge through (1) conduction via ions dissolved within the pore fluid filling the pore space (σ_f), (2) conduction via ions in the electrical double layer (EDL), forming at the grain-fluid interface in the so-called surface conduction (σ_s), and, in the presence of metallic minerals and semiconductors, (3) transportation of charge via mobile electrons in the electron conduction (σ_m) (Binley and Slater, 2020). In general, the conductivity (σ) of a material depends on the mobility and number of charges available. Considering a single charge carrier i, the conductivity is given by (Binley and Slater, 2020)

$$\sigma_i = \hat{n}_i \hat{Z}_i e \beta_i \tag{2.1}$$

where $\hat{Z}_i$ is the valence of charge carrier, $\hat{n}_i$ is the charge carrier density, e is the elementary charge ($1.6022 \times 10^{-19}\,\mathrm{C}$) and β_i is the mobility of the charge carrier (in $\mathrm{m^2 s^{-1} V^{-1}}$).

Provided the presence of water, ionic conduction is the dominant charge transportation process for earth materials without metallic minerals and semiconductors. In such, the mobility of the ions β substantially defines the fluid's conductivity. β_i is given by

$$\beta_i = \frac{\hat{Z}_i e D_i}{k_b T} \tag{2.2}$$

where D_i is the diffusion coefficient of the charged species (in $\mathrm{m^2 s^{-1}}$), T is the temperature in Kelvin (K), and k_b is Boltzmann's constant ($1.3806 \times 10^{-23}\,\mathrm{m^2 kg s^{-1} K^{-1}}$). Since the diffusion coefficient itself is also directly proportional to the temperature (Jost, 1952), the inverse relationship of β_i with temperature, as stated in equation 2.2 is only apparent. In fact, for low temperatures ($< 250°\mathrm{C}$), the conductivity σ_i increase with temperature (Glover, 2015; Binley and Slater, 2020). β_i can also be parameterized using the viscosity (η in Pa s) of the fluid and the radius r_i of the hydrated ion

$$\beta_i = \frac{\hat{Z}_i e}{6\pi\eta r_i}. \tag{2.3}$$

Inserting equation 2.3 into equation 2.1 yields an alternative expression (Glover, 2015):

$$\sigma_i = \frac{\hat{n}_i \hat{Z}_i^2 e^2}{6\pi\eta r_i}. \tag{2.4}$$

which highlights that the conductivity of a solution is proportional to the charge concentration, the square of the charge carried ($\hat{Z}_i^2 e^2$), and indirectly proportional to the fluid viscosity and radius of the hydrated ion (Glover, 2015). Considering that cations and anions have different hydrated radii, equation 2.4 lays the foundation for different conductivity contributions from cations and anions (Glover, 2015). Moreover, since viscosity decreases with temperature, σ_i will increase, given the inverse proportionality in equation 2.4.

The EDL forms at the interface between a charged solid surface (such as mineral grains) and a pore fluid (Figure 2.1). It consists of two distinct layers: the first layer, known as the Stern layer is composed of ions that are strongly adsorbed onto the surface of the solid due to electrostatic attraction and these ions are typically counterions that neutralize the surface charge of the mineral (Revil, 2012; Glover, 2015; Binley and Slater, 2020). Since the surface charge of the mineral cannot be balanced entirely (Glover, 2015), a diffuse layer develops beyond the Stern layer, where ions are more loosely associated with the surface trying to balance the remaining charge of the mineral grain (negative charge in Figure 2.1). In this region, the concentration of ions decreases exponentially with the distance from the surface (Binley and Slater, 2020). The overall effect of the EDL is the creation of a potential difference across the interface, which can influence the movement of ions in the pore fluid and affect the electrical conductivity of the material through surface conduction along the EDL (σ_s in Figure 2.1).

The EDL is particularly significant in fine-grained soils and clays, where the large surface area relative to volume enhances its impact on charge transport processes (Leroy and Revil, 2004; Revil, 2012). The effective width of the diffuse layer is assumed to be twice the Debye screening length (χ_d), given by (Revil and Glover, 1997):

$$\chi_d = \sqrt{\frac{\varepsilon k_b T}{2 N_A e^2 I_0}}. \tag{2.5}$$

ε is the dielectric permittivity, N_A is the Avogardo constant ($6.022 \times 10^{23}\,\mathrm{mol}^{-1}$) and I_0 is the ionic strength (in mol m^{-3}) given by (Revil and Glover, 1997)

$$I_0 = 0.5 \sum_i^n \hat{Z}_i^2 C_{(c)i} \tag{2.6}$$

where $C_{(c)i}$ is the concentration (in mol m^{-3}) of each ionic species (i) in the fluid. Hence, due to the lower number of cations in low-salinity fluids compared to high-salinity fluids, the diffuse layer is thicker at low salinities and is always significantly thicker than the Stern layer (Glover, 2015).

In absence of metallic minerals and semiconductors, the bulk conductivity (σ) of a porous medium is composed of the contributions of electrolytic conduction within the fluid (σ_f) and surface conduction (σ_s) along the mineral-grain interface in the EDL:

$$\sigma = \sigma_f + \sigma_s \tag{2.7}$$

whereas both conduction mechanisms are assumed to add in parallel (Waxman and Smits, 1968). Archie's law is an empirical relationship (Archie, 1942) that, for a fully saturated medium, relates the bulk conductivity ($\sigma_{[s]}$) to a conducting phase (σ_w) and a formation factor F, that accounts for the volume and connectivity of the conducting phase (Binley and Slater, 2020). This model can be readily extended to incorporate surface conduction, as follows

$$\sigma_{[s]} = \sigma_{f[s]} + \sigma_{s[s]} = \frac{1}{F}\sigma_w + \frac{1}{F_s}\sigma_{EDL} \tag{2.8}$$

where

$$F = \phi^{-m} \tag{2.9}$$

in which ϕ is the interconnected porosity and m is called the cementation factor, accounting for the reduction of connectivity and tortuosity of the pore space (Archie, 1942). $F_s \neq F$ because the interconnected pores may not equally contribute to electrolytic and EDL conduction, as evidenced by situations where the EDL maintains connectivity between closely spaced minerals that do not facilitate electrolytic con-

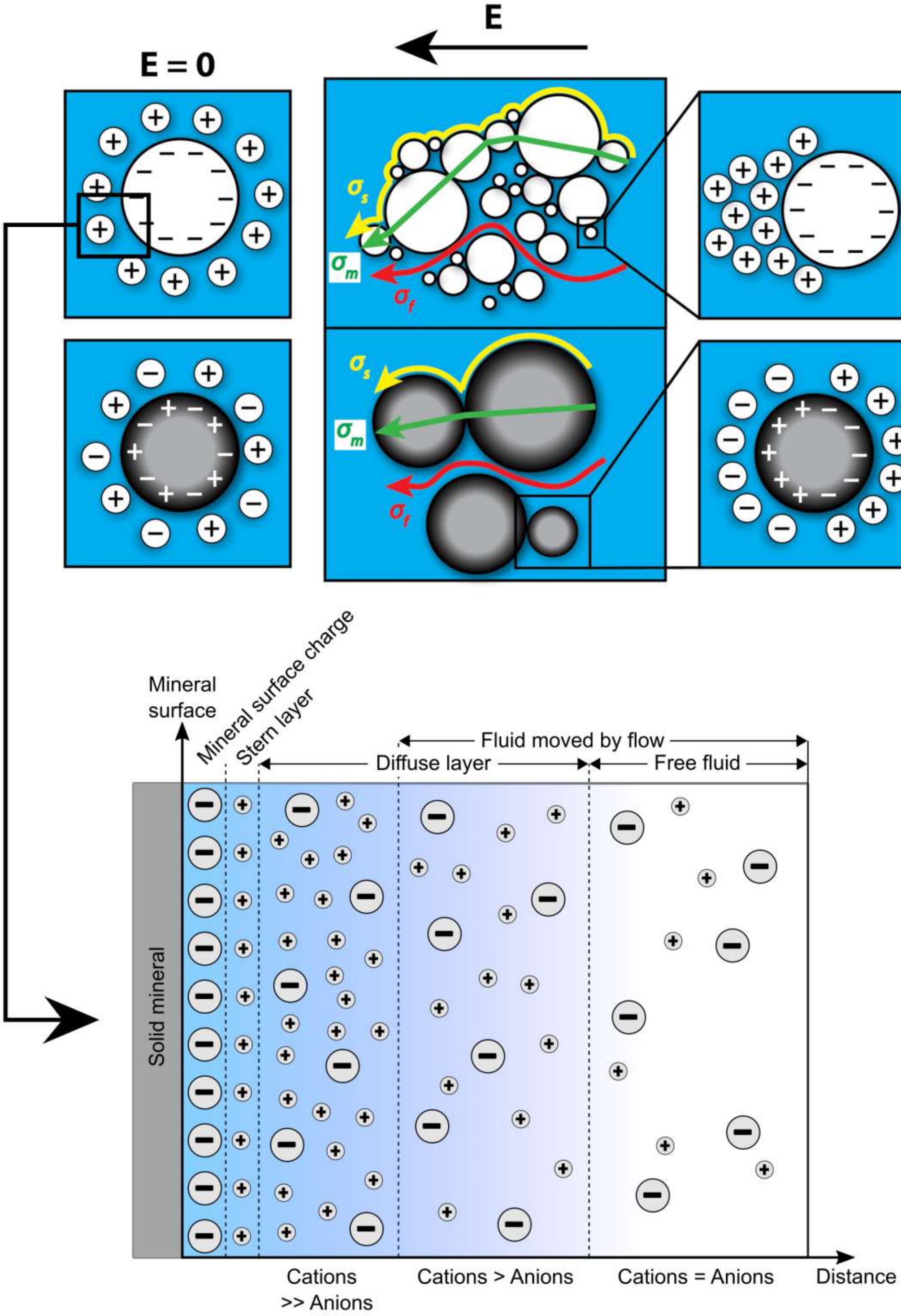

Figure 2.1: Conduction and polarization mechanisms for nonconducting particles (white spheres) and electron conducting particles (grey spheres) when an external field (E) is applied indicating the redistribution of ions for the different particles. The bottom plot illustrates the electrical double layer and the distribution of ions within it (modified after Glover, 2015; Binley and Slater, 2020).

duction (Binley and Slater, 2020). Equations 2.5 and 2.6 show that σ_{EDL} is related to the electrochemical properties of the charge carriers. However, it has been found that σ_{EDL} is in fact related to both the electrochemical properties and the interfacial geometry, which can be quantified by a characteristic length scale (Λ) (Johnson et al., 1986). σ_{EDL} can now be given as

$$\sigma_{EDL} = \frac{2\Sigma}{\Lambda} \tag{2.10}$$

where Σ denotes the surface conductance (in S). Σ can, for a single ion in the EDL, be approximated using equation 2.1, and, is thus, a function of ion mobility, charge density, and valence. Inserting equation 2.10 into equation 2.8 under the assumption that $F_s = F \neq \phi^{-m}$, yields

$$\sigma_{[s]} = \frac{1}{F}(\sigma_w + \frac{2\Sigma}{\Lambda}) \tag{2.11}$$

Alternatively, σ_{EDL} can be related to the pore volume normalized surface area (S_{por}), the thickness of the EDL (δ) and the intrinsic conductivity (σ_{diff}) of the diffuse layer as follows

$$\sigma_{EDL} = S_{por}\delta\sigma_{diff}. \tag{2.12}$$

For a capillary bundle (Weller and Slater, 2012), $\Lambda = 2/S_{por}$, and, thus

$$\sigma_{EDL} = \frac{2\Sigma}{\Lambda} \cong S_{por}\Sigma \tag{2.13}$$

which further simplifies equation 2.11 to

$$\sigma_{[s]} = \frac{1}{F}(\sigma_w + \frac{2\Sigma}{\Lambda}) \cong \frac{1}{F}(\sigma_w + S_{por}\Sigma). \tag{2.14}$$

Assuming that both σ_w and σ_{EDL} are a function of saturation S_w, equation 2.14 can be modified for partially saturated conditions as such (Binley and Slater, 2020)

$$\sigma_{[ps]} = \frac{1}{F}(\sigma_w S_w^n + \frac{2\Sigma}{\Lambda}S_w^p) \cong \frac{1}{F}(\sigma_w S_w^n + S_{por}\Sigma S_w^p). \tag{2.15}$$

where n and p are the saturation coefficients of the electrolytic and surface conductivity, respectively.

Having explored the electrical conduction mechanisms in porous media, it is important to consider the polarization mechanisms that contribute to their complex electrical behavior. In absence of electron conducting particles, these polarization processes are intimately linked to the EDL and the measured electrical conductivity effectively represents a complex property (σ^*), where the real part (σ') refers to energy loss (conduction) and the imaginary part (σ'') to temporary energy storage (polarization) with $\sigma^* = \sigma' + i\sigma''$. Moreover, the complex conductivity is a frequency dependent property and different polarization mechanisms can be observed in the investigated frequency range, and thus

$$\sigma^*(\omega) = \sigma'(\omega) + i\sigma''(\omega) \tag{2.16}$$

where ω is the angular frequency. Hence, the frequency dependent complex bulk conductivity ($\sigma^*(\omega)$) is now given as the parallel addition of a real valued electrolytic conductivity (σ_f) assumed to be non-polarizable and a complex valued surface conductivity (σ_s^*). Equation 2.16 can now be rewritten as (Vinegar and Waxman, 1984; Lesmes and Frye, 2001)

$$\sigma^*(\omega) = \sigma_f + \sigma_s^* = \sigma_f + \sigma'_s(\omega) + i\sigma''_s(\omega). \tag{2.17}$$

Therefore, the measured complex conductivity is related to the electrolytic and surface conductivity as

$$\sigma'(\omega) = \sigma_f + \sigma'(\omega) \tag{2.18}$$

$$\sigma''(\omega) = \sigma''_s(\omega) \tag{2.19}$$

The relevance of equations 2.18 and 2.19 is that while the real part of the complex conductivity depends on the combination of the electrolytic and surface conductivity pathways, the imaginary part only detects the surface conduction pathway (Binley and Slater, 2020). This fact potentially permits to solve the ambiguities regularly observed in the interpretation of conductivity alone (as obtained from direct current (DC) resistivity measurements), where the relative contributions of σ_f and σ'_s are unknown and highlights the added value of considering the polarization effect.

Kemna et al., 2012 identified five main polarization mechanisms that dominate at frequencies below 1 MHz:

1. Maxwell-Wagner polarization arises due to discontinuities in the electrical conductivity at interfaces between different phases (solid, liquid, gas) and is not

related to the surface conductivity (Binley and Slater, 2020). When an electric field is applied, free charge distributions form near the interfaces between different phases, leading to the accumulation of charges and the creation of an polarization effect at frequencies higher than 100 Hz (Chen and Or, 2006; Lesmes and Morgan, 2001; Binley and Slater, 2020).

2. Stern layer polarization at the inner part of the EDL related to tangential displacement of counterions in the Stern layer (Revil, 2012; Bücker et al., 2019a).

3. Diffuse layer polarization at the outer part of the EDL related to both radial and tangential fluxes of counterions in the diffuse layer (Revil, 2012; Bücker et al., 2019a; Niu, 2023).

4. Membrane polarization occurring at the EDL due to the formation of ion-selective zones resulting ion concentration gradients in the interconnected pore space (Marshall and Madden, 1959; Titov et al., 2002; Binley and Slater, 2020).

5. Electrode polarization, taking place in presence of electron conducting particles and can be typically observed at lower frequencies. To cancel out an external applied electric field, the mobile charges of the electron conducting particle redistribute along its surface. As a response, the induced surface charge attracts counterions and charges the electrolyte around the poles of the particle (Figure 2.1). Hence, electrode polarization also takes place at the EDL, but the main difference is that the particle itself polarizes (Wong, 1979; Bücker et al., 2018; Bücker et al., 2019b).

As stated by Kemna et al., 2012, and others, the current conceptualization of the Stern, diffuse and membrane polarization, all affected by characteristics of the EDL, are closely related. The driving factors for EDL polarization mechanisms include the pore geometry, i.e., the ratio of narrow to wide pores and pore throat sizes (Bücker and Hördt, 2013; Kreith et al., 2024), the surface charge affecting the ion distribution and transport in both Stern and diffuse layers (Bücker et al., 2019a; Kreith et al., 2024), characteristics of the electrolyte, such as salinity and temperature (Revil, 2012), and the specific surface area (c.f. equation 2.13) among other factors. While mechanistic, analytic, and semi-analytic models are being actively developed to understand the EDL polarization mechanisms and their frequency behavior (Schwarz, 1962; Leroy and Revil, 2009; Bücker et al., 2019a; Kreith et al., 2024), previous efforts were based on phenomenological models without physical foundations. Such dispersion models aim to describe the shape of the frequency response and permit to obtain a characteristic relaxation time (τ_0), defining the dominant length-scale of the polarization process Binley and Slater, 2020. One commonly used model, among others (Börner et al., 1996a; Weigand and Kemna, 2016), is the one proposed by Cole and Cole, 1941 which can be rewritten for complex conductivity as

$$\sigma^*(\omega) = \sigma_\infty - \frac{\sigma_\infty - \sigma_0}{1 + (i\omega\tau_0)^c} \tag{2.20}$$

where σ_0 and σ_∞ are the low and high frequency asymptotes, c describes the steepness of the curve and τ_0 is the characteristic relaxation time (i.e., the frequency where the model has its peak). The term $\sigma_\infty - \sigma_0$ is called normalized chargeability (m_n) and is a measure of overall polarization strength, thus, related to σ_s. τ_0 is of significant relevance given its correlation with grain or pore size (Pelton et al., 1978; Revil et al., 2012c) which has promoted extensive research into establishing relationships linking the polarization response to hydraulic properties (Revil and Florsch, 2010; Koch et al., 2011; Weller et al., 2015; Weller and Slater, 2019; Herold et al., 2024).

2.1.2 Predicting hydraulic properties from electrical properties

The concept of hydraulic conductivity is closely tied to Darcy's law, which describes fluid flow through porous media. Assuming a homogeneous, isotropic material, the fluid flux q (in m/s) and the gradient of the hydraulic head (h) are linked via the hydraulic conductivity K (in m/s)

$$q = -K\nabla h \tag{2.21}$$

with the negative sign indicating the direction of the flow opposite to the increasing hydraulic head. The permeability k, describing the geometrical properties of the porous medium, and K, are related by the fluid properties, namely the fluid density ρ (kg m^3) and dynamic viscosity η (N s/m^2) together with the gravitational acceleration g (m s^{-2}) as follows

$$K = \frac{k\rho g}{\eta}. \tag{2.22}$$

Geometrical models to determine k define an effective hydraulic radius r_{eff} representative of the pore size controlling fluid flow (Carman, 1939; Robinson et al., 2018). Such models were based on fluid flow through a network of capillary tubes (Carman, 1939) or based on percolation theory applied to a broad distribution of pore sizes (Katz and Thompson, 1987). Pape et al., 1987, for instance, related r_{eff} to S_{por} (μm), which yields the well-known PaRiS equation

$$k_{PaRiS} = \frac{475}{FS_{por}^{3.1}}. \tag{2.23}$$

Similarly, Katz and Thompson, 1987 showed that r_{eff} approximately relates to a characteristic length scale Λ (μm), here the dynamically interconnected pore radius, as derived from mercury injection capillary pressure method (MICP). Their model writes as

$$k_{KT} = \frac{\Lambda^2}{F8}. \tag{2.24}$$

Both models require properties defining a geometrical length scale (Λ, S_{por}) that cannot be directly measured and require intricate and costly laboratory testing. Moreover, F has to be known to apply the relationships, which is also difficult to estimate without knowledge of the fluid conductivity. Hence, extensive research focused on finding an equivalent geophysical length scale that can replace the geometrical length scale, while also investigating approaches to estimate F (Börner et al., 1996b; Robinson et al., 2018; Binley and Slater, 2020). In general, geophysical k-models will take the form

$$k_g = \frac{a}{F^b(\Upsilon)^d}. \tag{2.25}$$

where Υ is the geophysical length scale and a, b, and d are fitting parameters (Börner et al., 1996a; Weller et al., 2015). Possible substitutes for Υ are single frequency σ'' given the strong empirical correlation to S_{por} (Weller et al., 2010; Weller et al., 2015), or in case of frequency-dependent polarization behavior the normalized chargeability m_n (Weller et al., 2015) or a characteristic relaxation time τ (Revil et al., 2015a; Robinson et al., 2018). The estimation of F for field-scale applications is still related to considerable uncertainty, requiring an estimate of both the fluid conductivity and an appropriate value of the linear coefficient l relating the real part of the surface conductivity σ'_s to σ,″ so that F can be calculated as (Börner et al., 1996a)

$$F \cong \frac{\sigma_f}{\sigma'' - \frac{\sigma''}{l}} \tag{2.26}$$

Börner et al., 1996a suggested values for l in the range between 0.01 and 0.15, whereas other studies reported values of $l = 0.042$ (Weller et al., 2013) and $l = 0.037$ (Revil et al., 2015b).

2.2 Predicting hydraulic properties from non-geophysical data: pedotransfer functions

PTFs are empirical relationships that allow the estimation of difficult-to-measure soil properties from more easily obtainable soil data (Bouma, 1988). These functions serve as valuable tools in earth system sciences (Van Looy et al., 2017b) by providing a cost-effective means to predict complex soil attributes to model hydrological (Weber et al., 2024), climatological (Ya et al., 2024) and environmental processes (Neira-Albornoz et al., 2024) within the scope of land surface modeling (Overgaard et al., 2006; Blyth et al., 2021). PTFs typically utilize readily available soil information, such as texture, bulk density, and organic matter content, along with morphological properties and structural information, to estimate properties such as hydraulic and water retention characteristics (Minasny et al., 1999; Jana et al., 2007; Zhang and Schaap, 2019; Szabó et al., 2021), solute transport parameters (Minasny and Perfect, 2004) and more recently thermal conductivity (Markert et al., 2017; Tarnawski et al., 2020; Peng et al., 2024). The development and application of PTFs have significantly enhanced our ability to understand and model soil processes across various spatial and temporal scales (Nemes et al., 2003; Pringle et al., 2007; Weber et al., 2024), bridging the gap between easily measurable soil properties and those that are more challenging or expensive to determine directly, such as hydraulic conductivity functions and water retention characteristics (Vereecken et al., 1992; Van Looy et al., 2017b). In agriculture, PTFs permit to optimize irrigation schedules (Georgousis et al., 2009; Nemes et al., 2010), predict crop yields (Grassini et al., 2015), and to assess soil quality (Wösten, 1997); while hydrologists and environmental researchers use PTFs to estimate soil hydraulic properties (Zhang and Schaap, 2019; Weber et al., 2024) crucial to understand rainfall-runoff and water retention processes (Minasny et al., 1999; Sobieraj et al., 2001; Picciafuoco et al., 2019b), as well as processes related to contaminant and solute transport (Moeys et al., 2012; Achat et al., 2016). The significance and concurrent challenge of PTFs lie in their ability to leverage existing soil databases and surveys to generate valuable information about soil properties that would otherwise be impractical or infeasible to measure directly at large scales (Gutmann and Small, 2007; Shen et al., 2014). This capability has become increasingly crucial as the demand for high-resolution soil data grows in response to global challenges, such as water resource management and climate change adaptation (Gómez et al., 2023; Ya et al., 2024; Do et al., 2024). For conciseness, this introduction focuses on PTFs that permit the prediction of hydraulic conductivity.

2.2.1 Development of pedotransfer functions

To develop PTFs for predicting hydraulic conductivity K two approaches have to be considered: (a) point and (b) parametric PTFs (Zhang and Schaap, 2017; Szabó et al., 2021). Point PTFs relate the K values from field or laboratory measurements directly to the predictors (soil volume fractions, bulk density, organic matter content, etc.), while parametric PTFs use an adequate hydraulic model that describes the measured parameters (K and water retention parameters) in a closed-form equation and employ the predictors to develop empirical functions to estimate the parameters of the hydraulic model. As approach (b) can provide mathematical functions for the moisture retention and hydraulic conductivity curves used in mathematical models and modeling frameworks, it has been the preferred approach in the past three decades (Vereecken et al., 2010; Weber et al., 2024). Typical hydraulic models include the Brooks-Corey and Mualem-van-Genuchten models (Brooks and Corey, 1966; Mualem, 1976; van Genuchten, 1980), with the latter being widely employed but facing criticism due to its underlying assumption of a unimodal pore size distribution, which is rarely observed in natural soils (Vereecken et al., 2010). Approach (a) is typically applied for smaller catchments with soil characteristics not captured in the more generalized models such as (b), and, thus, are often site-specific (Picciafuoco et al., 2019b; Picciafuoco et al., 2019a) providing limited scalability.

The statistical methods to establish PTFs are manifold and are predominantly empirical in nature (Van Looy et al., 2017b). While approach (a) is typically developed for large databases, encompassing a wide range of soil types, climatic conditions and land use patterns in an effort towards generalizability (Rawls et al., 1982; Zhang and Schaap, 2017; Szabó et al., 2021), approach (b) is often targeted at specific use cases, such as catchments characterized by heavy soils (Picciafuoco et al., 2019b; Picciafuoco et al., 2019a), tropical regions (Gebauer et al., 2020; Gupta et al., 2021), or forest systems (Puhlmann and Wilpert, 2012; Lim et al., 2020), where the effect of roots control the pore structure. Due to their simplicity, the earliest approaches to develop PTFs were based on regression analysis using multiple linear and nonlinear regression (Gupta and Larson, 1979; Cosby et al., 1984), offering the advantage of being straightforward to implement and apply. However, regressions techniques may lack flexibility and tend to underfit, particularly when different predictors reveal different relationships to the soil properties within the database (Van Looy et al., 2017b). Consequently, machine learning techniques have gained prominence as they "can deal with non-linearities at the price of being susceptible to overfitting" (Weber et al., 2024, p. 3393). Many different approaches have been explored including artificial neural networks (Minasny and Perfect, 2004; Zhang and Schaap, 2017), support vector algorithms (Twarakavi et al., 2009), k-nearest neighbor methods (Nemes et al., 2006), decision or regression trees (Lilly et al., 2008; Jorda et al., 2015), random forests (Gupta et al., 2021; Jian et al., 2021; Darmann et al., 2024), and combinations of the aforementioned approaches in ensemble methods (Singh et al., 2022; Li et al., 2024b).

Evaluation of the established relationships typically involves two components: splitting of the dataset into calibration and validation subsets, and statistical analysis using metrics such as the root mean square error (RMSE), the coefficient of determination (R^2), the mean relative error (MRE) and the Akaike information critierion (AIC). Additionally, a functional evaluation can be conducted, where the applicability of the PTF is assessed by using the PTF as "input information in Earth system models and evaluating the Earth system model performance rather than just PTF performance" (Van Looy et al., 2017b, p. 1210), as, for instance, performed by Vereecken et al., 1992; Nemes et al., 2003; Chirico et al., 2010, among others.

2.2.2 About scales of pedotransfer functions

PTFs are applied at various scales, specifically: (i) local and field scale, (ii) regional scale, and (iii) coarse or large scale. Local- and field-scale PTFs, as their names imply, are typically derived based on laboratory (flow cell and constant head tests) and field measurements (infiltration and pumping tests) of K and represent the smallest scale at which PTFs are developed (Picciafuoco et al., 2019b; Weber et al., 2024). They are usually point PTFs developed for small soil and hydraulic datasets and often address specific use cases, where accuracy takes precedence over scalability. For scalability, regional scale PTFs are preferred, being developed for substantially larger databases, thus permitting to provide estimates for extensive areas and diverse soil conditions (Tóth et al., 2015; Nasta et al., 2021; Szabó et al., 2021). The largest application scale for PTFs is the coarse scale typically applied in land-surface models (Van Looy et al., 2017b). At this scale, the desired hydraulic properties cannot be directly measured (Weber et al., 2024) and sophisticated upscaling approaches are needed, which represents a significant challenge in developing coarse-scale PTFs (Imhoff et al., 2020; Li et al., 2024a).

2.2.3 Challenges associated with pedotransfer functions

In their extensive reviews Van Looy et al., 2017b and Weber et al., 2024 identified two major challenges with PTFs: extrapolation and scaling.

Extrapolation The applicability of PTFs is limited by the representativeness of the training data and extrapolating PTFs beyond their developed context may lead to poor results (McBratney et al., 2002; Nemes, 2015). Hence, providing metadata about the training data and the conditions under which the PTFs were developed is crucial for assessing their suitability (McBratney et al., 2011; Weynants et al., 2013); whereas uncertainty in their predictions should be quantified and propagated through subsequent models (Van Looy et al., 2017b). Efforts have been made to use published PTFs more efficiently through ensemble modeling and soil inference systems (McBratney et al., 2002; Guber et al., 2009; Li et al., 2024b). However, there remains a knowledge gap for specific, underrepresented soil systems, such as tropical regions (Gebauer et al., 2020; Gupta et al., 2021), or forest systems (Puhlmann and Wilpert, 2012; Lim et al., 2020).

Scaling Most PTFs are calibrated from point source data and assume no spatial correlation (Van Looy et al., 2017b), which poses difficulties when applying them to spatially distributed scenarios. Following the notion of Pringle et al., 2007, the evaluation of spatially distributed PTFs requires consideration of the correlation between observed and predicted quantities and the reproduction of observed variance across different scales, as well as the the analysis of the spatial pattern of model error (Van Looy et al., 2017b). While it is evident that PTFs can reproduce general spatial patterns, they often underestimate the magnitude of observed variance (Pringle et al., 2007). Moreover, upscaling of PTFs to provide information for coarse-scale modeling, presents additional challenges as soil and hydraulic parameters in these models cannot be directly measured (Van Looy et al., 2017b; Weber et al., 2024). While the scale dependence of PTFs has been recognized early (Pachepsky and Rawls, 2003; Pachepsky et al., 2006; Pringle et al., 2007), scaling still represents a field of extensive research, and sophisticated upscaling approaches using machine learning and data assimilation techniques are being actively developed (e.g., Imhoff et al., 2020; Li et al., 2024a, among others) in an effort towards PTFs that permit the prediction of hydraulic parameters across different scales.

3 Investigation of cable effects in spectral induced polarization imaging at the field scale using multicore and coaxial cables[1]

3.1 Introduction

Induced polarization (IP) is an extension of the DC-resistivity method, which provides information about the conductive and capacitive properties of the subsurface. The measurements can be collected at different frequencies, in the so-called spectral IP (SIP) method, to gain information about the frequency dependence of the electrical properties, commonly in the frequency range between 0.06 and 1000 Hz (e.g., Kemna et al., 2012; Flores Orozco et al., 2018b). Traditionally, SIP measurements are performed in the frequency-domain (FD), with imaging measurements deploying tens to hundreds of electrodes to perform thousands of readings based on four-electrode arrays (for further details on the method, see Binley and Kemna, 2005; Kemna et al., 2012). Taking into account the strong IP effect (hereafter referred to as polarization) of metallic minerals under the application of an external electrical field, SIP is a method commonly used for the prospection of mineral ores, among other mining applications (Pelton et al., 1978; Seigel et al., 2007). Developments in the accuracy of the measuring instruments (e.g., Zimmermann et al., 2008) and in the modeling algorithms (e.g., Binley and Kemna, 2005; Kemna et al., 2012; Günther and Martin, 2016) have permitted extension of the application of the SIP method to investigate processes and materials associated with much weaker polarization responses. To date, the SIP method has been applied in a variety of engineering, hydrogeologic, and environmental investigations (Kemna et al., 2012; Revil et al., 2012b; Binley et al., 2015; Flores Orozco et al., 2018b; Gallistl et al., 2018). In particular, within the past two decades, extensive laboratory studies have demonstrated a strong link between the SIP parameters and soil properties controlling water flow, therefore permitting the quantification of hydraulic conductivity (e.g., Börner et al., 1996a; Revil and Florsch, 2010; Weller et al., 2010; Binley et al., 2016). In addition, laboratory experiments have

[1] This chapter is based on: Flores Orozco, A., L. Aigner, and J. Gallistl (2021). "Investigation of cable effects in spectral induced polarization imaging at the field scale using multicore and coaxial cables". In: *Geophysics* 86.1, E59–E75. DOI: 10.1190/geo2019-0552.1

demonstrated the sensitivity of the SIP measurements to parameters of relevance accompanying different biological and geochemical processes in the emerging discipline of biogeophysics (Atekwana and Slater, 2009, for further references). Among these processes are the stimulation of microbial activity (e.g., Ntarlagiannis et al., 2005; Williams et al., 2005; Williams et al., 2009; Slater et al., 2007), the accumulation of biofilms (Aal et al., 2006; Revil et al., 2012a), and more recently, the geometry and growth of root systems (e.g., Corona-Lopez et al., 2019; Weigand and Kemna, 2019)

However, to date, SIP field applications are still rare. The necessity to collect data at different frequencies leads to significantly longer acquisition time for FD SIP imaging surveys than for standard electrical resistivity tomography (ERT), especially for data collected at low frequencies (< 1 Hz). Long acquisition times may hinder the collection of broadband SIP data in surveys performed under time constraints. Hence, some studies have reported field IP data collected only at a single frequency — or a few frequencies, for instance, for the monitoring of groundwater remediation by means of nanoparticle injections (Flores Orozco et al., 2015; Flores Orozco et al., 2019a), or for the investigation of bioremediation techniques (e.g., Williams et al., 2009; Flores Orozco et al., 2011). To date, broadband FD SIP imaging at the field scale has been reported for the estimation of hydraulic conductivity (Hördt et al., 2007), the monitoring of microbial activity during the immobilization of radionuclides (Flores Orozco et al., 2013), the delineation of hydrocarbon- impacted sites (Flores Orozco et al., 2012a), the investigation of landslides (Flores Orozco et al., 2018b; Gallistl et al., 2018), and — at smaller spatial scales — to detect fungi infection in trees (Martin and Günther, 2013). Recent studies have demonstrated that parameters describing the frequency dependence of the IP effect can also be retrieved from time-domain IP (TDIP) data, if the measurements record the full waveform and the inversion is performed with modern algorithms, opening the technique to new possibilities (e.g., Fiandaca et al., 2018; Olsson et al., 2019). Still, long pulse lengths (i.e., acquisition time) are required to gain information at low frequencies associated to slow polarization processes.

SIP surveys at high frequencies (i.e., above 1 Hz) are related to short acquisition times; yet they are subject to contamination of the data due to parasitic electromagnetic (EM) fields, commonly referred to as EM coupling (e.g., Pelton et al., 1978). EM coupling increases proportionally with the acquisition frequencies, and it is expected to contaminate measurements collected above 10 Hz (Wait and Gruszka, 1986; Binley et al., 2005; Kemna et al., 2012). Nonetheless, some studies have already observed that EM coupling dominates the SIP response at frequencies at approximately 5 Hz (e.g., Kemna et al., 2000; Gasperikova and Morrison, 2001; Williams et al., 2009;

Flores Orozco et al., 2011).

EM coupling is caused by either inductive or capacitive sources (e.g., Zimmermann et al., 2008; Zimmermann et al., 2019). Capacitive coupling (i.e., involving displacement currents) results from differences in the contact impedances between the electrodes and the subsurface or between the conductive shield of the cables and the surface, resulting in leakage currents (e.g., Zimmermann et al., 2008; Zimmermann et al., 2019; Zhao et al., 2013; Zhao et al., 2014). Capacitive EM coupling can also arise due to voltage differences between the cables used for voltage measurements and those used for current injection. The capacitive EM coupling (EM_{cc}) between parallel cables (of an infinite length) and an electrical field can be calculated (Charnock, 2005) as

$$\mathrm{EM}_{cc} \approx \frac{\pi \varepsilon_0}{\ln(D/a)}, \tag{3.1}$$

where D is the distance between the cables, a is the cable radius, and ε_0 is the electrical permittivity of free space.

Inductive coupling is related to temporal variations in the current flow (i.e., that produced by a magnetic field) along the wires connecting the electrodes and the measuring device, which result in the induction of parasitic fields in conductive materials (e.g., conductive soils, metallic wires in multicore cables). The inductive coupling is known to be proportional to the conductivity of the subsurface, the acquisition frequency, and the square of the cable length (e.g., Hallof, 1974; Pelton et al., 1978). Hence, many approaches have been suggested for the decoupling of SIP readings by removing the influence in the data of inductive fields associated with layered media and the cable geometry (e.g., Hallof, 1974; Coggon, 1984; Wait and Gruszka, 1986; Routh and Oldenburg, 2001; Zhao et al., 2013). Yet, inductive coupling can also take place within the cable bundle used in SIP field surveys. Assuming parallel cables with an infinite length and without considering coupling with the subsurface, the inductive coupling (EM_{ic}) can be calculated by

$$\mathrm{EM}_{ic} \approx 0.1 \ln(1 + (\frac{2h}{D})^2), \tag{3.2}$$

where h refers to the height of the conductors relative to the earth plane. EM coupling between the cables represents an inherent problem in SIP imaging applications, which to date still relies on the deployment of tens to hundreds of cable cores (i.e., one for each electrode), with the cable length increasing for deeper investigations.

To facilitate data collection at the field scale, the use of multicore cables is a common practice because these are easier to handle than separate wires and are low maintenance, permitting the collection of data in practically all environments from frozen rocks to landslides (e.g., Doetsch et al., 2015; Gallistl et al., 2018). However, the isolation between the independent wires might not provide enough separation to avoid coupling within the multicore cable. Some alternatives have been proposed, for instance, to digitize the response directly at the electrode using so-called remote units minimizing crosstalking between the transmitter and the receiver, or between the cables (Radic, 2016). However, commercially available instruments lack the robustness and flexibility of multicore cables, involve complicated field procedures, and limit the application of the method in rough terrains and for the mapping of extensive areas. The use of separate cables for current injection and potential readings (Dahlin et al., 2002) reduces the contamination of the data due to coupling within the cables by increasing their separation. However, such practice either reduces the depth of investigation or the resolution of the measurements. In the case that each electrode position requires two cables to separate current and voltage dipoles, the length of the profile is reduced by half and, thus, so is the nominal depth of investigation. Alternatively, it is possible to double the separation between electrodes in the multicore cables and alternate each cable and position with one potential and one current electrode to keep the length of the profile and still permit the use of two separate cables. However, this procedure increases the dipole length and consequently reduces the resolution of the imaging data set. Moreover, the separation between the separate cables needs to be large enough to minimize crosstalk (Telford et al., 1990). Alternatively, the use of shielded cables has been suggested to minimize capacitive crosstalking and inductive coupling between wires (Telford et al., 1990), which to date are deployed in some laboratory instruments. However, besides rare examples (e.g., Flores Orozco et al., 2013), such a practice has not been widely implemented in field investigations. Recent investigations (e.g., Zhao et al., 2013; Zhao et al., 2014; Huisman et al., 2016; Zimmermann et al., 2019) have proposed different techniques to model the EM response and correct SIP data at high frequencies; however, such methods require detailed knowledge on the geometric wire layout, which may hinder its application for large-scale surveys. Moreover, correction of the data does not substitute for proper field procedures.

Although the quality of the SIP readings over a broad frequency range is critical to extend the observations from the laboratory to the field scale, to date, few studies have addressed in detail the field procedures to enhance data quality in field FD SIP readings (see Dahlin et al., 2002; Flores Orozco et al., 2013; Huisman et al., 2016; Zimmermann et al., 2019). In this regard, there is a considerable gap between laboratory and field-scale studies addressing the methodologies for the collection of SIP data with high quality. In particular, the use of coaxial cables for the collection of field-scale SIP imaging data sets has not been evaluated in detail, even if this is a common practice for laboratory studies (e.g., Zimmermann et al., 2008; Huisman et al., 2016). Hence, in this study, we compare SIP imaging measurements performed with coaxial and standard multicore cables aiming at proposing a simplification of the field procedures for the collection of field SIP imaging with high quality. To better investigate cable effects, we compare measurements collected with a variety of multicore cables (covering different lengths and manufacturers) using a single layout and separate cables for current and potential dipoles.

The general expectation in our experimental setup is that SIP measurements collected with the same measuring device, under the same field conditions, and using the same electrodes, should result in nearly identical imaging data sets, even if the multicore cables are produced by different manufacturers. Likewise, we also assume that the EM coupling between the cables and the ground is the same. Such an expectation should be valid at least for data collected below 10 Hz, in which EM coupling is commonly assumed to be negligible. Consequently, distortions in the data can be only attributed to cable effects (i.e., inductive and capacitive coupling within the cables). Imaging data sets are compared with those collected with coaxial cables to investigate their benefits in field SIP imaging surveys. For completeness, we also investigate possible cable effects by deploying coaxial and different multicore cables (and setups) for the collection of TDIP measurements. We also present an analysis of the normal and reciprocal misfit for readings collected with multicore and coaxial cables to quantitatively compare variations in data error associated to the different cables.

3.2 Material and methods

We compare here the readings collected with three multicore cables purchased from different companies: Iris Instruments, Multi-Phase Technologies (MPT), and Pro-Seismic Services, which are hereafter referred to as MCX, MCY, and MCZ. For our measurements, we considered cables with 32 takeouts (i.e., electrodes) and mainly two different spacings between them: 5 and 1 m, referred to as the long and short cables, respectively. Accordingly, we refer to the different multicore cables as MCX5, MCY5, MCZ5, MCX1, and MCZ1, corresponding to the different manufacturers and the separation between takeouts. To extend the comparison, TDIP measurements were also collected using coaxial and different multicore cables. Table 3.1 presents a summary of the different cables deployed and the corresponding names.

The coaxial cable used in this study was constructed at the Technical University of Vienna (TU-Wien) using 32 independent wires with lengths between 5 and 155 m,

Table 3.1: Summary of the geometric characteristics and physical properties of the different multicore (MC) and coaxial (COAX) cables used in this study.

Cable ID	Total length (m)	Takeout spacing (m)	Resistance (Ω)	Capacitance (F)
MCX5	183.3	5	13.8	15.4
MCX1	38.3	1	2.9	3.9
MCY5	159.8	5	8.2	9.7
MCZ10	320	10	67.5	19.7
MCZ5	170	5	36	7.4
MCZ1	40.5	1	9.8	2.2
COAX2	64	2	0.3 Ω/m	0.1 nF/m
COAX5	157	5	0.3 Ω/m	0.1 nF/m
COAX10	315	10	0.3 Ω/m	0.1 nF/m

yielding 32 takeouts at 5 m separation between them, hereafter referred to as COAX5. The coaxial cables were twisted together and taped with thermal adhesive tape to form a single bundle and permit easy handling. In this way, the coaxial cable can be rolled into a cable reel and be used in the field in the same way as a multicore cable (see Figure 3.1). To investigate the effect in the data by deploying coaxial cables with different lengths, two additional coaxial cables were manufactured with separations of 2 and 10 m between takeouts (COAX2 and COAX10), for total lengths of 62 and 310 m, respectively. During the construction of each coaxial bundle, particular care was taken to connect the shield of each coaxial cable to the metallic plug to be connected with a measuring device, which has a ground connection through an external electrode (see Figure 3.1). Accordingly, the shields of the cables have the same voltage at the connection point to reduce EM coupling. The coaxial cable deployed here is a coaxial RG-174 A/U, with a characteristic impedance of 50±2 Ω, a capacitance of 101 pF/m, a propagation rate of 66%, and attenuation of 40 dB/ 100 m at 200 MHz. The outside diameter of the conductor is 0.48 mm, the internal diameter of the shield is 1.95 mm, and the entire cable has a diameter of 2.7 mm. The dielectric insulator is polyethylene, with a dielectric constant of 2.4±0.1 and a relative magnetic permeability of 1±0.05. The cable has a copper index of 5.4 kg/km and a weight of 12 kg/km.

For the collection of IP readings, we deployed a data acquisition system (DAS-1) instrument from MPT, which performs the TDIP and FDIP measurements. Consequently, we can investigate the influence of the cable effects on the data quality for both measuring techniques based on the same instrument. Our measurements were collected along two profiles, each with 32 stainless steel electrodes: profile P1, with a separation of 5 m between electrodes and roughly oriented north to south and profile P2, perpendicular to P1, with a separation of 1 m between electrodes. SIP data were

Figure 3.1: Coaxial cable (COAX2) used in this study, with the picture presenting (a) the twisting and tightening of the cable to make a single bundle, (b) the pins in the end connector referred to in the laboratory measurements, and (c) the attachment of the shields of the independent cables into the end connector to permit their grounding through an external electrode and, thus, leveling the voltages of the individual cable shields at the end connector.

collected in the frequency range between 0.5 and 225 Hz, whereas IP data in the time domain were collected with 0.5 s pulse length. This pulse length was selected because the EM coupling is expected to affect readings at frequencies above 1 Hz, i.e., in the early times. Hence, a pulse length of 0.5 s permits us to use the 35 sampling gates available in the DAS-1 device to capture the voltage decay at early times (i.e., just 20 ms after shutting the current off), which are the most affected by EM cable effects. Measurements were acquired with a dipole-dipole (DD) skip-0 configuration, meaning that the length of the current and potential dipoles is equal to the electrode spacing (as illustrated in Figure 3.2). Electrodes used for voltage measurements were always located ahead of the current dipole to avoid contamination of the IP readings due to polarization of the electrodes (e.g., Slater et al., 2000; Flores Orozco et al., 2018a). Our configuration contains a total of 435 quadrupoles covering between 1 and 29 levels, with the levels referring to the number of electrodes separating current and potential dipoles (as illustrated in Figure 3.2). This configuration was selected to record data with a large range in the transfer resistances aiming at capturing a large dynamic range in the S/N in our measurements. In this study, we do not discuss electrode configurations characterized by higher S/N, for instance, with a larger dipole length (DD skip > 0) because they do not provide further insights into the cable effects in the data. Moreover, the comparison of different electrode configurations in SIP imaging has been addressed in previous studies (e.g., Flores Orozco et al., 2018a).

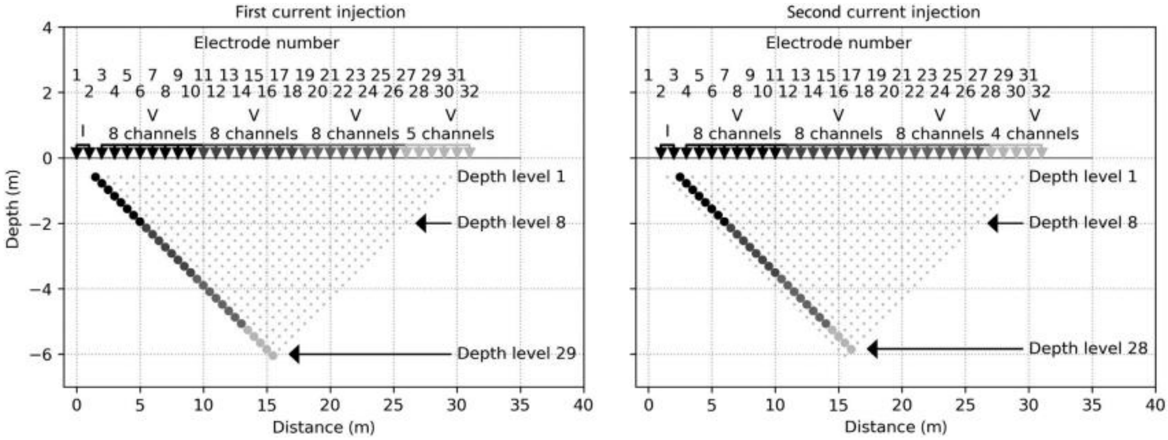

Figure 3.2: Representation of the dipole-dipole skip-0 configuration used in this study considering 32 electrodes, with all possible voltage measurements (indicated as V) for a given current dipole (indicated as I) and the levels representing the distance (given in terms of the electrode spacing) between the current and potential dipole.

We collected the measurements presented here at the Hydrological Open Air Laboratory (HOAL) located in Lower Austria (Austria). The HOAL site is a small catchment (66 ha), where different investigations are being conducted to understand runoff generation (Blöschl et al., 2016). The SIP data sets presented in this study were acquired in a forest-covered area characterized by heavy soils (clay and silt content above 70%). Due to the high content of fine particles, the electrical properties at the low frequencies (< 100 Hz) are expected to be dominated by conduction (i.e., the real component of the surface conductivity) over polarization (i.e., the imaginary component of the surface conductivity) due to the contribution of ionic and surface conduction mechanisms. However, at the selected location, previous measurements have revealed relatively high phase-lag readings ($\varphi > 10$ mrad) attributed to a biogeochemically active zone, which has been validated through analysis in the laboratory of recovered sediments after drilling (see Figure 3.3). Hence, the study area offers an excellent opportunity to investigate cable effects in SIP imaging measurements. On the one hand, conductive soils are commonly related to high coupling effects (e.g., Hallof, 1974). On the other hand, changes in subsurface properties lead to a polarizable anomaly, thus enhancing the S/N. A detailed interpretation of the electrical response of the subsurface is beyond the scope of this study.

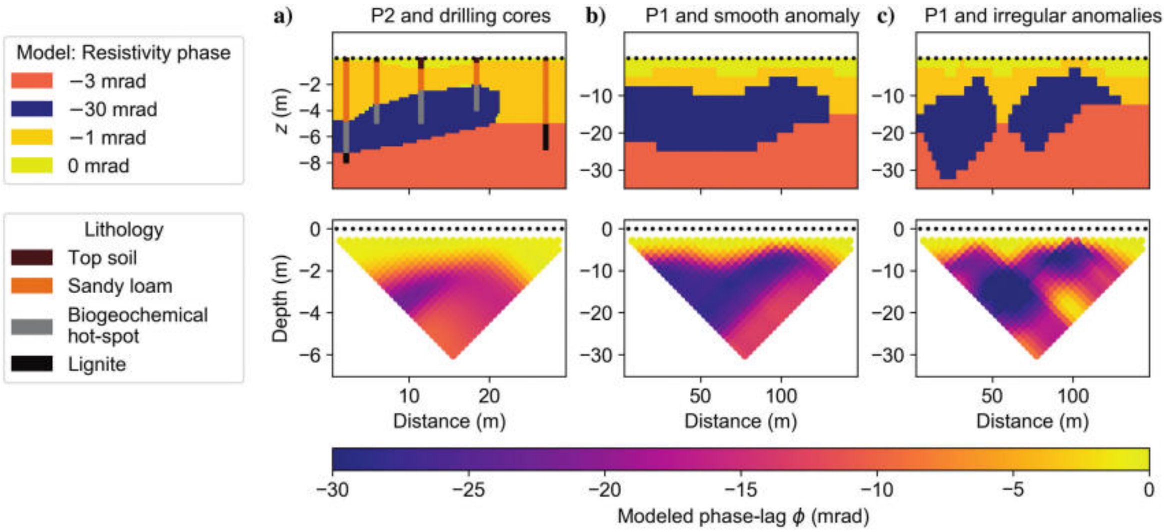

Figure 3.3: Numerical model to validate the assumption of smooth pseudosections. The assumed electrical units expressed in terms of the phase of the complex resistivity (top) and the pseudosections (bottom) for the modeled response, expressed in terms of the phase lag of the electrical impedance. Borehole information at the study area is imposed in the electrical model and is used to define the variations of the complex conductivity values in the subsurface.

For the investigation of cable effects, we want to avoid the inherent uncertainty associated to the inversion of the data. Hence, our study is based solely on the comparison of the measured phase lag (φ), hereafter referred to as phase for simplicity, for readings collected with different cables. We do not present plots of the apparent resistivity because all of the data collected with different cables revealed negligible differences. To present the raw data, we use a slightly modified version of the classic pseudosections, with the only difference being that the pseudosections presented here plot the actual measured phase values (φ) without interpolation. We believe that the pseudosections offer the best way to compare the data collected with different cables, permitting visualization of the distribution of the measurements and their spatial consistency. The expectation for “clean” data sets (e.g., without cable effects) is that the measurements should be distributed in a reduced range of values, with smooth variations along the pseudosection plane due to the (spatial) correlation between adjacent measurements (e.g., Flores Orozco et al., 2018a). Accordingly, “noisy” measurements are those in which the pseudosection shows large variability between the values in nearby measurements. We then quantify the variability in the readings by means of the standard deviation (s) of the φ values in the imaging data set collected for each cable and frequency after removal of erroneous measurements and outliers.

To support our expectation of smooth pseudosections independently of the complexity in subsurface architecture, we present in Figure 3.3 the pseudosections obtained for synthetic models with different degrees of complexity. The synthetic models are based on the expected geologic setting at the site, as resolved from wellbore data. The shape of the polarizable anomaly was modeled for the smooth and irregular geometries to investigate the resulting variations in the smoothness of the pseudosections. Our numerical investigation (see Figure 3.3) supports two assumptions in our study: (1) Subsurface structures with irregular shapes still result in smooth pseudosections, and (2) positive phase-lag readings (φ) in our measurements cannot be explained by changes in the sensitivity of the measurements and the distribution of the polarizable anomalies.

Measurements associated with a negative apparent resistivity were deleted as erroneous measurements. Similarly, positive φ values might be regarded as erroneous measurements, considering that those can only be explained by negative currents in a typical resistor-capacitor circuit. However, in our study, we filtered only φ values above 20 mrad, to take into account possible negative IP effects (for further details, refer to Dahlin and Loke, 2015; Flores Orozco et al., 2018a) and systematic patterns associated to cable effects. In addition, phase measurements below -100 mrads were also defined as outliers. This threshold value is based on a first inspection of the data collected with all the cables at P1, which revealed most of the φ readings in the range between -20 and 0 mrad, with a mean value of less than -7 mrads (Figure 3.4). Hence, the threshold value of -100 mrads was selected as a soft filter considering a potential increase in the polarization response for measurements at higher frequencies.

3.3 Results

FDIP data with 5 m separation between electrodes: Comparison between long multicore and coaxial cables using a single layout and separate cables

Figure 3.5 shows the pseudosections after removal of outliers for data collected with the long cables along P1, i.e., for spacing of 5 m between electrodes and takeouts in the cables. Besides the pseudosections obtained for measurements with different single multicore cables, we also present the pseudosections for data collected using a single coaxial cable (COAX5 and COAX10), and a separate cable layout. In the case of separate cables, we present two scenarios: (1) using two multicore cables for current (MCY5) and potential (MCZ5) readings and (2) using the combination of coaxial for current injection and multicore cables (MCY5) for potential readings. In

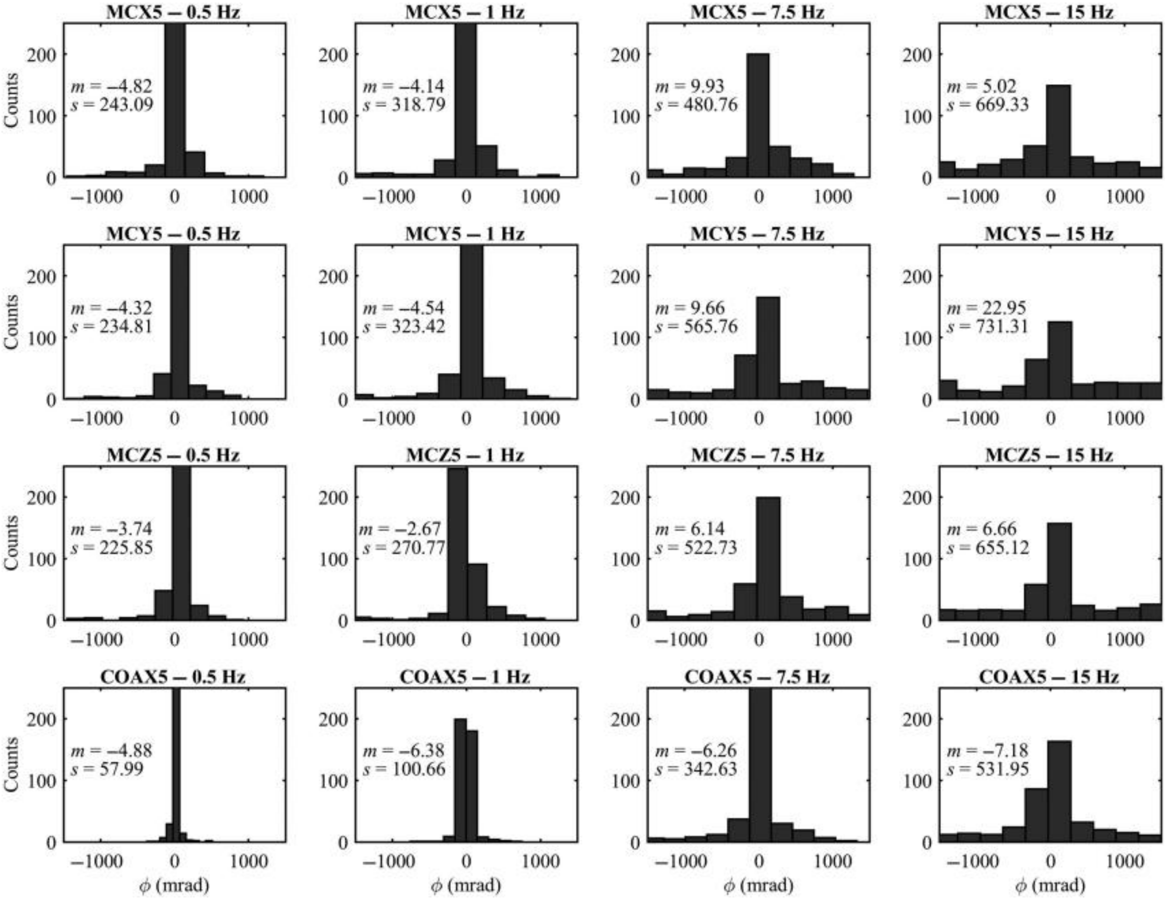

Figure 3.4: Histograms of the phase-lag readings in SIP measurements collected along profile P1 (5 m electrode spacing) with the long multicore and coaxial cables (5 m between takeouts). The median (m) and standard deviation (s, in mrad) for each imaging data set are indicated in each plot.

general, Figure 3.5 shows smooth pseudosections for measurements collected at the lowest frequency (0.5 Hz) within the first eight levels (pseudodepth $\leq$ 10 m) in which most of the phase readings are found in the range of values between -20 and 0 mrad. A similar distribution is also observed for readings collected at 1 Hz, yet the single multicore data sets reveal an increase in the variability of the readings (s increasing from approximately 18 to 22) and a larger number of spatially inconsistent measurements (i.e., noise) even within the first eight levels. The lack of spatially consistent deeper measurements (e.g., > 10 m in the pseudosection) corresponds to quadrupoles associated with a poor S/N. However, measurements collected with the coaxial cables — and to some extent with separate cables — show a clean (i.e., smooth) pseudosection even for a pseudodepth of 20 m, still evidencing a good S/N. Furthermore, measurements at 1 Hz collected with a single coaxial — and to lesser extent with separate cables — still evidence a high S/N and consistent readings up to 18 levels (a maximum pseudodepth of approximately 20 m). These observations make it clear that cable effects dominate 1 Hz measurements conducted with single multicore cables and separations larger than 35 m between current and potential dipoles (corresponding to seven times the electrode spacing).

The high number of measurements removed as outliers for data collected with multicore cables (between 40% and 45%) at the low frequencies points to clear systematic errors related to the cables, considering that at such low frequencies induction effects in the shallow soils might be negligible. This is particularly evidenced by the high quality revealed by the data collected with coaxial cables (and to a certain extent with separate cables), in which less than 25% of the readings are removed as outliers, with consistent readings still visible for the larger separations between current and potential dipoles. Moreover, data collected with a coaxial cable two times larger than the actual length of the profile (10 m separation between takeouts) reveal smoother pseudosections (with a lower standard deviation in the readings) and a lower number of filtered outliers than measurements collected with single multicore cables.

At 7.5 Hz, the coaxial cable still acquires data characterized by clean pseudosections for the first eight levels (e.g., a pseudodepth of 10 m), which are comparable only to the readings collected with separate cables. For measurements collected at 15 Hz, the pseudosection for the coaxial cables still shows many measurements within the first eight levels (i.e., the first 10 m of pseudodepth) with a high spatial consistency (i.e., smooth pseudosection), whereas most of the deeper measurements are removed as outliers. At 15 Hz, all multicore cables show poor performance, with more than 75% of the readings removed, and the remaining readings revealing a poor spatial consistency, with noisy pseudosections. The MCZ5 cables perform the best among the multicore cables, yet they reveal much more scattered readings and a higher number of removed outliers compared with the data set collected with the coaxial cables. Clearly, cable effects are the main reason underlying the poor quality in data collected at 1 Hz with single multicores, with a larger decrease in the quality and spatial consistency of φ readings at higher frequencies.

Surprisingly, SIP readings collected with two separate multicore cables reveal noisier pseudosections than those collected with a single coaxial one. This is unexpected, considering that EM coupling between wires decreases with increasing the separation between them (see equations 3.1 and 3.2) and both multicores were laid with a relatively large separation (approximately 50 cm). This observation may suggest that inductive coupling in conductive soils (such as those in the HOAL) plays a dominant role in the distortion of SIP readings collected with common multicore cables, even if different cables are used for current and potential dipoles. Accordingly, Figure 3.5

shows that the use of coaxial cables significantly improves the quality of SIP imaging readings over those collected with multicore cables. Measurements with separate cables can be improved using a coaxial cable. However, measurements at 7.5 and 15 Hz reveal relatively similar data quality within the first eight levels (i.e., up to 10 m depth in the pseudosection) when performed with a single coaxial cable and the combinations of the MCY5 coaxial. Nonetheless, at 0.5 and 1 Hz, only the measurements with a single coaxial cable provide clean pseudosections (including the deepest measurements).

Plots in Figure 3.5 reveal that SIP field surveys conducted with long multicore cables and electrode spacing (i.e., 5 m) might be limited in their depth of investigation due to the occurrence of cable effects in readings with a relatively large separation between the current and potential dipoles. Contrary to this, measurements collected with single coaxial cables are less affected by EM coupling. Moreover, the pseudosections presented in Figure 3.5 suggest that MCY5 cables might not be suited for collection of SIP data.

FDIP data with 1 m separation between electrodes: Comparison between long multicore and coaxial cables using single layout and separate cables

Figure 3.6 presents the pseudosections for measurements collected with the long cables (5 m spacing between the takeouts), but for an electrode separation of 1 m in P2. A shorter separation between electrodes favors a higher S/N and may help to reduce the contamination of the data due to EM coupling with the conductive soils. However, the long cables cannot be fully extended; thus, the exceeding cable was laid as perpendicular as possible to the profile.

As expected, the small separation between electrodes resulted in higher voltage readings, ranging between 0.5 mV and 1 V (data not shown), which are two orders of magnitude higher than those observed for measurements collected with 5 m separation between electrodes (data not shown). Given the enhanced S/N, Figure 3.6 reveals only minimal readings removed as outliers in the lower frequencies (0.5 and 1.0 Hz) for single multicore measurements ($< 30\%$). Moreover, pseudosections for data collected at 7.5 Hz show more than 50% valid readings for all multicore cables deployed, with the exception of MCY5. However, coaxial cables still perform the best, with less than 15% of the outliers removed at low frequencies (0.5 and 1.0 Hz). At higher frequencies, COAX5 measurements still reveal relatively clean pseudosections up to 7.5 Hz within the first 8–12 levels (pseudodepth < 3 m). At such frequencies, MCX5 and MCY5 exhibit noisy measurements with almost 60% of the readings removed as

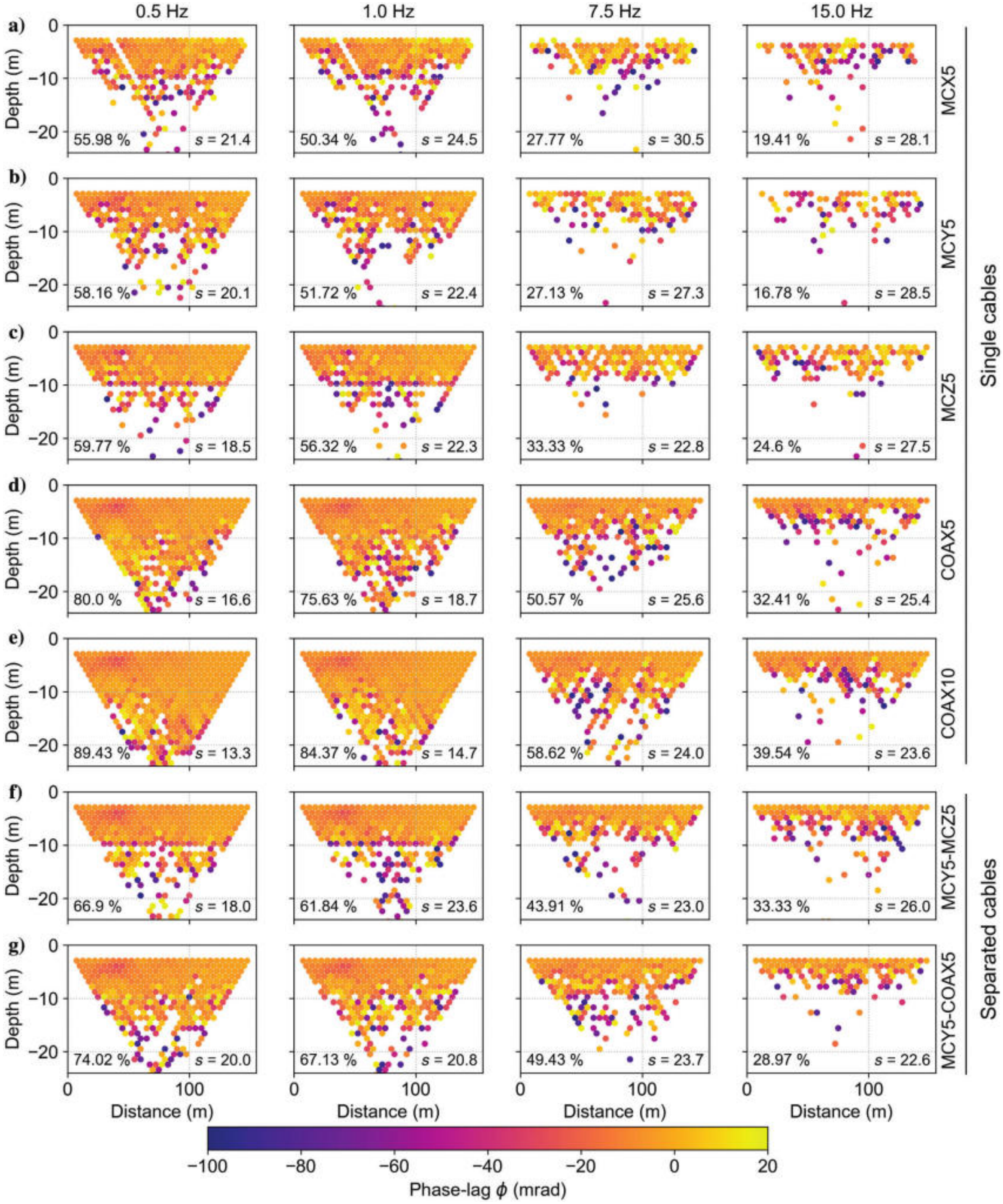

Figure 3.5: Pseudosections for SIP data collected at the HOAL site using 32 electrodes deployed with a separation of 5 m. SIP measurements were conducted using long multicore (MCX5, MCY5, and MCZ5) and coaxial cables (a total length of 155 m). Labels inserted show the percentage of remaining measurements after removal of outliers and the standard deviation (s) in the phase readings.

outliers and a standard deviation of approximately 8 mrad larger than for COAX5 readings. Only measurements collected with MCZ5 show some consistency with the

COAX5, suggesting the better performance of these multicore cables.

At 15 Hz, measurements collected with single MCX5 and MCY5 are scattered over a larger range ($s \sim 28$ mrad), yielding noisy pseudosections with a large number of removed measurements ($> 60\%$), indicating poor quality in the phase readings, whereas MCZ5 and coaxial cables show clean pseudosections within the first eight levels (depth < 2 m in the pseudosection) and relatively consistent distribution within the readings ($s \sim 21$ mrad). Clearly, the long cables enhance EM coupling (within the cables and the conductive soils) at 15 Hz, even if the separation between electrodes is small. Nonetheless, measurements collected with coaxial cables at 15 Hz still show a clean pseudosection with only a few outliers removed within the first eight levels, suggesting that such effects might be reduced through the deployment of shielded cables, albeit the long cable length.

In the case of measurements collected with separate cables, one being coaxial, Figure 3.6 reveals that the combination MCY5-COAX5 performs better than COAX5-MCY5. Hence, the use of the coaxial cable for current injection results in data sets with a standard deviation of approximately 3 mrad smaller and approximately 3% fewer measurements removed as outliers in comparison to those when the coaxial cable is used to connect the potential electrodes. Such an observation might be explained as a higher EM coupling between the conductive soils and the shield of the coaxial cables (in the voltage dipoles) than the coupling between the conductive soils and the multicore cables. Nonetheless, Figure 3.6 shows that measurements with a single coaxial cable are comparable to those collected with separate cables. Moreover, Figure 3.6 demonstrates that measurements collected with a coaxial cable much longer than the actual separation between electrodes (five times longer in the case of our measurements) still provide comparable quality to measurements collected with separate cables.

FDIP data with 1 m separation between electrodes: Comparison between short multicore cables and long coaxial cables using a single layout and separate cables

Pseudosections presented in Figure 3.7 show the data quality in measurements collected with a short electrode separation and short multicore cables (1 m for a total profile length of 31 m), in comparison with single long coaxial cables (COAX5, with 5 m spacing between takeouts), as well as separate short multicore cables. Measurements with MCY1 were not conducted. In general, Figure 3.7 shows that the data quality is significantly improved by reducing the length of the multicore cables to the

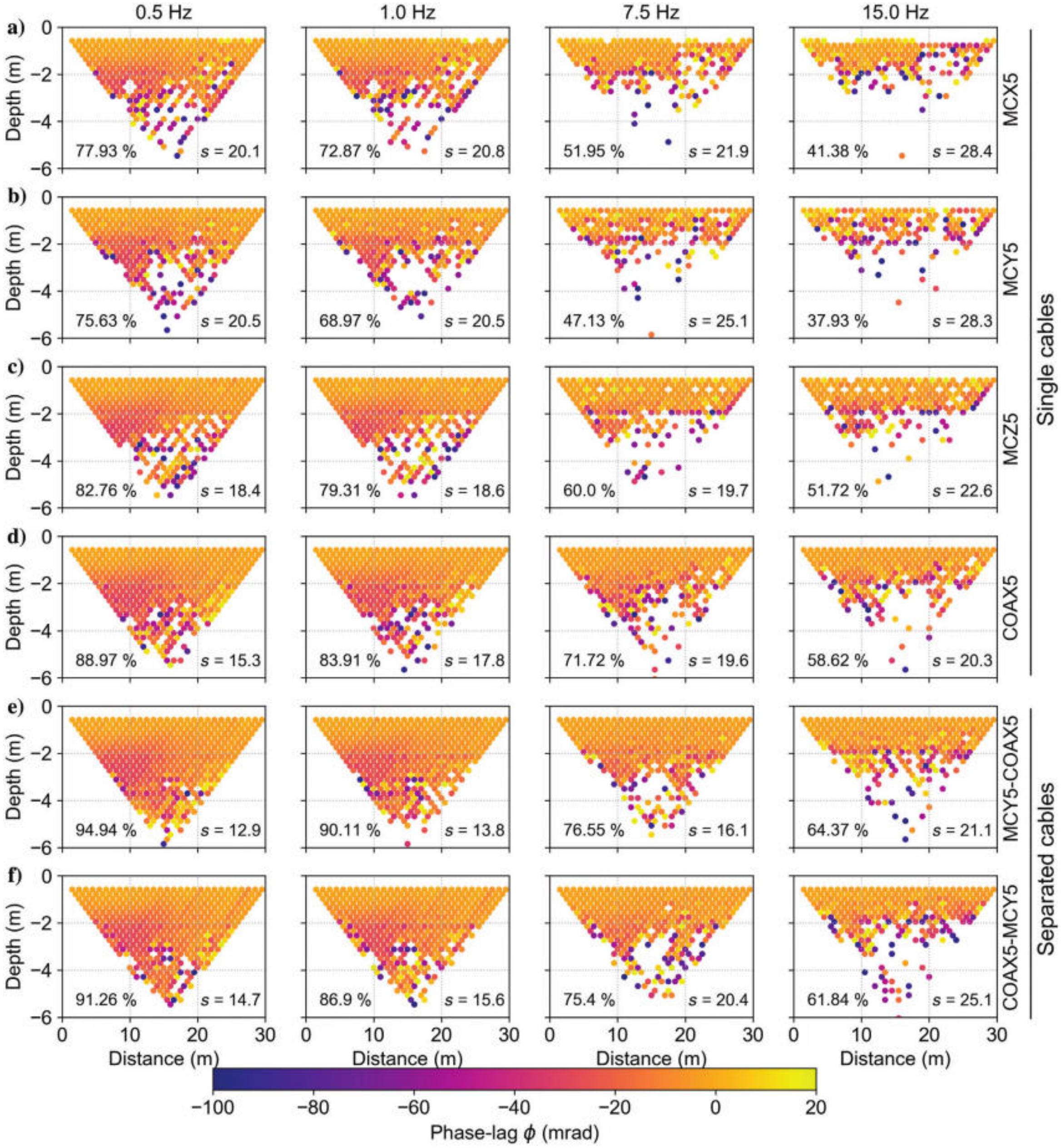

Figure 3.6: Pseudosections for SIP data collected at the HOAL site using 32 electrodes deployed with a separation of 1 m. SIP readings were collected using long multicore (MCX5, MCY5, and MCZ5) and coaxial cables (a total length of 155 m each). The inserted labels show the percentage of remaining measurements after removal of outliers and the standard deviation (s) in the phase readings.

exact size of the separation between electrodes.

In general, all measurements presented in Figure 3.7 show smooth pseudosections for all cables in the low frequencies (0.5 and 1.0 Hz), with fewer than 10% of measurements removed as outliers for multicore cables. Moreover, pseudosections reveal consistent phase readings for 16 levels (pseudodepth < 5 m) for measurements collected at low frequencies, as well as within the first 8 and 10 levels (for maximum depth of 2.5 m in the pseudosections) at high frequencies (7.5 and 15 Hz). Unavoidably, the data quality decreases with increasing the acquisition frequency for larger separations between current and potential dipoles (i.e., pseudodepth), yet in the case of short multicore cables, data collected at 15 Hz still reveal clean pseudosections only within the first eight levels (a depth of 2 m). Consistent with previous observations, the MCZ cables outperform the MCX cables.

Clearly, the short cables minimize EM coupling within the cables and possible inductive coupling with the conductive soils, permitting collection of SIP phase readings with a higher quality, even with a single multicore cable. Thus, field procedures deploying the smallest possible multicore cables are recommended to significantly improve the quality of SIP data. Contrary to this observation, data collected with a single long coaxial cable reveal still comparable pseudosections at the different frequencies, with a similar variability in the data (s varying at different frequencies between 15 and 20 mrad) and the number of removed readings as outliers. Hence, Figure 3.7 demonstrates that the quality of SIP measurements collected with single coaxial cables is less sensitive to the length of the cable.

Pseudosections for data collected at 0.5 and 1.0 Hz using separate short multicore cables (MCX1-MCZ1) reveal high spatial consistency between the readings ($s \sim 10$ mrad) and a minimal number of outliers (less than 5% of the readings removed). At 7.5 Hz, separate short cables still result in smooth pseudosections in almost 15 levels (i.e., a depth of 3 m in the pseudosections) and with still less than 20% of the outliers removed. In the case of data collected at 15 Hz, the use of short separate cables results in approximately 3% fewer measurements removed as outliers and a standard deviation of approximately 3 mrads smaller in comparison with the measurements with a single multicore cable. The comparison of pseudosections presented in Figures 3.6 and 3.7 shows that the deployment of multicore cables longer than the actual separation between electrodes significantly reduces the quality of SIP readings, even at low frequencies, as observed for 0.5 Hz readings with MCX5 and MCY5.

Comparison of coaxial, multicore, and separate cables for TD measurements

Regarding EM coupling, TDIP measurements offer the advantage that potential readings are collected with a delay after the current injection is switched off, which permits minimization of EM inferences in the data. However, for completeness, here we investigate variations in the quality of the TDIP measurements collected with different

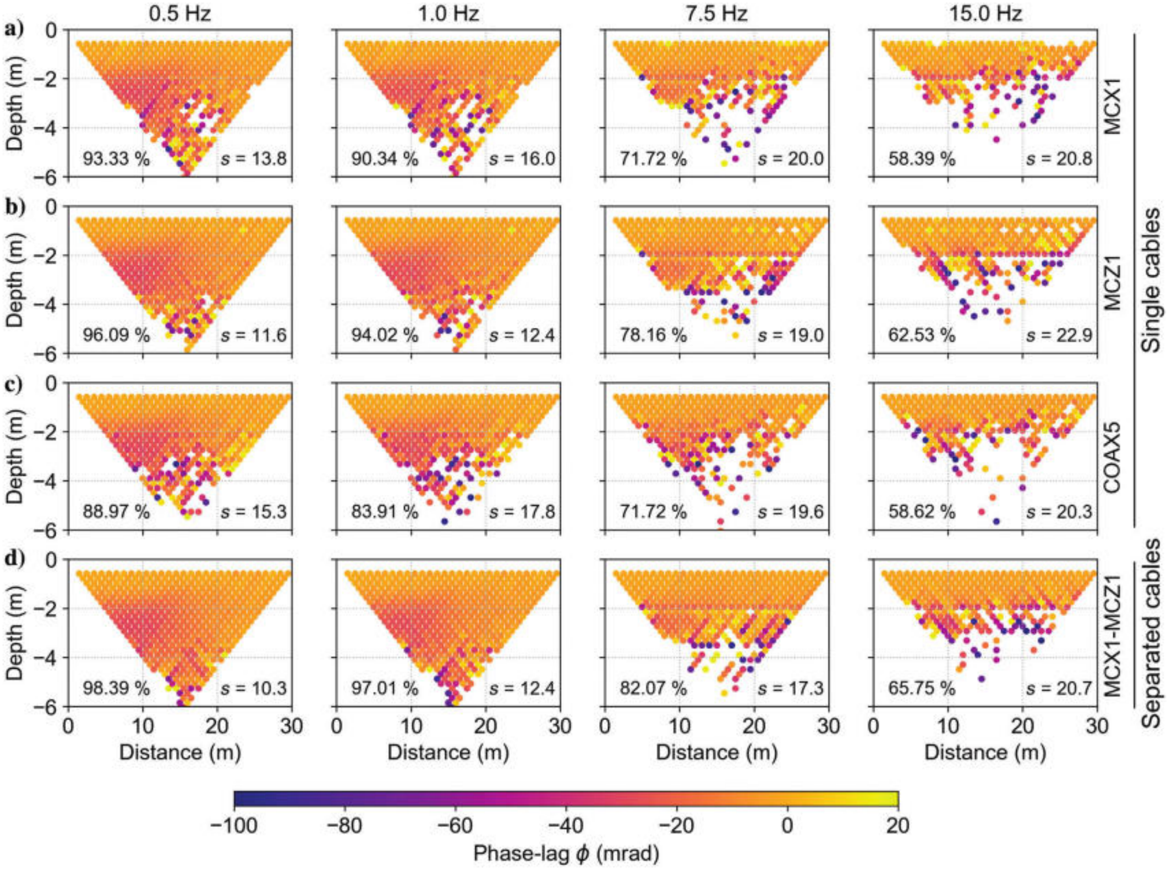

Figure 3.7: Pseudosections for SIP data collected at the HOAL site using 32 electrodes deployed with a separation of 1 m. SIP readings were collected using short multicore (MCX1 and MCZ1 — a total length of 31 m each) and long coaxial cables (a total length of 115 m). The inserted labels show the percentage of the remaining measurements after removal of outliers and the standard deviation (s) in the phase readings.

cables. TDIP measurements were acquired for pulse lengths of 500 ms, using a square wave, with a 50% duty cycle. After current switch-off, the decay curve was sampled after an initial delay of 10 ms using 24 windows, with a constant width of 20 ms.

For our analysis, we present the pseudosections for chargeability measurements at three different sampling windows (2, 10, and 20 for a 500 ms pulse length), analogous to the high, intermediate, and low frequencies in FDIP. We also present pseudosections for the integral chargeability (M_{tot}), which is a quantity commonly used for the interpretation of TDIP surveys (more details can be found, for instance in Binley and Kemna, 2005). Similar to the FDIP data, the apparent resistivity pseudosections are consistent for measurements with different cables and are not discussed here. We define and remove as outliers those measurements for which the corresponding chargeability exceeds the limits of −20 to 100 mV/V, with the broad range selected to permit the visualization of possible negative chargeability values (e.g., Dahlin and Loke, 2015) or contamination in the data due to EM coupling.

In general, Figure 3.8 shows clean pseudosections, at least to a depth of 4 m (at least 14 levels), and with less than 5% of the data removed as outliers (for the M_{tot} plots), clearly evidencing the good quality of the TDIP readings. As expected, the noisier pseudosections are those related to measurements collected with the long MCZ10 cables (10 m separation between takeouts for a total cable length of 310 m), which reveals the poor spatial consistency between the readings collected below 10 levels (i.e., 10 electrodes separating the current and potential electrodes). Such poor data quality might be related to cable effects or inductive coupling with the conductive soils dominating over the low voltage measurements (i.e., lower S/N). The data quality improves significantly for data collected with shorter multicore cables (from the same manufacturer), as evidenced by pseudosections for MCZ1 data. These readings show smooth pseudosections, with some noisy measurements only for the deepest measurements (below 5 m pseudodepth), TDIP measurements collected with the single coaxial cable show the smoothest pseudosections and the lowest amount of removed outliers ($< 1\%$ for the M_{tot}), for all data sets collected with a single cable. However, TDIP pseudosections show in general high spatial consistency and indicate fewer outliers than the FDIP pseudosections. This is expected considering that the voltage readings are collected after the current in the transmitter is switched off, and, thus, are less affected by EM coupling, namely, by crosstalking between cables, between the transmitter and receiver in the DAS-1, and induction effects between the cables and the ground.

As expected, early IP windows (i.e., M_2 and M_{10}), reveal the largest number of filtered data (15% and 5% for long and short multicore cables, respectively, and 10% for coaxial cables), and noisy pseudosections for the readings with large levels (> 4 m pseudodepth). EM coupling effects are expected in the early times (analogously to high frequencies in FDIP) and clearly affect the quality of the measurements with a weak S/N associated to a large separation between current and potential dipoles (i.e., a large pseudodepth). Such data contamination is only visible for the longest cables (MCZ10) in the integral chargeability plots, but it is almost negligible for the coaxial cable and the short multicore cable.

In Figure 3.8, we also present data collected with a single coaxial, two separate coaxials, two separate multicores, and separate multicore and coaxial cables, with all of these combinations revealing practically similar pseudosections (less than 3% of the data removed as outliers) with high spatial consistency ($s < 10$ mV/V) for integral chargeability values (M_{tot}). Our data show larger discrepancies in early time readings for deep measurements (pseudodepth > 4 m), which are related to large separations between the current and potential dipoles, as mentioned above. EM coupling plays a more dominant role in readings at early times (i.e., M_2), analogously to the high frequencies. Accordingly, we observe a larger variation in the readings in M_2 ($s \sim 19$ mV/V) than in, e.g., M_{20} ($s \sim 13$ mV/V), as well as a larger number of measurements removed as outliers. Hence, pseudosections for M_2 provide the best overview regarding cable effects in TDIP. In such case, Figure 3.8 reveals that measurements collected with MCZ1 as a single cable provided the best quality, followed by readings collected with a single coaxial. Although not discussed here, further improvements in data quality could also be expected through the deploying of shorter coaxial cables, for instance, to the exact separation between electrodes.

Figure 3.8 also shows that coupling effects cannot be neglected in TDIP measurements, at least in early times, for instance, in the pseudosections for M_2, even if two coaxial cables are used to separate the current and potential dipoles. It might be argued that such distortions are only visible for the deep measurements, in which the lowest S/Ns are expected. However, the pseudosections (e.g., M_{20}) corresponding to later times are clean even if associated to lower chargeability values. The cable effects at early times might be relevant for the case of TDIP measurements of the full waveform, or using a 100% duty cycle, yet such discussion is beyond the scope of this study. Nonetheless, Figure 3.8 suggests that the use of a single short coaxial cable might also permit enhancement of the quality of the TDIP data.

3.4 Discussion

Analysis of normal and reciprocal misfit

The analysis of the raw data clearly demonstrates a significant improvement in SIP readings for measurements collected with coaxial cables when compared with those acquired using multicore cables. Already for measurements at 1 Hz, imaging data sets collected with a single multicore cable result in a larger number of filtered data and a broader variance than those collected with a single coaxial cable. Moreover, it has been observed that the length of the multicore cables plays a critical role in the quality of the SIP readings, whereas this may be not relevant for measurements performed with coaxial cables. To quantitatively evaluate the data uncertainty associated to the different cables, we present in Figure 3.9 the analysis of misfit between normal and reciprocal phase readings ($\Delta\varphi$) collected along profiles P1 and P2. Reciprocal readings refer to the recollection of a given quadrupole (i.e., normal measurements) after interchanging the electrodes used for the current and potential dipoles (LaBrecque et al., 1996). Statistical analysis of normal-reciprocal misfit ($\Delta\varphi$) is a well-established method to quantify data error in electrical imaging (e.g., LaBrecque et al., 1996; Slater et al., 2006; Flores Orozco et al., 2012b; Flores Orozco et al., 2018b; Flores Orozco et al., 2018a); thus, it can be used here as a tool to quantitatively compare the data collected with different cables. For the sake of consistency, in Figure 3.9, we compare only the $\Delta\varphi$ for data collected with MCX5 and COAX10 cables along P1 (5 m spacing between electrodes), whereas MCX1 and COAX2 are compared for measurements collected along P2 (1 m separation between electrodes). In the case of multicore cables, we present measurements collected with cables having the same length as the profile (i.e., the separation between electrodes and cable takeouts being the same), whereas coaxial cables used for this analysis are always two times longer than the profile length.

During the analysis of the $\Delta\varphi$, the only filtering in the data refers to the removal of erroneous measurements (readings associated with a negative apparent resistivity) and outliers (i.e., -100 mrad $< \varphi <$ 20 mrad), independent of the resulting misfit between the normal and reciprocal readings. Figure 3.9 shows that data sets collected with coaxial cables result in a larger number of normal-reciprocal pairs (N) than measurements collected with multicore cables, along P1 and P2, and for all frequencies. At low frequencies (0.5 and 1.0 Hz), the data collected with multicore cables result in approximately 3% fewer measurements than those data sets collected with coaxial cables. Nonetheless, MCX5 and COAX10 yield similar values of the standard deviation of the reciprocal misfit ($s(\Delta\varphi)$) at low frequencies (variations $<$ 1 mrad).

Measurements collected with multicore and coaxial cables at 7.5 and 15 Hz reveal consistent values in the $s(\Delta\varphi)$ only for data sets collected along P2, which refers to the 1 m spacing between electrodes. However, measurements collected with the multicore cable MCX5 at P1 reveal a poor reciprocity at 7.5 and 15 Hz, with less than 30 normal-reciprocal pairs and a larger $s(\Delta\varphi)$ than the data sets collected with the COAX10 cable. Moreover, such measurements exhibit a normal distribution of the $\Delta\varphi$, as expected for measurements contaminated by random noise (e.g., LaBrecque et al., 1996; Slater et al., 2006). Such a normal distribution in the $\Delta\varphi$ is also observed for all measurements collected in P2 and at low frequencies in P1. Accordingly, Figure 3.9 demonstrates the possibility to collect high-quality SIP imaging data with a single coaxial cable, even if this is much longer than the actual length of the profile.

Comparison between coaxial and multicore cables: Implication for field surveys

Results presented in Figures 3.5-3.9 demonstrate that the use of multicore cables in SIP imaging surveys results in large distortions in the data already at 1 Hz. Moreover, measurements collected with long multicore cables reveal a poor reciprocity for readings collected at 7.5 and 15 Hz, and a larger reciprocal misfit ($\Delta\varphi$) for measurements collected at 1.0 Hz in comparison to measurements collected with the coaxial cables. Distortions in the imaging data sets vary in their amplitude and distribution unsystematically for the different multicore cables deployed. Hence, removing such cable effects during the processing of the data might be impossible. Accordingly, we do not recommend the use of traditional multicore cables as a single layout for the collection of FDIP imaging data, even at 1 Hz. We believe this is an important observation, considering that 1 Hz has been suggested as the best compromise between relatively low acquisition times and negligible EM coupling.

The distortions in measurements at 1.0 Hz when using multicore cables increase with increasing the cable length, even if the cables are fully extended. We observed that the deployment of multicore cables longer than the actual separation between electrodes significantly reduces the quality of SIP readings even at low frequencies such as 0.5 Hz, independently of whether the multicore cable is used in a single layout or using two cables to separate the current and potential dipoles. Thus, the collection of reliable SIP imaging field surveys demands the use of shortest possible cables, if only multicore cables are available.

TDIP readings collected using a 50% duty cycle and multicore cables revealed the same data quality than those collected with the coaxial cables with only a minimal improvement when readings were collected with separate cables. Such measurements benefit from sampling the decay curve only after the current injection is switched off, thus minimizing the influence of parasitic EM fields. Accordingly, TDIP measurements favor the use of multicore cables. Nevertheless, chargeability measurements collected at early times revealed larger inferences (i.e., outliers) when collected with single cables than using two cables to separate the current and potential dipoles, likely indicating distortions due to coupling effects.

SIP imaging data sets collected with coaxial cables revealed an improved data quality, especially at low frequencies (0.5 and 1.0 Hz). Moreover, we observed good data quality using coaxial cables much longer than the actual profile length. Even for measurements collected with COAX10, readings revealed a significant improvement in the normal-reciprocal misfit ($\Delta\varphi$) in comparison with data collected with shorter multicore cables. Moreover, measurements conducted with a single coaxial cable revealed at least the same quality as those using two multicore cables to separate the current and potential dipoles. Hence, the use of coaxial cables may represent the best alternative for field surveys, permitting use of the same cable for collection of data with different electrode spacing, as well as to double the resolution or maximum depth of investigation by avoiding the necessity to lay two different cables to separate potential and current dipoles.

The poor quality of SIP readings at frequencies greater than 15 Hz might be related to sources of contamination beyond the cable effects, such as low-frequency electrical fields associated to fluctuating telluric currents in conductive soils (Serson, 1973). Moreover, further sources of capacitive coupling can be related to variations in the contact resistances between electrodes and the soil or between electrodes and cables (Zimmermann et al., 2008; Zimmermann et al., 2019). In addition, conductive soils enhance inductive coupling (e.g., Wait and Gruszka, 1986; Routh and Oldenburg, 2001).

To investigate EM coupling in multicore and coaxial cables without the interactions with subsurface materials, we performed a laboratory test. This test was conducted with each multicore cable used on the field, with the exception of the MCZ1, which is used for measurements in boreholes and the end connector is sealed. As illustrated in the schematic diagram presented in Figure 3.10a, we injected a sinusoidal current across one of the wires of the multicore cable with an effective input voltage (V_i) of 1 V, corresponding to a current of approximately 0.2 mA. During the current injection, we used an oscilloscope to measure the output voltage (V_o) in each one of the remaining 31 wires (against the mass of the oscilloscope). To avoid overloading the measuring channels, we connected a 50±1 Ω resistance in series between the signal generator and the pins used for current injection, as illustrated in Figure 3.10a. For verification, readings of the V_o were collected in both end connectors, illustrated as NEXT and FEXT in Figure 3.10a, with the measurements in each connector corresponding to the average value of nine waveforms (commonly exhibiting fluctuations of approximately 4 mV). The experiment was repeated for all multicore cables at two different frequencies: 1 Hz and 2 kHz. Similar measurements were also conducted between the two longest wires of the COAX2 cable, yet we did not collect measurements for all wires, due to their different lengths. EM coupling in the cables is exhibited by the observed V_o in the wires of the multicore cables during the current injection, which is presented in terms of the noise at low (Figure 3.10b) and high (Figure 3.10c) frequencies.

Figure 3.10b and 3.10c shows the highest coupling for readings collected in the pin (i.e., wire) closest to the current injection, yet the distortions show erratic behavior for different wires. Nonetheless, consistent patterns can be observed for cables built by the same manufacturer, thus suggesting that such variations in the EM coupling within the multicore cables are related to the twisting of the independent wires. Similar to the field results, the shortest cable, i.e., MCX1, reveals the lowest EM coupling, whereas MCY5 exhibits the highest coupling. The longest cable tested (MCZ10) reveals intermediate coupling values, which can be explained by the high electrical resistance measured in the wires (Table 3.1). As expected, coupling is approximately two orders of magnitude higher for current injections at 2 kHz than at 1 Hz. Moreover, coupling in the coaxial cables is at least one order of magnitude smaller than the one observed in the MCX1. Hence, the results presented in Figure 3.10b support our field observations and demonstrate that multicore cables can result in EM coupling even at low frequencies, causing important distortions in SIP readings.

Besides the EM coupling between cables at 1 Hz evidenced in Figure 3.10b, the decrease in the data quality for our SIP field measurements might point out possible coupling effects within the measuring device (i.e., within the transmitter and receiver). Such a limitation needs to be addressed in the next generation of field-scale SIP instruments. In this regard, the Multi-Source instrument (from MPT LLC) or the V-FullWaver (from Iris Instruments) may provide an improvement in the data quality for IP field surveys because they permit remotely synchronization of the transmitter and the receiver. However, the Multi-Source instrument is still under development and the V-FullWaver does not permit collection of SIP data in the FD.

Different correction methods taking into account the geometry of the cables (e.g., Zhao et al., 2013; Zhao et al., 2014) can still be performed to further improve the quality of the phase measurements at higher frequencies, yet their application is beyond the scope of the present study. Likewise, the collection of IP data deploying other configurations characterized by higher S/N, such as Wenner or multiple gradient, are also not addressed within this study because they do not provide new insights into the discussion.

3.5 Conclusion

Our results demonstrate that SIP measurements conducted in the FD with multicore cables result in significant distortions in the phase readings even at low frequencies such as 0.5 and 1.0 Hz. Consistent to previous studies, the use of separate multicore cables for current and voltage readings revealed an improved data quality in comparison to single cables. However, the data quality is still dependent on the construction and length of the multicore cables deployed, with cleaner pseudosections observed only for data collected with short cables (1 m spacing in the takeouts). Contrary to those observations, data collected with a single coaxial cable revealed high data quality, even if the cable is five times longer than the actual separation between electrodes. The improved quality in SIP imaging data sets collected with coaxial cables was demonstrated through the analysis of normal and reciprocal measurements. Our study demonstrated that the use of single multicore cables with 5 m separation between electrodes resulted in less than 10% of valid normal and reciprocal measurements at 7.5 Hz, whereas more than 50% of the measurements still show reciprocity when collected with a single coaxial cable. Accordingly, the deployment of coaxial cables removes the necessity of using separate cables, consequently increasing the depth of investigations or resolution of SIP imaging surveys. Moreover, the use of coaxial cables permits to deploy the same field procedures for the collection of SIP data as used for ERT surveys. The simplification of field procedures represents an important step forward to make the SIP imaging an attractive method for applications beyond academia.

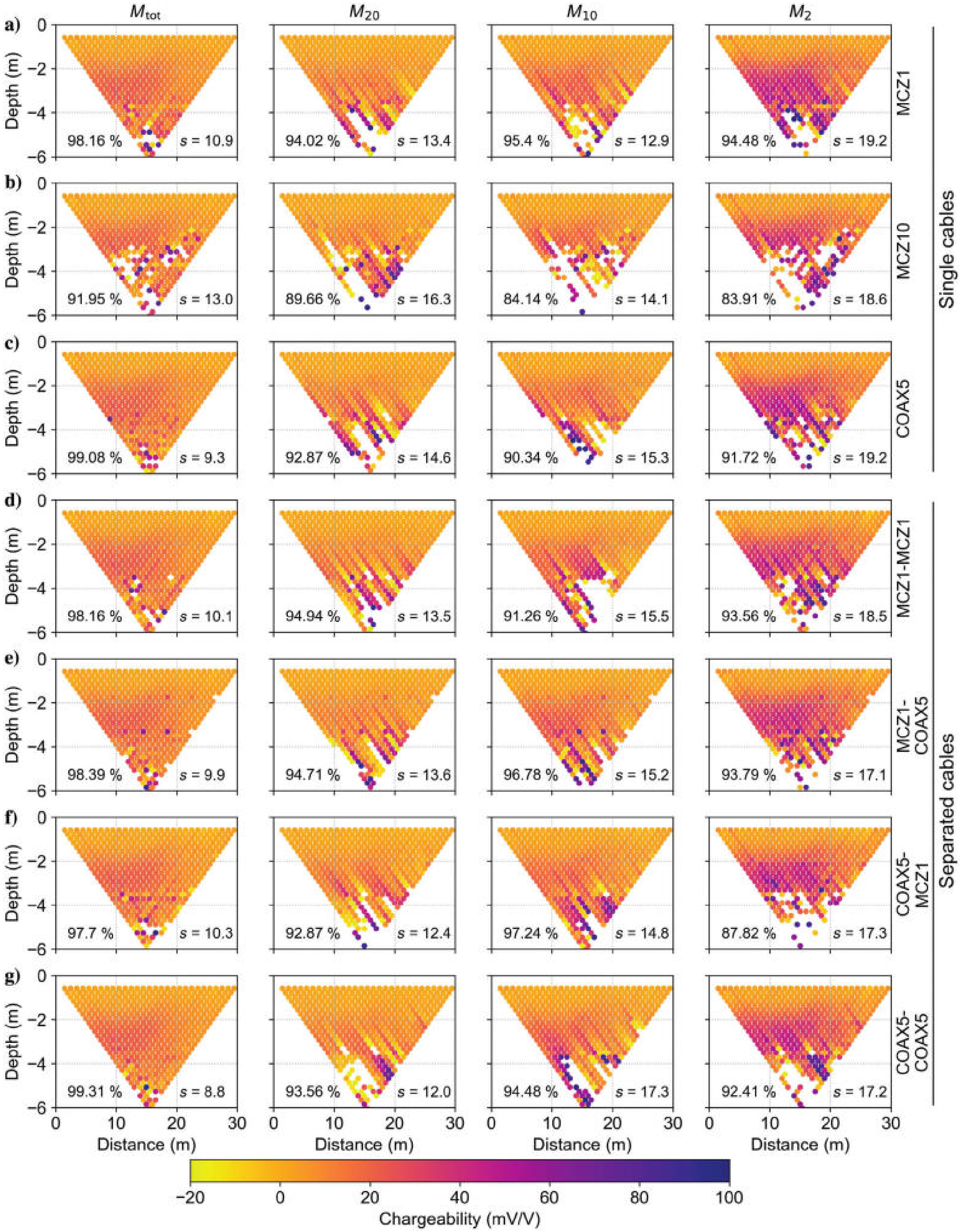

Figure 3.8: Pseudosections for TDIP data collected at the HOAL site using 32 electrodes with a separation of 5 m between them. TDIP readings were collected using (1) current injections and potential readings in a multicore cable (the plots in the first row) followed by (2) current injections in the multicore cable and potential readings in the coaxial (the plots in the second row). For comparison, pseudosections are also presented for data collected with a single coaxial cable (the third row). The inserted labels indicate the total of the remaining measurements after the removal of outliers and the standard deviation (s) in the phase readings.

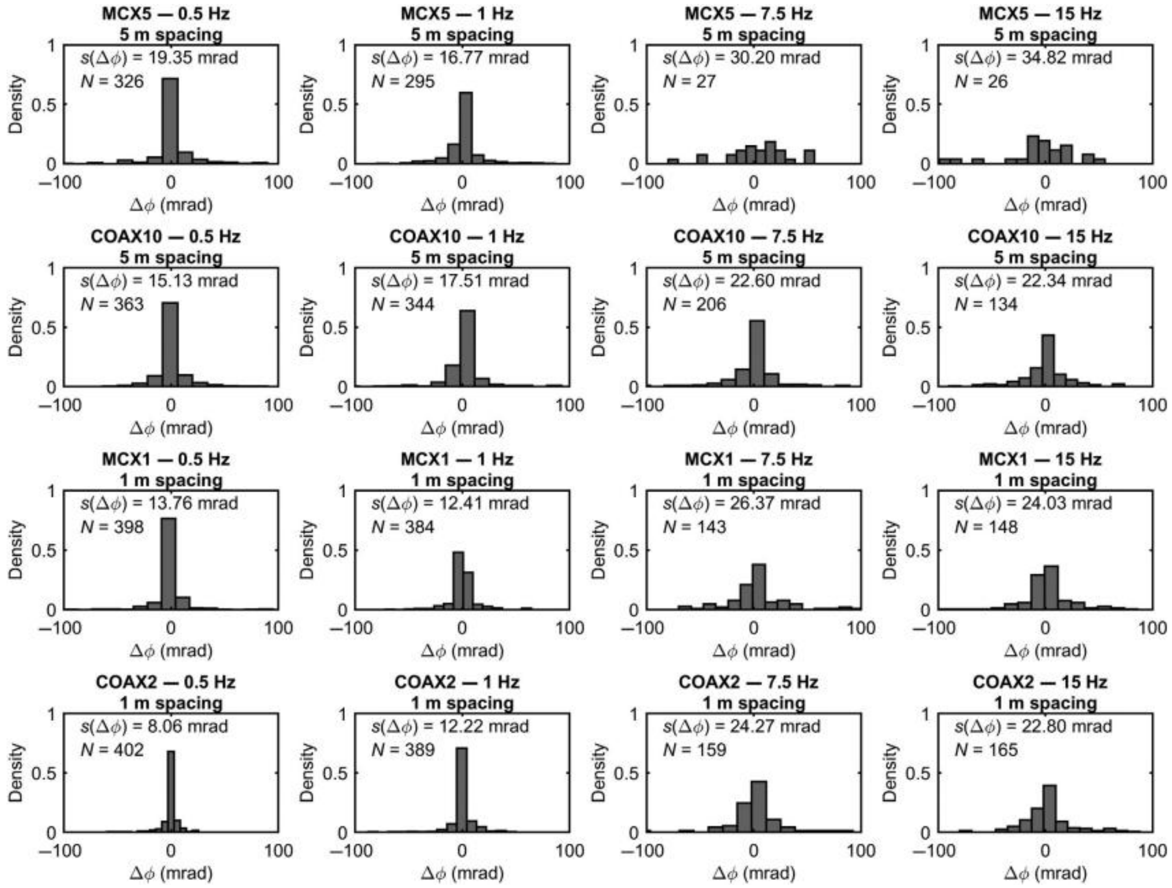

Figure 3.9: Analysis of the misfit between normal and reciprocal phase readings ($\Delta\varphi$) for imaging data sets collected along P1 with the long multicore MCX5 and coaxial COAX10 cables, as well as along P2 with the short multicore MCX1 and COAX2 cables. In each subplot, we include the standard deviation of the normal reciprocal misfit ($s(\Delta\varphi)$) and the total number of normal-reciprocal pairs (N). Filtering of the data was performed only before the analysis of $\Delta\varphi$, corresponding only to the removal of erroneous measurements and outliers.

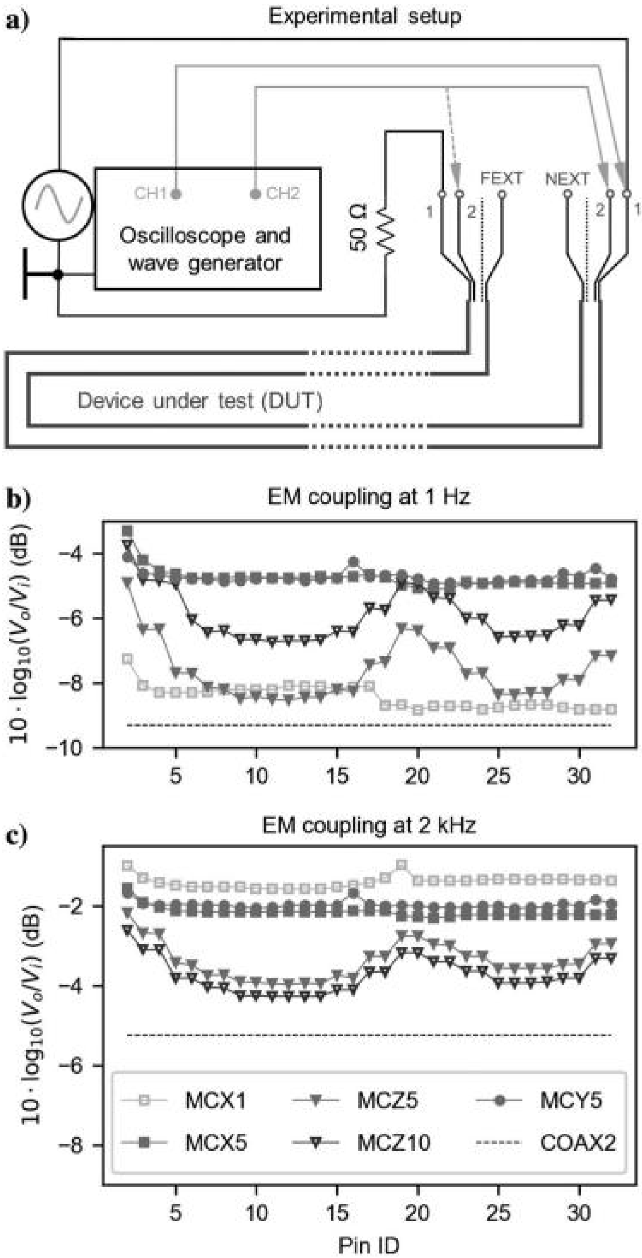

Figure 3.10: Experimental set-up and results for laboratory measurements, where a sinusoidal voltage (V_i) was established across one wire (i.e., core) of a multicore cable, and measurements of the observed voltages (V_o) were collected to assess EM coupling within the cables. (a) Presents the schematic diagram of the measurements with NEXT and FEXT represent the end connectors of multicore cables (i.e., DUT), with symbols within each connector representing the pins related to each independent wire of the multicore cable. Plots of the EM coupling observed in each of the pins for the different multicore cables associated to current injections at 1 Hz (b) and 2 kHz (c), while the values observed in the COAX2 cable are indicated by the dashed lines.

4 Delineation of subsurface variability in clay-rich landslides through spectral induced polarization and electromagnetic methods[1]

4.1 Introduction

Landslides in urban settlements are global socio-economic geohazards, particularly those developed in clay-rich formations due to their hardly predictable accerlation and liquefaction phases as well as high sediment volumes (Malet et al., 2005). Landslide mobilization typically occurs as a result of intense and long-lasting precipitation which can lead to a built-up of positive pore-pressure and an associated reduction of shear strength, particularly for clayey and silty textures (Campbell, 1975; Rogers and Selby, 1980). Hence, knowledge of the internal structure and textural composition of landslides is an important prerequisite for hydrogeologic and hydraulic modelling (e.g. the deduction of water-circulation within the landslide body), which is further needed for the understanding of internal processes associated with triggering mechanisms (Merritt et al., 2014). Traditionally, direct ground-based hydrogeological and geotechnical measurements, using piezometers, inclinometers, dynamic probing and laboratory textural analysis from soil samples have been used to provide information on the subsurface properties of landslides (Glade and Dikau, 2001; Petley et al., 2005; Perrone et al., 2014). However, such investigation techniques are spatially constrained to specific point locations and require spatial up-scaling, which, particularly for heterogeneous areas, is associated with an undesirable increase in data uncertainty (Binley et al., 2015; Wainwright et al., 2016). This lack of spatial resolution may be mitigated by the use of geophysical techniques (e.g., Jongmans and Garambois, 2007)), which permit to gain quasi-continuous information about subsurface physical properties, which in turn are linked to hydrogeological (e.g., Binley et al., 2005; Weller et al., 2015)), lithological (e.g., Hack, 2000; Bell et al., 2006)) and geotechnical parameters (e.g., Cosenza et al., 2006; Sass et al., 2008; Fressard et al., 2016)). Of such

[1]This chapter is based on: Gallistl, J., M. Weigand, M. Stumvoll, D. Ottowitz, T. Glade, and A. F. Orozco (2018). “Delineation of subsurface variability in clay-rich landslides through spectral induced polarization imaging and electromagnetic methods”. In: *Engineering Geology* 245, pp. 292–308. DOI: 10.1016/j.enggeo.2018.09.001

geophysical methods, electromagnetic induction (EMI) and induced polarization (IP) imaging appear as promising techniques for the investigation of clay-rich landslides, considering their ability to solve for the subsurface distribution of the electrical properties, which are strongly linked to clay and water content and can be used to derive hydrogeological information (e.g., Grandjean et al., 2011; Sirles et al., 2013; Merritt et al., 2014; Altdorff and Dietrich, 2014)).

The EMI method has relatively low application costs and, more importantly, is a contactless technique well-suited to map large areas in relatively short acquisition times (e.g., Everett, 2012; Doolittle and Brevik, 2014a; Binley et al., 2015)). EMI measurements provide depth-integrated values of the in-phase and quadrature components of the secondary EM field, which in turn can be transformed into apparent electrical conductivity σ_a (ECa) given a low-induction number assumption. The resulting bulk ECa can then be interpreted in terms of clay-content, porosity, temperature changes, electrolyte salinity and water saturation given a calibrated petrophysical relationship (Brevik et al., 2006). EMI methods are widely used in soil studies (Doolittle and Brevik, 2014a), and monitoring measurements can be applied for the quantification of soil moisture changes (Robinson et al., 2012; Shanahan et al., 2015). It has been suggested that in the scope of slope instability studies, maps of σ_a permit the identification of zones with different soil properties relevant for the characterization of infiltration and surface run-off regimes (e.g., Kušnirák et al., 2016). Hence, a few studies have referred to the application of EMI techniques for the characterization of landslides (e.g., Mauritsch et al., 2000; Grandjean et al., 2011; Altdorff and Dietrich, 2014; Kušnirák et al., 2016). Moreover, the application of airborne electromagnetics (AEM) has drawn attention as a suited technique to investigate areas a the large scale (Nakazato and Konishi, 2005; Lysdahl et al., 2017).

However, typical geophysical investigations of landslides target the delineation of both the vertical and lateral distribution of physical properties, as needed, e.g., for the delination of the sliding plane or the estimation of mobilized volumes. On that account, electrical resistivity tomography (ERT) is a method which permits to solve for the subsurface distribution of electrical resistivity (or its inverse electrical conductivity) in 2D and 3D models and it has been extensively applied in the last 20 years for the characterization of landslides (see Perrone et al., 2014, for an overview). Resistivity images can be explored for resistivity contrasts, which can be indicative for lithological changes and thus, the sliding materials and the stable unit and the geometry of the sliding plane (Lapenna et al., 2003; Bell et al., 2013), as well as the areas of the landslide characterized by higher water content (e.g., Lebourg et al., 2005; Sass et al., 2008; Lehmann et al., 2013). However, clay-rich sediments are also related to low electrical resistivity values due to conduction mechanisms taking place at the negatively-charged surface of clay minerals (e.g., Revil and Glover, 1998). Hence, the quantitative interpretation of the ERT results may be challenging, taking into account the impossibility to discriminate whether the electrical conductivity models are controlled by variability in water or clay content. Hence, some authors have referred to the application of the Induced Polarization (IP) method for the structural characterization of landslides (Marescot et al., 2008; Perrone et al., 2014). The IP method is an extension of the ERT technique, which provides information about the electrical conduction and capactive (polarization) properties of the subsurface (e.g., Kemna et al., 2012, and references therein). Initially, the IP method was developed for mining applications due to the strong polarization response observed in the presence of iron sulphides (e.g., Pelton et al., 1978). However, in recent years it has emerged as a promising technique for hydrogeological and environmental applications (e.g., Kemna et al., 2012). Studies demonstrate the successful application of the IP method for an improved lithological discrimination (Kemna et al., 2004), the assessment of permafrost degradation (Doetsch et al., 2015), the monitoring of bioremediation processes (Flores Orozco et al., 2011; Flores Orozco et al., 2013), the mapping and characterization of contaminant plumes (Flores Orozco et al., 2012b; Ntarlagiannis et al., 2016), and the monitoring of microscale particle injections (Flores Orozco et al., 2015). Furthermore, IP laboratory measurements performed at different frequencies, in the so-called spectral IP (SIP), have shown a characteristic frequency dependence of the IP effect linked to textural parameters of soil (e.g., Binley et al., 2005; Weller et al., 2010; Revil, 2012). Based on such findings, there is an extensive research into the application of the SIP method to characterize the hydraulic conductivity (Slater, 2007; Weller et al., 2015). Nevertheless, the mechanisms underlying the IP response are still not fully understood (e.g., Kemna et al., 2012); thus correlation with ground-truth information is required for an adequate interpretation of the IP imaging results.

To date, only a limited number of studies report the application of the IP method for the characterization of landslides (Marescot et al., 2008; Taboga, 2011; Sastry et al., 2012; Dahlin et al., 2013; Sirles et al., 2013). However, in such studies the evaluation of the IP images is mostly based on cross-validation with other geophysical data or limited lithological information provided by core drillings. Geotechnical testing such as penetration tests or textural analysis of recovered sediments have not been considered for a quantitative interpretation of the IP imaging results. Furthermore, and to the best of our knowledge, no studies have yet reported the application of SIP imaging for the characterization of landslides. Hence, we believe that a case study presenting extensive (S)IP imaging results and their evaluation through geomorphological and geotechnical data is required to better assess the applicability of this technique for an improved investigation of landslides.

To fill this gap, we present here a case study for the characterization of a landslide in Lower Austria through a combined investigation of EMI and IP mapping and geotechnical data. The landslide is characterized by high fractions of clay-rich sediments of the Flysch and Klippen Zone (Wessely et al., 2006), which imposes some limitations on the interpretation based solely on ERT results. Through extensive geotechnical information available at the study area, we evaluate the geophysical results and their applicability to determine relevant landslide characteristics such as the accumulation and infiltration zones, the sliding plane, and ground water flow paths. Available information about textural soil parameters allows us to discuss the value of the added information gained from the capacitive properties of the subsurface provided by the IP method. Furthermore, we present SIP imaging results to investigate the frequency dependence of the subsurface electrical properties and their correlation with geotechnical and textural parameters. In the next section, we provide a description of the study area as well as the geophysical and non-geophysical data, followed by the presentation and discussion of EMI maps. Then we present and discuss the IP imaging results and the SIP data, as well as their correlation with ground-truth data, followed by the final interpretation of the geophysical investigation and the conclusions.

4.2 Site description

The study area is located in the southwestern part of Lower Austria, Austria (Figure 4.2). Several investigations have been carried out at the study area by the local authorities, thereby gathering extensive information about the surface deformation by means of geomorphological mapping, geodetic monitoring techniques and terrestrial laser scanning. Further subsurface investigations have been conducted through direct methods, namely dynamic probing heavy, percussion drilling and inclinometer measurements. Variations in the groundwater level and soil moisture have been measured using a piezometric network and time-domain reflectrometry (TDR) respectively. Previous geotechnical investigations at the study area have suggested the existence of a shallow sliding plane in approximately 2 to 3 m depth (for further details refer to Stumvoll et al., 2020).

Based on geomorphological mapping the extension of the active landslide area has been estimated to cover approx. 4000 m^2. The inclination of the slope ranges between 5° and 15°, with steeper part up to 20° in the bulged areas, which are related to the recently most active sections. The geological setting of the study area is characterized by three different tectonic units: (i) the Penninic (Rhenodanubian) Flysch Zone (FZ) in the north, (ii) the (Upper) Austroalpine Norther Calcareous Alps (NCA) in the south, (iii) and the Helvetic unit of the Gresten Klippen Zone (GKZ) in between. Such compound settings result in diverse lithological contacts, which promote landslide occurrence in the region (e.g., Ruttner and Schnabel, 1988; Schnabel et al., 2002). From 1100 landslides reported in Lower Austria between 1965 and 2006, 62% of them occurred in the Flysch and Klippen Zones (42% Flysch and 20% Klippen Zone (e.g., Gottschling, 2006; Petschko et al., 2014). The GKZ and FZ units are intricate regarding their stratigraphy, lithology and facies, with both units mainly characterized by marine sandstones, clays, clayey shales, marly shales and marly limestones, yet conglomerates and breccia have been reported in the GKZ (for more details see, e.g., Ruttner and Schnabel, 1988; Wessely et al., 2006).

The first slope movement in the area was reported in 1975, and it has been suggested its triggering was related to heavy precipitation events occurring between June 29th and July 3rd. The landslide was reactivated in 1978 after heavy precipitation on Mai 31th, with further displacements reported in 2006. Between 2007 and 2012, displacements were monitored via tachymetric surveys, which have been stopped after 2012 due to only minimal displacements observed (e.g., max. 20 cm in 2009). Since the first displacements occurred in 1975, remediation techniques at the site have included the removal of displaced material, filling of tension cracks and depletion zones (1975 and 1978), leveling of the upper area and the installation of a drainage system in the eastern part of the study area in 2009.

4.3 Material and methods

4.3.1 Low induction number electromagnetic imaging

Electromagnetic induction (EMI) imaging results presented in this study were performed with the so-called terrain conductivity meters, or more precisely, low induction number electromagnetic methods (e.g., McNeill, 1980b; Everett, 2005). EMI exploits the principle of electromagnetic induction by making use of a sensor system that generates a primary magnetic field by applying an alternating current at a fixed frequency which passes through a transmitter coil. Due to the time-varying character of the magnetic field, eddy currents are induced in a conductive subsurface, which subsequently generate a secondary magnetic field sensed by the receiver coil. The induction number (b) for a given system is a function of the angular frequency of the primary field (ω), the separation between the transmitter and receiver coils (l), the magnetic permeabil-

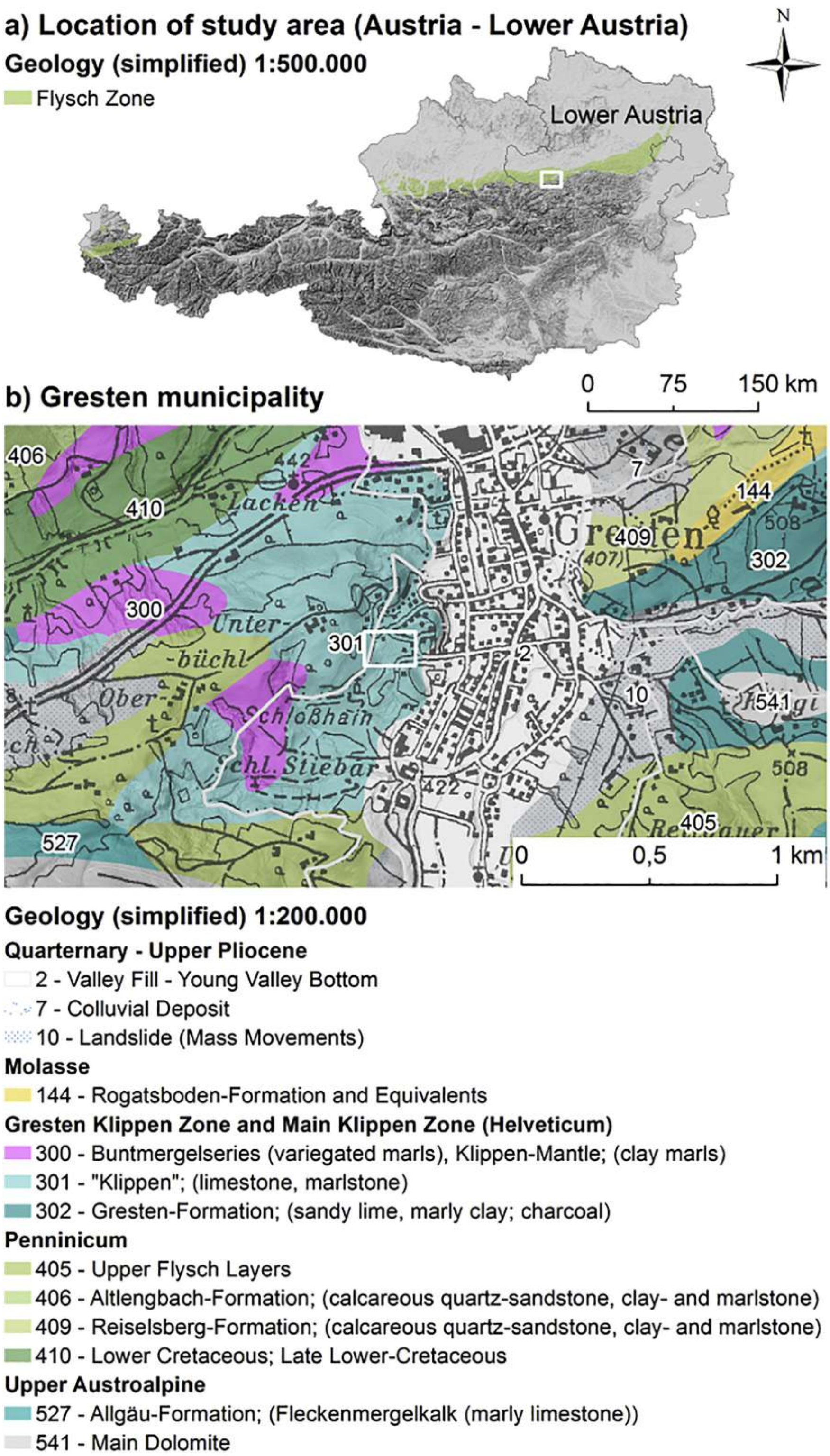

Figure 4.1: Location of the study area in the geological unit of the (Rhenodanubian) Flysch Zone in the western part of Lower Austria, Austria (Figure 4.1a). Geological setting of the study area (Figure 4.1b). Geological maps modified after Weber (1997) and Schnabel et al. (2002)

ity (μ) and the bulk electrical conductivity (σ) of the earth, and can be written (e.g., McNeill, 1980a) as:

$$b = \mu\sigma\omega l^2 \tag{4.1}$$

Terrain conductivity meters are instruments where l and ω are designed to work at low induction number ($b < 1$), at which the response is dominated by the ratio between secondary and primary magnetic field. Assuming that μ in subsurface materials is close to one as in vacuum, the measured response is then only controlled by the electrical properties, thus permitting to obtain the apparent electrical conductivity σ_a in the subsurface quasi in real time (Keller and Frischknecht, 1966; Ward and Hohmann, 1988). As a contactless techniques EMI permits to map large areas in reasonably low acquisition times (up to 5000 m^2/h depending on the study site).

Values of σ_a represent a nonlinear average of the electrical conductivity values of the examined (sensitive) volume across a depth range that depends on the coil separation and orientation (McNeill, 1980b). The transmitter and receiver coils can be orientated horizontally (horizontal coplanar, HCP) or vertically (vertical coplanar, VCP) with respect to the ground surface. Increasing l in combination with VCP loops increases the depth range for the σ_a measurement (e.g., McNeill, 1980b; Callegary et al., 2007). Modern commercial instruments typically provide more than one transmitter/receiver pair and therefore can provide σ_a for different depth ranges. Vertical profiles of the electrical conductivity (σ) of the examined volumes can be obtained from inverse modelling (e.g., Mester et al., 2011; Hebel et al., 2014) of σ_a data sets measured for different depths of investigations (i.e., varying coil separation, coil orientation).

4.3.2 EMI mapping

In this study we applied EMI measurements to map lateral changes in the subsurface electrical properties using the CMD-Explorer (by GF Instruments), which uses three receiver coils with separation of 1.48 m, 2.82 m, and 4.49 m to the transmitter coil simultaneously, at an operating frequency of 10 kHz. All measurements on the landslide were performed in VCP mode for effective depth ranges of 2.2 m, 4.2 m and 6.7 m. The sampling frequency was 1 Hz, hence at an average walking speed σ_a values were collected approximately every 0.7 m along the walking tracks presented in Figure 4.2. The measured conductivity values were geo-referenced by means of differential GPS measurements. In total, the data set consists of approximately 30.000 σ_a values with survey performed within 3 h. EMI measurements were planned to map the entire

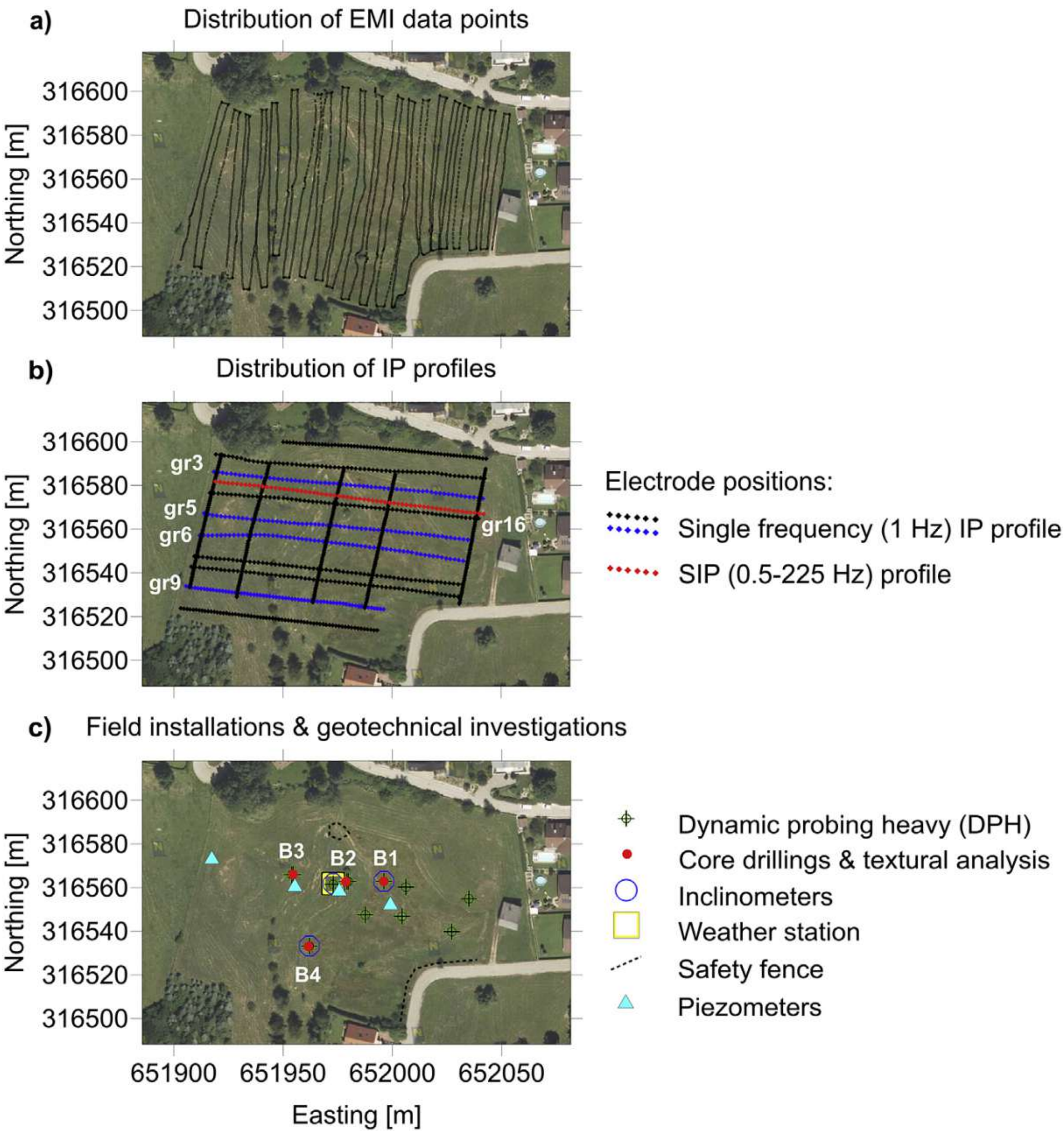

Figure 4.2: Experimental set-up at the study area showing the transects for the collection of the EMI mapping data (indicated by the black dots in Figure 4.2a), the orientation of the IP profiles (position of the electrodes indicated by the black, blue, and red symbols in Figure 4.2b), and the location of the measuring points of direct methods, as well as field installations (Figure 4.2c).

extension of the recently active landslide area and delineate lateral variations in the electrical conductivity. In this study, we do not discuss the inversion of EMI data and associated uncertainties, which is required to solve for vertical variations in σ_a. Instead, we present maps of the σ_a directly recovered from measurements recorded with different coil separation. The maps were obtained by spatially interpolating all positive measured σ_a values (negative values were removed) using the kriging method. For the interpolation we used a linear variogram and an elleptical search space stretching into the direction of the landslide movement (axis ratio 1:2).

4.3.3 Complex conductivity imaging

Similar to ERT, the induced polarization (IP) method is based on four-electrode configurations, where two of them are used for current injection and the other two to record the resulting voltage. In case of frequency-domain, current injection is performed using a sinusoidal waveform and data collection includes the measurement of the ratio between the measured voltage and current, as well as the time delay between both, resulting in a complex-valued electrical transfer impedance. Measurements can be repeated at different frequencies to gain information about the frequency dependence of the electrical properties, in the so-called spectral IP (SIP). SIP measurements are commonly conducted at the low frequencies (between 10 mHz and 1 kHz), with lower frequencies (< 1 Hz) associated to long acquisition times, whereas high frequencies ($>$ 10 Hz) bear the risk of contamination of the data due to electromagnetic effects (Flores Orozco et al., 2013). In case of time-domain surveys, IP measurements record the remnant voltage after current injection is switched off (e.g., Binley and Kemna, 2005). Both frequency and time-domain measurements are theoretically equivalent, coupled by a Laplace transformation, and can both be used to investigate the distribution of complex electrical conductivity in subsurface materials (Flores Orozco et al., 2012b). A detailed review of the IP method can be found Ward (1990), Binley and Kemna (2005), and Kemna et al. (2012).

The low frequency electrical properties of the subsurface are commonly expressed in terms of the complex electrical conductivity $\sigma^*(\omega)$ (with ω denoting the angular excitation frequency), which can be parameterized by means of its real,$\sigma'(\omega)$, and imaginary, $\sigma''(\omega)$ components, or by its magnitude $|\sigma^*(\omega|$ and phase-shift $\varphi(\omega)$, such that:

$$\sigma^*(\omega) = |\sigma^*(\omega)|e^{i\varphi} = \sigma'(\omega) + i\sigma''(\omega) \tag{4.2}$$

with $i = \sqrt{-1}$, and

$$\varphi = \arctan\frac{\sigma''(\omega)}{\sigma'(\omega)}. \tag{4.3}$$

The real part of the complex conductivity accounts for energy loss (ohmic conduction) and, for sediments without metallic minerals, is mainly controlled by the porosity, connectivity of the pore space, saturation, and the fluid electrical conductivity of the pore-filling electrolyte (e.g., Revil and Glover, 1998; Lesmes and Morgan, 2001). The imaginary component is related to energy storage (polarization), which, in absence of metallic minerals, ig given by: (1) the occurrence of clay minerals that can act as ion selective membranes, in the so-called membrane polarization (e.g., Titov et al., 2010; Bücker and Hördt, 2013; Hördt et al., 2017), and (2) electro-chemical polarization taking place at the electrical double layer (EDL), which is formed at the grain-fluid contact (e.g., Leroy et al., 2008; Leroy and Revil, 2009). In case of the membrane polarization the magnitude of the polarization effect is mainly a function of pore-space geometry (i.e, the sequence of wide and narrow pores and their lengths and radii), and for further details we refer to the studies of Bücker and Hördt (2013), Hördt et al. (2016), Chuprinko and Titov (2017), and Hördt et al. (2017).

4.3.4 Inversion of IP imaging data sets

Inversion techniques are used to reconstruct the spatial distribution of complex conductivity from measured data. In this study, inversion of the IP data was performed using CRTomo, a complex resistivity inversion algorithm (Kemna, 2000), using the sensitivity-controlled focusing (SCF) regularization scheme presented in Blaschek et al. (2008). This regularization scheme is based on the minimum gradient support (MGS) described in Portniaguine and Zhdanov (1999) and permits to solve for images with sharp contrasts between structures characterized by different electrical properties, yet allowing smooth parameter changes within them (Blaschek et al., 2008). This is particularly important, as landslides are typically complex systems which cannot be explained by simple two layer cases without variations in the electrical properties within the layers. We opted for this regularization scheme, over the commonly used smooth-regularization, to properly solve for the interface between the sliding material and the bedrock, which is expected to form a sharp contrast between materials with contrasting electrical properties (e.g., Lapenna et al., 2003). Although CRTomo permits the definition of error models to fit the data to a confidence inteval within the inversion (Kemna, 2000; Flores Orozco et al., 2012a), in case of data sets presented here we used a robust inversion schemes based on an iterative re-weighting of poorly fitted data points (referred to as IRLS, e.g., LaBrecque and Ward, 1990; Kemna, 2000), which are less sensitive to incorrect estimates of the random data error, as discussed in Morelli and LaBrecque (1996). Model appraisal was performed based on the analysis of cumulated sensitivity (e.g., the sum of absolute, data-error weighted sensitivities of all considered measurements), as performed in previous studies (Kemna et al., 2002; Weigand et al., 2017). Accordingly, we masked pixels in the imaging results associated to poor sensitivity, i.e., those pixels associated to $\log_{10}$ cumulated sensitivities 2 orders of magnitude smaller than the highest cumulated sensitivity.

4.3.5 Single frequency IP mapping and SIP imaging

In this study, single frequency (1 Hz) IP imaging measurements were collected along 15 profiles distributed over the active landslide area: ten profiles orientated parallel to the landslide axis (west-east, WE), and five profiles perpendicular to it (north-south, NS), as depicted in Figure 4.2. Profiles collected in WE direction had an average distance of 10 m between them, using 64 electrodes in each profile with 2 m separation between electrodes. The profiles at the boundaries of landslide (gr1, gr9, gr10) were collected with 1.5 m spacing between electrodes to avoid placing electrodes close to anthropogenic structures, commonly related to the contamination of IP data by cultural noise (e.g., Flores Orozco et al., 2012b). The separation between the NS profiles ranges between 20 m to 40 m (Figure 4.2), with measurements collected with 64 electrodes and a separation of 1 m between electrodes in each profile. Aiming for a depth of investigation of 15 m, IP measurements were conducted with a dipole-dipole configuration combining skip-0, skip-1 and skip-2 protocols. The skip refers to the dipole length, defined by the number of electrodes skipped between the two current electrodes, as well as between the two potential electrodes (Slater et al., 2000). Such configuration permitted an acquisition time of 45 min (at 1 Hz), aiming for the collection of the 15 mapping IP profiles within 2.5 days from May 10th to 12th to warrant similar meteorological and subsurface conditions. Particular care was taken to avoid potential readings with electrodes previously used for current injection and the contamination of the data due to polarization of the electrodes (e.g., LaBrecque and Daily, 2008; Flores Orozco et al., 2012a).

To investigate the spectral behavior of the subsurface materials in the landslide, SIP data were collected along one profile in WE direction (gr16 in Figure 4.2) with 64 electrodes and 2 m separation between electrodes. Here, 12 frequencies in the range between 0.5 Hz to 225 Hz Hz were used with the same dipole-dipole configuration previously applied in the single-frequency surveys. All measurements were collected using a DAS-1 instrument (from MultiPhase Technologies), with the instrument placed at the center of the profile (between electrode 32 and 33). A control of the contact resistances between adjacent electrodes was performed before data collection, with the re-installation of electrodes performed in case of high values ($> 1\,\mathrm{k}\Omega$), to ensure a good contact between electrodes and the ground, aiming for current injections in the range between 100 mA to 400 mA.

To illustrate the quality of the measured data, in Figure 4.3 we present the pseudosection of the IP measurements in terms of the apparent resistivity (ρ_a) and apparent phase-shift (φ_a), for data collected along profile gr5, as well as their corresponding histograms. This particular profile was selected as it is expected to be representative for the study area and it is close to most of the geotechnical measurements, permitting a direct comparison with ground-truth information (c.f., Figure 4.2). Due to the nature of IP imaging measurements, pseudosections are expected to reveal smooth variations of ρ_a and φ_a, and abrupt changes may be indicative of a data set containing systematic errors, i.e., outliers, which need to be removed before the inversion. Plots in Figure 4.3 reveal smooth variations in the pseudosection of ρ_a, with values ranging between 10 Ωm to 80 Ωm, without any observable outlier. In case of the φ_a readings, the pseudosection reveals mainly values between 0 mrads to −10 mrads for short dipole lengths (located at the shallow levels of the pseudosection). Measurements located at larger pseudodepths reveal poor spatial consistency with larger variations between adjacent readings, suggesting readings with a poor signal-to-noise ratio (S/N). In order to remove outliers, we adapted the filtering approach proposed by Flores Orozco et al. (2018b). The automatized data processing consists of a four step procedure: 1) the data set is partitioned into subsets defined by potential readings collected by the same current dipole, 2) the median φ_a for each subset is computed, as well as 3) the deviations to such median value ($\Delta\varphi$) from each reading in the subset, 4) removal of all readings associated with an absolute deviation $|\Delta\varphi|$ exceeding two times the standard deviation of $\Delta\varphi$ of the entire data set. Furthermore, we analyse the distribution of the measurements. To this end, the remaining measurements are binned using the rule proposed by Sturges (1926) and Larson (1975), and further outliers are defined as those measurements located in bins separated from the main distribution. As discussed in Flores Orozco et al. (2018b), the presence of gaps in the histogram indicates measurements without spatial correlation within the data set. Figure 4.3b presents the pseudosections for ρ_a and φ_a, as well as the corresponding histograms, after following the steps defined above. Such plots show pseudosections less affected by outliers, with φ_a values ranging between −10 mrads to 0 mrads, with consistent results observed for the rest of the IP profiles (data not shown).

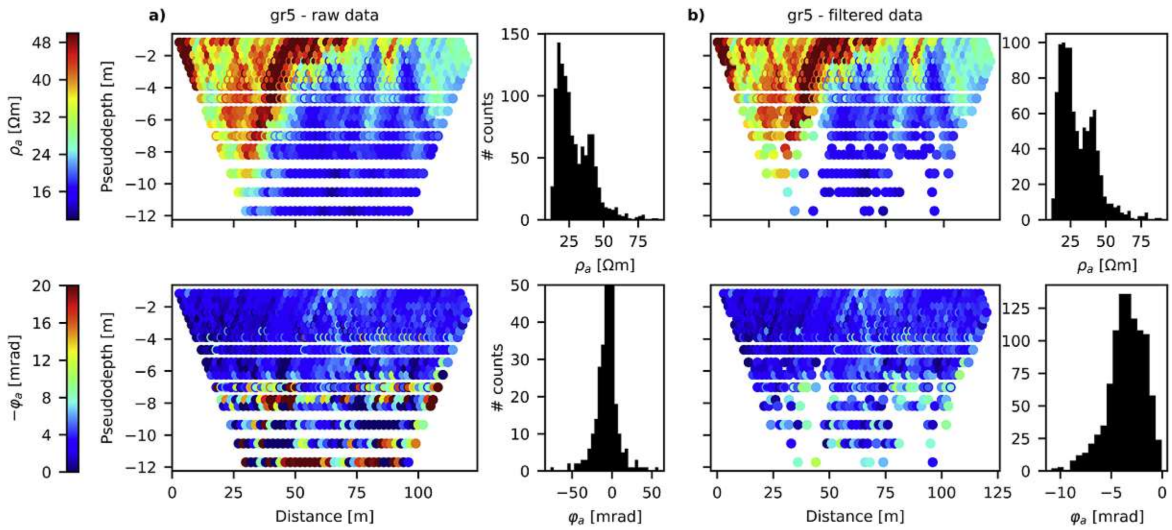

Figure 4.3: Raw data analysis: Plots present the measured values in terms of the apparent resistivity (first row), and the apparent phase-shift (second row) for data collected along profile gr5 (Figure 4.2b). Plots show the pseudosections and histograms for the raw data (Figure 4.3a) and after the removal of outliers (Figure 4.3b).

4.3.6 Complementary geotechnical and hydrogeological methods

At the landslide, dynamic probing heavy (DPH) was performed with a pneumatic heavy dynamic penetrometer (SRS-15), using a drop weight of 50 kg, a cone diameter of 43.7 cm and a drop height of 0.5 m, with the results presenting the blow counts needed to insert the probe for a 10 cm increment. In this study we present data collected along thirteen DPH soundings performed along the landslide axis, as depicted in Figure 4.2c. Additional six core drillings (only four presented in this study) were retrieved from perforations with a maximum depth of ∼9 m in the vicinity of the DPH locations, as presented in Figure 4.2c. Soil samples taken from the core drillings were analysed in the laboratory to gain the particle size distribution using sieving (based on ÖNORM L1061–1/ DIN-ISO 3310/1) and sedimentation analysis (with reference to ÖNORM L 1061–2).

For the monitoring of subsurface displacement and the delineation of possible shear zones, one automatic chain inclinometer with an installation depth of 13 m, and two manual inclinometers with installation depths of 6.5 m, are operated at the study site, as presented in Figure 4.2c. Measurements were taken for the sequential segments of 1 m for the 13 m inclinometer, whereas segments of 0.5 m were used for the 6.5 m inclinometers. Furthermore, variations in the groundwater levels are monitored by means of a piezometric network, with sensors installed to a depth of 7 and 8 m respectively (Figure 4.2c). For more details on the geotechnical investigations at the study site we refer to Stumvoll et al. (2020).

4.4 Results and discussion

4.4.1 EMI mapping

Figure 4.4 presents the interpolated maps of the apparent conductivity values for the three collected depth ranges (i.e., 2.2, 4.2, 6.7 m), in the following referred to as $\sigma_{2.2}$, $\sigma_{4.2}$ and $\sigma_{6.7}$. We note here, that anomalously high σ_a values ($> 40\,\mathrm{mS/m}$) are associated with the response of metal from anthropogenic structures and other measuring instruments (e.g., fences, inclinometers, and the weather station; c.f. Figure 4.2c) and will not be further addressed.

In general maps for $\sigma_{2.2}$ and $\sigma_{4.2}$ reveal consistent patterns and σ_a values, permitting the identification of two main regions: (i) an area of elevated σ_a ($> 25\,\mathrm{mS/m}$) in the central region of the landslide, as well as (ii) areas characterized by low σ_a values ($< 20\,\mathrm{mS/m}$), located at the western and north-eastern regions of the site, corresponding to the highest (> 455 m above sea level, asl) and lowest topography levels (< 440 m asl) respectively, as observed in Figure 4.4f. To evaluate the similitudes for the different depth ranges, in Figure 4.4d and 4.4e we present difference images for consecutive depth ranges. Considering the minor differences between the maps of$\sigma_{2.2}$ and $\sigma_{4.2}$ (Figure 4.4d), characterized by an only modest variation in σ_a ($\sim 2\,\mathrm{mS/m}$), we can interpret only minimal vertical variations in shallow subsurface materials (between 0.5 m to 4 m depth). Nevertheless, the map for $\sigma_{6.7}$ reveals visible variations, in comparison with shallower maps, with a broader range in the measured σ_a values, as also evidenced in Figure 4.4e.

Comparison of the shallow maps ($\sigma_{2.2}$, $\sigma_{4.2}$) and the $\sigma_{6.7}$ map reveal two major differences: (i) a significant increase in the σ_a values for the central area of the landslide, suggesting an increase in saturation or clay content at depth in that area; as well as (ii) an increase in the variability of σ_a in the western part of the landslide, where higher σ_a values can be observed. Given the higher variability in σ_a observed in the deeper EMI measurements (Figure 4.4c), we classify the $\sigma_{6.7}$ maps into four main regions arranged in west-east direction: (1) a low conductivity region ($< 20\,\mathrm{mS/m}$) related to topographical highest areas (> 455 m asl), (2) a region of intermediate conductivity values ($\sim 26\,\mathrm{mS/m}$), (3) a region of elevated conductivity values (30-38 mS/m) associated to topography values between 444 and 455 m asl, and (4) low to intermediate conductivity values (18–26 mS/m) located at the foot of the landslide ($\sim$ 440 m asl). A color-coded map using such classification is presented in Figure 4.4g, which reveals consistent features to surface topographical discontinuities, as observed in the hillshade model of the DEM (Figure 4.4f).

4.4.2 Interpretation of the EMI mapping in combination with geomorphological data

The correlation between the changes in topography and the σ_a features suggests a link between the EMI maps and geomorphological patterns. To better investigate this, we overlapped the EMI maps with geomorphological features, namely, the limits of the landslide scarps, waterlogged areas and the accumulation zone as obtained from geomorphological mapping (Figure 4.4a, b, c). Plots in Figure 4.4 show in general that the three σ_a depth ranges solve consistently for high σ_a values in waterlogged areas, with an observed increase in σ_a with increasing the depth range (e.g., an increase from 30 to 40 mS/m for the waterlogged area in the center of the study site for the $\sigma_{6.7}$ map). For waterlogged areas, which can be expected to be fully saturated, such increase in the electrical conductivity suggests an increase in clay content and thus, the possible contact between units with different hydrogeological properties, a common factor associated to the accumulation of pore-water pressure and the triggering of landslides (e.g., Samyn et al., 2012). In particular, the observed change between the shallow-to-intermediate and the deep maps might be related to the contact to the shallow sliding plane delineated in a previous study located in approximately 2–3 m depth (Stumvoll et al., 2020).

Yet, to interpret EMI maps at different depths, it is necessary to take into account the sensitivity at depth associated with the geometry of the instrument. The normalized sensitivity function Φ for EMI measurements in the VCP mode can be computed using the well-known equation (McNeill, 1980b):

$$\Phi = \frac{4\frac{D}{l}}{[4\frac{D}{l}^2 + 1]^{\frac{3}{2}}} \tag{4.4}$$

in which D represents the depth as continuous variable. Plots for the instrument used in our study (Figure 4.4h) reveal the highest sensitivity for $\sigma_{2.2}$ and $\sigma_{4.2}$ maps between ~ 0.25 and 3 m depth, clearly demonstrating the influence of sliding materials, and shallow waterlogged areas, on the σ_a values. Whereas, deepest EMI measurements ($\sigma_{6.7}$) are sensitive to depths between 0.5 and 4 m (Figure 4.4h). Hence, the increase in σ_a values at depth for the central area of the landslide (c.f. Figure 4.4e) seems to be related to the contribution of both the sliding materials and the stable unit.

The different landslide scarps show a spatial correlation with lateral variations in the σ_a values in all EMI maps. Furthermore, σ_a patterns observed also in all EMI maps are consistent with the location of the accumulation zone, which in the case of

$\sigma_{6.7}$ is characterized by a transition from high ($\sim$ 36 mS/m) to intermediate ($\sim$ 28 mS/m) conductivity values. The slightly lower conductivity values of the materials in the accumulation zone could be explained by the higher degree of compaction as a result of the accumulating pressure from sliding downhill.

4.4.3 Interpretation of IP imaging in combination with soil-physical and geotechnical data

4.4.3.1 Single frequency IP

For completeness, the evaluation of the resolved complex conductivity variations at depth for a given point and its correlation with ground-truth data is assessed prior to the presentation of the IP imaging results. Figure 4.5 presents relevant textural and geotechnical parameters, namely, the soil type (Figure 4.5a, e) and particle size distribution (Figure 4.5b, f) as obtained from the analysis of core drillings, as well as the blow counts from co-located DPH surveys (Figure 4.5c, g) for the wells B3 (Figure 4.5a-4.5c) and B4 (Figure 4.5e-4.5g), as well as the electrical model parameters expressed in terms of σ' and σ'' (Figure 4.5d, h) extracted from IP imaging results (at 1 Hz in the vicinity of wells B3 and B4.

The comparison of particle size distribution and the electrical properties shows the sensitivity of σ'' to variations in the textural composition. In particular for B3, Figure 4.5 shows that an increase in clay content ($> 40\%$) is related to a significant decrease in the polarization effect (from 50 to 25 μS/m), as observed at depths between 2 and 4 m. For lower clay fractions ($< 20\%$) and increasing the content of gravel and coarse sands (e.g., between 4 and 9 m depth), σ'' increases, whereas the increase appears to be correlated with the silt fractions that reveal an increase over the same depth range. Below 9 m depth, where no textural information is available, σ'' continues to increase and reaches its maximum value ($\sim$ 500 μS/m) at 12 m depth. Such maximum correlates with high blow counts ($>$ 79 blows) and likely indicates the transition to un-weathered bedrock.

The σ' profile reveals only minor changes down to 9 m. There is a decrease in conductivity values from $\sim$ 25 mS/m between 1 and 3 m depth to $\sim$ 10 mS/m between 3 and 10 m, clearly indicating a poor sensitivity to textural variations. Nevertheless, the profile shows an increase in σ' values to the maximum value of 60 mS/m (Figure 4.5d) at 12 m depth, which is in agreement with the increase in blow counts as previously discussed. Furthermore, Figure 4.5 clearly reveals no correlation between the blow counts and the changes in the textural parameters in this core. For instance, the shallow soil samples (between 1 and 4 m depth) associated with the highest clay content ($> 40\%$), and the deeper recovered materials (between 4 and 9 m depth) associated with coarser materials (gravels $> 20\%$ and $\sim 12.5\%$ clays), do not reveal any significant changes in the number of blow counts in DPH. This might be related to an unevenly distributed soil moisture in depth and needs further investigations.

The variations in σ'' and textural parameters observed in well B4 (Figure 4.5f, h) are consistent to those described above for B3: a decrease in the polarization effect for soils dominated by clay (e.g. from 60 to 15 μS/m between 3 and ≈ 4 m depth) and an increase in σ'' with increasing the gravel, sand and silt content. The observed increase in the polarization effect with increasing the content of coarse sediment is consistent with the recent developments in the understanding of the membrane polarization mechanism (e.g., Bücker and Hördt, 2013; Hördt et al., 2017). Such studies have demonstrated that an important parameter controlling the membrane polarization for a homogenous mineral composition is the contact between micro- and macropores, as well as the ratio between the pore-radii and pore-lengths. Furthermore, Chuprinko and Titov (2017) recently demonstrated that variations in the mineral composition of the different pores can also result in a polarization effect superimposing the polarization effect due to the pore-space geometry. Thus, we hypothesize that the observed increase in σ'' is consistent with the contact of macropores in the coarse materials, and the micropores due to the fine grains. Accordingly, the σ'' decreases in horizons dominated by fine silts and clays, where micropores dominate, and most of the energy is conducted along the mineral surface, thus, also explaining the relative high σ' values in the landslide.

The observed correlation between the textural, geotechnical and electrical parameters demonstrates that variations in σ' and σ'' (at 1 Hz) can be used to delineate areas rich in fine-grained minerals (associated to low σ'' at 1 Hz), which may also act as low hydraulic permeable layer hindering the infiltration of surface water. Consequently, high σ'' values may indicate soils with variations of fine and coarse grains which may facilitate groundwater flow and act as drainage systems in the landslide.

4.4.3.2 SIP imaging

We present in Figure 4.5a the SIP imaging results for data collected along gr16 at three representative frequencies to investigate the frequency dependence of the electrical properties and its correlation with ground-truth data. As observed in Figure 4.5a, the electrical conductivity (σ') reveals a negligible frequency dependence (in the frequency bandwidth analysed in this study) and will not be further addressed here. Textural analyses of sediments recovered after the drilling in B1 (Figure 4.5b) and B2

(Figure 4.5e) are shown to better investigate the control of the spectral response (i.e., the frequency dependence) of σ''. Moreover, Figure 4.5 shows the DPH soundings conducted in the vicinity of the wells B1 (Figure 4.5c) and B2 (Figure 4.5f). Figure 4.5d and g presents the spectral amplitude, i.e. σ'', as a function of depth and frequency. The σ'' values were extracted from the electrical images after independent inversion of data collected at each frequency. In general the analysis of soil samples revealed high fractions of fine-grained minerals: clay (20–50%) and silt (10–25%) and low contents of coarser grains (sand and gravel roughly $< 10\%$). The abundance of fine grains is consistent with the relatively modest σ'' response in the low frequencies (< 15 Hz); yet a linear increase in the σ'' values can be observed with increasing the frequency. Such increase in the polarization effect with increasing the frequency is related to the fastest polarization processes in fine grains, where the ions move along shorter trajectories, as observed previously in laboratory studies conducted in clay-rich samples (e.g., Slater and Lesmes, 2002b; Slater et al., 2006; Jougnot et al., 2010). The increase at high frequencies is nevertheless only visible in the saturated materials (below 2 m depth), as pore water is necessary for the development of the electrical double layer where the polarization takes place. The increased σ'' response for B2 between 0 and 1.5 m might be a result of a separated fully saturated patch, as for instance expected for the waterlogged areas. The unsaturated zone is also interpreted as weak materials following the DPH (< 5 blows), with an increase in the DPH counts also observed below 2 m depth.

We observe a noticeable change of σ'' below 6 m depth for B1 and below 9 m depth for B2, at depths where no textural information is available. In particular, plots in Figure 4.5d reveal (i) an overall increase in σ'' for frequencies $>> \sim 1.66$ Hz and (ii) a noticeable peak for σ'' with values well above 700 μS/m. Such peak is situated in the frequency range of 7.5–15 Hz and appears to shift towards lower frequencies with increasing depth, indicating a change in the dominating length scale towards coarser grains (medium to coarse silts), i.e., and slower polarization processes. The DPH also reveals an increase in the material strength below 6 m depth for B1 and below 9 m depth for B2 (> 40 blows). Furthermore, the shift of the σ'' peak to even lower frequencies at 9 m depth for B1 and 11 m depth for B2 is also accompanied by a transition to blow counts above 79 and likely indicates the contact to un-weathered bedrock and larger length-scales dominating the polarization response. Hence, it appears that analysis of the frequency dependence of the polarization effect could be used to distinguish contacts between materials with different mechanical properties.

Nevertheless, analysis of high frequency IP data for field measurements needs to be performed with caution, considering that increasing the frequency (> 10 Hz) also leads to the induction of parasitic electromagnetic fields that contaminate the SIP data (Flores Orozco et al., 2013). Commonly referred to as electromagnetic coupling (EM-coupling), it arises due to current flow along the cables connecting the instrument and the electrodes, due to differences in the contact between electrodes and the ground, and due to self-induction effects between the cables (e.g., Zimmermann et al., 2008; Flores Orozco et al., 2013). It is proportional to the σ' and the square of the excitation frequency (Dey and Morrison, 1973). In case of clay-rich minerals, EM-coupling might superimpose the actual response from the subsurface; thus, in Figure4.5f we do not present data collected at higher frequencies (> 100 Hz), as such data revealed EM-coupling.

4.4.4 IP mapping

Figure 4.7 presents the IP imaging results for the profile gr5 expressed in terms of σ' and σ'', with the related geomorphological features, groundwater levels and blow counts measured by DPH superimposed over the electrical images. The imaging results reveal two main units: (i) a top layer characterized by low σ' (< 30 mS/m) and σ'' (< 150 μS/m) values, with a varying thickness along the profile, and (ii) a deeper unit associated to high spatial variability and a broader range in the σ' and σ'' values. We observe a significant decrease in thickness of the σ' top layer from 12 m to ~ 4 m at the location of the top-scarp. From the position of the top-scarp (~ 48 m), the vertical contact observed in the σ' image from low to intermediate (> 30 mS/m) σ' values is consistent to the vertical contact interpreted from DPH (Stumvoll et al., 2020), interpreted as the location of the sliding plane, as depicted in Figure 4.7. Moreover, the σ' contact observed at larger depth (> 12 m below ground surface), associated to a transition to the highest σ' values (> 70 mS/m), is in agreement with highest blow counts (> 79 blows) in the DPH and likely suggest the contact to bedrock consisting of sedimentary rocks (mottled marls or Flysch materials, e.g., sandstone). Furthermore, only a poor correlation of variations in σ' with the groundwater levels can be observed, which indicates that surface conduction mechanisms (due to overall high clay content) dominate over ionic conduction (through water-filled pores).

Imaging results for the polarization effect (σ'') reveal higher spatial variability than those for σ', in particular for the unit below the sliding plane (as interpreted from the σ' image). In the stable material, lateral variations in σ'' values range between 150 and 550 μS/m suggesting differences in soil properties. In particular, in Figure 4.7, we observe an anomaly in the highly polarizable layer (> 500 μS/m) at ~ 12 m depth, between 45 and 65 m along the profile, which roughly corresponds with the position of the top and central-scarp. We interpret this discontinuity as a transition from marlstone or sandstones ($\sigma' < 60$ mS/m, $\sigma'' > 400$ μS/m) to fractured marlstone ($\sigma' > 60$ mS/m, $\sigma'' \sim 300$ μS/m). However, the lack of deep core-drillings impedes a quantitative interpretation of the electrical properties at depth. Subsurface materials between the sliding plane and the layer at depth can be interpreted as variably weathered marlstones or Flysch materials. Considering the high variability in σ' and σ'' values, areas associated to different stages of weathering can be outlined.

As discussed earlier, variations in σ'' values are associated with changes in clay content and not compaction, therefore variations in σ'' values do not necessarily need to trace the increase in blow counts observed in the DPH data. The assessment of clay-rich zones in landslides is of high relevance, as those may represent important variations in the subsurface hydraulic properties, with such clays commonly related to zones of low hydraulic permeability (e.g., Slater and Lesmes, 2002b). Thus, spatial characterization of clay-rich zones is critical for the delineation of interflow or groundwater flow paths and, thus, a better understanding of possible triggering mechanisms. Based on the interpretation of single-frequency and SIP signatures discussed above, imaging results presented in Figure 4.7 reveal a zone of low hydraulic conductivity, characterized by low σ'' (< 200 μS/m) and intermediate σ' (~ 40 mS/m) values, between 45 and 55 m along profile direction. Consistently, this particular area corresponds with the location of the topscarp and the start of the shallow sliding plane, defined by geomorphological surveying and geotechnical data. Hence, it is possible to suggest that such area may act as a hydraulic barrier retaining groundwater and promoting the built-up of positive pore-water pressure, thus, facilitating the mobilization of the materials due to the reduction of shear strength. In a similar way, the shallow σ'' anomaly observed between 75 and 85m (along profile direction) may also indicate an area of low hydraulic conductivity, hindering the percolation of surface water; thus, resulting in the waterlogged zone defined during the geomorphological mapping. Hence, variability in σ'' solved in the imaging results seems to be well correlated with changes in the hydraulic properties of the subsurface, as evidenced by the geomorphological features of the landslide.

Furthermore, Figure 4.8 presents the imaging results for three WE profiles which are representative for the northern (gr3), the central (gr5) and the southern (gr9) regions of the landslide. Consistently to gr5, IP imaging results reveal the existence of two main units: a top layer characterized by low σ' (< 30 mS/m) and σ'' (< 150 μS/m) values, on top of a more conductive unit (> 45 mS/m) associated to high spatial variability in σ'' . The observed decrease in the σ' top layer at the location of the top-scarp for gr5 is consistently resolved for all profiles and again indicates the transition to the active landslide body. Consistently, the deep σ'' anomaly, located between the top and central-scarp, can also be observed in plots for gr3 and gr6, and to certain extent also gr9. Such anomaly, as discussed before, is most probably related to different stages of weathering and therefore zones of contrasting hydraulic properties; thus, of high relevance for the understanding of water flow within the landslide.

4.4.5 Interpretation of the landslide

Maps of the σ_a obtained from EMI mapping reveal clear units consistent with geomorphological characteristics of the landslide, namely, the top and central-scarp, as well as with the accumulation zone and the waterlogged areas. However, due to the nature of the EMI measurements representing a non-linear average over a specific depth range, no information on the depths of the delineated structures can be provided. Yet, the discussion of the IP imaging results presented earlier has demonstrated that the changes in the electrical properties are well correlated with the different ground-truth data (e.g., grain size analysis, DPH). Therefore, we present in Figure 4.9 interpolated maps of the σ' and σ'' for different depths (1–1.5 m, 2.5–3m, 5–5.5 m, 8.5–9 m, 10.5–11 m) as obtained from the inversion of the entire data sets (gr1 to gr16) at 1 Hz, superimposing the geomorphological information (landslide scarps and accumulation zone). High σ' and σ'' ($>$ 60 mS/m, $>$ 500 μS/m) values observed at the northern part of the landslide are the effect of anthropogenic structures (e.g., power line cables) and will not be further discussed here.

Plots presented in Figure 4.9a reveal that for shallow depths the highest σ' values are located mainly at the foot of the landslide (i.e., to the east of the accumulation zone). With depth, an increase in σ' (from $\sim$ 20 to 70 mS/m) values can be observed for the eastern region of the landslide, which is accompanied by a transition of the conductive anomaly towards the center of the study site (Figure 4.9b-4.9i). Images of the polarization effect (Figure 4.9b-4.9j) show similitudes to those obtained for σ', yet maps of the polarization effect are characterized by a higher spatial variability (e.g., Figure 4.9j). The top-scarp (located at the topographical highest area of the landslide) shows a stronger correlation with the contacts in the electrical properties for deep maps (Figure 4.9g-4.9j). In the case of the central-scarp, its geomorphological features appear to be better resolved for σ' maps constructed at intermediate depths (Figure 4.9c-4.9f) and for σ'' maps for intermediate and large depths (Figure 4.9f, 4.9h, 4.9j), demonstrating that σ'' patterns do not necessarily mirror the patterns observed for σ'.

Maps of the electrical properties further reveal that areas located above the top-scarp are characterized by the lowest σ' and σ'' (< 10 mS/m, < 100 μS/m) values, and therefore can be associated to clay-rich zones. Such low permeable zones reduce the infiltration of surface water and foster surface run-off towards the active transportation zone (below the top-scarp). The excess of surface water in the respective area will lead to more water in the lower reaches, where it can infiltrate in the soil and further increase the soil moisture of the already weakened sliding material. The increase in soil moisture is a well-known triggering mechanism for shallow landslides and has been often investigated (e.g., Van Asch et al., 1999). Furthermore, the topographical bulge at the accumulation zone leads to the development of a surface pan, additionally accumulating the surface water and enhancing its infiltration into the ground. In a similar way, interflow and groundwater flowing down-gradient from the hilltop will reach a poorly permeable subsurface zone between the top and central scarp characterized by low σ'' (< 100 μS/m) values as discussed in a previous section (e.g. Figure 4.9b, 4.9d, 4.9f). In this respective area, groundwater and soil water retention will occur, which in turn can promote a built-up of positive pore-water pressure and the reduction in shear-strength. Hence, possible remediation actions might include the removal of the flat surface pan and the installation of a drainage system.

Plots presented in Figure 4.9 also demonstrate that there seems to be no significant change in the conductivity and polarization patterns explaining the accumulation zone. This might be a result of the spatial dimension of such zone, with a west-east extension in the order of magnitude of the electrode spacing (2 m). Hence, the accumulation zone might not be resolved with the conducted IP surveys; yet it is properly delineated through the EMI mapping. When comparing the $\sigma_{6.7}$ maps (c.f. Figure 4.4c) with the shallow interpolated σ' maps (Figure 4.9a, 4.9c), we observe a close similarity in the patterns of σ_a and σ'. Moreover, such depth between 1 and 3 m represents the expected location of the sliding plane as obtained from geotechnical investigations (Stumvoll et al., 2020). Thus, the changes observed in the conductivity patterns in Figure 4.9a and c, i.e. an increase in σ' (from 25 to 50 mS/m) values particularly for the area below the central scarp, validates the interpretation made earlier for the EMI maps regarding the contact to the sliding plane.

Figure 4.10 shows the conceptual model of the landslide as derived from a joint interpretation of geophysical, hydrogeological, geomorphological and geotechnical data. The plot presents the different interpreted soil types and hydrogeological units and their geophysical indicators (σ', σ''), the location of the sliding plane, as well as the corresponding groundwater flow paths. In particular, four types of run-off were interpreted: 1) groundwater flow through strongly weathered sedimentary materials above the top-scarp (black arrows in Figure 4.10), 2) seepage and retarded groundwater flow through variably weathered marlstone as delineated by spatial variations in σ' and σ'' below the sliding plane (red arrows in Figure 4.10), 3) interflow within the mobilized material and along the sliding plane, and 4) surface run-off due to high clay content. Figure 4.10 clearly demonstrates the benefit of using multiple geophysical, hydrogeological, geomorphological and geotechnical methods for landslide characterization.

4.5 Conclusion

In this study, we have presented the joint application of the EMI and IP methods, and the corresponding interpretation of the mapping data for the characterization of a shallow, clay-rich landslide. Extensive geotechnical, geomorphological and hydrogeological data available at the study area allowed to evaluate the geophysical response and formulate a conclusive interpretation of the imaging results. Based on the EMI maps lateral changes in the electrical conductivity could be identified. The main patterns correlate well with geomorphological features, namely, with the main scarps, the accumulation zone and waterlogged areas, as well as preferential areas for the infiltration of surface water. The latter represents relevant information for the potential design of drainage systems. Moreover, IP imaging results were used to delineate the geometry of the sliding plane and the different soil types and hydrogeological units, which, in combination with the available information from a piezometric network, dynamic probing and grain size analyses in recovered drilling cores, permitted to delineate groundwater flow patterns. Additionally, information about the subsurface capacitive properties provided by the images of the polarization effect allowed to discriminate between materials of different textural composition. Furthermore, our SIP imaging results clearly revealed changes in the frequency dependence of the polarization effect associated to changes in the grain size. Such findings again correlate with geotechnical and soil textural data. The validation of our results using extensive ground-truth data clearly shows the suitability of combined EMI mapping and IP imaging methods for a better characterization and understanding of clay-rich landslides.

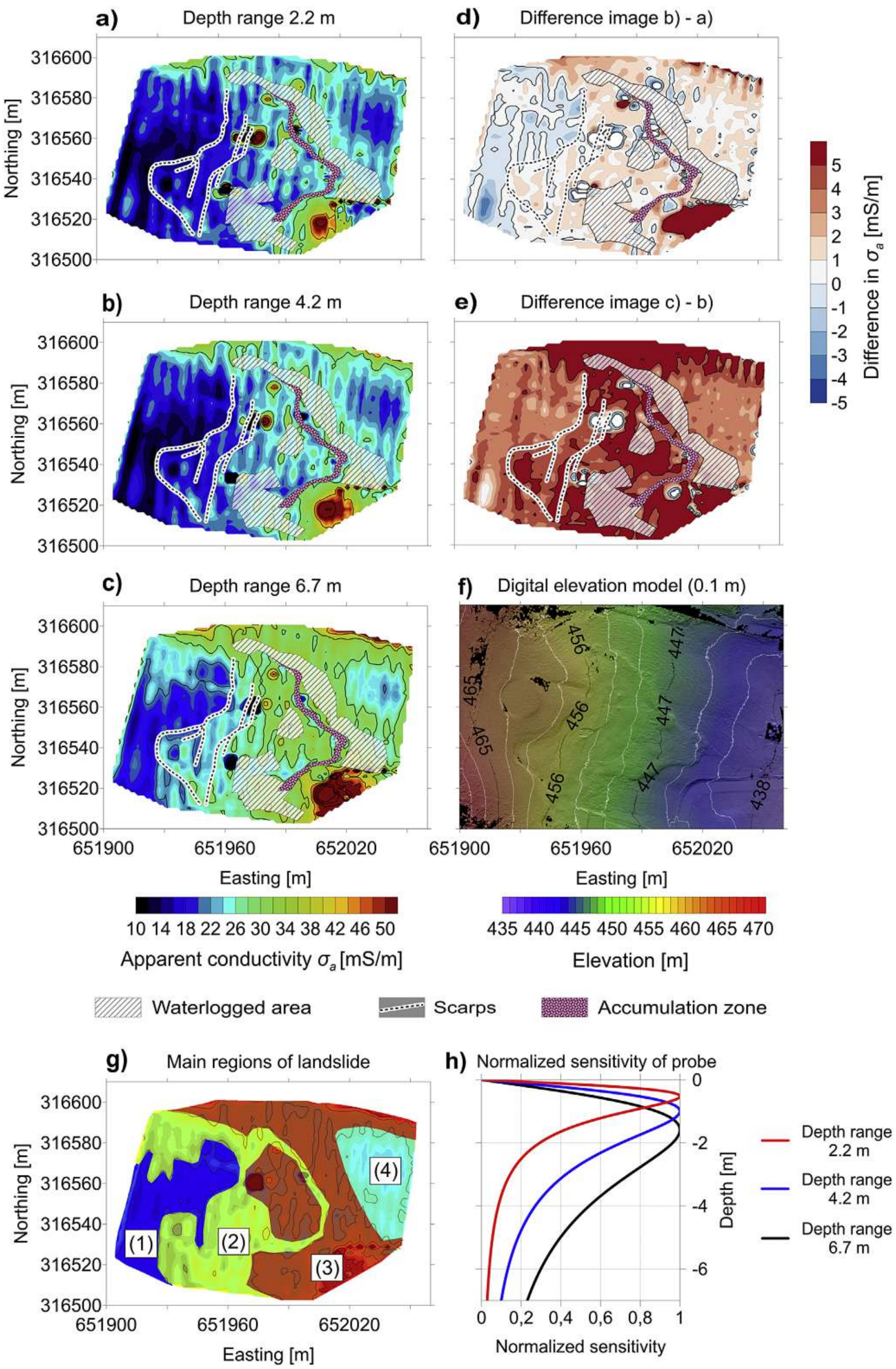

Figure 4.4: EMI maps of the apparent electrical conductivity corresponding to the depth ranges of 2.2, 4.2, 6.7 m (Figure 4.4a, 4.4b, 4.4c respectively), with the geomorphological features superimposed over the σ_a maps. Difference images for the σ_a maps for the depth ranges 2.2 and 4.2 m (4.4d) and 4.2 and 6.7 m (4.4e) are also presented to evaluate changes at different depth. The DEM (4.4f) of the landslide and the main regions interpreted from σ_a maps (4.4g) are presented for comparison. Plots of the normalized sensitivity function for the three depth ranges (4.4h).

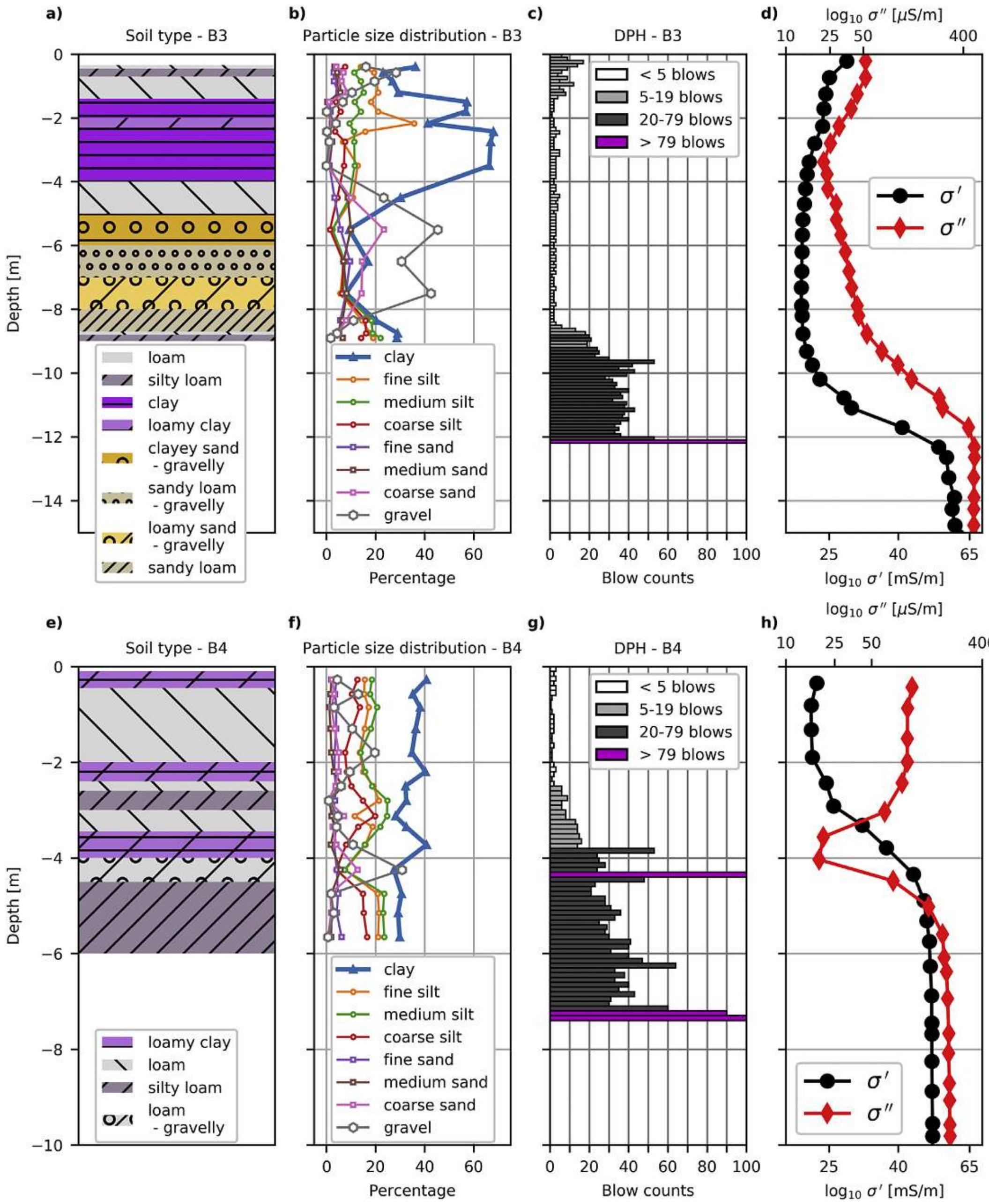

Figure 4.5: Comparison of ground-truth and geophysical data: soil type (4.5a, 4.5e) and particle size distribution (4.5b, 4.5f) as obtained from the analysis of core drilling in B3 (4.5a, 4.5b) and B4 (4.5e, 4.5f); blow counts obtained from dynamic probing heavy (DPH) in the vicinity of B3 and B4 given in 10 cm increments (4.5c, 4.5g) and electrical parameters (σ' and σ'') representing the median value from model parameters extracted from inverted profiles next to the wells (4.5d, 4.5h).

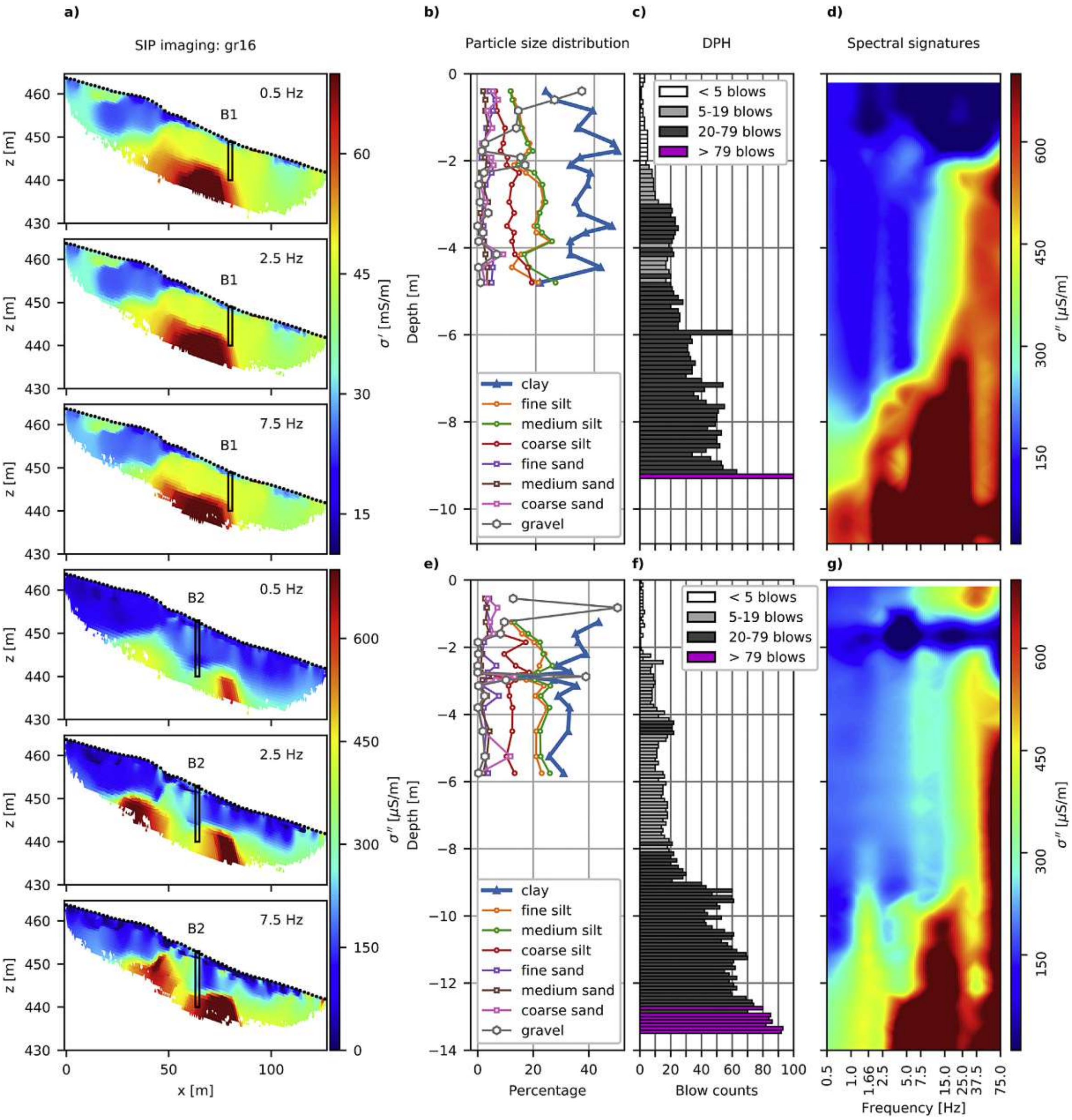

Figure 4.6: Comparison of ground-truth and geophysical data. SIP imaging results (σ', σ'') for the frequencies of 0.5, 2.5, and 7.5 Hz to investigate the frequency dependence of the polarization effect (4.6a). Particle size distribution as obtained from the analysis of core drilling at B1 (4.6b) and B2 (4.6e) and blow counts from dynamic probing heavy (DPH) in the vicinity of B1 (4.6c) and B2 (4.6f) given in 10 cm increments. Spectral amplitudes (σ'') as a function of depth and frequency as extracted from the imaging results of gr16 (4.6d, 4.6g).

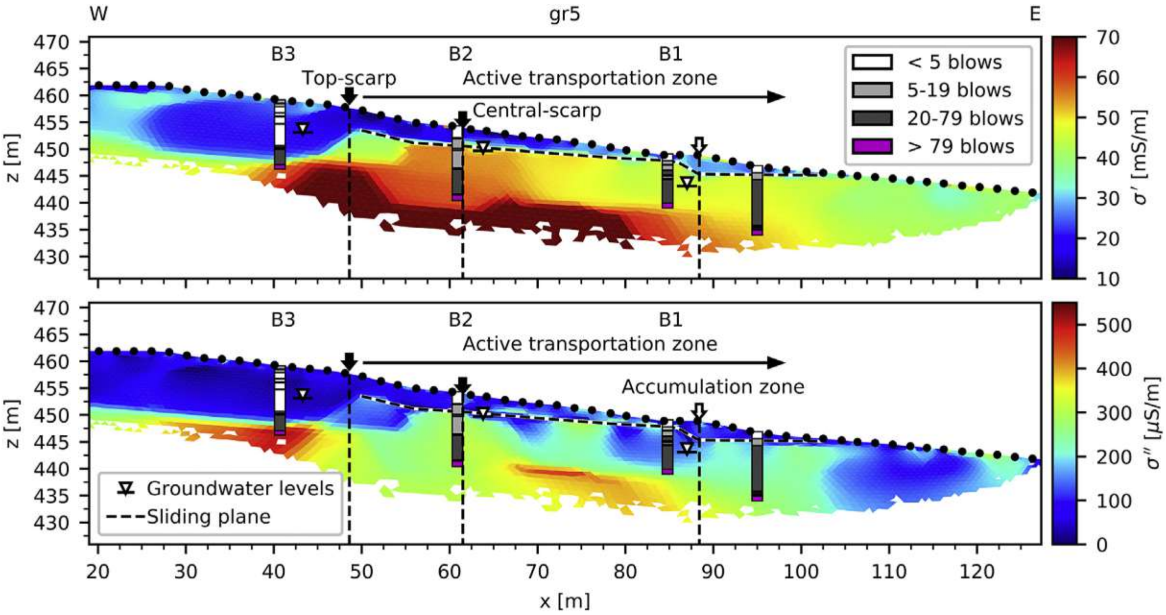

Figure 4.7: Imaging results expressed in terms of the real (top) and imaginary (bottom) components of the complex electrical conductivity. The blow counts measured by DPH, the groundwater levels, as well as geomorphological features, namely the landslide scarps, the accumulation zone and active transportation zone are superimposed over the electrical images.

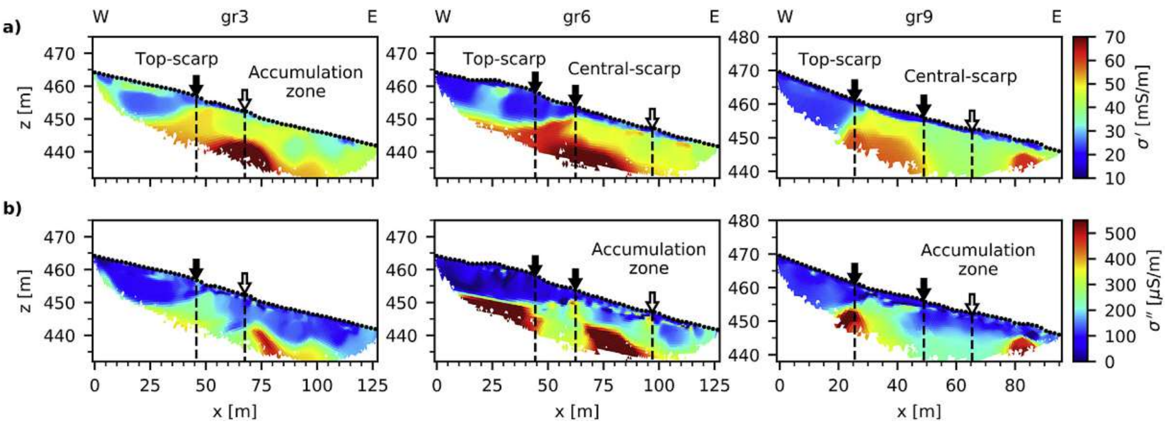

Figure 4.8: Imaging results for three WE profiles in terms of the real (4.8a) and imaginary (4.8b) components of the complex electrical conductivity. The geomorphological features (top-scarp, central-scarp and accumulation zone) are indicated by surface arrows.

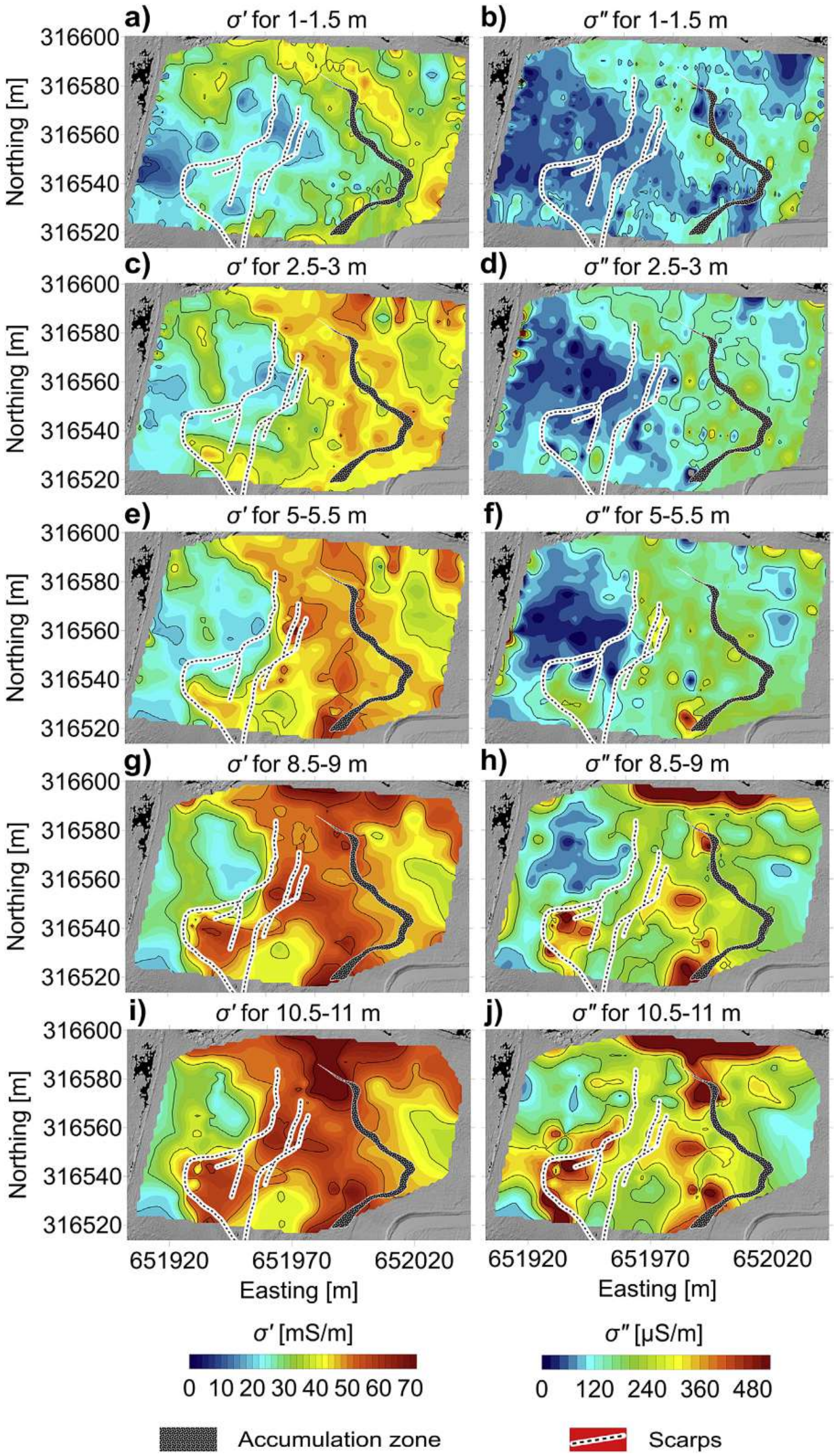

Figure 4.9: Maps constructed for different depths based on the IP imaging results in terms of the real (σ' – 4.9a, 4.9c, 4.9e, 4.9g, 4.9i) and imaginary (σ'' – 4.9b, 4.9d, 4.9f, 4.9h, 4.9j) components of the complex electrical conductivity.

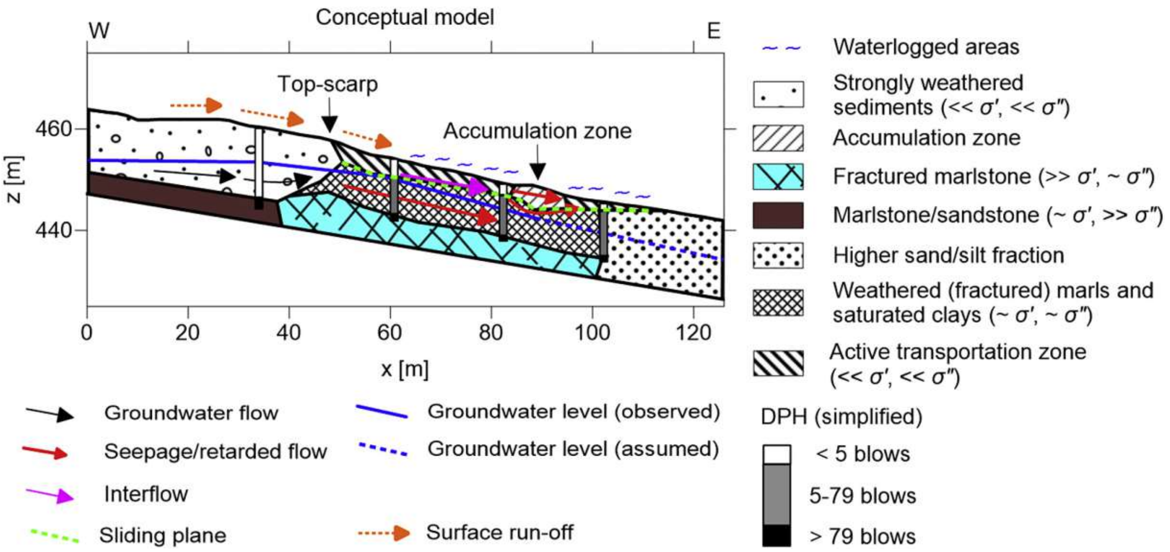

Figure 4.10: Conceptual model of the landslide indicating the different soil types and hydrogeological units as derived from the joint interpretation of geophysical, hydrogeological, geomorphological and geotechnical data.

5 | Quantification of soil textural and hydraulic properties in a complex conductivity imaging framework: Results from the Wolfsegg slope[1]

5.1 Introduction

Current forecasts assume that the trend towards rising temperatures and precipitation extremes (Dunn et al., 2020) will continue and that the occurrence of droughts (e.g., Cook et al., 2018; Balting et al., 2021) and heavy rainfall (Ban et al., 2015; Papalexiou and Montanari, 2019) will increase in the next years. Such meteorological changes affect ecosystems (e.g., Weiskopf et al., 2020), land use (Searchinger et al., 2018), water availability (Konapala et al., 2020), but also natural disasters such as floods (Tabari, 2020) and mass movements (Alvioli et al., 2018; Lin et al., 2020). In this context, a comprehensive understanding of the hillslope hydrology is of fundamental importance, to predict runoff responses (Blume and Van Meerveld, 2015), but also in the understanding of the hydraulic properties of the subsurface triggering landslide processes (Bogaard and Greco, 2016). The complex sedimentary structures in hillslopes, as a result of geological disposition and local geomorphodynamics, make prediction of hydrological processes immensely difficult (Sidle et al., 2019). Small-scale variations in sediment characteristics and the associated hydraulic properties affect infiltration, percolation, but also evaporation (Lehmann et al., 2018) as well as water storage (Berg et al., 2017) and affects hydrologic connectivity via surface runoff and subsurface flow. As a consequence, slope architecture may be related to areas of waterlogging, small-scale slumping or subsidence as well as major mass movements. Moreover, Blume and Van Meerveld (2015) conclude, that the subsurface hillslope-stream connectivity is difficult to observe and quantify, and, due to the high variability in hillslope responses, results are hard to extrapolate to other hillslopes. Blume and Van Meerveld (2015) also point out, that multimethod approaches might be useful, as they strengthen the interpretation of individual measurements.

While the description of hillslope properties is often based on point data from core

[1] This chapter is based on: Gallistl, J., D. Schwindt, J. Birgit, L. Aigner, M. Peresson, and A. Flores Orozco (2022). "Quantification of soil textural and hydraulic properties in a complex conductivity imaging framework: Results from the Wolfsegg slope". In: *Frontiers in Earth Science* 10

soundings, a spatial approach is needed to deal with the complexity of the slope sediments and the associated hydrology. In recent years, geophysical methods have been increasingly used to spatially characterize the shallow subsurface (Flores Orozco et al., 2018a; Gallistl et al., 2018; Watlet et al., 2018; Huntley et al., 2019; Holmes et al., 2020). Furthermore, approaches to use geophysical imaging as landslide early warning systems, by monitoring short- and longterm moisture dynamics are developed (Whiteley et al., 2021).

Geophysical methods commonly applied in hillslope characterization include the Electrical Resistivity Tomography (ERT) (Perrone et al., 2014), Refraction Seismic Tomography (RST) (Samyn et al., 2012; Uhlemann et al., 2016), and, to a lesser extent Electromagnetic Induction at low induction number (EMI) (Grandjean et al., 2011; Kušnirák et al., 2016), Transient Electromagnetic Sounding (TEM) (Godio and Bottino, 2001; Li et al., 2020b) and Induced Polarization Imaging (IP) (Flores Orozco et al., 2018b; Gallistl et al., 2018; Revil et al., 2020).

IP, also referred to as Complex Conductivity Imaging (CCI), is an extension of the ERT method and provides information about the electrical conductivity and capacitive (polarization) properties of the subsurface (Kemna et al., 2012). The IP method was developed for the prospection of metallic mineral ores given the strong IP response in the presence of iron sulphides (Pelton et al., 1978). In recent years, IP has emerged as a promising method for various environmental and hydrogeological applications including the mapping of geochemical active zones (Flores Orozco et al., 2020; Katona et al., 2021), the monitoring of changes in pore-space geometry accompanying bioremediation processes (Flores Orozco et al., 2011; Flores Orozco et al., 2019b) and the assessment of permafrost degradation (Doetsch et al., 2015; Maierhofer et al., 2022), just to name a few. In the context of characterizing hillslopes affected by landslides, IP has revealed promising results (Flores Orozco et al., 2018b; Gallistl et al., 2018; Revil et al., 2020), as numerous laboratory studies reported a sensitivity of the IP method to soil-textural properties of the subsurface (Slater and Glaser, 2003; Tarasov and Titov, 2007; Revil and Florsch, 2010) and, thus, the improved estimation of hydraulic conductivity (Slater et al., 2014; Weller et al., 2015; Weller and Slater, 2019). Since landslides are frequently triggered by heavy precipitation events, resolving changes in textural properties of hillslopes is of great interest as they will determine areas of low hydraulic conductivity (i.e., with a poor drainage) where pore-pressure may accumulate resulting in the triggering of mass movements (Campbell, 1975; Rogers and Selby, 1980). Thus, IP could permit to directly provide estimates of hydraulic conductivity without the need of direct in-situ testing not possible in landslides. Unfortunately, the upscaling and transferring of laboratory findings to field-scale measurements has proven difficult so far (Binley et al., 2015).

Over the last few decades, a multitude of pedotransfer functions (PTFs) have been developed that permit the prediction of soil-hydraulic properties based on commonly available soil information such as soil texture, bulk density and grain size without the need of labor intensive and timeconsuming direct measurements (Van Looy et al., 2017a; Zhang and Schaap, 2019). Such PTFs provide a viable alternative, if it is possible to define site-specific equations relating the IP effect to soil texture (i.e., the soil volume fractions of sand, silt, clay and gravel) for a quantitative interpretation of IP imaging results in a hydrogeological context. The predictors in PTFs range from relatively simple power model relations (Cosby et al., 1984) to more complex artificial neural networks (Schaap et al., 2001), support vector machines algorithms (Twarakavi et al., 2009), k-nearest neighbor methods (Nemes et al., 2006) and decision/regression trees (Jorda et al., 2015). Rosetta (Schaap et al., 2001), is one of many PTFs that is based on an artificial neural network and uses a hierarchical approach to predict saturated hydraulic conductivity K_s and van Genuchten (VG) water retention parameters (van Genuchten, 1980). The model input parameters may be given in terms of textural classes, the soil volume fractions of sand, silt and clay (SSC), or as a combination of SSC, bulk density and a referential grain size. As discussed in Zhang and Schaap (2017) the initial version of Rosetta had several deficiencies, which lead to a weighted re-calibration of Rosetta in order to improve the predicted soil-hydraulic properties and reduce uncertainties in their prediction.

The objective of this work is to investigate the spatial prediction of soil-hydraulic properties at the slope scale, based on derivation of soil texture from complex conductivity information and subsequent use of a pedotransfer function (Rosetta). To the best of our knowledge such approach has not been tested for the interpretation of IP imaging data at the field scale. To reduce the uncertainty in IP inversion results, we also present the incorporation of a priori information about electrical units obtained from TEM data; additionally, we include refraction seismic tomography as well as soil textural information in boreholes. Using this information, we derive relationships between the complex conductivity and the different soil volume fractions and characterize the main geological units of the study area. To permit a thorough evaluation of our results in a later step, we exclude the information from one borehole. With the obtained prediction functions, we first predict and discuss the soil fractions for a given CCI profile and then use Rosetta to predict K_s. This is followed by a discussion of the implications on water-flow within the slope. We evaluate the performance of our approach based on independent borehole data and discuss our results compared to those obtained by upscaling of laboratory-derived relationships between the IP response and directly measured K_s values.

5.2 Site description

The study area is located in the municipality of Wolfsegg am Hausruck in Upper Austria, Austria (48°6′34.3″N, 13°40′9.6″) and comprises an agriculturally used west-east tilted hillside with average slopes of 5–10° and descents with maximum slopes of up to 35°. The area under investigation is limited by a street and settlements to the eastern, and a small stream to the western boundary. The total mean annual precipitation (for the last 23 years) is about 910 mm and the largest precipitation events typically occur between May and August.

The geological frame is given by the Molasse zone that embodies a large Foreland basin from Switzerland in the west across Germany and Austria into the Carpathian Foredeep in the east. The basin fill comprises a section of mainly clastic sediments from the Late Eocene to Late Miocene due to uplift and erosion of the Alpine Orogen (e.g., Rögl, 1997; Hinsch, 2008; Grunert et al., 2010). Stratigraphically, the study area encompasses three main units, which can be listed from top to bottom (Krenmayr and Schnabel, 2006; Rupp et al., 2011) as: the 1) Hausruck, 2) Ampflang, and 3) Ottnang formation, which are partly overlain by quarternary deposits consisting of gravels, sands and silts (see Figure 5.1). The predominant unit in the area is the Hausruck formation and comprises fluvial, sandy, and fine to coarse gravels. The Ottnang formation, which constitutes the basal layer of the study area, mostly consists of shallow marine clay silts and marls. Sporadic layers of the Ampflwang formation can be found intercalated within the Hausruck and Ottnang units (Figure 5.1). The Ampflwang formation consists of clay-bearing coal (from limnic and fluvial deposits) with different maturity, which has been exploited sporadically (Rupp et al., 2011). Weathering of the materials of the Hausruck formation resulted in the development of weathered loam, which, in combination with the confining characteristics of the clays in the Ampflwang formation, constitute an ideal setting for landslides (Supper et al., 2014).

Baumann et al. (2018) show that landslides are a primary controlling factor for landscape morphology in the Hausruck area. Thus, mass movements have also shaped the slope on which the study area is located. Both, the settlement area on the upper slope, as well as the agricultural areas on the mid- and footslope have been subjected to continuous subsidence over the last 25 years and have called for numerous geotechnical investigations and remediation measures (personal communication with leaseholder of slope). However, even though the slope of the study area was clearly formed by mass movements, anthropogenic overshaping by construction, tillage and drainage works has severely compromised a precise geomorphological site analysis. Based on the analysis of shaded digital terrain models (based on Airborn Laserscanning data at a resolution of 0.5 m, Datasource: Land Oberösterreich - data.ooe.gv.at) in combination with field-based mapping, four morphological zones (c.f. Figure 5.1B,C) can be identified and adopted to the landslide classification according to Cruden (1996).

Regarding the four morphological zones, the zone I corresponds to the main scarp, with a height of 30 m and the crown at an elevation of 672 m. A slight flattening at the base of the scarp suggests deposits from rockfall or minor secondary landslide processes. Zone II corresponds to the main landslide body, which extends for about 250 m horizontal distance and an elevation ranging from 600 to 642 m. Due to construction, zone II exhibits the most severe reshaping. Hence, a too detailed description of its morphology does not seem useful. Nevertheless, two landslide blocks, can be differentiated in this area. A slight dip of the upper block in the direction of the incipient crack indicates a rotational slide (c.f. Figure 5.1). Zone III, which is adjacent below, corresponds to the foot of the landslide. Despite the severe anthropogenic overshaping, tongue-like structures suggests that this area was formed by a mudflow during the landslide process. Zone IV, which adjoins below zone III, is characterized by undulating relief and is interpreted as landslide foreland. The relief formation in this zone is due to deformation of the slope sediments by the surcharge of the landslide masses deposited upslope. Small steps at cropland boundaries indicate prolonged tillage. In the boundary between the landslide toe and zone IV, a morphological hollow form is found that has been interpreted as a former source or waterlogged area (c.f. Figures 5.1B,C). This area has been drained in the last years (c.f. Figure 5.2D). Below the formerly waterlogged area, erosional structures are found in the shaded terrain model that indicate intermittent surface runoff. At 574 m above sea level (a.s.l.), the toeslope is bordered by a small creek in the West of the study site.

In Figure 5.1C, we present our geomorphologic analysis of the site using the description of rotational slides proposed by Cruden (1996). We assume that the sliding process was initiated on the clay silts of the Ottnag formation. Accordingly, the rotated blocks of the main landslide body in zone II consist of the morphologically hard material of the Hausruck formation (rounded gravels in sandy matrix). The partially tongue-shaped mudflow deposits of zone III are predominantly built up by the materials of the Ampflwang formation (coal-bearing clays and sands). Our conceptual model assumes that a partial mixing of sediments of the Ampflwang formation with materials of the Hausruck formation and slope sediments occurred during the flow process. The shallow subsurface of zone IV, the foreland of the landslide, is built up by old slope sediments. These are most likely composed of a mixture of weathering products of the Ottnang formation intermixed with deposits of the Ampflwang and Hausruck formations. According to our subsurface model, the mudflow on the midslope has overlain old slope sediments, some of which have been incorporated into the mudflow. The uplift pressure of the landslide deposits has caused deformation of the plastic-reacting slope sediments, resulting in the undulating relief at the footslope in zone IV.

5.3 Material and methods

5.3.1 Complex conductivity imaging

The induced polarization (IP)–also known as complex conductivity (CC) or complex resistivity (CR) imaging, is an electrical method that permits to recover information on the subsurface distribution of the resistive (or conductive) and capacitive (or polarization) electrical properties of the subsurface (Ward, 1988; Binley and Kemna, 2005). IP measurements, which can be performed in both time and frequency domain (e.g., Martin et al., 2020), use four electrode configurations–two of them are used for current injection and the other two to record the corresponding voltage. For measurements performed in the frequency domain, a sinusoidal current waveform is used and data collection comprises the measurement of the voltage-to-current ratio and the time delay of the voltage, and therefore, the measurement of a complex-valued electrical impedance (Binley and Kemna, 2005). The collection of such data with different frequencies (10 mHz to 1 kHz), in the so-called spectral IP (SIP), can provide additional information regarding the frequency dependence of electrical properties. IP imaging data sets typically deploy up to hundreds of electrodes for the collection of thousands of four electrode measurements are used in conjunction with inversion algorithms to recover spatially quasi-continuous subsurface models of the electrical properties (Oldenburg and Li, 1994; Kemna et al., 2000; Binley and Kemna, 2005; Loke et al., 2006).

Inversion results can be given in terms of the complex electrical conductivity $\sigma^*(\omega)$ (where $\omega = 2\pi f$ and f is the excitation frequency), or its inverse, the complex electrical resistivity ρ^* (with $\rho^* = 1/\sigma^*$). The complex conductivity can be expressed by means of its real $\sigma'(\omega)$, and imaginary $\sigma''(\omega)$ components, or by its magnitude $\sigma^*(\omega)$ and phase-shift ($\varphi(\omega)$), such as:

$$\sigma^*(\omega) = |\sigma^*(\omega)|e^{i\varphi} = \sigma'(\omega) + i\sigma''(\omega) \tag{5.1}$$

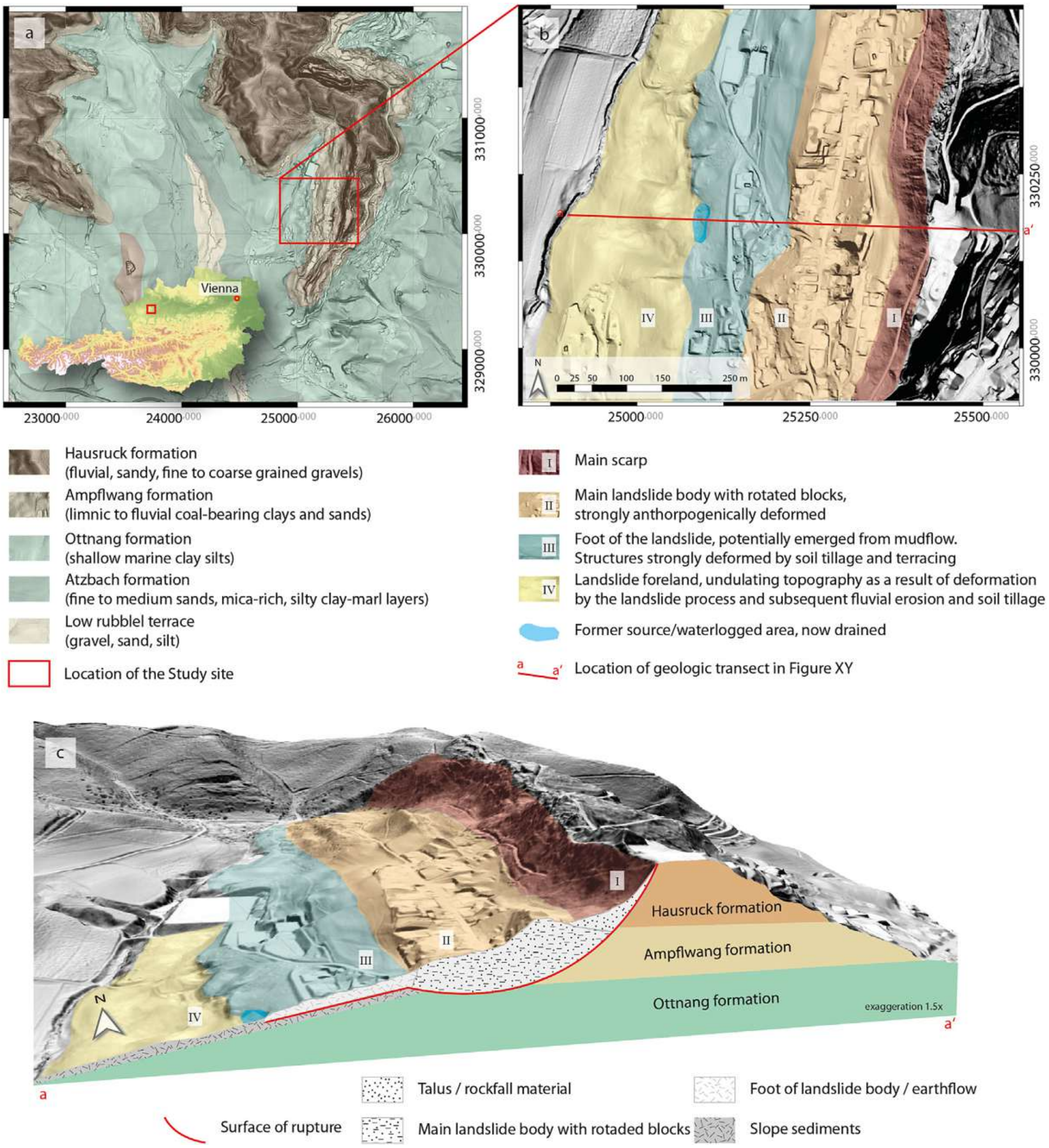

Figure 5.1: Details on the study site Wolfsegg with (a) geological overview of the south-eastern parts of the Hausruck mountain range in Austria (Krenmayr and Schnabel, 2006), (b) shaded digital terrain model with interpreted morphological zones (I-IV) and (c) 3D-scene of the study site with interpreted morphological zones, geology as well as a subsurface model of the slope and landslide body. The reconstruction of the subsurface characteristics is based on the geomorphology of the study site and adopts to the classification of rotational slides by Cruden (1996). Elevation data for Figures a–c are based on airborne laserscanning data, resolution 0.5 m, April 2015 (Datasource: Land Oberösterreich—data.ooe.gv.at)

with $i = \sqrt{-1}$, and further:

$$\varphi = \arctan \frac{\sigma''(\omega)}{\sigma'(\omega)}. \tag{5.2}$$

The real (or in-phase) component of the complex conductivity represents the conduction (energy loss) properties, while the imaginary (or quadrature) component represents the polarization/capacitive properties (energy storage) of the subsurface. For a detailed review of the IP method we refer to (Ward, 1988; Binley and Kemna, 2005; Binley and Slater, 2020).

The low-frequency (< 100 kHz) complex conductivity $\sigma^*(\omega)$ of soils and rocks can be written as a function of a real-valued bulk conductivity, and a complex-valued surface conductivity, such as:

$$\sigma^*(\omega) = \sigma_{bulk} + \sigma'_S(\omega) + i\sigma''_S(\omega). \tag{5.3}$$

Equation 5.3 shows that $\sigma^*(\omega)$ consists of a real component that contains contributions from the bulk conductivity σ_{bulk} and a frequency dependent surface conductivity $\sigma'_S(\omega)$, while the imaginary component of $\sigma^*(\omega)$ is only defined by the frequency dependent imaginary surface conductivity $\sigma''_S(\omega)$. The bulk conductivity for an unsaturated sample is given by Mualem and Friedman (1991)

$$\sigma_{bulk} = \sigma_f + \Phi^m S^n \tag{5.4}$$

in which Φ is the porosity, S the saturation of the pores, σ_f is the conductivity of the fluid and m, n are empirical coefficients that represent the connectivity between the pores (m) and the saturation degree (n). In case of soils and rocks with clay, organic matter and other minerals with high surface charge and surface area the influences of σ_{bulk} and $\sigma^*_S(\omega)$ and particularly the frequency dependence of the latter cannot be neglected. Therefore, the estimation of quantitative petrophysical relationships might be hindered when the surface conductivity is ignored, resulting in poor estimations of hydrogeological parameters, such as hydraulic conductivity or water content. Surface conductivity plays a critical role in presence of grains with a high surface area, and high surface charge (e.g., Waxman and Smits, 1968; Revil et al., 2017). Accordingly, clay minerals are linked to dominating surface conduction mechanisms, and commonly exhibit a high cation exchange capacity (CEC) and electrical conductivity (Revil et al., 2017). Furthermore, Revil et al. (2014) have shown that even for sandstones without clay content the surface conduction might dominate over electrolytic conduction (σ_f).

Hence, the knowledge of the contribution of the surface conductivity to the complex conductivity is critical for an adequate interpretation. The imaginary surface conductivity $\sigma''_S(\omega)$ is only related to the imaginary component of the complex conductivity $\sigma''(\omega)$ obtained with IP, such as

$$\sigma''_S(\omega) = \sigma''(\omega). \tag{5.5}$$

The IP response of soil arises due to polarization processes taking place at the grain-fluid interface, in the so-called electrical double layer (EDL). The polarization of the EDL is caused by the transport and accumulation of electrical charge carriers when subject to an external electrical field during the current injection (Kemna et al., 2012). Electrochemical polarization occurring at the EDL, which includes polarization of the Stern layer (Leroy and Revil, 2009; Revil, 2012) and the diffuse layer (Revil et al., 2017; Bücker et al., 2019a) depends on the electrochemical properties at the grain-fluid interface, i.e., the surface charge of the grain, the specific surface area and salinity of the surrounding electrolyte, as well as the pore-space geometry. For the case of metallic grains, charge carriers inside of the particle also polarize, which further enhances the IP response in the so-called electrode polarization (Revil et al., 2015b; Bücker et al., 2018; Bücker et al., 2019b).

5.3.2 Data collection and processing

To map the complex conductivity response throughout the study area, single frequency (1 Hz) IP imaging data were collected between 12th and 21st June in 2017, along 24 profiles with an orientation west-east deploying in each 64 electrodes with a 2.5 m spacing between the electrodes. 1 Hz as the excitation frequency was chosen as it offered the best compromise between data quality and acquisition time, as higher frequency measurements with reduced acquisition times are highly likely to be distorted by sources of electromagnetic noise (Flores Orozco et al., 2021). We used a DAS-1 instrument (from MultiPhase Technologies, United States) for the collection of the data, always ensuring contact resistances below 5 kΩ resulting in injected currents ranging between 50 and 200 mA. The data were collected using two different electrode configurations: 1) dipole-dipole (DD) combining different skip protocols, where the skip refers to the numbers of electrodes “skipped” in each dipole in order to increase the dipole length (e.g., Flores Orozco et al., 2018b) and 2) multiple-gradient (MG) after Dahlin and Zhou (2006). The characteristics of both configurations can be found in Table 5.1. Both configurations were designed for an approximate depth of investigation of 30 m and in such a way, that the data cannot be affected by the polarization of the electrodes themselves, i.e., no voltage measurements were performed with electrodes previously used for current injection (Flores Orozco et al., 2018b). To provide a dense distribution of profiles in the area of interest (see Figure 5.2A), the profile separation was set to 5 m (i.e., twice the electrode spacing). All electrode positions were determined with an RTK-GNSS.

Processing of the data (i.e., outlier removal) is based on the methodology outlined by Gallistl et al. (2018), that originates from the time-domain IP processing scheme proposed by Flores Orozco et al. (2018a). The fundamental idea is that pseudosections (i.e., a representation of the measured raw data), due to the nature of IP imaging data sets, should reveal spatial consistent patterns, i.e., "smooth" changes in the measured phase-shift φ without the occurrence of large discrepancies or abrupt changes. Those measurements with poor spatial consistency can be considered outliers and should be removed prior to inversion. The processing scheme presented in Gallistl et al. (2018) quantifies this spatial consistency in the phase-shift data by grouping measurements collected with the same current dipole, a subsequent computation of a median phase value for measurements in the corresponding group and the computation of a deviation value $\Delta\varphi$ for each measurement in the group to the median value. Spatial consistent measurements are then defined as those with a small deviation, whereas measurements related to large deviations are considered outliers and are removed.

Inversions of the imaging data sets were performed with CRTomo (Kemna, 2000), using a robust inversion scheme. Such an approach permits to improve the convergence of the inversion and it is less sensitive to wrong estimates of the data error (LaBrecque and Ward, 1990; Morelli and LaBrecque, 1996; Kemna, 2000). All inversions converged to a root-means-square error close to 1 and a slightly preferential smoothing in horizontal to vertical direction (10:1) was used. We selected this smoothing factor based on the assumption that deformation of the old slope materials in Zone IV (c.f. Figure 5.1) will follow the uplift pressure of the landslide deposits, resulting in an undulating relief and likely only minor deviations from a horizontal layering. For materials associated to the mudflow in Zone III, intermixing of materials of the Ampflwang, Hausruck and old slope sediments is likely to have occurred. However, we do not believe that the individual layers will deviate much from a horizontal position and a slight smoothing in horizontal direction is justified.

Table 5.1: Characteristics of the used electrode configurations, namely, dipole-dipole combining different dipole lengths and multiple-gradient. For the latter, the dipole lengths refer to the size of potential dipoles nested inside the current dipole.

Protocol	Number of quadrupoles	Dipole lengths [m]
Dipole-dipole	2095	2.5, 5, 7.5, 10, 12.5, 15, 17.5, 20, 22.5, 25
Multiple-gradient	1791	2.5, 5, 7.5, 10, 12.5, 22.5, 27.5, 32.5

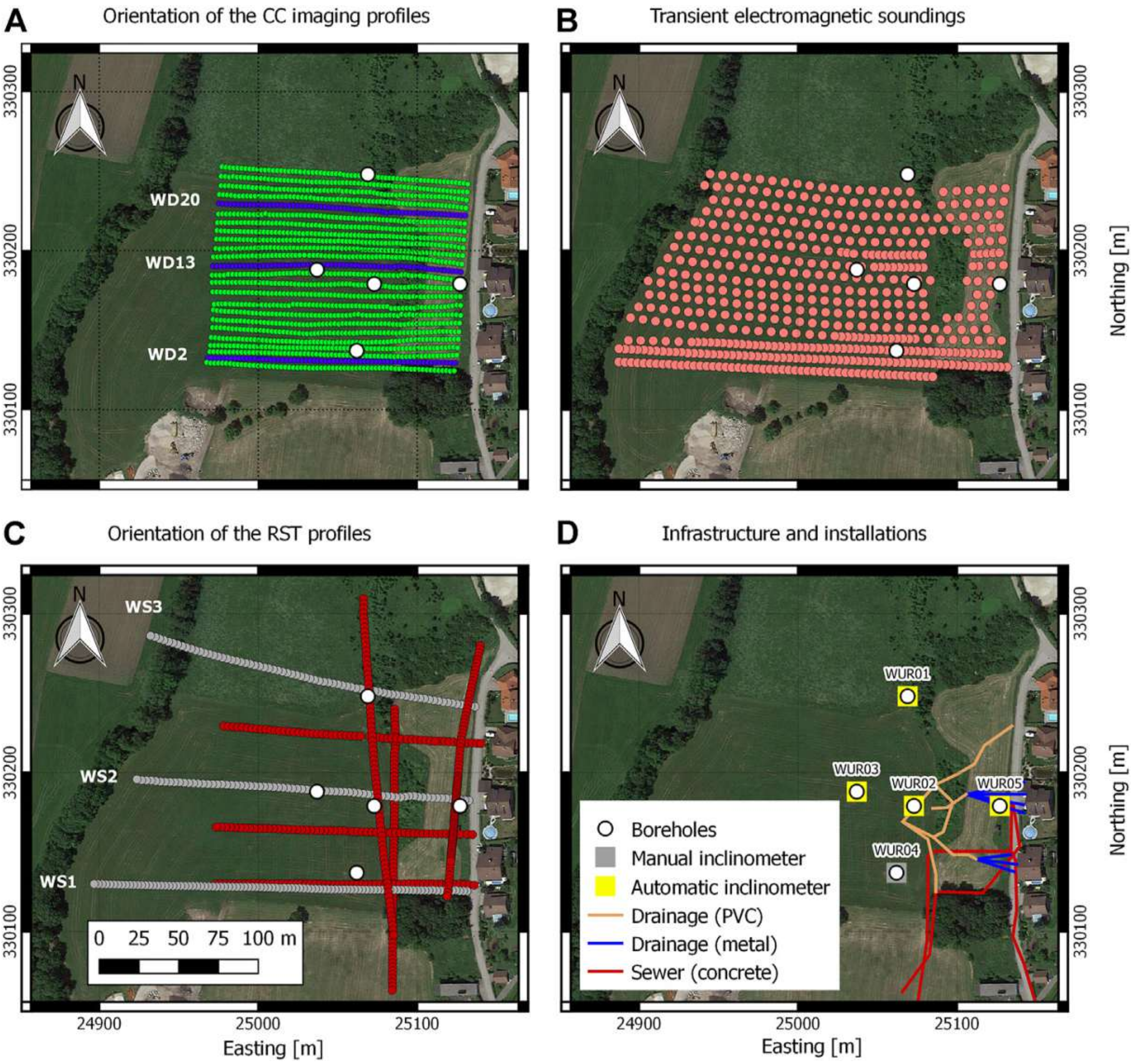

Figure 5.2: Overview of geophysical and geotechnical surveys as well as known infrastructure. The colored dots in (A–C) represent the location of the (A) electrodes and (C) geophones in each profile as well as the location of the (B) individual TEM soundings.

5.3.3 Complementary geophysical data: Transient electromagnetic and seismic methods

5.3.3.1 Transient electromagnetic soundings

Transient electromagnetic (TEM) soundings were used to gain information about vertical variations of the electrical properties across the study area. Measurements were conducted using a single-loop geometry, where the same cable is used as transmitter and receiver, typically in a closed square or circular geometry. The method is based on the circulation of a direct current in the transmitter loop, which generates a primary magnetic field. The abrupt switch-off of the direct current induces eddy currents into the subsurface. This system of eddy currents decays over time and generates the secondary magnetic field (Ward and Hohmann, 1988). The temporal variations of this secondary magnetic field are measured in the receiver loop in terms of a voltage that is sampled along logarithmically distributed time windows. Since the measured decay of the secondary magnetic field depends on the subsurface electrical resistivity, inverse modelling can be used to reconstruct resistivity changes at depth along 1D profiles below the sounding position (e.g., Christiansen et al., 2006).

Single-loop TEM data was collected along 16 profiles for a total of 517 soundings between the 1st and 4th June in 2018 using a TEM-FAST 48 manufactured by AEMR (Applied Electromagnetic Research). We used a circular loop with a radius of approx. 4 m for a cable length of 25 m (i.e., transferring to a square loop of 6.25 m side length) and a 12 V power source with a 1 A direct current, corresponding to a magnetic momentum of 39 Am^2, to collect the data. The voltage decay was sampled along 24 time windows up to 256 μs after current shut-off and we used a total stacking of 9,984 transients to increase the signal to noise ratio. The average sounding spacing was about 8 m except for the southern part of the study area where overlapping measurements were performed (i.e., a loop center separation of 4 m; c.f. Table 5.2 and Figure 5.2B). The location of each sounding was determined with an RTK-GNSS.

Preprocessing of the TEM data consisted of a visual inspection of the TEM soundings and a manual removal of erroneous voltage readings, i.e., readings that deviate from the expected smooth decay or negative voltage readings. Early-time readings up to 25 μs were particularly affected by noise likely related to an enhanced turn-off ramp effect caused by a highly conductive ($< 0.5\ \Omega$) loop cable (Aigner et al., 2021). Therefore, the first 10 time gates of each sounding were removed from the entire data set. Furthermore, we filtered additional readings in the late-times depending on the observed curve smoothness and the presence of negative voltage readings. 1D sections of the vertical changes of electrical resistivity were obtained by inverting the data with

Table 5.2: Number of TEM soundings in each profile (with profile 1 starting in the south) and indication if overlapping measurements were performed (i.e., subsequent TEM loops overlap).

Profile	Number of soundings	Overlap
1	51	complete profile
2	63	complete profile
3	55	partly overlapping
4	37	partly overlapping
5	29	-
6	27	-
7	25	-
8	24	-
9	25	-
10	29	partly overlapping
11	31	partly overlapping
12	24	-
13	25	-
14	24	-
15	23	-
16	23	-

ZondTEM1D (Kaminsky, 2001) using a smoothness-constraint regularization. To permit a fair discretization over the entire model depth, a model with16 layers with fixed thickness was chosen. Using a number of layers in the model much larger than the actual number of lithological layers observed in the boreholes permits a fair discretization in the inversion. We then evaluated the data fit and removed additional voltage readings where the measured data was not fitted by the inverted model.

5.3.3.2 Refraction seismic tomography

The refraction seismic method (RST) is based on the propagation and refraction of artificially generated seismic waves in the subsurface and the measurement of ground motion in order to measure travel times of the refracted waves between the shot point and geophone locations. Such travel times can then be inverted to construct a continuous model of the subsurface velocity of P-waves, which depends on the density and the elastic properties of the material (Lankston, 1990). Contrasts in P-wave velocity can be used to infer the contact between unconsolidated sediments and the bedrock (Leucci et al., 2007; Parasnis, 2012).

To support the interpretation of the electrical results, 10 RST profiles (Figure 5.2C) were measured between 12th to 16th June in 2017 and between 23rd to 26th April in 2019. Summit seismic recorders (by DMT, Germany) with 24 channels were used to

Table 5.3: Number of deployed geophones, the geophone spacing, the orientation and year of collection of the seismic profile.

Profile	Number of geophones	Geophone spacing [m]	Orientation	Year collected
1	96	2.5	E-W	2019
2	72	3	E-W	2019
3	72	3	E-W	2019
4	72	3	N-S	2019
5	72	2.25	N-S	2019
6	48	1.2	N-S	2019
7	48	3	E-W	2017
8	48	3	E-W	2017
9	48	3	E-W	2017
10	72	2.5	N-S	2017

record the seismic wave-field. For our surveys we deployed 30 Hz vertical geophones and collected 1,024 ms traces with a sampling of 1/4 ms. A 5 kg sledgehammer was used as a seismic source and a stack of three shots was made at each geophone location. Table 5.3 presents the orientation of each profile, as well as the corresponding number of geophones and geophone spacing. The signal processing, consisting of a low-pass filter and an amplitude amplification, and the first break picking were performed with formikoj (Steiner and Orozco, 2023). The refraction module of pyGIMLi (Rücker et al., 2017) was subsequently used to invert the travel times to recover 2D sections of seismic velocity using a smoothness-constraint inversion scheme.

5.3.4 Borehole data

In April of 2017, five boreholes were drilled across the study area (Figure 5.2D) in depths varying between 16 and 30 m (c.f. Table 5.4). For each borehole, coring was performed with a diameter of 180 mm and the retrieved sediments were stored for subsequent laboratory analysis and geological description. The lithological composition of the boreholes was similar and featured sediments of the Hausruck, Ampflwang and Ottnang formation and materials of the first two formations were found to be variably disturbed and mixed due to past landslide processes.

After the drilling of the boreholes, electromagnetic well-log measurements were conducted at each location using a Dual Induction Probe (by Robertson Geologging Ltd., UK), including continuous logs of the natural gamma radiation and apparent conductivity (Spies, 1996). Gamma logging is a widely used methodology to investigate formations (Schnyder et al., 2006) as specific minerals and sediments, such as feldspar, clays and shales host a larger number of radionuclides (Thorium, Potassium and Ura-

Table 5.4: Drilled depth, performed laboratory investigations and associated number of samples in each borehole. The mineralogical investigations included both bulk rock and clay mineralogy.

Borehole	Number of samples: Grain size distribution and mineralogy	Cation exchange capacity	Plasticity	Drilled depth in m
WUR01	11	4	-	30
WUR02	6	2	4	16
WUR03	9	4	-	20
WUR04	7	3	-	20
WUR05	10	6	7	22

nium) that emit gamma rays. Hence, gamma logs were used here to aid in the interpretation of clay-rich layers. Yet, the occurrence of organic matter might impose limitations on its interpretation (Myers and Wignall, 1987).

In total, 43 samples of the predominant layers within the core were probed and analyzed at the Geological Survey of Austria. The analysis included: 1) bulk rock mineralogy and clay mineralogy (< 2 μm fraction) determined by XRD (PANalytical X'Pert Pro Powder), 2) grain size distribution based on a combined analysis of wet sieving and Sedigraph (< 0.032 mm), and 3) cation exchange capacity (CEC) together with a chemical analysis of major and trace elements. CEC was determined with the barium chloride method (ÖNORM L 1086–1). Moreover, 11 samples were tested on their liquid and plastic limits at a certified testing laboratory (TPA, Vienna). Table 5.4 presents the number of samples and their distribution for each borehole.

5.4 Results

5.4.1 Improving electrical imaging results by incorporating a TEM based reference model

Figure 5.3A presents the CC imaging results for the profile WD2 (c.f. Figure 5.2A) expressed in terms of the real σ' and imaginary σ'' components of the complex conductivity σ^* as well as the phase-shift φ of the complex conductivity. Both the real and imaginary component reveal three main features, which can be described, from shallow to depth, as: 1) a shallow anomaly characterized by low conductivity ($\sigma' > 15$ mS/m) and polarization ($\sigma'' < 30$ μS/m) values between 40 and 100 m with a thickness varying between 5 and 10 m, 2) a spatially limited anomaly between 100 and 120 m characterized by increased σ' values above 40 mS/m and σ'' values above 100 μS/m, and 3) a conductive and polarizable ($\sigma' > 40$ mS/m, $\sigma'' > 100$ μS/m) unit below 1) and 2). The electrical images in Figure 5.3A reveal electrical units that are roughly horizontal, yet lateral variations are observed, which cannot be easily explained from the geological background of the site but are assumed to be related to slope processes and resulting redistribution and deformation of slope sediments.

Figure 5.4B presents the inverted TEM models collected along the same profile. The TEM models indicate practically only two layers: a shallow one with resistivity values larger than 20 Ωm and a thickness of 5–10 m, whereas a low resistivity layer ($\rho_{TEM} < 8$ Ωm) can be found below it. Compared to the CCI images, the TEM results provide an increased contrast at depths larger than 12 m and at the edges of the CCI profile. The contact to materials with high electrical conductivity (and therefore low resistivity) cannot be resolved with a standard inversion of the CCI data, which favors smooth variations in both lateral and vertical direction.

TEM inversion results have been used to support the interpretation of ERT and to a lesser extent CCI, for instance to delineate regional aquifer geometry (Meier et al., 2014), to trace saline contamination due to coastal salt water intrusion (Balia and Viezzoli, 2015; Ardali et al., 2018) and to investigate karst lakes (Bücker et al., 2021). Caterina et al. (2014) have shown that the incorporation of prior information in the inversion can help to obtain a more geologically plausible subsurface model. This can be achieved by modifying the regularization operator to account for a reference model (e.g., Oldenburg and Li, 1994) and was done for example by Catt et al. (2009) using EM data from a ground conductivity meter. Hence, we use the inverted TEM model as a reference model for the inversion of the CCI data in order to enhance the horizontal layering and to improve the vertical contrast between the electrical units. Other studies have proposed a joint inversion, where ERT and TEM data are solved simultaneously for the same resistivity model (e.g., Martínez-Moreno et al., 2017; Christensen, 2022). However, the inclusion of CCI data in such scheme is beyond the scope of this manuscript.

For the construction of the TEM reference model, in a first step, we selected those TEM soundings that are located along to the CCI profiles. We note here that the inverted 1D TEM resistivity models are always considered to be perpendicular to ground surface; thus, these are tilted to account for the topography changes and mapped to the inversion mesh using nearest neighbor interpolation. Yet, due to the nature of the nearest neighbor interpolation, the so obtained models are not smooth (Figure 5.4C) and would likely lead to implausible inversion results. Hence, we perform a topography constrained bounding box smoothing filter to smooth the TEM models. Accordingly, for each model cell, we define a rectangular bounding box with given x- and z-axis lengths (32 and 12 m; i.e., 2.6:1 smoothing) which is then rotated based on the slope of the topography. After that, the median value of all model cells inside the bounding box is computed and reassigned to a second mesh. We use a second mesh for the reassignment to avoid mutual dependencies of the smoothing outcome due to the sequence of model cells selected. Figure 5.4D presents the final reference model after mapping of the TEM values and the smoothing procedure revealing a “smooth” resistivity model.

The resistivity models from CCI and TEM are consistent, as observed in Figure 5.4A and Figure 5.4B, thus permitting to incorporate the electrical layer distribution computed for the TEM data (Figure 5.4C) as described above. Following this approach, we obtain the model presented in Figure 5.4D. The comparison of the models in Figure 5.4A and Figure 5.4D shows consistent models with variations in the magnitude of the electrical resistivity values. Such discrepancy is related to the different volumes for each measurement (i.e., quadrupoles with an electrode separation of 2.5 m when compared with a transmitter loop with an area of 39 m^2, (e.g., Auken et al., 2006). To overcome this, we scaled the resistivity values retrieved from the inversion of TEM data by the computation of a transfer function. In detail, we extracted the $|\rho^*|$ values from the inverted CC imaging section at the location of the tilted TEM soundings, and computed a linear regression as presented in Figure 5.5. We used individual transfer functions for each electrical profile. Furthermore, we investigated the use of the reference model without a rescaling of the resistivity values, which revealed only minimal changes in the solved images compared to the rescaled ones, as expected, considering that during the inversion the actual resistivity values are fitted to the measured data and the reference model only aids within the regularization (Caterina et al., 2014). Hereafter, we refer only to CCI results obtained using a reference model in the inversion based on the rescaled TEM model.We note here that we used a homogeneous half space with $\varphi = 0$ for the impedance phase of the reference model. In Figure 5.3B, we present the CCI images for the profile WD2 after inversion with the TEM reference model. As it can be seen in Figure 5.3B (bottom row), the use of a homogeneous reference model for the phase-shift has only minor effects on the obtained phase-shift image. A comparison with Figure 5.3A also shows that small scale lateral changes in shallow depths (e.g., the polarizable anomaly, with $\sigma'' > 100\ \mu\mathrm{S/m}$, at 110 m along the profile) are preserved while solving for a continuous layer with an increased contrast at depth.

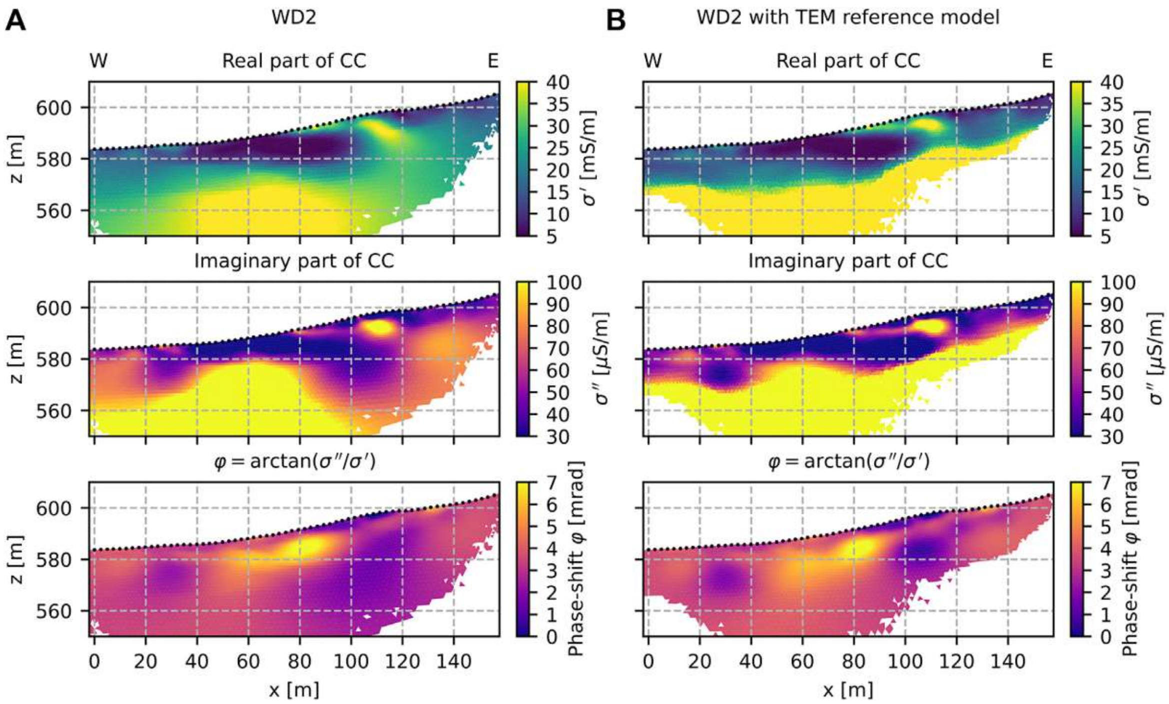

Figure 5.3: Complex conductivity imaging results for the profile WD2 expressed in terms of the real σ' and imaginary σ'' component of the complex conductivity σ^* as well as the phase-shift φ for (A) "standard" inversions without the incorporation of complementary information and (B) for inversions performed with a reference model based on TEM data collected along WD2.

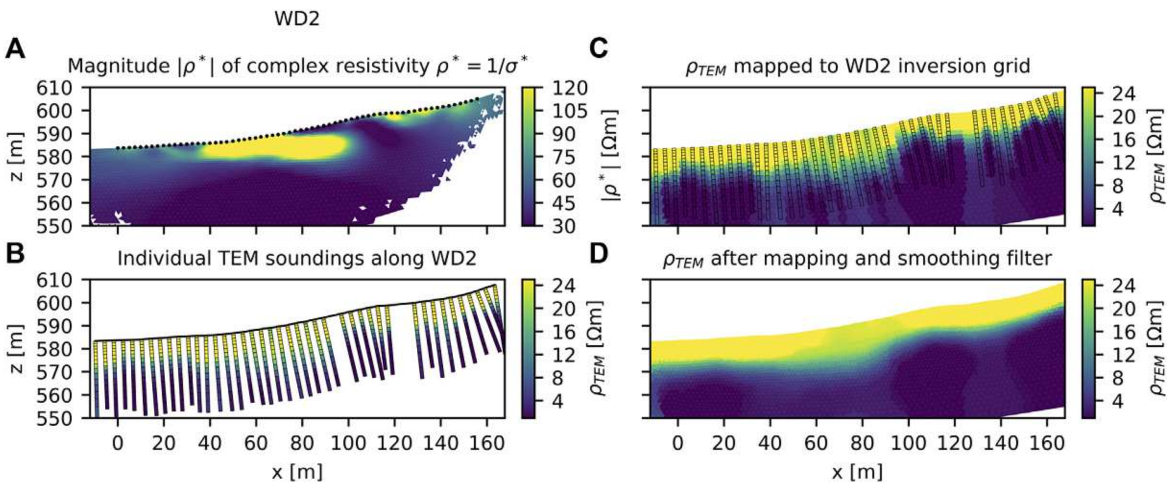

Figure 5.4: (A) Electrical imaging results for the profile WD2 expressed in terms of the magnitude $|\rho^*|$ of the complex resistivity $\rho^* = 1/\sigma^*$, as well as (B) the inverted TEM data collected along the same profile. (C) shows TEM resistivity values ρ_{TEM} mapped to the inversion grid of WD2 using nearest neighbor interpolation and (D) the same section after applying a smoothing filter.

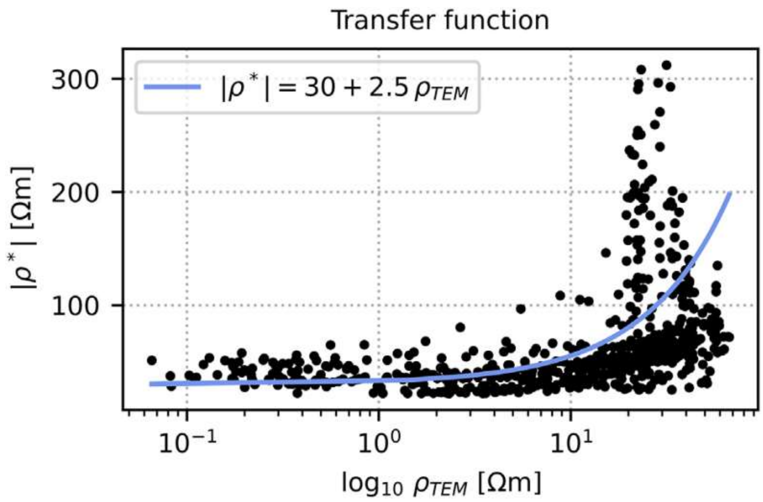

Figure 5.5: Linear transfer function used to scale ρ_{TEM} to fit the order of magnitude of $|\rho^*|$ observed in the electrical imaging.

5.4.2 Using CC imaging and RST to delineate subsurface architecture

We present in Figure 5.6 the seismic P-wave velocity and improved CC imaging results for profiles located at the southern border, in the center and at the northern border of the study area (Figure 5.2). Moreover, to evaluate the seismic and electrical response in comparison to actual soil-physical properties, we present lithological logs overlapping the seismic and CC imaging results. The lithological logs correspond to the soil textural analysis of subsurface materials recovered during the drilling of the boreholes WUR02 and WUR03 collocated to the profile WD13 and borehole WUR04 collocated to profile WD2.

Images of the real conductivity σ' presented in Figure 5.6A, in general, reveal two electrical units consisting of a conductive layer in the bottom ($\sigma' > 30$ mS/m) and a less conductive layer on the top ($5 > \sigma' < 30$ mS/m). The interface between the two layers lies at a depth of 15–20 m, with lateral variations not necessarily following the changes of the surface topography, as evidenced, for instance, in the abrupt change observed in WD13 between 140 and 180 m along the profile direction. The top layer generally reveals σ' values between 5 and 30 mS/m and is characterized by small-scale lateral σ' changes in shallow depths that can be observed between 150 and 180 m in WD2 and between 90 and 110 m in WD13. Images of the imaginary conductivity σ'', as presented in Figure 5.6B, reveal similar features, namely a two-layer model with a polarizable bottom layer ($\sigma'' > 100$ μS/m) and low polarizable top layer ($\sigma'' < 70$ μS/m). Low polarization in the top layer could be linked to previously mobilized materials, as for instance, reported by Flores Orozco et al. (2018b). In such study, the authors argue that low compaction and low saturation in sliding materials leads to a low polarization response. Yet, σ'' imaging results for WD13, when compared to σ', reveal spatially limited polarizable anomalies in shallow depths, particularly visible from 135 m on. Moreover, the σ'' bottom layer in WD2 shows a distinct anomaly between 120 and 150 m that is not visible in the corresponding σ' image.

To facilitate the comparison between the CCI and RST results, the interface between the two electrical units in the σ' images, as described above, is superimposed in RST images. These RST images reveal consistent features to those observed in the σ' images, i.e., a two-layer model comprised of a bottom layer with velocities larger than 2,200 m/s, likely associated to consolidated sediments; whereas the top layer reveals velocities between 700 and 1,500 m/s, likely associated to previously mobilized materials. In general, the depth and topography of the bottom layer resolved by the RST is in agreement with the electrical images. However, particularly to the end of the seismic profiles (e.g., from 160 m on for WS1 and from 140 m on for WS2) differences in the seismic and electrical images can be observed. The convex anomaly in the σ' images is not resolved in the seismic sections, which indicate a more concave structure. We explain such differences by changes in the composition of the bottom layer, which does not necessarily provide the same response in seismic and electrical measurements. For instance, we interpret such differences as an increase in clay content, a factor that does not necessarily represent an increase in seismic velocity, which is more sensitive to changes in compaction/consolidation. Furthermore, shallow anomalies within the top layer that reveal high seismic velocity ($> 1{,}500$ m/s), as for example visible in WS2 between 100 and 140 m, are also consistent with anomalies observed in the σ'' images ($\sigma'' > 100$ μS/m). Such anomalies reveal an existing heterogeneity in the shallow subsurface properties, possibly related to lenses with compacted materials, which again, could point to previous landslide events and corresponding dislocation of lithological formations. Alternatively, such heterogeneities could indicate the start of undisturbed slope sediments in the foreland of the landslide (c.f. Figure 5.1C).

The layered model interpreted from both the σ' and σ'' images can be fairly tied to the borehole information (c.f. Figure 5.6), yet the polarization image (σ'') yields a better agreement with the borehole data. Here, the conductive and polarizable bottom layer can be related to fine-grained sediments (clay, silt loam and loam), whereas the sandy gravels are represented by a low polarization response and low conductivity values ($\sigma'' < 70$ μS/m and $\sigma' < 20$ mS/m). Moreover, the shallow polarizable units ($\sigma'' > 100$ μS/m) observed between 110 and 170 m along WD13 are in agreement with peat as observed in WUR02, which is a material known for its high polarization response (Slater and Reeve, 2002; Comas and Slater, 2004; Katona et al., 2021). Differences in the lateral changes of the interface between the top and bottom layer, as retrieved from seismic and electric methods for WD13 and WS2 between 140 and 200 m along the profile can now be explained by a change in texture from loam to silt loam, and the likely associated change in soil moisture, both factors that will probably not affect the seismic velocity as significantly as it does the complex conductivity.

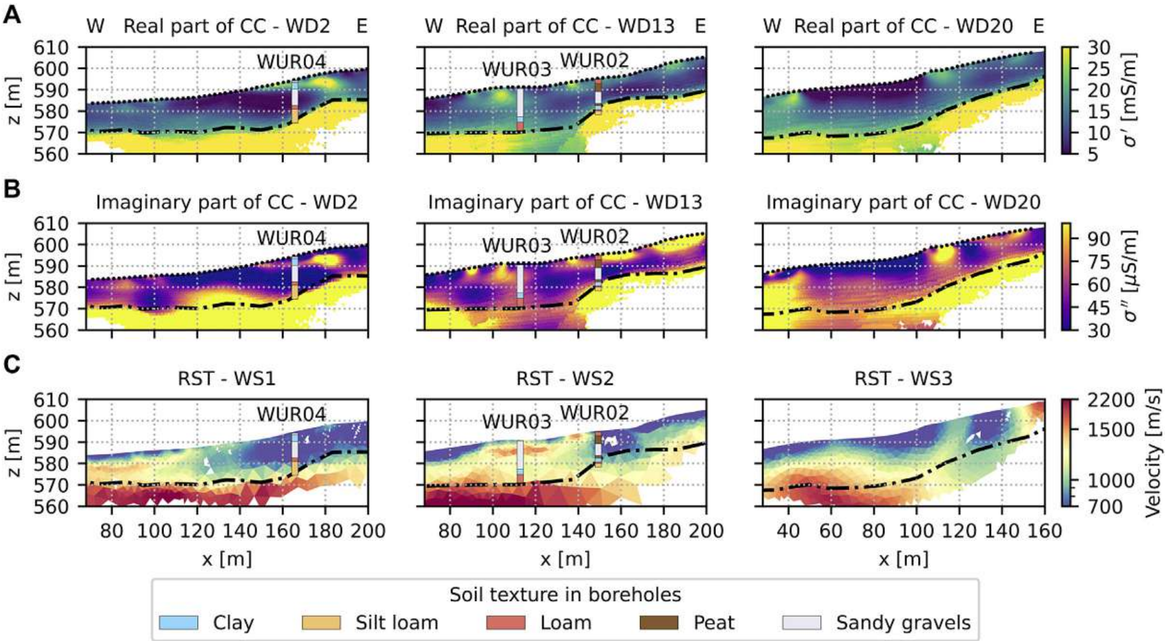

Figure 5.6: (A,B) Complex conductivity imaging results expressed in terms of the real σ' and imaginary σ'' components of the complex conductivity for electrical profiles collected at the southern border (WD2), in the center (WD13) and the norther border of the study area (WD20). (C) presents the corresponding seismic P-wave velocity images as obtained from RST for data collected along the electric profiles (c.f. Figure 5.2). The dashed black line indicates the depth and topography of the bottom layer as delineated from the σ' imaging results.

5.4.3 Site-specific correlations between soil-physical parameters and imaginary conductivity: A potential for upscaling to spatial continuous information

We observe a fair qualitative agreement between borehole information and the inverted electrical data. Hence, in a first step, we extracted the model parameters from the electrical images at the depth and location of the boreholes. The extracted model parameters are computed as the median value of a k-nearest neighbor search (with k being five elements of the electrical model) and the starting point for the search being the depth and location of the borehole relative to the profile. In a second step, we correlated the available soil-physical and extracted electrical model parameters. For this analysis, we only used borehole data from the wells WUR01, WUR02, WUR03 and WUR05, while the information corresponding to well WUR04 will be used in a later step to evaluate the retrieved petrophysical models. For the sake of brevity, we only present the most significant correlations that are later on discussed in the upscaling approach.

Our analysis revealed that the most significant correlations were observed between the grain size distribution (i.e., the different soil volume fractions of gravel f_g, sand f_{sa}, silt f_{si} and clay f_c) and the polarization response expressed in terms of the imaginary component σ'' of the complex conductivity. Accordingly, in Figure 5.7 we present the imaginary conductivity σ'' plotted against f_g, f_{si} and f_c, as well as the adjusted regression functions and their confidence bounds. The σ''-f_g scatter plot reveals a negative correlation, more precisely, an approximately linear decrease in gravel fraction in the polarization range between 1 and 175 μS/m (σ''), from which on the gravel fraction remains constant at 1–3%, and hence, independent of σ''. We model this nonlinear relationship with a high degree polynomial function that writes

$$f_g = -4.069\times10^{-8}(\sigma'')^4+2.661\times10^{-5}(\sigma'')^3-4.615\times10^{-3}(\sigma'')^2-0.125\,\sigma''+64.21 \quad (5.6)$$

and fits our data to a reasonable R^2 score of 0.71. The σ''-f_{si} scatter plot reveals a more complex relationship, that is, a nonlinear increase in silt fraction in the range between 1 and 150 μs/m (σ''), where the silt fraction reaches its maximum of about 70%, and, a moderate decrease in silt fraction for σ'' values larger than 150 μS/m. We found that a cubic function captures the characteristics of the described relationship fairly well with a R^2 score of 0.87 and the obtained function writes as:

$$f_{si} = 9.458 \times 10^{-6}(\sigma'')^3 - 6.165 \times 10^{-3}(\sigma'')^2 + 1.186\,\sigma'' - 9.614\,. \quad (5.7)$$

Finally, σ'' plotted against the log-converted fraction of clay f_c indicates two regimes. On the one hand, 1) a narrow band of clay fractions above 70% corresponding to σ'' between 120 and 170 μS/m; while on the second hand 2) a step response for clay fractions below 30% that is characterized by low contents of clay (< 7%) for σ'' below 120 μS/m, and moderately increased clay content up to 20–25% for σ'' values above 170 μS/m. The analysis of the clay mineralogy revealed clear differences in the fraction of kaolinite, smectite and illite, with an abundance of kaolinite for regime 1) and a combined percentage over 70% of smectite and illite for regime 2). As previously discussed by (e.g., Leroy and Revil, 2009; Okay et al., 2014; Lévy et al., 2018), there is a dependence of the polarization response on the type of dominant clay mineral. Hence, we explain the observed changes in σ'' for the clay fraction associated to variations in clay mineralogy. Since only 4 out of 36 samples were associated to kaolinite we decided to omit them and only model the response for regime 2) with a logistic function that adjusts the data to a R^2 score of 0.81. Hence, the σ''-f_c function can be written as:

$$f_c = 14.5\,(1 + e^{-0.07\,\sigma'' + 12.5})^{-1} + 4.6. \tag{5.8}$$

The correlation of σ''-f_{sa} did not reveal any clear relationship. Hence, we determine the missing sand fraction f_{sa} as a loss function, knowing that all fractions combined should add up to 100

$$f_{sa} = 100 - (f_g + f_{si} + f_c) \tag{5.9}$$

Implicitly, this approach also ensures that the total fraction is always capped at 100%. Figure 5.8 presents the shape of the prediction functions for f_g, f_{si}, f_c as well as f_{sa} as a loss function. In general, we predict coarser textures (sand and gravel) for σ'' below 75 μS/m, mostly silt for the middle range ($75 > \sigma'' < 200$ μS/m) and a mixture of sand, silt and clay for σ'' larger than 200 μS/m.

5.4.4 Quantification of soil-textural and hydraulic properties in a complex conductivity framework

Given the relationships that link the imaginary conductivity to soil fractions, we now have a practical tool to upscale from borehole information (i.e., retrieved samples from drilling) to spatially continuous information over the entire study area. In Figure 5.9, we use the Equations (5.6)-(5.9) for the estimation of gravel, silt, clay and sand from the electrical imaging results from profile WD13 across the entire imaging plane. Based on the soil classification system (NRCS, 1993 - from the United States Department of Agriculture, USDA), we include a classification of soil texture in Figure 5.9, as well as the soil texture reported from the core analysis of the boreholes WUR02, WUR03 and WUR05.

The comparison of borehole and electrical data reveals a good agreement between the predicted and reported soil textures, with exception of the deep fine-grained units in WUR03. For the hydrogeological interpretation of our results, we now define two main units. A top layer, from the surface to a depth varying between 12 and 18 m, which consists of sandy gravels intercalated by peat, loam and silt loam. Below there is a bottom layer, characterized mostly by fine-grained sediments. Such bottom layer consists of a thin clay unit on top of loam and silt loam. In terms of the stratigraphy, the top layer can be related to the Hausruck formation, whereas the bottom layer

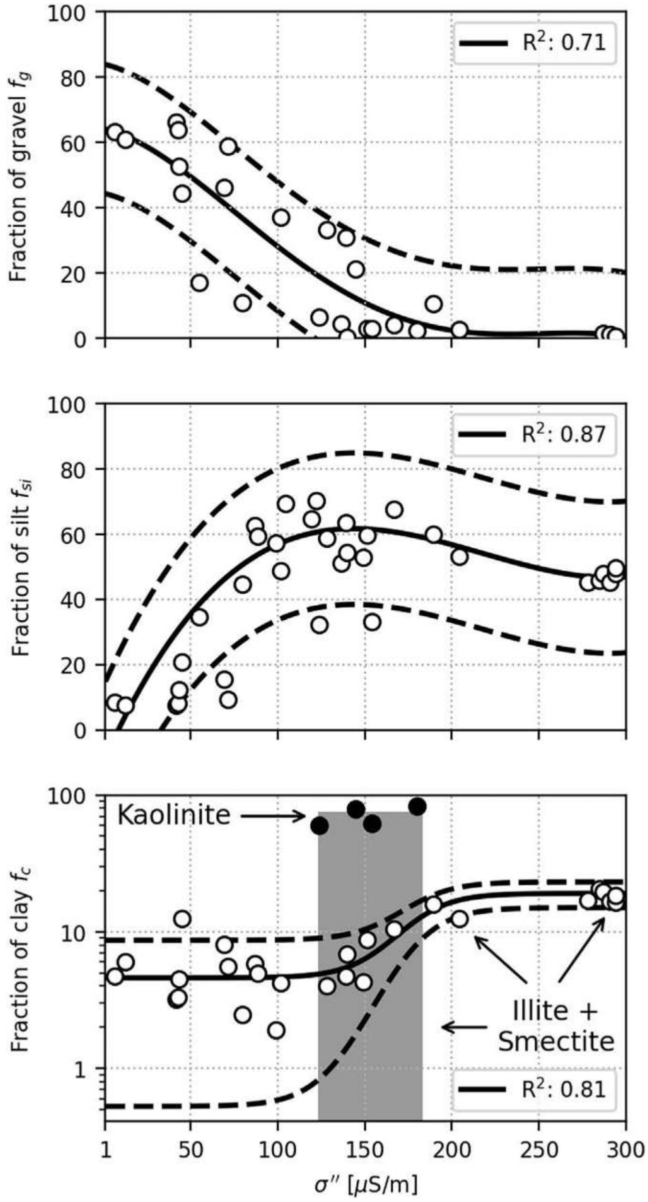

Figure 5.7: Scatter plots of the imaginary conductivity σ'' (white circles) and volume fraction of gravel (top) and silt (center) and clay (bottom) reveal well-determined relationships, with the adjusted regression functions (black line) reaching R2 scores > 0.7. The black dashed line indicates the confidence bounds computed for two times the standard deviation of the corresponding regression function.

corresponds to the Ampflwang and Ottnang formation respectively. Albeit mixtures of different formations, due to past landslide events, can be expected in both layers.

Soil hydraulic properties are preferred over soil texture alone as it provides direct information about water flow. Hence, in a second step, we investigate the possibility to retrieve hydraulic conductivity estimates in an imaging framework built on the quantitative correlation of geophysical and borehole data. We used the recent adaption

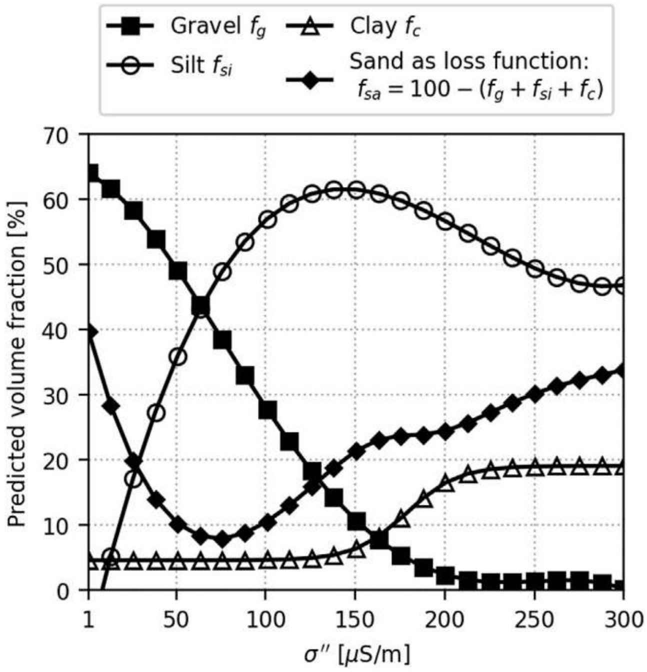

Figure 5.8: Shape of the modelled functions used to predict the different soil fractions for gravel f_g, sand f_{sa}, silt f_{si} and clay f_c based on their dependence on σ''.

of Rosetta (Zhang and Schaap, 2017) to estimate K_s (along with the VG parameters) from our predicted soil fractions. As Rosetta uses the volume fractions of sand, silt and clay as input with the requirement that the fractions sum up to 100% soil volume, we had to modify our sand prediction function. Accordingly, our sand prediction (f_{sa}) accounts for both sand and gravels, such as:

$$f_{sa} = 100 - (f_{si} + f_c) \tag{5.10}$$

In particular, Equation 5.10 predicts larger fractions of sand for $\sigma'' < 150$ μS/m (c.f. Figure 5.8). We argue that this could be used as a first proxy for the missing gravel fraction, i.e., increasing the fraction of the next smallest grain size class.

Figure 5.10 presents the resulting K_s distribution for WD13 applying Rosetta to our data. For completeness, the VG parameters as well as the soil texture classification when using the adapted sand computation are presented in the (Figure 5.14). In general, the predicted K_s values are roughly distributed over two orders of magnitude (4×10^{-6} to 1×10^{-5} m/s) with largest values observed for gravelly textures in the top layer, e.g., at the location of WUR02 and WUR05. At depth, the model predicts the lowest K_s values ($K_s < 4 \times 10^{-6}$ m/s) that seem to trace the layers of clay, loam and silt loam in WUR02 and WUR05.

WUR03 shows only moderate K_s values (6×10^{-6} m/s). As depicted in Figure

5.14, the overall texture in WD13 is dominated by loamy components (silt loam and sandy loam), which is also reflected in the predicted homogeneous K_s values. In this context, both lateral and vertical variations, e.g., at WUR02, can be explained by either a higher portion of sand that leads to an increase of $K_s > 8 \times 10^{-6}$ m/s, or larger fractions of silt corresponding to a decrease in $K_s < 7 \times 10^{-6}$ m/s.

Considering the implications of the K_s prediction on the slope hydrogeology, the bottom layer with K_s values below 4×10^{-6} m/s is expected to act as hydraulic barrier for interflow, whereas the top layer can be considered as an unconfined aquifer that permits infiltration of surface water. This interpretation is supported by water tables reported during drilling, which were found at the depth of the clay layer or slightly above it (as depicted in Figure 5.10). Interflow along the interface between bottom and top layer will likely result in weathering of slope materials (i.e., the dissolution and accumulation of fine grains) and, therefore, development of weathered loam.

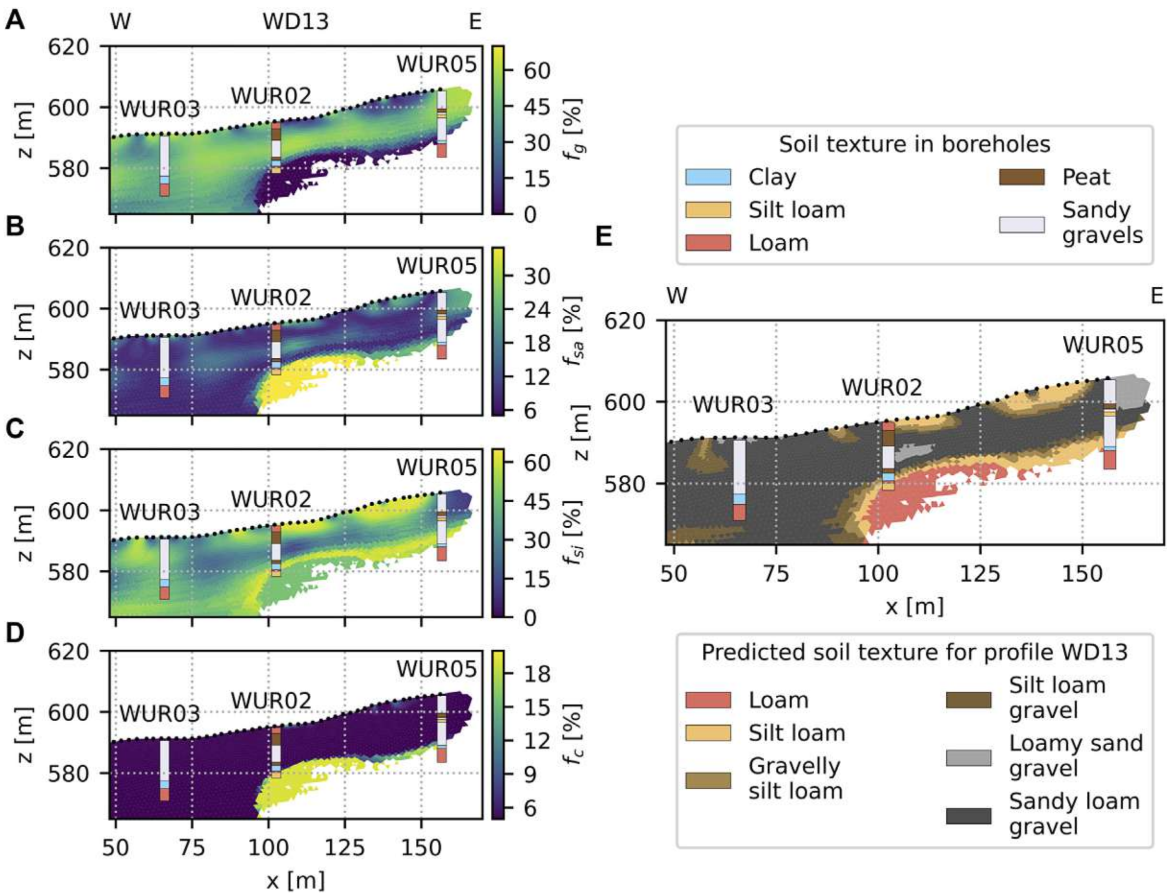

Figure 5.9: Predicted fractions of (A) gravel (f_g), (B) sand (f_{sa}), (C) silt (f_{si}) and (D) clay (f_c) for the profile WD13 and (E) the corresponding predicted soil texture with ground-truth information from boreholes WUR02, WUR03 and WUR05 superimposed over each section.

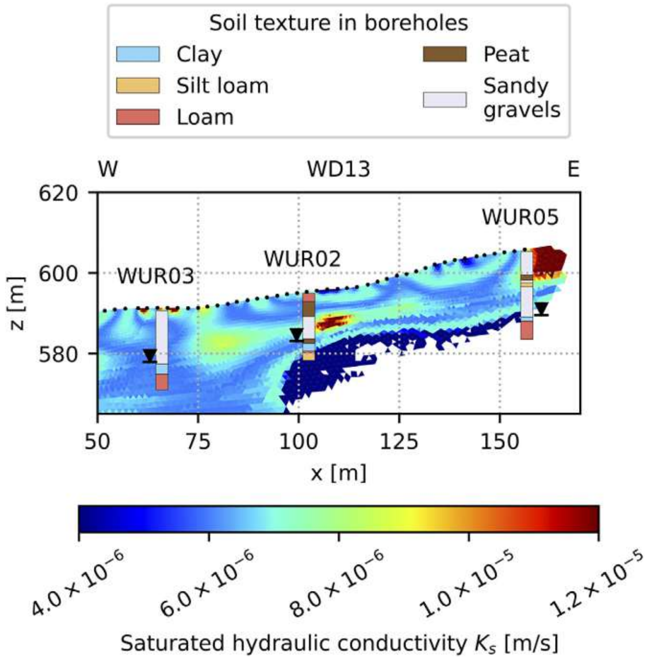

Figure 5.10: Predicted saturated hydraulic conductivity K_s for the profile WD13 using the Rosetta PTF (Zhang and Schaap, 2017), which uses the volume fractions of sand, silt and clay as input parameters. To aid the interpretation of the K_s patterns, the soil texture observed in the boreholes WUR02, WUR03 and WUR05 is also presented. The reversed black triangles indicate the water tables reported during drilling.

5.4.5 Preferential water-flow paths and their implication on slope morphology

We have shown that for WD13 the hydrogeological system is governed by practically two layers: an unconfined aquifer with a thickness of 12–18 m on top of a unit with low hydraulic conductivity. Hence, in a next step we investigated how the interface topography changes for the entire study area, as well as the possibility to delineate possible preferential water-flow paths based on a combined interpretation of the interface topography and the geomorphological surface features.

The comparison of Figure 5.6 and Figure 5.10 clearly shows that the transition from low to high σ'' values at depth (from 40 to > 90 μS/m) also marks the transition to the lowest K_s values ($< 4 \times 10^{-6}$ m/s). Thus, we compute the interface geometry for the entire study area. To achieve this, we manually extracted the interface in the σ'' images in all profiles. For those profiles that resolved a discontinuous interface in the CC, we included the analysis of the transition from P-wave velocity from 1,500 to 2,200 m/s for the location of the discontinuity. The obtained interfaces were converted from 2D coordinates to their respective 3D coordinates using an affine transformation, with a subsequent interpolation to a uniform 3.6 m grid using the kriging method to obtain a quasi-continuous model.

Figure 5.11 shows the so obtained aquiclude interface for the entire study area as well as the DEM hillshade with a color-coded surface elevation overlay. Furthermore, to aid the interpretation of the topographical changes of the aquiclude interface, the gradient vector magnitude in each grid cell is also presented. In general, the interface reveals a decrease in the elevation from east to west consistent to the surface elevation. However, clear differences can be observed in the eastern part of the study area (X > 25,050 m) where the interface reveals a much steeper dipping (i.e., densely grouped isolines) compared to surface topography.

In a similar manner, the surface topography shows a bulge north-west of WUR03; whereas the interface topography indicates a depression. Based on the isolines and gradient magnitudes of the interface layer, we propose two possible preferential water-flow paths, as depicted in Figure 5.11. In particular, Figure 5.11 shows 1) a channel starting in the north-eastern part of the study area and continuing north of WUR03 to the south-western part of the study area; and, 2) a roughly direct channel from the south-eastern to the south-western part of the study area. The pathway 1) can clearly be traced by the form of the isolines and gradient vector magnitudes which indicate a depression and likely channeling of interflow, while for pathway 2) a small bulge for the eastern part (X > 25,060 m) and a more pronounced depression of the western part (X < 25,040 m) can be observed. Both 1) and 2) seem to merge in a common location (roughly at X=24,990 m, Y=330,165 m).

Figure 5.11 indicates that the largest surface topographical changes are associated to those locations where the topography of the interface exhibits the largest gradient vector magnitudes, particularly visible in the eastern part of the study area. We argue that the channeling of interflow through preferential flow paths will likely accelerate weathering or changes in pore-pressure and, therefore, could promote subsidence in those particular areas. Following this argumentation, the bulge in the surface topography northwest of WUR 03 is interpreted as deformation of the plastic-reacting slope sediments or materials of a former mudflow as a reaction of the uplift pressure of the main landslide (c.f. Figure 5.1C). To attenuate this effect, a possible countermeasure could include extending the drainage system downslope below the former source/waterlogged area. This could mitigate the channeling of subsurface water-flow along the interface topography.

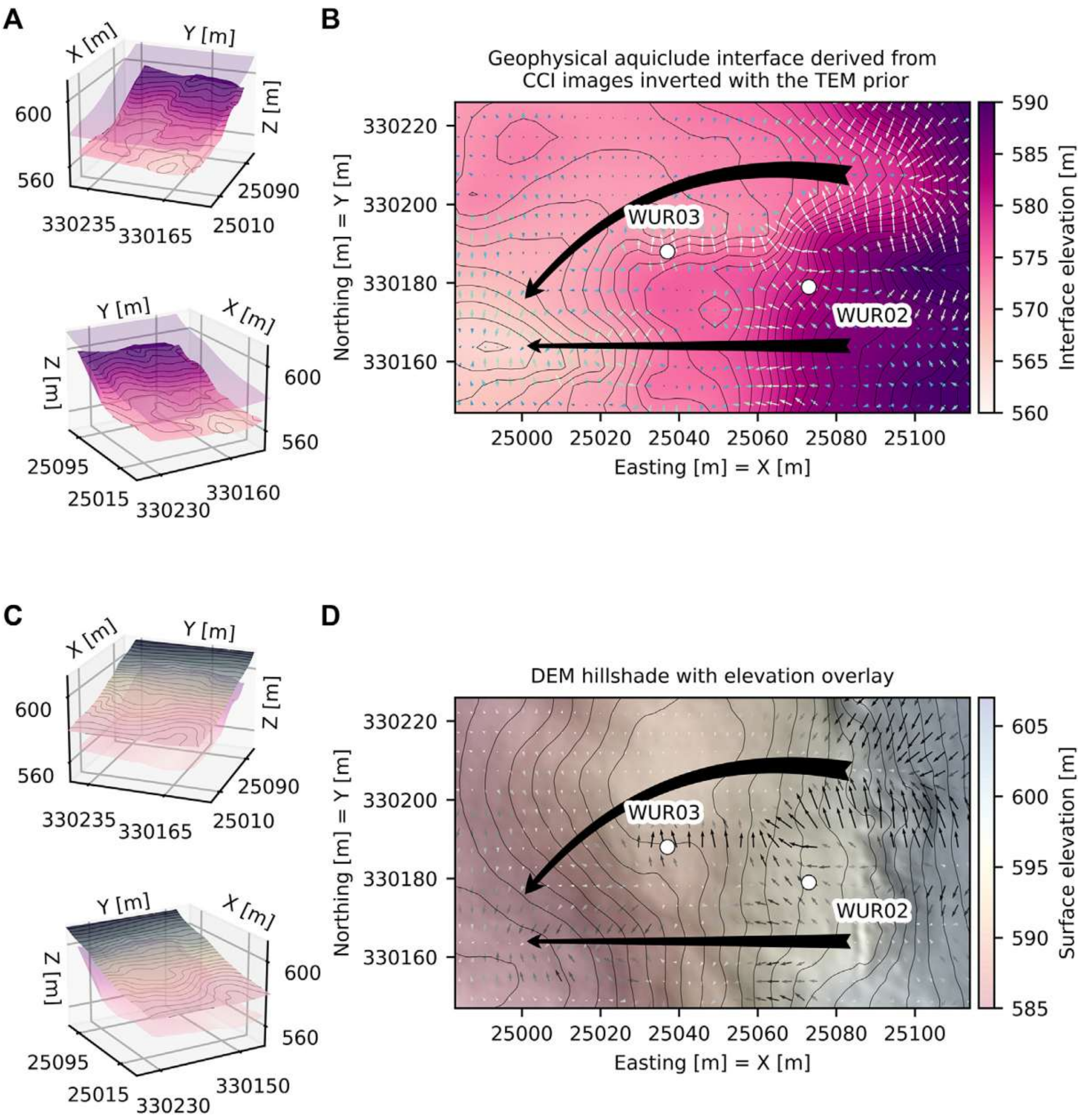

Figure 5.11: Aquiclude interface derived from combination of CCI (using the TEM reference model) and RST in (A) 3D representation (grey shading indicates the DEM) and (B) as map with the corresponding gradient vector magnitudes (small regularly distributed and color-coded arrows) and interpreted preferential water-flow paths (black arrows) superimposed on it. (C) and (D) present the corresponding 3D view and map of the color-coded surface topography, again superimposing both the gradient vectors magnitudes and preferential flow paths from the aquiclude map.

5.5 Discussion

Figure 5.10 and Figure 5.11 demonstrate the ability of the geophysical data to recover subsurface heterogeneity regarding the variations in textural parameters. We propose the combination of geophysical data with Rosetta for the estimation of subsurface hydraulic conductivity in an imaging framework. However, to properly evaluate the accuracy of our approach, it is necessary to compare the estimated values with independent data. To this end, we evaluate here the textural parameters estimated at the position of the borehole WUR04, where ground-truth data is available but was not used for the calibration of petrophysical parameters conducted above.

Figure 5.12 shows the complex conductivity and seismic velocity extracted from the inversion results (obtained for WD4 and WS1) and the predicted soil fractions at the location of WUR04 as well as borehole data (grain size of recovered samples, natural gamma radiation and conductivity logging). The geophysical data was obtained from an extraction box with a width of 1.5 m. For the prediction of textural parameters, we computed the moving average of the quadrature 1D profile (σ''). This is due to the higher amount of data points in the extraction box near to the surface scattering over a larger range than values at depth. The higher amount is stemming from the denser discretization of the inversion grid in the vicinity of the electrode locations.

For the predicted soil fractions, we observe a good agreement for the gravels, especially at the depth of 7.5 m, where both the predicted and the measured grain size indicate a fraction of gravel of 50%, with the content of coarse materials decreasing at 12.5 m depth, and becomes negligible at a depth of 16 m. The predicted fraction of silt below 12.5 m depth is in line with the measured values in soil samples; however, our model appears to slightly overestimate the silt content (approx. 10%) for the sandy gravels at 7.5 m depth. Accordingly, our model predicts ca. 10% less sand content for the layer at 7.5 m depth. The prediction of clay content reveals a constant value of 5% from the surface to a depth of ~13 m, where it increases to a value of 20%, which is in agreement with the values reported from the analysis of samples. However, the clay-rich layer (clay > 85%) at 4.5 m is not resolved in our prediction. As previously mentioned, in our correlation function (Equation 5.8) we decided to exclude large clay fractions related to kaolinite, as they seem to be clustered in a single location. Accordingly, our approach is not able to predict clay fractions larger than 20%. Considering that such high clay contents are only rarely observed, the approach proposed represents the best compromise to simplify our model linking the polarization response (σ'') and the textural parameters.

The predicted K_s profile presented in Figure 5.12 shows intermediate values ($K_s \sim 5 \times 10^{-6}$ m/s) between (roughly) 0.5 and 4 m depth, where the seismic velocity data shows maximum values around 700 m/s corresponding to a coalbearing clay layer occurring at this depth. The velocity maximum likely indicates a higher degree of compaction for the clay layer, in turn explaining the low hydraulic conductivity values resolved. Below 4 m depth, our prediction shows the largest values ($K_s >$

5×10^{-6} m/s) associated to sandy gravels (gravel fraction 50%) down to a depth of 12 m and a smooth transition to slightly lower values ($K_s < 2 \times 10^{-6}$ m/s) for the silt layer (with a combined clay and silt content above 75%) below 12 m depth. Moreover, below 12 m depth the seismic velocity increases from 600 m/s to 1,000 m/s, which indicates an increase in compaction, in agreement with the estimated K_s values. Between 10 and 12.5 m depth, the estimated K_s indicates a slight decrease that could be related to a clay-rich lens. Although no analysis was conducted on samples of this particular location, the natural gamma indicates a significant spike at this depth, similar to the one associated to the coalbearing clay layer mentioned above, therefore sustaining the resolved change in the K_s values.

Besides the evaluation of our estimations with independent data from borehole WUR04, we also compare our estimated K_s prediction with hydraulic conductivity values computed using existing $\sigma'' - K_s$ relationships. Such relationships have been obtained from laboratory studies where both the complex conductivity and the hydraulic conductivity have been measured in small samples, yet in fully saturated conditions. In particular, we compare our K_s values to those computed with the model by Slater and Lesmes (2002a) and the one proposed by Weller et al. (2015). The former is based on a Hazen-type equation (Price et al., 1911), and can be written as:

$$K_{s,SL} \approx 0.0002\, \sigma''^{-1.1}. \tag{5.11}$$

In their study, Weller et al. (2015) investigated 38 unconsolidated soil samples, demonstrating an inversely linear correlation between σ'' and the permeability k for data collected at 1 Hz. Such model can be written as (Weller et al., 2015):

$$k^*_W \approx \frac{2.14 \times 10^{-14}}{\sigma''^{2.04}}. \tag{5.12}$$

In this study we used a dynamic viscosity ($\mu = 0.0010518$) and density ($\rho = 998.59$) for water at 18°C and an acceleration due to gravity ($g = 9.8073$) to transform the permeability values k^* to hydraulic conductivity values $K_{s,W}$. For the sake of completeness, we also computed the hydraulic conductivity values using the model by Revil and Florsch (2010), which also links the imaginary component σ'' to hydraulic conductivity, based on the relationship written as:

$$K_{s,RF} \approx \frac{\rho_w g\, (C^S)^2 \sigma''^{-2}}{\mu\, 4.5 F^3}. \tag{5.13}$$

in which C^S is the specific conductance of the Stern layer assumed equal to 4×10^{-9} and

F the electrical formation factor describing the ratio between tortuosity and porosity (Katz and Thompson, 1987). Following the approach by Weller et al. (2010), we used a first order approximation for the computation of F based on the ratio of the bulk conductivity (σ_0) to fluid conductivity (σ_w), such as

$$F = \frac{\sigma_w}{\sigma_0}. \tag{5.14}$$

In our case, σ_0 was given by the real component of the complex conductivity (σ') and σ_w to three different values equal to 19, 35 and 60 mS/m, corresponding to values observed in monitoring stations around the study site. The comparison of the different K_s predictions is presented in Figure 5.13.

$K_{s,SL}$ estimates are consistent to those predicted by our approach; however, $K_{s,SL}$ values fluctuate around 1×10^{-6} m/s, representing one order of magnitude smaller than our predictions. Actually, vertical variations of the $K_{s,SL}$ values are identical down to a depth of 10 m, for the unconsolidated materials with coarse grains. At this depth $K_{s,SL}$ monotonously decreases with depth; whereas our prediction shows two peaks, one related to high hydraulic conductivity values (between ~12 and 14 m depth) and the lowest values resolved between 16 and 17.5 m depth corresponding to the clayey silt layer. Since the $K_{s,SL}$ estimation is a direct function of σ'', it can only capture the dynamics resolved in the σ'' distribution. In this regard, the mismatch between the two estimates below 10 m depth is due to the two-step approach proposed, where the polarization values (σ'') are used first to estimate the soil fractions, which are subsequently included in Rosetta for the K_s predictions. On the opposite, the $K_{s,SL}$ model uses a single-step approach, where the polarization is inversely related to the hydraulic conductivity as presented in Equation 5.11. Binley et al. (2016) also noted that sites with relatively low contrast in K are expected to exhibit low structural resolution of the complex conductivity distribution. In this regard, our approach permits to resolve for a larger dynamic in the predicted hydraulic conductivity values as these are estimated from the soil fractions and not directly from the inverted complex conductivity.

The use of the model proposed by Weller et al. (2015) shows a larger range of hydraulic conductivity values (between 2.2×10^{-6} and 6×10^{-4} m/s). However, such variability cannot easily be understood in the study area, where high contents of fine grains are also observed in the top layer. Moreover, the $K_{s,W}$ cannot resolve for the increase in the hydraulic conductivity resolved at the contact between the silt sand and the silt (ca. 13 m depth). Similar to the approach by Slater and Lesmes (2002a), the model by Weller et al. (2015) is only related to the changes in the polarization

(σ''); thus, it is not sensitive to changes in the grain size underlying our approach. We believe that discrepancies in the values obtained between the $K_{s,SL}$, $K_{s,W}$ and our approach are mainly due to the use of fitting parameters that cannot be extrapolated from laboratory to field scale, where large heterogeneities dominate, in contrast to well-sorted laboratory samples. In this case, our approach offers the possibility to experimentally fit the hydraulic conductivity to the polarization response through Rosetta and, thus, consider subsurface variations and existing ground truth. Moreover, it needs to be taken into account that the models by Slater and Lesmes (2002a) and Weller et al. (2015) are based on measurements in fully saturated samples, whereas our measurements are conducted in materials with varying water content. In this regard, the applicability of the $K_{s,SL}$ and $K_{s,W}$ models may be hindered for field investigations in slopes characterized by clay rich sediments, where water flow rather occurs along preferential water flow paths. We also note here that laboratory measurements of the CC are commonly conducted on small soil samples; thus, unable to capture the response due to the presence of coarse sediments as those observed in our study area.

Albeit the discrepancies observed in Figure 5.13, the three methods (Slater and Lesmes, 2002a; Weller et al., 2015) and our approach) solve for the same maximum between 7.5 and 10 m depth, which corresponds to the gravels and the low polarization response. For the sake of completeness, we also present estimated values using the model proposed by Revil and Florsch (2010) based on the polarization of the Stern layer. Such model results in hydraulic conductivity values much lower than the rest of the predictions. Such discrepancy may be explained by the rough estimation of the formation factor due to the lack of more detailed information. It seems that the crude approximation, based on the ratio of the fluid-to-bulk conductivity (Equation 5.14), fails to solve for adequate F values, resulting in inaccurate estimations of the hydraulic conductivity. In this regard, the use of equations with less parameters (e.g., the one by Slater and Lesmes (2002a) provides clear advantages for field investigations. Accordingly, our approach permits to estimate hydraulic conductivity based solely on geophysical data and grain size analysis, which is one of the common measurements in landslide investigations. Further methods requiring measurements of the formation factor, or other parameters may be limited to areas where such information is available.

As previously stated, Rosetta can only be applied to SSC data and therefore the initial set-up did no incorporate training data containing gravel fractions. Further studies may investigate the use of more complex PTFs that permit the incorporation of the gravel fraction. However, originating from soil science, most readily available PTFs are restricted to SSC only (Van Looy et al., 2017a). Hence, we believe that our approach offers a flexible tool able to quantify hydraulic conductivity variations at the field-scale based on complex conductivity imaging results. It is important to note that the use of the complex conductivity permits to explicitly take the surface conductivity into account, which may explain high conductivity values in clayey areas. Hydraulic estimations based only on real-valued electrical resistivity, may fail to account for surface conductivity, misinterpreting clay rich formations as areas with high water content. The application of the two-step approach proposed here (first the soil fraction and only then the K_s values) seems to account for existing ground truth data, for subsurface heterogeneity as well as variations in the geophysical properties (complex conductivity and to certain extent seismic velocities). Therefore, our approach may represent a step forward in the upscaling of the relationship between σ'' and K that has been observed in different investigations (see Kemna et al., 2012).

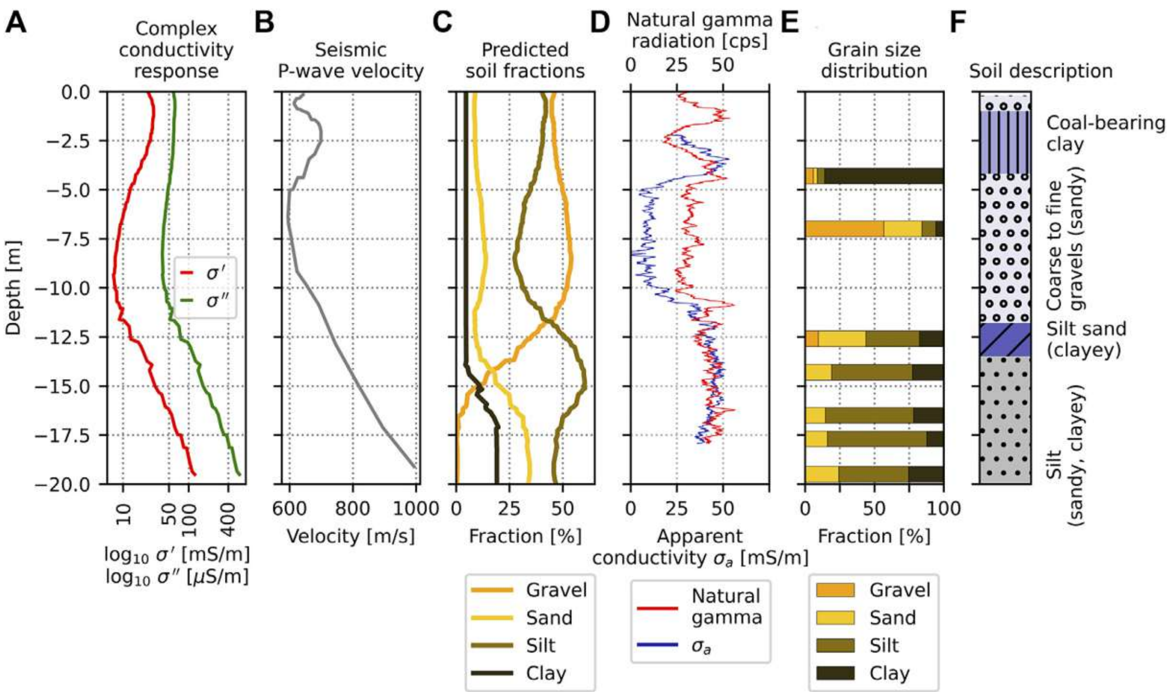

Figure 5.12: Comparison of ground-truth information, complex conductivity response and predicted parameters: (A) complex conductivity response in terms of real σ' and imaginary component σ'', (B) seismic p-wave velocity and (C) the predicted soil fractions (gravel, sand, silt and clay). (D) presents the natural gamma radiation and apparent conductivity σ_a measured with a Dual induction probe inside the borehole WUR04 and (E) grain size distribution, and (F) soil description for samples retrieved from sediments during drilling in WUR04.

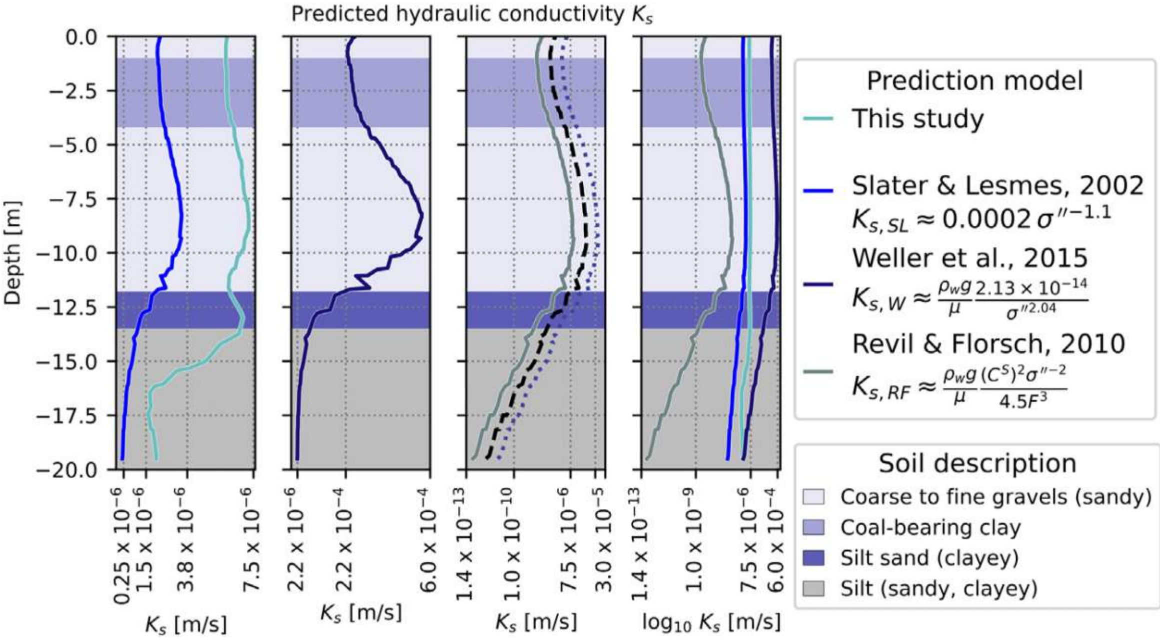

Figure 5.13: Predicted hydraulic conductivity K_s using our approach (cyan) and the relationships by Slater and Lesmes (2002b) (blue), Weller et al. (2015) (dark blue) and Revil and Florsch (2010). The dotted, dashed and solid line refer to formation factors computed for fluid conductivity values of 19, 35, and 60 mS/m. The color-coded backgrounds indicate the textural units.

5.6 Conclusion

We have shown that complex conductivity imaging permits to solve for changes in electrical properties consistent with lithological contacts recovered from boreholes. The lithological units resolved in our study correspond to, from top to bottom: a layer with moderate conductivity values ($5 > \sigma' < 30$ mS/m) and an average thickness of 15 m on top of a conductive bottom layer ($\sigma' > 30$ mS/m). This model is supported by information about electrical units, as obtained from TEM soundings, and RST imaging results. The extensive complex resistivity data permitted to construct a 3D subsurface model, which is then used to delineate the geometry of an aquiclude as well as preferential water-flow paths within the slope. Based on the spatial variations of the hydraulic conductivity (K_s) solved, we can also identify a spatial correlation between the aquiclude interface and the morphological features. In this regard, our hydrogeophysical model offers a possibility to design adequate measures to attenuate build-up of pore-pressure along preferential flow paths that may trigger landslides.

We present a quantitative interpretation of the complex conductivity images, using both soil-textural data and well-logging information. Within this study we derive site-specific petrophysical relationships that link the imaginary complex conductivity to the fractions of gravel, silt and clay. These well-determined relationships – with R^2 scores of 0.71 for gravel, 0.87 for silt and 0.81 for clay – permitted to estimate the textural properties of the resolved geophysical units, which were found consistent to grain size distribution measured in soil samples recovered from core drilling. The textural information was used in the Rosetta pedotransfer function to predict K_s from the complex conductivity imaging results. Hence, an estimation of hydraulic conductivity values was obtained for the entire study area.

The application of the two-step approach proposed here (i.e., first the soil fraction and then the K_s values) provides comparable values to those computed using existing petrophysical equations developed from laboratory investigations. Such petrophysical equations consider the polarization response at 1 Hz yet are based on measurements typically performed on small, well sorted samples under fully saturated conditions. Therefore, those equations may be limited in field applications, associated to large degrees of heterogeneity and variations in water content. Hence, the approach proposed here permits to derive K_s based solely on available data, namely complex conductivity and grain size distributions, without the need to upscale petrophysical equations resolved in the laboratory.

Appendix

Additionally to the saturated hydraulic conductivity K_s the Rosetta PTF (Schaap et al., 2001; Zhang and Schaap, 2017) predicts the parameters of the van Genuchten water retention function (van Genuchten, 1980):

$$\theta(\psi) = \theta_r + \frac{\theta_s - \theta_r}{[1 + (\alpha|\psi|)^n]^{1-1/n}} \tag{5.15}$$

in which $\theta(\psi)$ is the water retention curve in $\mathrm{cm^3 cm^{-3}}$ as a function of soil water pressure ψ, θ_r and θ_s are the residual and saturated water contents in $\mathrm{cm^3 cm^{-3}}$ and n (dimensionless) and α (1/cm) are curve shape parameters. Figure 5.14 shows the predicted van Genuchten parameters for the profile WD13 and the soil texture that was used as input for Rosetta.

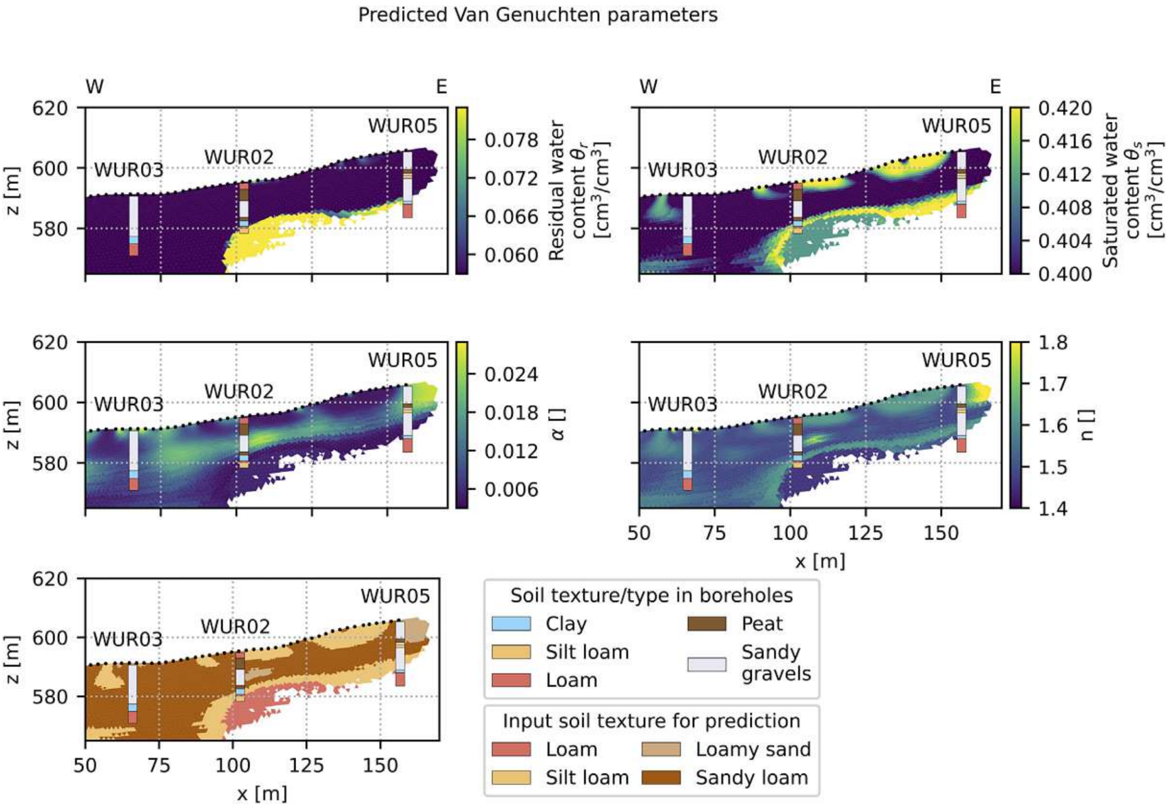

Figure 5.14: Van Genuchten water retention parameters for the profile WD13 as predicted with Rosetta (Zhang and Schaap, 2017) using the soil texture presented in the bottom subplot. Each subplot further contains the soil texture observed in the boreholes WUR02, WUR03 and WUR05

6 From electrical conductivity to hydraulic conductivity: a multi-step framework using electromagnetic induction imaging and deep learning[1]

6.1 Introduction

Frequency-domain electromagnetic induction (FDEM) methods are currently applied in the field of hydrogeophysics (e.g., Binley et al., 2015, and references within), as they can provide a cost-effective investigation of subsurface properties controlling water-flow dynamics, such as pore structure and water content (e.g., Boaga, 2017, and references within). Initially, FDEM methods were mainly used to obtain dense maps of apparent electrical conductivity (ECa) (e.g., Lesch et al., 1995)), which were interpreted as lateral variations in soil properties (for example Robinson et al., 2009; Martinez et al., 2010; Doolittle and Brevik, 2014b, and references within). With the development of multi-configuration FDEM instruments (i.e., multicoil and multifrequency tools), simple field procedures allow simultaneous collection of data with sensitivity at different depths. Together with modern inversion strategies, it is possible to compute electrical conductivity (EC) maps at different depths (e.g., Auken et al., 2015; Heagy et al., 2017; McLachlan et al., 2021a).

Most of the current inversion strategies adopt either linear (McNeill, 1980b) or nonlinear Maxwell-based forward models (e.g., Hendrickx et al., 2002; Schultz and Ruppel, 2005; Brosten et al., 2011; Deidda et al., 2020). Deterministic inversion algorithms have been proposed (Deidda et al., 2020; Klose et al., 2022) aiming to solve the inherent ill-posed inverse problem, characterized by the non-uniqueness of the obtained conductivity model (Zhdanov, 2023). To stabilize the solution, such inversion algorithms commonly rely on smoothness-constraint regularization, where overfitting the data is minimized by searching for a solution with smooth changes in space. Alternatively, probabilistic approaches (e.g., Minsley, 2011; Moghadas et al.,

[1]This chapter is based on: Gallistl, J., Roser, N., Strauss, P., Blöschl, G. and A. Flores-Orozco. "From electrical conductivity to hydraulic conductivity: A multi-step framework using electromagnetic induction imaging and deep learning". Submitted to: *Water Resources Research*.

2017)) have also been suggested to estimate the distribution of EC values without relying on smooth-constraint approaches and compute the associated uncertainty of the final model. A novel deep learning (DL) inversion strategy based on convolutional neural networks (CNN) was proposed by Moghadas, 2020. The DL approach allows for rapid estimations of subsurface conductivity and is more computationally efficient than the classical (deterministic, probabilistic) inversion approaches. Moreover, the suggested DL approach is not subject to the non-uniqueness of classical inversion frameworks (Moghadas, 2020). Building upon these advancements in FDEM inversion methods, researchers have explored various applications in hydrogeophysics, including the investigation of pore water and salt dynamics in different environments (Robinson et al., 2009; Martinez et al., 2010; Jiang et al., 2016; Martini et al., 2017b), soil texture (Abdu et al., 2008; Triantafilis and Lesch, 2005), and peat thickness (Boaga et al., 2020; Beucher et al., 2020). Moreover, Brosten et al., 2011 reported a correlation between co-located hydraulic conductivity K measurements and inverted EC values obtained from FDEM data. Their empirical relationship was then used to produce a dense K map for their study area. Similarly, Uhlemann et al., 2022 established a relationship between measured saturated K (K_s) values and EC, which they used to identify ground water recharge and flow in a managed aquifer system. While significant developments have been made in the instrumentation (Heil and Schmidhalter, 2015; Wolf and Flores Orozco, 2024; Blanchy et al., 2024), field procedures (Christiansen et al., 2016; De Smedt et al., 2016; Tazifor et al., 2022) and inversion of FDEM data (Deidda et al., 2020; Klose et al., 2022), there is still a gap regarding the quantification of hydraulic properties from inverted EC maps at different depths.

To address this research gap, we present extensive FDEM data collected across 66 ha of the Hydrological Open Air Laboratory (HOAL). The objective of the survey was to quantify spatial changes in the hydraulic properties of the soil controlling surface-groundwater interactions. The proposed approach is based on three steps: (1) the inversion of FDEM data to obtain continuous EC maps at different depths, (2) correlation of EC and soil-textural information in terms of the soil volume fractions of sand, silt and clay; followed by the (3) quantification of hydraulic conductivity K using a pedotransfer function (PTF). We recalibrate the field-scale PTF proposed by Picciafuoco et al., 2019a, which is based on double-ring infiltration measurements and incorporate the soil-textural predictions obtained in step (2). For the inversion of the FDEM data, we investigate the potential of a deep learning network for the prediction of 1D EC depth models. Large-scale, detailed information about soil-textural properties is essential for the vulnerability assessment of groundwater from fertilizer and pesticide application as well as yield and erosion estimation, whereas detailed knowledge about the hydraulic conductivity is prerequisite for enhancing our understanding of the mechanisms controlling rainfall-runoff processes and groundwater recharge. Given the simplicity and scalability of the proposed approach, it presents a significant advancement towards understanding catchments such as the HOAL.

6.2 Material and methods

6.2.1 Study area

All experiments were conducted in the Hydrological Open Air Laboratory (HOAL), which is a 66 ha research catchment located in Petzenkirchen, Lower Austria (48° 9′ N, 15° 9′ E). Designed for advanced hydrological studies and experiments, it serves as an observatory for understanding water-related flow, runoff generation, and transport processes involving sediments, nutrients, and microbes and fosters interdisciplinary research (Blöschl et al., 2016). It is characterized by gentle slopes with elevations between 268 to 323 m asl, and a mean slope of 8%. The majority of the land is used for agriculture (87%), with the remainder being made up of woods (6%), pasture (5%), and paved areas (2%). A high-voltage power line, many electricity lines linking farmhouses, and a gas pipeline all traverse the catchment, as presented in Figure 6.1.

The soil textural composition of the catchment was mapped during a comprehensive soil survey that included sampling at 300 locations, distributed on a 50 by 50 m grid (Picciafuoco et al., 2019a). Samples were taken at each location at varying depth ranges (2–3), with a maximum depth of 0.7 m and provided information about volume fractions of organic matter (f_{OM}), clay (f_c), silt (f_{si}), and sand (f_{sa}). The soil survey revealed that the catchment is characterized by heavy soils with silty loam (75%) predominating, followed by silty clay loam (20%) and silt (5%). In addition to the soil survey, the textural composition can be found, where a piezometer station was drilled (P21 in Figure 6.1).

6.2.2 Frequency-domain electromagnetic methods (FDEM)

Electromagnetic induction imaging (EMI) at the low induction number is a FDEM method that uses a sensor system to generate a primary magnetic field by applying an alternating current to a transmitter coil with a fixed frequency. This generates eddy currents in a conductive subsurface, which then generate a secondary magnetic field sensed by the receiver coil. The separation between transmitter and receiver, as well as the excitation frequency are fixed in the instrument to permit an operation at the low induction number (LIN) ($\beta \ll 1$), at which the measured response is only controlled

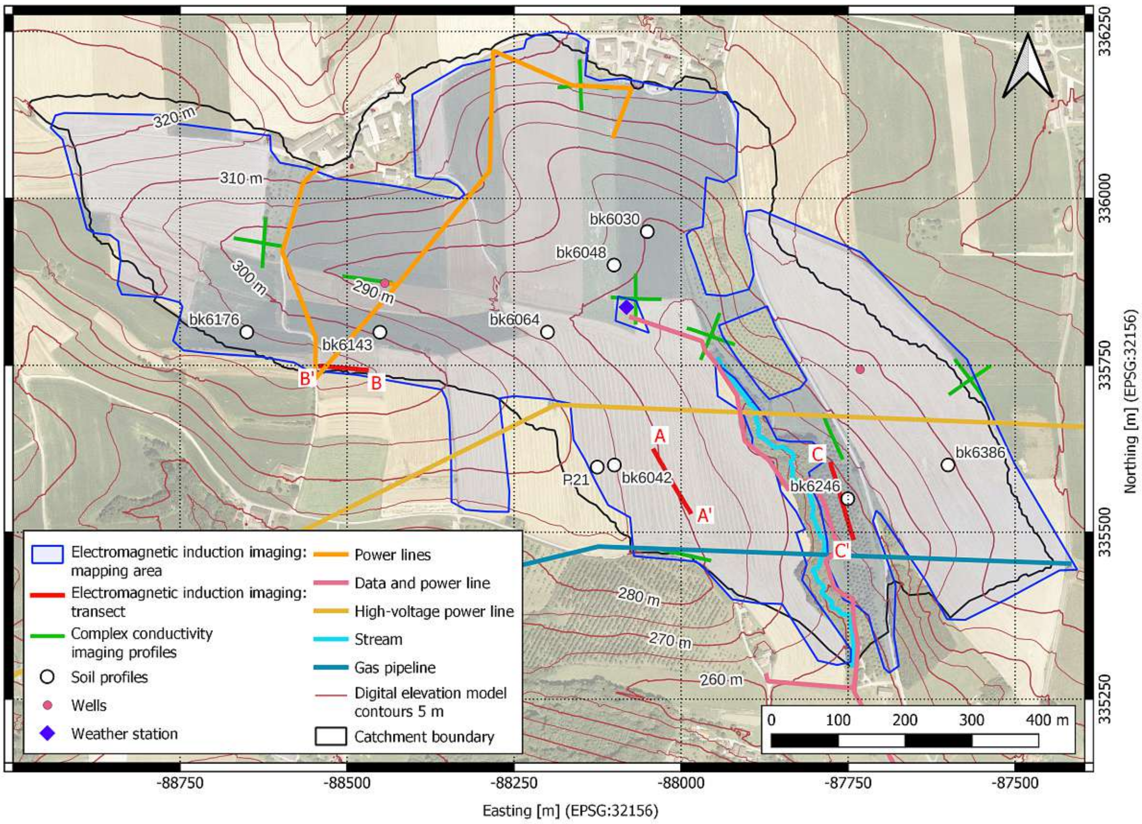

Figure 6.1: General overview of the catchment, installations on site, areas mapped with electromagnetic induction imaging (EMI), and location of complex conductivity imaging (CCI) profiles used to generate the training data (see Appendix 6.5). Moreover the location of extracted soil profiles, as well as EMI transects later used in the evaluation of the presented approach are shown.

by the electrical properties and EC can directly be computed from the ratio between the secondary and primary magnetic field (McNeill, 1980b). In case of heterogeneous materials, i.e., field measurements, the data recorded is then the apparent electrical conductivity (ECa). The induction number for a given system is defined by (McNeill, 1980b):

$$\beta = \frac{r}{\sqrt{\frac{2}{\omega\mu\sigma}}} \tag{6.1}$$

in which ω is the angular frequency of the primary field, r is the separation between the transmitter and receiver coils, μ is the magnetic permeability, and σ is the bulk electrical conductivity of the earth. The transmitter and receiver coils can be oriented horizontally (horizontal coplanar, HCP) or vertically (vertical coplanar, VCP) with respect to the ground surface, and modern commercial instruments typically provide ECa for different depth ranges (i.e. multicoil systems).

Electromagnetic induction measurements were conducted using a CMD-MiniExplorer (GF Instruments), which employs three receiver coils with distances of 0.32, 0.71, and 1.18 m from the transmitter coil simultaneously at an operating frequency of 30 kHz. The VCP mode was utilized for all measurements, providing nominal depth of investigations of 0.5, 1, and 1.8 m. The sensor was positioned as close to the ground as possible, oriented parallel to the direction of walking (approximately between 0.1-0.25 meters). The sampling frequency was 1 Hz, resulting in ECa values being collected approximately every 0.25 meters along the walking tracks. The measured apparent conductivity values were georeferenced using a RTK-GNSS and the mapped areas are presented in Figure 6.1. The dataset comprises approximately 103,600 ECa readings and was completed within three days. At least 10 minutes prior to data collection the sensor system was assembled and turned on to equilibrate the system. Preprocessing of the dataset included (1) the removal of negative ECa values and (2) the removal of obvious outliers. The outliers were defined as ECa readings that either exceeded the mean ECa plus three times the standard deviation of the dataset or were smaller than the mean ECa minus three times the standard deviation of the dataset. Both processing steps were performed for each of the three available VCP readings separately.

6.3 Deep learning (DL) for 1D EMI inversion

Deep learning (DL) networks are foundational to the field of artificial intelligence, providing the means to solve complex tasks such as classification and regression (Li et al., 2019; Shrestha and Mahmood, 2019; Mohammadi Foumani et al., 2024). These networks consist of a series of different layers, including an input layer, one or multiple hidden layers, and an output layer. Each layer features a number of predefined neurons and each neuron in one layer can be connected to all neurons in the subsequent layer. For a DL network to be able to learn intricate patterns, non-linearity has to be introduced in the form of non-linear activation functions that can be specified for each neuron in each layer individually. Given an adequate choice of the activation function, the hidden layers are able to perform the majority of the computational processing through a series of transformations. The term hidden layer stems from the fact that their output is typically not visible to the user. Finally, the output layer provides the final predictions or classifications (Li et al., 2019; Mohammadi Foumani et al., 2024; Ismail Fawaz et al., 2019).

6.3.1 DL network structure

The objective is to design a DL network that enables the prediction of 1D EC depth models from multi-configuration ECa, in this particular case, only from VCP readings similar to the implementation by Moghadas, 2020. The input of such a network is then a $[3 \times 1]$ vector, or more correctly, a tensor ($I = [\mathrm{ECa}_{VCP,1}, \mathrm{ECa}_{VCP,2}, \mathrm{ECa}_{VCP,3}]$) and the output is an $[n \times 1]$ tensor ($X = [\mathrm{EC}_{D_1}, \mathrm{EC}_{D_2}, ..., \mathrm{EC}_{D_n})$, where n denotes the number of specified depth layers. The network presented here consists of three subnets (termed Subnets 1 to 3 in Figure 6.2) that are linked by a forward computation. The forward computation involves calculating the VCP and HCP responses for the given outputs, that is, the EC depth model, of the previous subnet. Hence, the input of the following subnet is the forward-modelled output of its predecessor. We use the linear cumulative sensitivity forward model with LIN approximation (McNeill, 1980b), as presented in Appendix 6.5. Figure 6.2 shows that subnets 1 to 3 consist of two fully connected hidden layers (denoted as Dense 1 to 3) with six neurons each. To introduce the required non-linearity, each neuron in the hidden layer uses a rectified linear unit (ReLU) layer as activation function (Puzyrev, 2019; Banerjee et al., 2019). The output layers in each subnet are also fully connected dense layers; however, they do not incorporate activation functions. What changes in each subnet are the size of the input and output tensors, for instance, for subnet 1, we have an input of $[3 \times 1]$ and an output of $[4 \times 1]$, meaning that three VCP readings predict a 4-layered EC model, whereas in subnets 2 and 3, the sizes of both the input and output tensor increase. As shown in Figure 6.2 the inputs for subnets 2 and 3 increase to $[6 \times 1]$ tensors consisting of the forward modelled VCP and HCP responses of the previous subnet. Furthermore, subnets 2 and 3 increased their output tensors to EC depth models with six and 12 layers, respectively. The final output of the DL network is an EC depth model comprising 12 layers. Moreover, intermediate output results, that is, the EC depth models with 4, 6, and 12 layers, referring to subnets 1 to 3, can be obtained. The network was implemented in Python using the open-source libraries Tensorflow (Martín Abadi et al., 2015; Abadi et al., 2016) and Keras (Chollet et al., 2015) and is available on GitHub (https://github.com/TUW-GEO/emiAI).

6.3.2 Generation of training datasets

For any neural network to work properly the selection of adequate training datasets, describing the problem or characteristics of the objective at hand, is essential. In this regard, utmost care was taken in the design of the generation workflow for the training datasets. We refrained from generating completely random datasets with specified

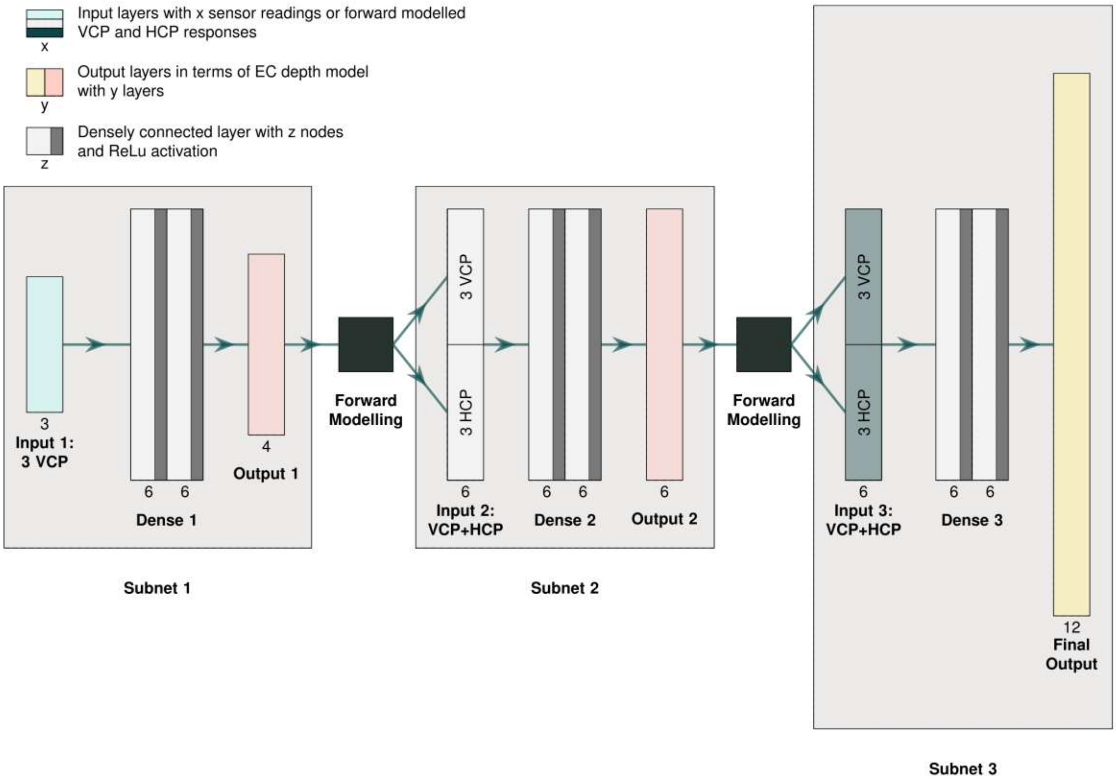

Figure 6.2: Structure of the deep neural network consisting of three subnets. The network permits the prediction of 12-layer EC model from the three VCP ECa values typically measured in the field.

upper and lower EC limits as proposed by Moghadas, 2020 and others. Instead we used selected inverted conductivity sections from electrical profiles collected using complex conductivity imaging (CCI) to guide the generation process. All details on the CCI data collection, processing and inversion are presented in Appendix 6.5. In the following, we discuss the different steps of the workflow, namely: (1) sampling of the conductivity sections at random locations for a given depth and width (cf. different depth models in Table 1), (2) binning of the extracted EC values for a given depth model (e.g., 12 layers), (3) pseudo-random generation of EC depth models based on the binning results, and (4) forward modeling to obtain the VCP and HCP readings.

The major assumption of this workflow is that the EC sections obtained from the inversion of the CCI data properly describe the characteristics of the near-surface EC distribution in such a manner that it can be used as a guide in the generation process. Although the spatial scale might be different, we assumed that a data-driven starting point in the generation process is better suited than generating completely random models without any relation to the study area. Following this notion, for each of the available EC sections, we randomly selected 5-10 locations, where the EC was

Table 6.1: Layer thicknesses of the three different EC depth models with 12, 6 and 4 layers used in the DL network.

Number of layers	12		6		4	
Layer	From [m]	To [m]	From [m]	To [m]	From [m]	To [m]
D_1	0.00	0.12	0.00	0.25	0.00	0.37
D_2	0.12	0.24	0.25	0.50	0.37	0.75
D_3	0.24	0.36	0.50	0.75	0.75	1.12
D_4	0.36	0.48	0.75	1.00	1.12	1.50
D_5	0.48	0.60	1.00	1.25		
D_6	0.60	0.72	1.25	1.50		
D_7	0.72	0.84				
D_8	0.84	0.96				
D_9	0.96	1.08				
D_{10}	1.08	1.20				
D_{11}	1.20	1.32				
D_{12}	1.32	1.50				

extracted at a specified depth and extraction width (Figure 6.3a). The latter was selected as 1.5 times the mean electrode spacing ($\sim$ 1.5 m), which was found to be a width large enough to provide sufficient samples for the binning process. The random location sampling integrated a check that the extraction boxes did not overlap over half of their size. Furthermore, low-sensitivity areas at the model boundaries were excluded from the selection process.

Given one of the specified depth models, the EC values were binned, where binning comprised the computation of the mean EC and the corresponding standard deviation in each bin. The grey bounding boxes in Figure 6.3b illustrate the bounds defined by two times the standard deviation in each bin. The obtained binned model (Figure 6.3c) is now the starting point for the generation of pseudo-random models. This generation is termed pseudo-random, because it implements some design choices, as discussed below. Gap filling of the standard deviations and EC model values is performed, that is, for the case where no values are inside the bin, the median value of all bins is computed and assigned. This applies to both EC and standard deviation. To provide a smooth model without spikes and sharp edges, the model is then smoothed by applying a moving average filter with a smoothing window of three bins. This applies only to the EC values. Commonly, the first bin often has a much larger standard deviation than the other bins, due to larger model variations adjacent to the electrode locations. To restrict this large variation in the top layer, the standard deviation is downscaled by a factor of 0.35. The same applies to the deepest layer, where we downscale the standard deviation by a factor of 0.1 to restrict large variations in the deepest layer.

By computing the difference between adjacent values we determines the direction in which the new model is allowed to change. If there is a sign change, the direction reverses. The last layer is not allowed to change direction and follows the direction of the layer above it. The so computed direction refers to forward direction. To increase the number of possible models and freedom in the training datasets, new models are computed in reverse direction, which is specified by inverting the sign changes in the forward direction (Figure 6.3d). To allow more freedom in the generation of the models, we specify an exaggeration factor that scales all standard deviations (in both directions) by a factor of seven to increase the bounds in which the model can vary.

For each bin, sampling from a truncated normal distribution, centered around the median value in the bin and truncated by the exaggerated standard deviations is performed in the forward and reverse directions for a specified number of models. To handle values outside the sensible range, we introduce some hard boundaries ($0.1 >$ EC < 1000 mS/m) and restrict the values for which the sampled value would exceed such limits to stay within the chosen boundary values. Each new model is smoothed with the same smoothing operator, as described previously. As all required depth models with 12, 6 and 4 layers should represent identical sampled volumes of the CCI sections, the depth models with 6 and 4 layers were down-sampled from the 12 layer models (c.f. Table 6.1).

In total 102 locations along the 13 EC sections were sampled during the pseudo-random generation process. Combined with generating 281 new models (the binned model and 140 in each forward and reverse direction) at each sampled location, a total number of 28662 training models were obtained. The VCP readings, representing the DL input, were obtained from forward modeling using the cumulative sensitivity forward model with LIN approximation (McNeill, 1980b). All details on the forward model are presented in Appendix 6.5. During the forward modeling process, no noise was added and the layer depths for 12 layer depth model (c.f. Table 6.1) were used.

6.3.3 DL network training

Prior to training, the input and output datasets are normalized to the range between 0 and 1 and subsequently divided into three subsets: 70% for training, 15% for validation, and 15% for testing. The training subset is used to train the network, whereas the validation subset is employed to provide an unbiased evaluation of the model fit on the training dataset and can help prevent overfitting, which occurs when a model learns the training data too well, including noise and outliers, and performs poorly on unseen data (Shrestha and Mahmood, 2019). Conversely, underfitting occurs when

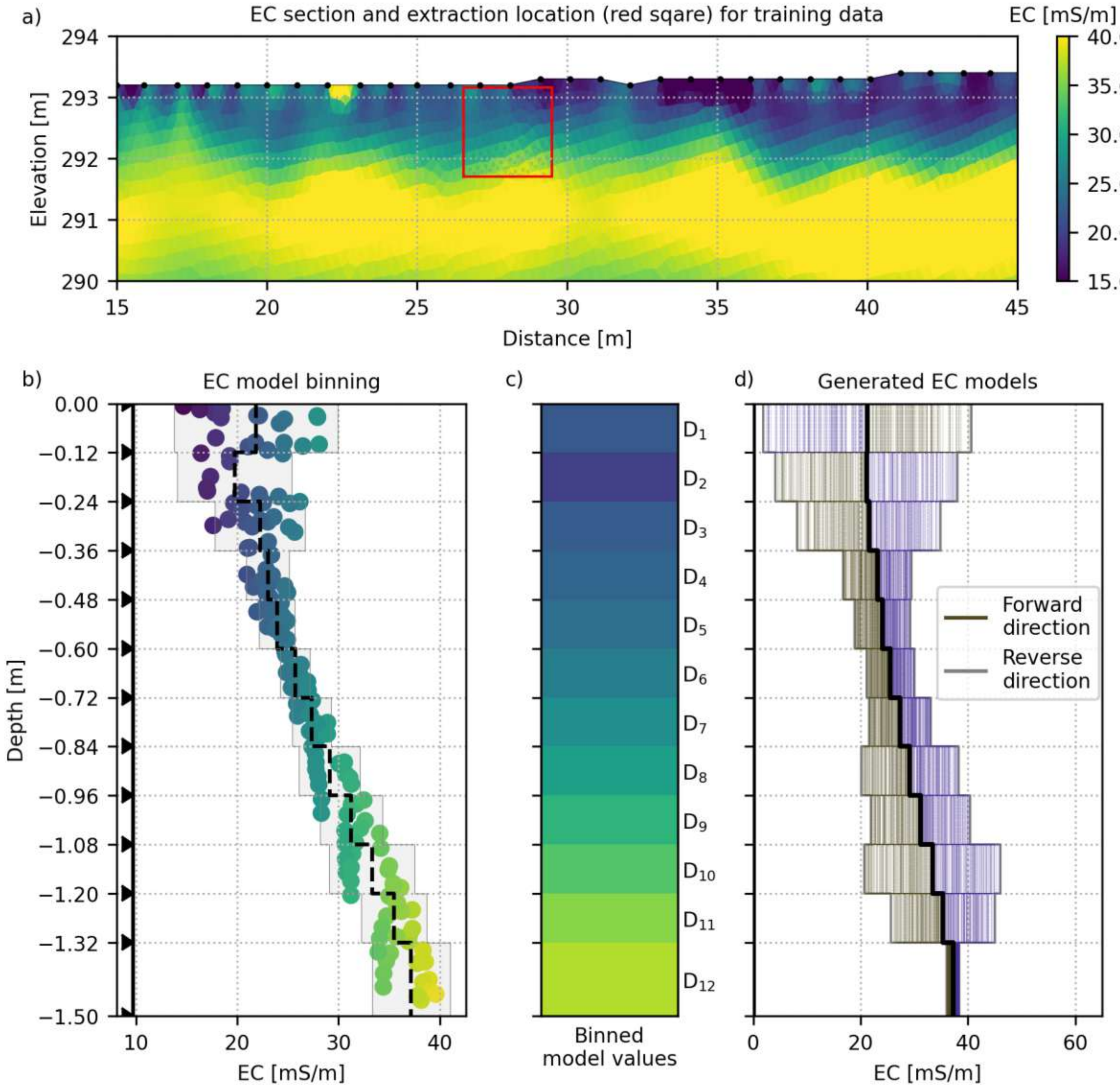

Figure 6.3: Workflow for the generation of training datasets: a) random sampling of an EC section obtained from the CC profile for a given depth, b)-c) binning of the EC values for the specified depth model, d) pseudo-random generation of EC depth models based on the binned model, and forward modeling to obtain the corresponding VCP readings (not shown).

a model is too regularized and fails to describe the underlying relationship in the dataset. The testing data, which is kept separate, is only employed after the training and validation phases are complete and permits an unbiased evaluation of the model's performance.

The networks presented herein employ RMSProp as the optimization algorithm during training (Tieleman and Hinton, 2012), utilizing a learning rate of 0.0001 and 512 epochs (iterations) and mean squared error (MSE) as the loss function which writes as:

$$\mathrm{MSE} = \frac{1}{n}\sum_{i=1}^{n}(X_t - X_p)^2. \tag{6.2}$$

n is the number of training models, X_t are the training models (X_t = [EC_{D_1}, EC_{D_2}, ..., EC_{D_n}) and X_p are the predicted models. To mitigate the risk of overfitting the training data, early stopping is implemented. In the absence of early stopping, the model trains for the entirety of the specified iterations, irrespective of improvements in model fit. As outlined above, the different subnets of the DL network are coupled by forward computation to obtain the VCP and HCP responses. Hence, the subnets were trained sequentially. Training all networks together requires several minutes (< 10 minutes: AMD Ryzen 5 5600X 6-Core Processor 3.70 GHz; 32 GB RAM), and the predictions are available instantaneously.

6.4 Results and discussion

6.4.1 Evaluating the DL network performance

The loss metrics for each subnet are presented in Table 6.2, which shows no significant mismatch between the training and validation errors, thereby indicating that the subnets did not overfit. Likewise, the testing error is within the same range of values, which indicates that the performance of the network on unseen data is likely to be similar to that observed for the training and validation sets and the network is likely to generalize well to new data. Table 6.2 shows that the loss first increases when moving from subnets 1 to 2 with an increase in the MSE from ca. 0.00079 to 0.00173 for the training set and then decreases again when moving to subnet 3 (here, the MSE for the training set is 0.00132). As the network dimensions, are identical for subnets 2 and 3, except for the output layer, this change in the loss value cannot be explained by changes in the network dimensions.

We opted for this sequence of individual subnets, as described above, as this architecture showed the most promising results in a synthetic forward modeling study (results not shown), when compared to other architectures consisting of single networks with a greater number of neurons in the hidden layers, or an increased number of hidden layers. Furthermore, convolutional neural networks (CNN), such as the implementation by Moghadas, 2020 were explored, but were not able to reach the performance of the network presented here. We note here, that more sophisticated network architectures, such as Auto-encoders (Li et al., 2020a; Wu et al., 2022b), recurrent neural networks

(Wu et al., 2022a; Gan et al., 2024) or physics-driven deep learning (Guo et al., 2023; Wu et al., 2024) exist and are being actively investigated in the scope of airborne EM. However, we did not explore their potential in this manuscript.

Figure 6.4 shows the EC sections obtained from the prediction with the DL network (top) and deterministic inversion with EMagPy (McLachlan et al., 2021a) (bottom) for three sections distributed in the study area. Details on the deterministic inversion approach are presented in Appendix 6.5. Generally, both approaches solve for consistent EC models, and only minor differences can be observed for larger depths, particularly in section A-A', where the predicted section shows more conductive values ($>$ 30 mS/m) below 1 m depth. Furthermore, compared to the predicted EC sections, the inverted sections seem to show a slightly increased contrast between shallower layers, for example in sections B-B' and C-C'.

When we compare the results for the entire catchment, as presented in Figure 6.5, which shows cross-plots of the predicted (x-axis) and inverted EC (y-axis) for each of the 12 available depth layers separately, it can be observed that the deterministic inversion tends to overfit the data, resulting in negative EC values. Conversely, the DL network is much more robust in this regard. Figure 6.5 also shows that the largest differences between the approaches can be observed for the shallowest depths up to D_4. This observation also applies to the range of EC values, wherein the prediction appears to be constrained to values between approximately 0 and 50 mS/m, while the inversion resolves for a range between -10 and 100 mS/m.

The proposed DL network is not constrained to the use of a linear forward model or a forward model that adheres to the LIN approximation. In fact, the DL network was trained and evaluated using a Maxwell-based forward model without LIN approximation, yielding results consistent with those presented herein, with only minor deviations observed, mostly limited to small absolute changes in the observed EC values. Consequently, the linear forward model was selected due to its reduced computational time compared to the nonlinear Maxwell-based approaches. Given that the DL network involves two forward computations, a computationally intensive model would constitute a serious bottleneck during training and prediction, particularly for large datasets. Furthermore, the current forward model can be easily substituted, permitting the use of a forward model that accounts for both the electrical conductivity and magnetic permeability of the subsurface (Klose et al., 2018; Hanssens et al., 2019; Deidda et al., 2020).

Table 6.2: Loss (mean squared error) for the different subnets after training.

	Mean squared error		
Subnet	Training set	Validation set	Testing set
Subnet 1	0.0007868	0.0007882	0.0008719
Subnet 2	0.0017339	0.0017244	0.0017935
Subnet 3	0.0013174	0.0012983	0.0014313

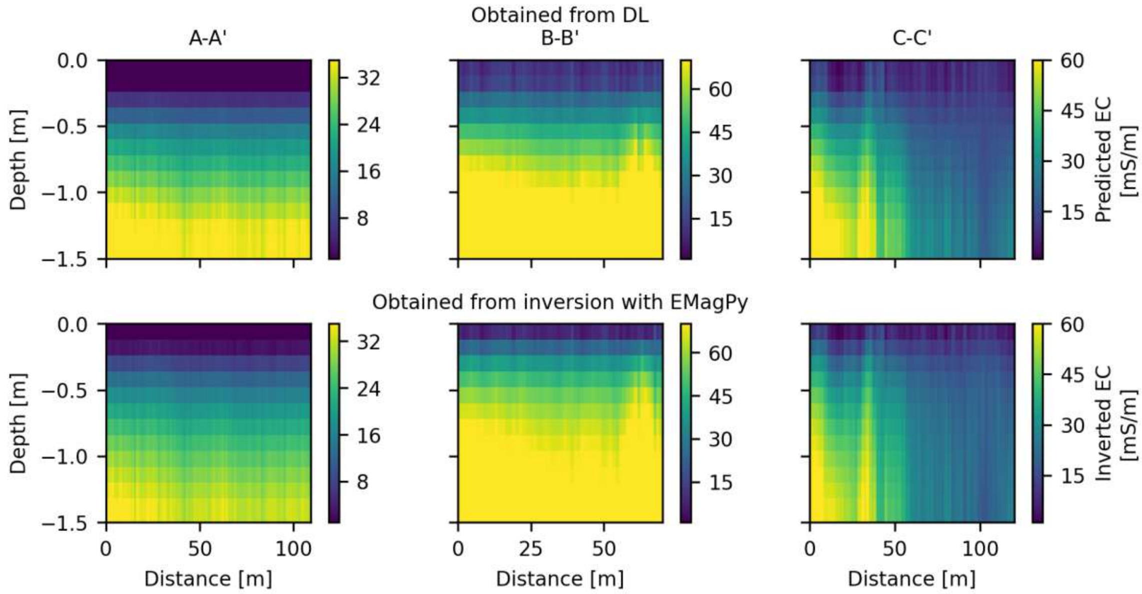

Figure 6.4: Evaluation of DL prediction performance based on the comparison with EC sections obtained from deterministic inversion along three transects (c.f. Figure 6.1).

6.4.2 Electrical conductivity and soil texture maps and their spatial correlation

We compared the predicted EC depth slices to maps of the mean soil volume fractions of sand (f_{sa}), silt (f_{si}), and clay (f_c), in short SSC, as illustrated in Figure 6.6. The mean soil volume fractions were computed at a mean depth of 32.5 cm, corresponding to a depth section of 0-65 cm. Since the soil information from the soil survey is available for 0-15 cm up to 70 cm depth, homogenization of the data, namely, inter- and extrapolation of the available depth information for the aforementioned mean depth of 32.5 cm was conducted. The obtained sand, silt, and clay fractions were then spatially interpolated to a 2.5x2.5 m grid utilizing natural neighbor interpolation. A linear variogram and a circular search space (i.e., no directional smoothing) were used.

The left panel of Figure 6.6 presents the mean soil volume fractions as color-coded maps, whereas the right panel displays the predicted EC maps for depth layers D_1, D_4,

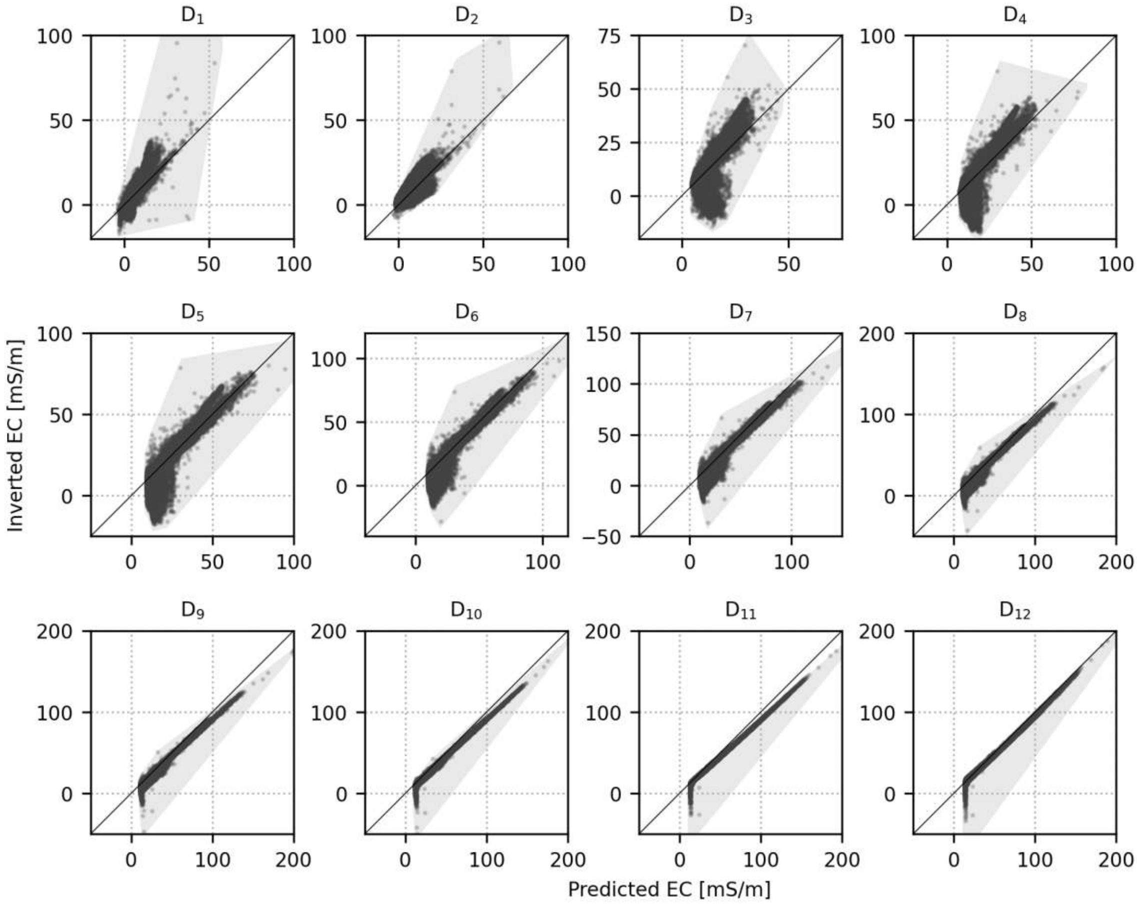

Figure 6.5: Cross-plots of the EC values predicted with DL and from deterministic inversion for the entire catchment and for each depth layer (D_1, D_2, ...; see Table 6.1). The light grey rectangle is the convex hull of the scatter to indicate its boundaries.

and D_6, corresponding to depth ranges of 0.00-0.12 m, 0.36-0.48 m and 0.60-0.72 m. Due to the dense distribution of EMI measurements, no interpolation was performed on the EC maps. Figure 6.6 demonstrates that the fraction of sand is generally low (< 10%), with some areas of high concentration in the northeastern region as well as adjacent to the stream, with values up to 20%. Figure 6.6 further shows, that there is a predominance of silt in the catchment, with values reaching up to 80% in the southern area. Conversely, areas characterized by lower values of silt (< 50%) were associated with increased proportions of clay (> 25%). Generally, the maps of silt and clay exhibit similar patterns and differ primarily in the magnitude of the observed values. Nevertheless, both fractions reveal a channel-like feature along the west-east direction, leading to the weather station and subsequently to the stream area (c.f. Figure 6.1). This channel can be attributed to the former location of the stream prior to its canalization.

The channel is also clearly evident in the predicted EC maps, particularly for D_4 and D_6, as areas characterized by EC values ~ 10 mS/m. Generally, the EC maps exhibit an increase in EC with depth, as evidenced by comparing D_4 and D_6. In contrast to the deeper layers, D_1 displays the lowest EC values (ranging between 1 and 15 mS/m) and divergent features, which cannot be easily explained by changes in soil composition. The low EC values could be attributed to the roughness of the topsoil, characterized by large air pockets (i.e., high porosity) and low levels of soil moisture, both of which lead to a decrease in EC. Moreover, the LIN approximation assumes that there is no air column between the sensor and ground (i.e., zero elevation). Consequently, the divergent features in D_1 may also be explained by changes in sensor elevation due to field crops or roughness of the topsoil due to plowing, resulting in anomalous readings with decreased magnitude (Beamish, 2011).

As expected, an increase in EC values correlates with increasing the clay content, due to the larger surface area and cation exchange capacity of the clay minerals and thus a greater contribution of surface conductivity (e.g., Okay et al., 2014; Flores Orozco et al., 2018b; Gallistl et al., 2022). This increase in both EC and clay content can be observed in the central part of the catchment, with f_c values between 30-40% corresponding to elevated EC values larger than 40 mS/m.

6.4.3 Experimental petrophysical relationships to predict textural properties from EC

The EC predictions were referenced to the soil data by calculating a radius of 3 m around the sampling point and computing the mean value of all EC values inside the radius. This approach can be thought of as a smoothing filter applied to the EC values and aims to align the spatial scales between the soil and EC data. The optimal agreement was observed using D_6 as the EC input data. Despite a slight depth discrepancy, specifically 32.5 cm for the soil and 66 cm for the EC data, we argue that the range of EC values (10-100 mS/m) in D_6 was sufficiently large to be a reliable predictor. Furthermore, for the given EMI system, this depth is approximately associated to the highest normalized sensitivity in the HCP configuration (Bonsall et al., 2013; McLachlan et al., 2021a). Alternative approaches, such as utilizing a mean EC value of a combination of different depth layers or exclusively using a single shallow layer, have been explored; however, they have not yielded robust relationships.

The rows in Figure 6.7 illustrate the results of the correlation analysis for the three fractions of interest: sand (f_{sa}), silt (f_{si}), and clay (f_c). The correlation was conducted utilizing the split-sample validation (SSV) methodology, dividing the 203 samples

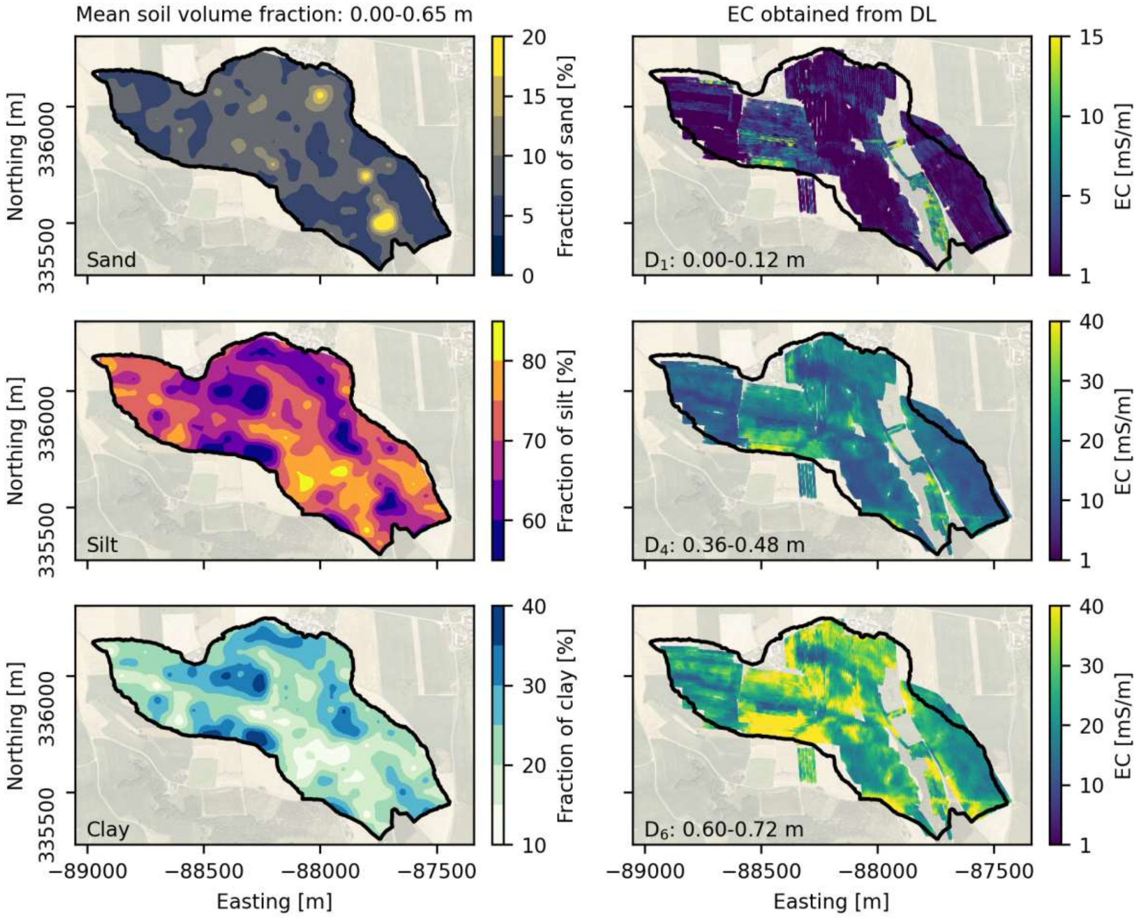

Figure 6.6: Comparison of maps of the mean soil volume fraction of sand, silt and clay and the predicted EC models for three different depths.

into calibration (80%, n=162) and validation (20%, n=41) sets, which facilitates the evaluation of the performance and generalizability of the derived relationships (Snee, 1977; Kohavi, 1995). Columns 1 and 2 of Figure 6.7 present the scatterplots for the calibration and validation sets and the fitted linear regression models for each fraction. Columns 3 and 4 compare the measured and predicted fractions using the derived regression model. The model performance is quantified by the root-mean-square error (RMSE) computed as

$$\mathrm{RMSE} = \sqrt{\frac{1}{n}\sum_{i=1}^{n}(f_m - f_p)^2} \tag{6.3}$$

in which n is the number of observations and f_m, f_p are the measured (f_m) and predicted (f_p) soil volume fractions; whereas the f_p is computed using the fitted regression model.

As anticipated, the fraction of sand exhibited no correlation with the EC data, as can be observed in the scatterplots. In contrast, the regressions for silt and clay demonstrate relatively well-defined relationships with R^2 values of 0.4 for silt and 0.33 for clay. Although these values are comparatively low, the relationships, characterized by a decrease in silt content with increasing EC, and conversely, an increase in clay content with increasing EC, are also observable in the validation set. Regarding performance, specifically the comparison of measured and predicted soil fractions, both soil fractions exhibited RMSE of approximately 5% for the calibration and validation sets. The positive correlation of EC with volumetric clay content has been observed in previous studies (e.g., Scanlon et al., 1999; Weller et al., 2007; Cockx et al., 2009; Harvey and Morgan, 2009; Zhao et al., 2019, and others). In contrast to that, the relationship between EC and volumetric silt content appears to be under-investigated (Heil and Schmidhalter, 2012; Heil and Schmidhalter, 2015). This could be partly explained by the fact, that recent research efforts are directed at the quantification of soil water content (Huang et al., 2017; Robinet et al., 2018; Visconti and Paz, 2021; Mensah et al., 2023), hydrogeological properties (Brosten et al., 2011; McLachlan et al., 2021b; Dragonetti et al., 2022), or soil salinity (Paz et al., 2020; Gu et al., 2023; Paz et al., 2024), in which the volumetric clay content, due to its confining characteristics, plays a more critical role than other textures. Nonetheless, for the silty loam soils of the HOAL, with a dominance ($> 75\%$) of silty textures, it is clear that the geophysical parameters are strongly dependent on this texture; thus EMI data can be used to assess variations of finer and coarser grains; which in turn are also strongly linked to hydraulic properties.

Figure 6.8 depicts the prediction functions for sand, silt, and clay. As f_{sa} did not demonstrate any significant correlation with the predicted EC data, it was computed as a loss function (Equation 6.4). This approach also ensures that the total fraction is consistently limited to 100% (Gallistl et al., 2022).

$$f_{sa} = 100 - (f_{si} + f_c) \tag{6.4}$$

The derived relationships permit the prediction of soil textural characteristics for all depth layers throughout the entire catchment up to a depth of 1.5 m. Figure 6.9 illustrates the results for three depth layers, specifically D_3, D_7 and D_{11}, corresponding to depth ranges of 0.24-0.36 m, 0.72-0.84 m and 1.20-1.32 m. The color-coded maps of the predicted soil volume fractions for sand f_{sa} (top row), silt f_{si} (middle row), and clay f_c (bottom row) are based on natural neighbor interpolation (using the parameters presented above), with areas of no coverage and areas outside of catchment blanked.

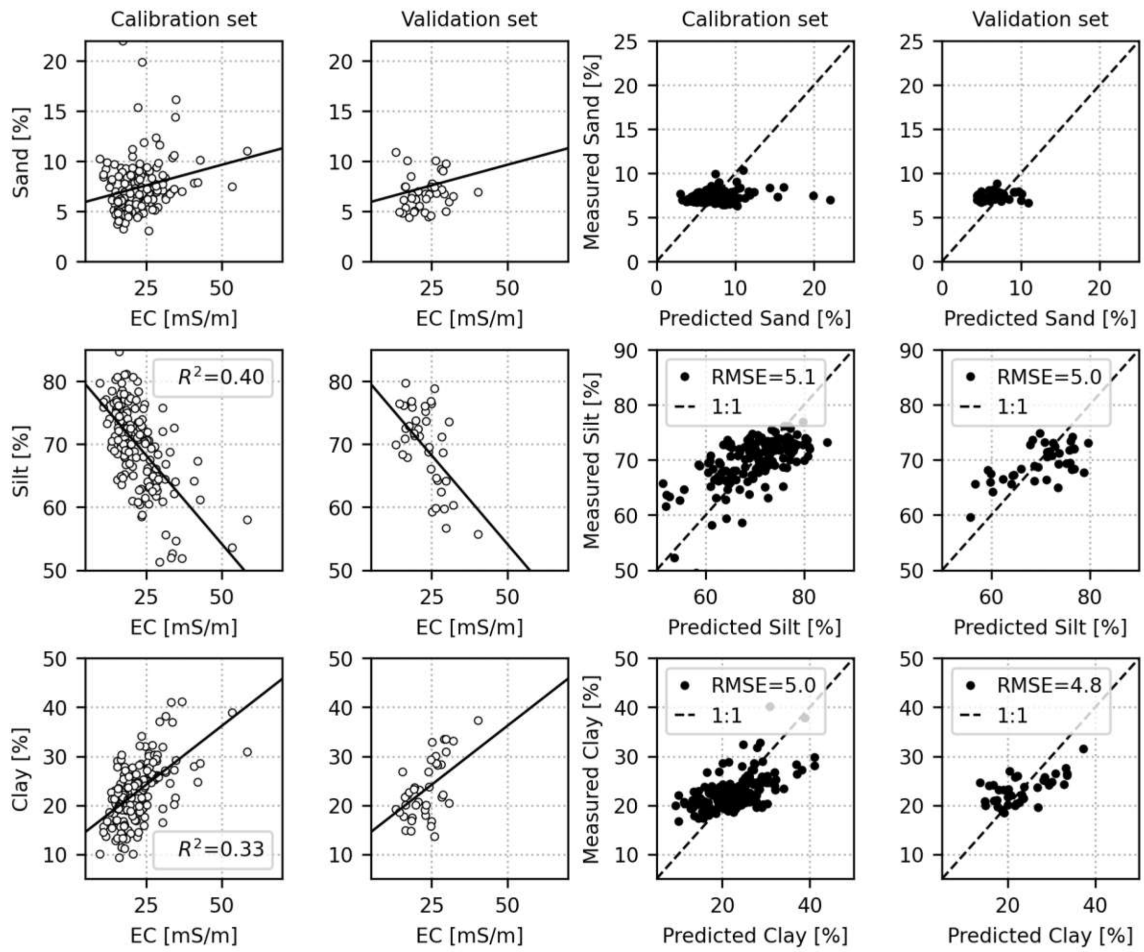

Figure 6.7: Correlation and split-sample validation of the predicted EC model values and the different soil volume fractions of sand, silt and clay.

Moreover, such plots present the associated normalized histograms. Clear differences in the range of the predicted values and their distributions can be observed for different depths and soil volume fractions. In particular, f_{sa} at the shallowest depth is relatively low (below 6%), and the main histogram distribution is limited to the range of 5-7%. As depth increases, both the magnitude of the observed values as well as the histogram distribution change and a shift to higher percentages (although still relatively low with values below 15%) can be observed. Moreover, the histograms broaden and have their maximums at $\sim$ 7% for D_7 and $\sim$ 8% for D_{11}. Hence, a general trend towards an increase in magnitude and a broader range of predicted values can be observed. When compared to the mean soil volume fractions obtained from the soil survey (Figure 6.6), it is evident that the absence of a relationship with the EC and the approximation of the sand fraction as a loss function cannot represent specific details of the catchment. Nevertheless, the general distribution and range of values ($<$ 15% sand) is resolved by

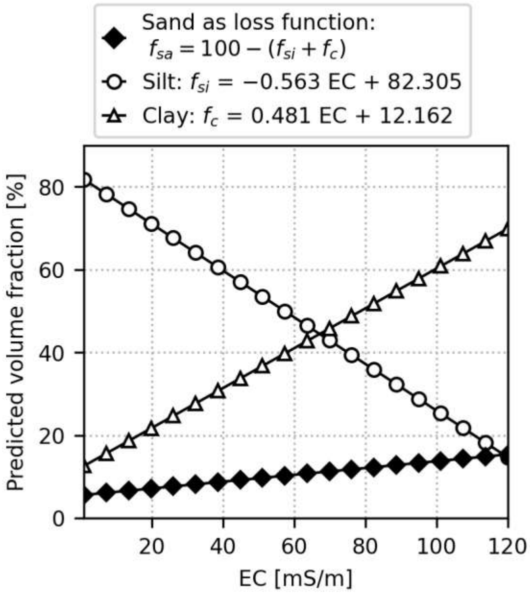

Figure 6.8: Functions to predict the different soil fractions of sand, silt and clay based on their dependence on EC.

the prediction.

In general, and as observed for the sand fraction, the distribution of the predicted silt fractions and their range for D_3 is rather limited, with its maximum at $\sim 80\%$ and spanning between 75-85%. This pattern significantly changes for D_7, where the resolved silt fractions now range between 55-75% and the map depicted in Figure 6.9 resembles the one presented for the mean soil volume in Figure 6.6. For the deepest layer, D_{11}, a further shift in the histogram distribution (with a maximum of $\sim 65\%$) and a spread between $\sim$ 50-75% can be observed. Hence, the predicted silt fractions indicate both a decrease in the magnitude and broadening of the value range with an increase in depth. Analogous observations can be made for the predicted clay fractions, namely, an underestimation of the predicted values for D_3, nearly indistinguishable patterns and ranges between the predicted and measured values for D_7 and a further divergence with increasing depth.

The analysis of the predicted and mean soil volume fractions has demonstrated promising results that promote confidence in the proposed approach and established relationships. For further evaluation, in Figure 6.10, we present vertical profiles of the soil fractions for the predicted and in the soil survey sampled values, as well as soil data collected during the drilling of a piezometer station (P21 in Figure 6.1). It should be noted that the soil information from the latter has not been used in the development of the petrophysical models.

The soil profiles presented in Figure 6.10 were selected to be representative of the soil textural characteristics of the catchment, with the majority of the soil profiles situated in agriculturally used areas and one in the stream area (i.e., woodland). Furthermore, a range of different elevations is covered (c.f. Figure 6.1). The plots in Figure 6.10 clearly demonstrate that the predicted soil profiles are capable of following the general trends in the catchment, as evidenced by the sampled soil profiles. An increase in clay content with increasing depth can be observed; whereas the silt fraction exhibits opposing behavior and generally decreases with depth. Minor discrepancies between the predicted and measured values (ranging between 2-5%) can be observed for the majority of the soil profiles, with bk6143 being an exception. In this case, the sampled soil volume fraction for silt and clay depict the largest mismatches of values up to 15% at a depth of approximately 0.5 m. As illustrated in Figure 6.1, of all profiles in consideration, this one is closest to a power line. The discrepancy observed could be explained by the unintended influence of the power line's electromagnetic field on the measured ECa values and, consequently, the predicted EC and soil textural information.

Regarding the soil profile where additional ground-truth information about the textural information for deeper layers is available (bk6042 and P21 in Figure 6.10), significant discrepancies of values up to 15% for the silt and clay fractions can be observed at a depth of approximately 0.5 m. Nevertheless, the decrease in silt, and conversely the increase in clay with increasing depth, is resolved in our prediction. However, there might be a slight underestimation of the silt and clay fractions at depth when using the approach presented here. Considering that the relationships obtained are based on soil samples within the top 0.3 m and for silty loam soil they are associated with a high porosity. Increasing the depth will reduce the porosity; however, the contribution of surface conductivity remains largely unaltered, thus explaining the high electrical conductivity and the underestimation in our model. Moreover, as illustrated in Figure 6.1, P21 and bk6042 are not directly co-located with a distance of ~ 25 m between them, which could further explain this mismatch. Additionally, varying sampling strategies and soil-textural analysis of the recovered materials could contribute to the observed discrepancies. As evidenced in Figure 6.10, a notable difference in the fractions of silt and clay of approximately 7% exists at roughly 0.5 m depth, when comparing the ground truth data from the soil survey with that obtained from the piezometer station drilling.

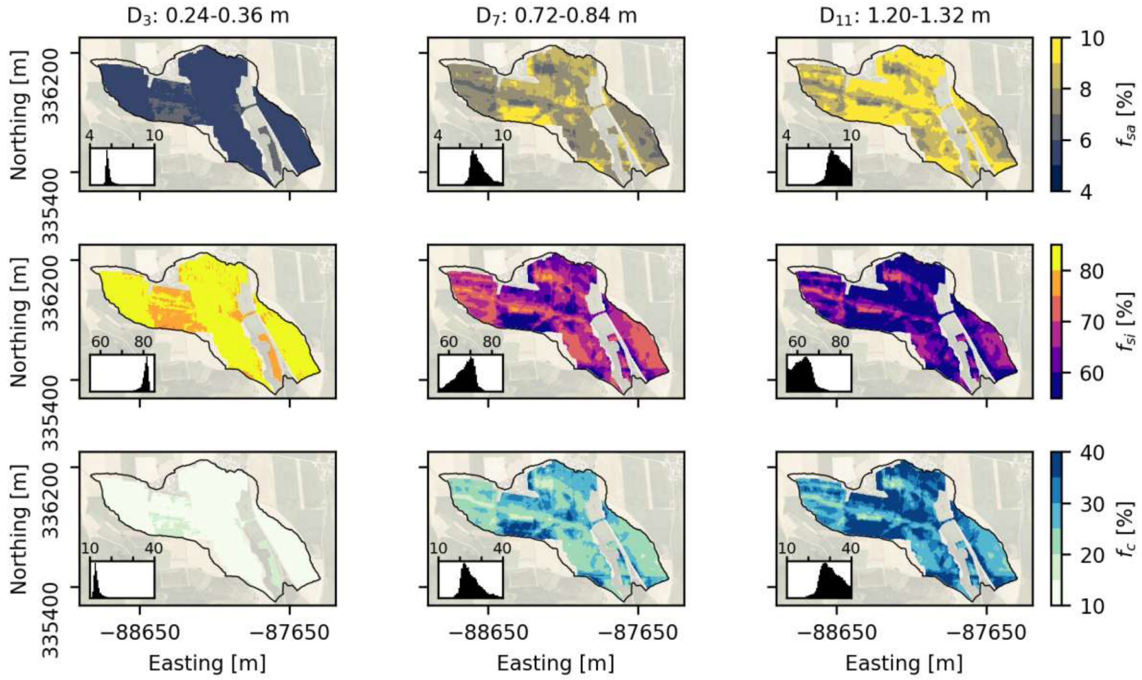

Figure 6.9: Maps and associated normalized histograms of the predicted soil volume fractions for three different depths indicate significant variations in the predicted values for different depths.

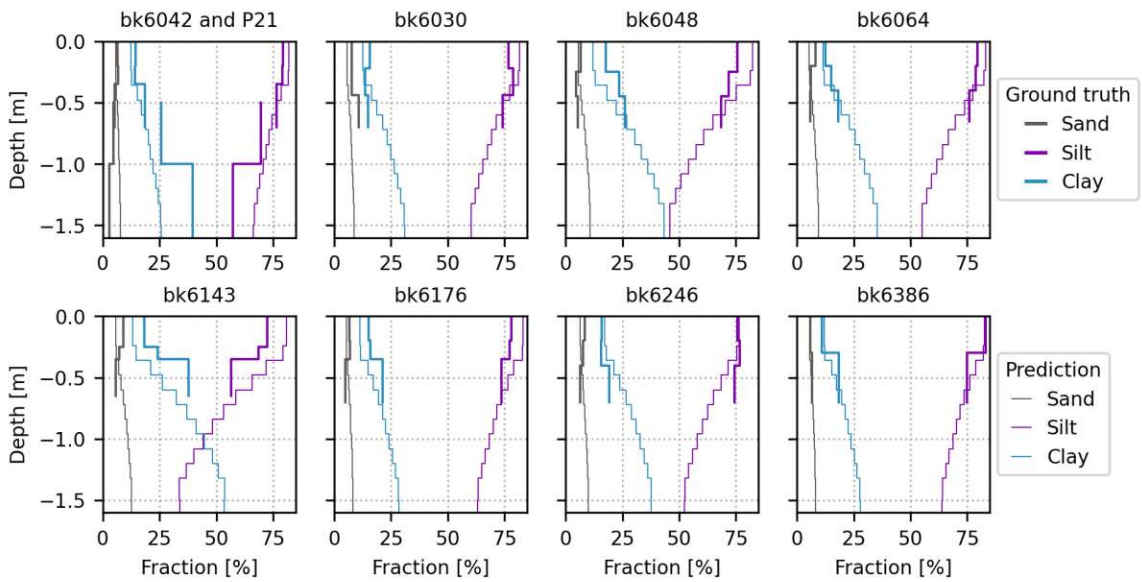

Figure 6.10: Predicted soil profiles (thin lines) using the functions presented in Figure 6.8 in comparison to in-situ values (thick lines) obtained from sampling in the field. bk6030-bk6386 refers to names of the sampling locations of the soil survey, whereas P21 is the soil profile recovered from drilling of a piezometer (c.f. Figure 6.1).

6.4.4 Predicting catchment-scale hydraulic conductivity

We opted to recalibrate an existing PTF for the catchment using the K_s dataset initially presented by Picciafuoco et al., 2019b; Picciafuoco et al., 2019a and the SSC prediction described herein, excluding the fraction of organic matter (f_{OM}) as a predictor variable. Our approach enables the prediction of K_s through SSC, slope S, and elevation EL and given the established relationships, consequently, K_s can basically be estimated from ECa (VCP) measurements. Prior to recalibration, the soil physical dataset (i.e., the predicted SSC values) were prepared in accordance with the methodology outlined in Picciafuoco et al., 2019b; Picciafuoco et al., 2019a, wherein SSC values were computed for a mean depth between 0.00 to 0.36 m. The radius search strategy discussed above, using a 3 m radius, was used to reference the SSC values to K_s dataset. The parameters of the employed ridge regression model were obtained through cross-validation; while model evaluation was performed using split-sample validation with 66% reserved for the calibration, and the remaining 34% for the validation set. Further details regarding the ridge regression model and the cross-validation approach can be found in Appendix 6.5.

The SSV analysis of the recalibrated PTF, as depicted in Figure 6.11, indicates that the ridge regression model is reasonably well-defined with a R^2 score of 0.52 and demonstrates comparable performance on the calibration and validation set (evidenced by the similar RMSE values of 7.53 mm/h for the calibration and 6.11 mm/h for the validation set). The model generally predicts K_s values consistent with the measured data across the entire range of observed values, exhibiting only minor deviations from the 1:1 line. However, for measured values in the range of 5 to 10 mm/h, the model appears to overestimate and the predictions cluster around 15 mm/h. This can also be observed in the predictions using the validation set. Moreover, the model slightly underestimates for $K_s > 30$ mm/h. Similar behavior has been reported by Picciafuoco et al., 2019b and could be attributed to the soil physical dataset defined by low variation in the prediction variables. This factor, in conjunction with the use of ridge regression, may constrain the model's ability to generalize to a higher degree.

The performance of the PTF in predicting K_s from EMI data was evaluated through visual inspection of the spatial prediction results for the different depth layers, as presented in Figure 6.12. Additionally, these plots present the associated normalized histograms of K_s. Significant variations in the K_s patterns are observable for the uppermost depth layers until approximately 0.5 m with the observed K_s values ranging between 10 to 40 mm/h (D_1, D_2) and 8 to 30 mm/h (D_4), indicating substantial variability in soil hydraulic properties near the surface. Below this depth, the spatial patterns remain largely consistent with only localized changes observed. However the histograms demonstrate a notable shift towards lower K_s values with increasing depth, with the peak shifting from ~ 24 (at D_5) to ~ 16 mm/h at the deepest layer. K_s variations at depths down to 0.5 m can potentially be attributed to the influence of agricultural practices, with soil compaction through heavy machinery and the development of plough horizons likely driving K_s patterns and associated changes at depth.

To the best of our knowledge, only three studies have reported the prediction of hydraulic conductivity from inverted EMI data. Vervoort and Annen, 2006 used a methodology similar to that used in this study. Specifically, they compared different algorithms to invert the measured data and then linked the inverted EC to the soil volume fractions of sand and clay, which permitted the estimation of SSC. Subsequently, the authors used the NEUROTHETA PTF (Minasny and McBratney, 2002), which employs a neural network in conjunction with the van Genuchten model (van Genuchten, 1980), to estimate K_s. Notably, despite a significantly larger fraction of sand at their study site, with values between 20 to 60%, the authors reported predicted K_s values predominantly lower than those presented here, with values of 1 to 20 mm/h. This discrepancy is likely attributed to two factors: (1) the substantially higher clay fraction, with reported values up 60%, and (2) the employed PTF, which was calibrated for the national scale (Australia wide), rather than the required field scale. Such models often fail to represent field-scale heterogeneity due to the inability to quantify random variability sources (Picciafuoco et al., 2019a). In this regard, our approach to recalibrate a field-scale PTF may be preferable, as catchments such as the HOAL with its heavy soils will not be adequately resolved by regional- or national-scale PTFs. Brosten et al., 2011 employed an alternative methodology that does not rely on the application of a PTF. In their publication they derived a relationship directly linking the inverted EC to K obtained from slug tests at 10 wells distributed across the study area. This approach permitted the prediction of K maps for 4-6 layers down to a depth of 5 m. Given the distinctly different soil textural setting, specifically an unconfined aquifer composed of sand, gravel, and cobbles, the predicted K values are one to two orders of magnitude larger than our predictions. Nevertheless, and consistent with our approach, the authors suggest that the EC response, and consequently the K_s prediction, is primarily influenced by the clay content resulting in the negative EC-K relationship, where an increase in clay is associated with increased EC values, and conversely, due to its confining properties, with decreasing K. Moreover, the survey by Brosten et al., 2011 addresses much greater depths, primarily due to the instrument used and the spatial scale of K (~ 1.5 m) obtained from the slug tests.

Our methodology is tailored for the CMD-MiniExplorer, however, the frameworks are generalized, and the training datasets along with the DL network can be readily modified to accommodate other EMI sensors or multi-configuration datasets combining VCP and HCP readings, potentially enabling much greater depths of investigation for the K_s predictions. Similarly, Uhlemann et al., 2022 developed an empirical relationship directly linking the inverted EC to K_s, which permitted to derivation of a 3D hydraulic conductivity model below percolation ponds. As with Brosten et al., 2011, the authors reported a negative EC-K_s relationship, strongly indicating that the EC response was dominated by the clay content.

The original version of our recalibrated PTF, as presented in Picciafuoco et al., 2019b; Picciafuoco et al., 2019a, necessitates estimates of the fraction of organic matter f_{OM} for a successful prediction. Consequently, we investigated the correlation between the predicted EC and f_{OM}; however, they were found to be uncorrelated ($R^2 < 0.05$). Furthermore, a sensitivity analysis using constant values for f_{OM}, along with the mean and standard deviation for f_{OM} reported by Picciafuoco et al., 2019a revealed unsatisfactory results (not shown). Alternatively, published petrophysical relationships between EC and f_{OM} could be used. One of the few studies that addressed the quantitative relationship between soil organic matter and electrical conductivity provided by EMI (e.g., Garcia-Tomillo et al., 2017) was performed in a study area with a substantially different soil type (sandy-loam), only using ECa in conjunction with a different instrument, thereby significantly limiting its applicability to our study site. Given these challenges, we decided against using proxy solutions to estimate organic matter content, as they would likely introduce additional uncertainty into our predictions. This decision underscores the importance of site-specific calibration and the need for caution when applying relationships derived from different environmental contexts. Our approach prioritizes minimizing prediction uncertainty by avoiding potentially unreliable proxy methods, emphasizing the need for direct measurements or more robust estimation techniques tailored to the specific characteristics of our study area.

6.5 Conclusions

This study demonstrates the potential of using EMI within a multi-step framework to predict soil textural and hydraulic properties at the catchment scale. The key findings and contributions include:

1. The development, evaluation, and application of a DL network that permits the rapid and accurate prediction of 1D EC depth models from multicoil ECa VCP

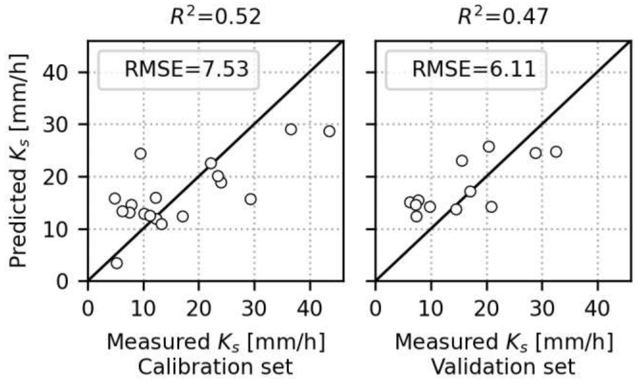

Figure 6.11: Split-sample validation for the recalibrated pedotransfer function to predict saturated hydraulic conductivity K_s. The measured and predicted K_s values refer to a depth range between between 0.00-0.36 m.

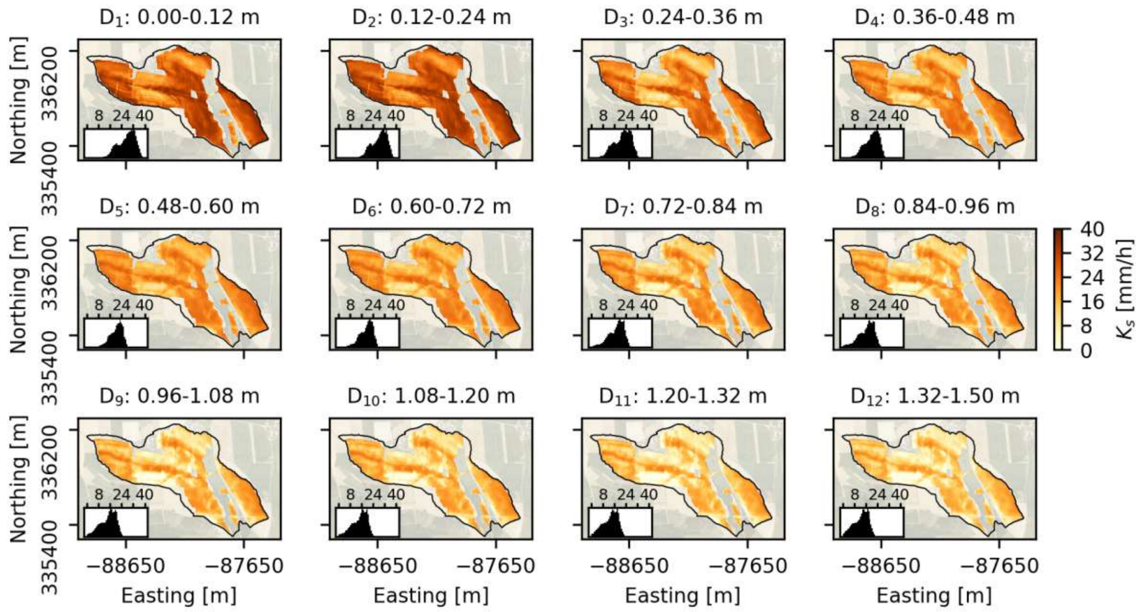

Figure 6.12: Predicted saturated hydraulic conductivity maps for the 12 depth layers.

measurements. Its performance was evaluated based on a comparison with a classic deterministic inversion approach, and only minor discrepancies were observed between the EC models. Moreover, compared to deterministic approaches, the DL network permits a significantly faster estimation of the EC models, which, considering that EMI surveys have become increasingly motorized, could facilitate large-scale investigations and decision-making processes.

2. The establishment of site-specific petrophysical relationships linking the predicted EC to soil textural properties, specifically, the soil volume fractions of

sand, silt, and clay. These relationships were evaluated through split-sample validation, and reasonably well-defined correlations for silt (R^2=0.4) and clay (R^2=0.33) could be established, permitting the prediction of soil textural information for the entire catchment. Consistent trends (with discrepancies of 2-5%) between the predicted and measured soil properties, as evidenced in extracted soil profiles, could be observed, promoting confidence in the proposed approach and the established relationships.

3. The recalibration of an existing field-scale PTF available for the catchment to predict K_s, using the predicted soil textural properties and topographic variables. This permitted the generation of high-resolution maps (2.5x2.5 m) of the spatial K variations for 12 depths down to 1.5 m, with predicted K_s values ranging between 8-40 mm/h for the upper 0.5 m, whereas a constant decrease in K_s values ($<$ 24 mm/h) below that depth can be observed.

The proposed multi-step framework has significant potential to enhance hydrological modeling and support water resource management in agricultural catchments, particularly for catchments characterized by heavy soils such as the HOAL. The integration of EMI measurements, DL techniques, and PTFs provides a comprehensive approach to predicting soil properties at high spatial resolution. Further research is needed to test the transferability of this method to other soil textural settings, deeper investigations and other EMI sensor systems.

Appendix

Electromagnetic induction imaging: forward modeling and deterministic inversion

All forward modeling throughout this manuscript is based on the linear cumulative sensitivity (CS) forward model using the LIN approximation as provided by McNeill, 1980b. The cumulative sensitivity functions, which describe the relative contribution of materials below a normalized depth $\tilde{z} = z/r$ can be written as follows

$$R_V(\tilde{z}) = \sqrt{4\tilde{z}^2 + 1} - 2\tilde{z} \tag{6.5}$$

$$R_H(\tilde{z}) = \frac{1}{\sqrt{4\tilde{z}^2 + 1}} \tag{6.6}$$

in which $R_V(\tilde{z})$ and $R_H(\tilde{z})$ are the functions for VCP and HCP configurations, respectively. The use of the normalized depth $\tilde{z}$ was proposed by Callegary et al., 2007 to account for different coil separations r. For a given 1D model, composed of N EC layers over an infinite half space with conductivity EC_{N+1}, and assuming LIN conditions, the forward response can be computed using Equations 6.5 and 6.6, as:

$$\mathrm{EC}_a = \sum_{i=0}^{N} \mathrm{EC}_{i+1}[R_{V|H}(\tilde{z}_{b,i}) - R_{V|H}(\tilde{z}_{b,i+1})] \tag{6.7}$$

where $\tilde{z}_{b,i}$ is the depth of the bottom edge of layer i and $\tilde{z}_{b,0} = 0$, $\tilde{z}_{b,n+1} = \infty$. We used the implementation of the forward algorithm provided by EMagPy (McLachlan et al., 2021a).

As an ill-posed problem, deterministic inversion involves minimizing a regularized misfit function, which is typically written as

$$\Phi = \Phi_d + \alpha\Phi_m \tag{6.8}$$

in which Φ_d is the data misfit, Φ_m is the model misfit and α is the regularization parameter. α governs the regularization strength, and consequently, the influence of the model misfit on the total misfit. Using L2 regularization, the data misfit function can be formulated as:

$$\Phi_d = \frac{1}{N}\sum_{i=1}^{N}(d_i - f_i)^2 \tag{6.9}$$

where N denotes the number of measurements, d_i represents the measured value and f_i is the forward response. The model misfit function is defined as:

$$\Phi_m = \frac{1}{M}\sum_{k=1}^{M-1}(\mathrm{EC}_k - \mathrm{EC}_{k+1})^2. \tag{6.10}$$

where M represents the number of layers of the 1D EC model and EC_k is the conductivity of layer k.

Deterministic inversion results presented in this manuscript were obtained using the implementation within EMagPy (McLachlan et al., 2021a) using the CS forward model with LIN approximation for f_i presented above and the L2 regularization outlined here. The 12 layer depth model presented in Table 6.1 was used and no noise was specified during inversion. Inversions were performed on selected sections in the catchment (c.f. Figure 6.1) as well as for the entire dataset ($\sim$ 30 minutes: AMD Ryzen 5 5600X

6-Core Processor 3.70 GHz; 32 GB RAM).

Complementary geophysical data: complex conductivity imaging

Complex conductivity (CCI) or complex resistivity (CRI) imaging is an extension of the electrical resistivity tomography (ERT) method that permits to obtain 2D or 3D information of both the resistive (or conductive) and capacitive electrical properties within the subsurface (Ward, 1990; Binley and Kemna, 2005). Analogous to the ERT method, the measurements consist of four electrode configurations - two of which are used for current injection and the other two to record the corresponding voltage. Depending on whether the measurements are performed in the time or frequency domain, the determination of the so-called induced polarization (IP) effect (which describes the capacitive response of the subsurface) consists of the measurement of the voltage decay after current shut-off (time domain) or the measurement of the phase-shift between the injected sinusoidal current and measured voltage signal (frequency domain). To provide subsurface models of the electrical properties, inversion algorithms for measurement performed in the time and frequency domain have been formulated (Kemna, 2000; Loke et al., 2006; Fiandaca et al., 2012; Madsen et al., 2020).

Inversion results can be given in terms of the complex electrical conductivity $\sigma^*(\omega)$ (where ω is the angular excitation frequency). The complex conductivity can be expressed by means of its real, $\sigma'(\omega)$, and imaginary, $\sigma''(\omega)$ components, or by its magnitude $|\sigma^*(\omega)|$ and phase-shift $\varphi(\omega)$. Both expressions are related:

$$\sigma^*(\omega) = |\sigma^*(\omega)|e^{i\varphi} = \sigma'(\omega) + i\sigma''(\omega) \tag{6.11}$$

with $i = \sqrt{-1}$, and further:

$$\varphi = \arctan \frac{\sigma''(\omega)}{\sigma'(\omega)}. \tag{6.12}$$

The conduction properties, which relate to energy loss, are represented by the real (or in-phase) component, while the polarization/capacitive properties, associated with energy storage, are represented by the imaginary (or quadrature) component of the subsurface (Ward, 1990; Binley and Kemna, 2005).

CCI data were collected prior to the drilling of shallow boreholes (< 15 m depth) in the catchment (Figure 6.1). The objective was to provide a-priori information to be able to adjust the drilling depths or locations if needed. Where possible, the profiles were aligned perpendicular to each other in an effort to characterize possible anisotropy effects of the subsurface electrical properties and to permit the determination of possible 3D geometries. The data were collected using a Syscal Pro (Iris Instruments), deploying 72 electrodes with 1 m spacing. A multi-skip dipole-dipole protocol was used as electrode configuration, combining different skip values, whereas skip refers to the number of electrodes skipped in each dipole to adjust the dipole length (Gallistl et al., 2018; Flores Orozco et al., 2018b). Due to the heavy soils, low contact resistances (< 0.5 kOhm) were observed resulting in high injected currents between 300-700 mA. A pulse length of 2000 ms was chosen to obtain information on the IP effect. Data processing consisted of a removal of outliers by applying the filter methodology outlined by Gallistl et al., 2018 and a subsequent inversion with ResIPy (Blanchy et al., 2020). Although relatively large IP effects can be observed in the catchment, hereafter we only present results expressed as the magnitude $|\sigma^*|$ of the complex conductivity, i.e. only the conductive properties of the subsurface are described.

Ridge regression and cross validation approach

The PTF describes a linear regression model, comprised of the regressor matrix X $(n \times p)$, the vector of dependent variables y $(x \times 1)$, the unknown parameter vector β $(p \times 1)$, and an error vector ϵ $(n \times 1)$, and can be written in vector form as:

$$y = X\beta + \epsilon. \tag{6.13}$$

The regressor matrix X contains the standardized regressors, whereas the order of the columns is f_c, f_c^2, f_{si}, f_{si}^2, f_{sa}, f_{sa}^2, S, EL, and each element $x_{i,j}$ is given by:

$$x_{i,j} = \frac{x_{i,j} - \mu_j}{SD_j}. \tag{6.14}$$

μ_j and SD_j are the mean and standard deviation of the jth elements of X. The linear regression model can be solved provided that the columns of the regressor matrix are linearly independent as follows:

$$\tilde{\beta} = (X^T X)^{-1} X^T y \tag{6.15}$$

In the case of multicollinear columns, which is true for the predicted SSC data, the linear model in Equation 6.15 tends to perform poorly as $X^T X$ might become singular. Ridge regression (Hoerl and Kennard, 1970) aims to stabilize the model by imposing a penalty parameter α (≥ 0) on the model, which helps to keep $X^T X$ invertible by adding positive elements to the diagonals:

$$\tilde{\beta_R} = (X^T X + \alpha I)^{-1} X^T y \tag{6.16}$$

where I denotes the identity matrix. For $\alpha = 0$ the above model reduces to Equation 6.15. As for example discussed in Dorugade, 2014 the selection of an appropriate value for α is critical and numerous approaches have been proposed. In this study, cross-validation was used to determine the optimal value for α. The dataset was first divided into a calibration (66%) and validation dataset (34%); with the former used for the cross-validation parameter search, and the latter used for the split-sample validation discussed above. Subsequently, the calibration dataset was divided into 15 shuffled random folds, which were further split into training and testing datasets, with 66% and 34% of the data reserved, respectively. For each fold, the ridge regression model was fitted to the training data using 10,000 α values in the range between 0.001 and 250, and the R^2 score for each associated testing dataset was computed. Consequently, for each fold, an R^2 curve for the testing dataset as a function of α values could be derived, and using all 15 curves, a mean curve across all folds could be obtained. The optimal α was selected as the value that maximizes the R^2 score for the mean curve. The calibration dataset was refitted using this α value. The so obtained PTF using ridge regression writes as:

$$\langle K_s \rangle = 16.46 + \tilde{X}\hat{\beta} \tag{6.17}$$

with $\hat{\beta}$ being the vector of ridge coefficients

$$\hat{\beta}^T = [-0.82 \quad -0.88 \;\; 0.67 \;\; 0.65 \quad -0.76 \quad -0.79 \quad -3.74 \quad -0.30] \tag{6.18}$$

and μ and SD are the mean and standard deviations to compute the regressor elements of $\tilde{X}$:

$$\mu = [17.91 \;\; 328.13 \;\; 75.39 \;\; 5693.81 \;\; 6.53 \;\; 42.82 \;\; 6.60 \;\; 272.86] \tag{6.19}$$

$$SD = [2.70 \quad 92.72 \;\; 3.16 \;\; 482.07 \;\; 0.46 \;\; 5.89 \;\; 1.71 \;\; 13.31]. \tag{6.20}$$

7 Developing a catchment-scale hydrogeophysical model: insights from complex conductivity imaging at the HOAL

7.1 Introduction

The previous chapter highlighted the critical role of soil-textural and hydraulic information as a prerequisite in hydrogeological modeling (Slater, 2007; Zhang et al., 2007; Enemark et al., 2019). While the results presented in Chapter 6 provided valuable insights into near-surface textural and hydraulic properties, representing a significant step towards an enhanced understanding of surface and near-surface run-off processes (Carey et al., 2019; Fiener et al., 2011), deeper subsurface information about hydraulic properties is required to conceptualize and understand the hydrogeological setting of the research catchment under consideration and to address the modeling of groundwater recharge and groundwater availability (Tanner and Hughes, 2015; Doble and Crosbie, 2017; Waseem et al., 2020). Currently employed hydrogeological models in the catchment (Pavlin et al., 2020) are oversimplified in terms of subsurface structure and rely on discrete borehole information and hydraulic conductivity predictions without depth information, that is, relating to the uppermost subsurface layers (Picciafuoco et al., 2019b; Picciafuoco et al., 2019a). While the multi-step framework outlined in Chapter 6 can potentially be adapted for sensors with greater investigation depths, complex conductivity imaging (CCI) offers an alternative and valuable geophysical method for obtaining deeper subsurface information within the catchment.

Over 100 CCI profiles distributed throughout the catchment have been collected with the objective of a hydrogeophysical characterization of the catchment. As previously discussed, CCI permits to quantify both the capacitive and conductive electrical properties and, thus, is well-suited for application in a catchment rich in fine-grained sediments (combined silt and clay $> 90\%$), where electrical resistivity tomography (ERT) might fail to discriminate between saturated and clay-rich zones (Flores Orozco et al., 2018b; Gallistl et al., 2018; Gallistl et al., 2022). Various electrode spacings in the CCI profiles were employed to obtain information about the subsurface electrical properties at different resolution scales, from shallow (down to 10 m) to deep (down to 60 m) depths. Such dataset, together with extensive borehole information, should permit the development of a hydrogeophysical model of the catchment, which can subsequently be deployed for model calibration in hydrogeological modeling and represents a significant advancement towards an enhanced understanding of the hydrogeological environment of the catchment.

This chapter presents borehole information and discusses two potential conceptual hydrogeological models of the catchment. CCI is then used to parameterize one of the models in a two-step procedure: (1) delineating the topography of a confining layer at depth, and (2) predicting catchment-scale hydraulic conductivity using the pedotransfer function recalibrated in Chapter 6. Such an approach permits the first realization of a three-dimensional hydrogeophysical model of the catchment, providing valuable insights in the catchment's subsurface hydraulic characteristics.

7.2 Material and Methods

7.2.1 Complex conductivity mapping for catchment characterization

Large-scale CCI data were collected along 76 profiles (c.f. Figure 7.1) in the Hydrological Open Air Laboratory (HOAL) - a 66 ha well-instrumented research catchment located in Petzenkirchen, Lower Austria, focusing on long-term scientific experiments that investigate surface-groundwater interactions (Blöschl et al., 2016). For further details on the study area revisit Chapter 6. The objective was the geophysical characterization and subsequent development of conceptual hydrogeological model of the catchment. The majority of the 76 profiles were collected as frequency-domain induced polarization (IP) measurements at 1 Hz excitation frequency, applying a range of electrodes spacings between 1-5 m and a multiple-gradient (MG) electrode configuration (Dahlin and Zhou, 2006), targeting a depth of investigation between 15-60 m. The data were collected using a DAS-1 instrument (from MultiPhase Technologies). Most of the profiles in the stream area were collected as time-domain IP measurements using smaller electrode spacings between 0.5-2 m and a dipole-dipole (DD) electrode configuration combining different skip-values (Slater et al., 2000; Flores Orozco et al., 2018b). Consequently, the targeted depth of investigation was shallower with a maximum of approximately 30 m depth. Data collection was performed with a Syscal Pro (from Iris Instruments) using pulse lengths of 500-2000 ms to obtain information on the IP effect.

Additional to the large-scale CCI mapping, 13 time-domain IP profiles were collected to provide detailed information about the subsurface electrical properties down to 15 m depth, as required prior to planned drilling of eight boreholes in the catchment (Figure 7.1). A multi-skip DD electrode configuration along with 72 electrodes and 1 m spacing was deployed and the data collection was performed using a Syscal Pro with a pulse length of 2000 ms. Where applicable, perpendicular profiles were collected to obtain information about possible 3D subsurface geometries. For all profiles in consideration (mapping and boreholes profiles), low contact resistances (< 0.5 kΩ) were observed, due to the fine-grained sediments typical for the HOAL, resulting in injected currents between 300-700 mA.

Processing of the data consisted of (1) removal of outliers and (2) inversion of the imaging datasets. In a first step, measurements characterized by negative transfer resistances $R = V/I$ (with V and I being the measured voltage and injected current, respectively) were removed. Such measurements are related to low signal-to-noise ratios, typical for excessively conductive or resistive environments, with the HOAL, characterized by its heavy soils, representing a particularly conductive environment. In a second step, different processing approaches were applied, depending on the type of IP measurement (time or frequency domain). For time-domain IP measurements, the decay-curve analysis (DCA) processing methodology (Flores Orozco et al., 2018a) was employed to remove measurements associated to erroneous decay curves (i.e., the voltage decay after current shut-off) by comparing each decay curve to an average decay curve computed for a subset of the imaging dataset. For frequency-domain IP data, the processing methodology outlined by Gallistl et al. (2018) was used, which is a modification of the DCA scheme adapted to frequency-domain data and is based on the same fundamental assumption that pseudosections (i.e., the representation of measured raw data), should reveal spatial consistent patterns with gradual changes in the measured IP effect. For further details on the approach, refer to Gallistl et al. (2018). The inversion of the filtered imaging datasets was performed using ResIPy (Blanchy et al., 2020), a smoothness constrained complex resistivity inversion scheme. For this purpose the time-domain IP datasets were linearly converted to frequency domain datasets assuming a constant-phase response (Van Voorhis et al., 1973; Flores Orozco et al., 2012a). All inversions converged to a root-mean-square error of approximately 1.

7.2.2 Complementary geophysical data: seismic imaging

To evaluate the CCI imaging result at the planned borehole locations, seismic imaging in terms of refraction seismic tomography (RST) and multichannel analysis of surface waves (MASW) was conducted (Lankston, 1990; Everett, 2013; Park et al., 1999).

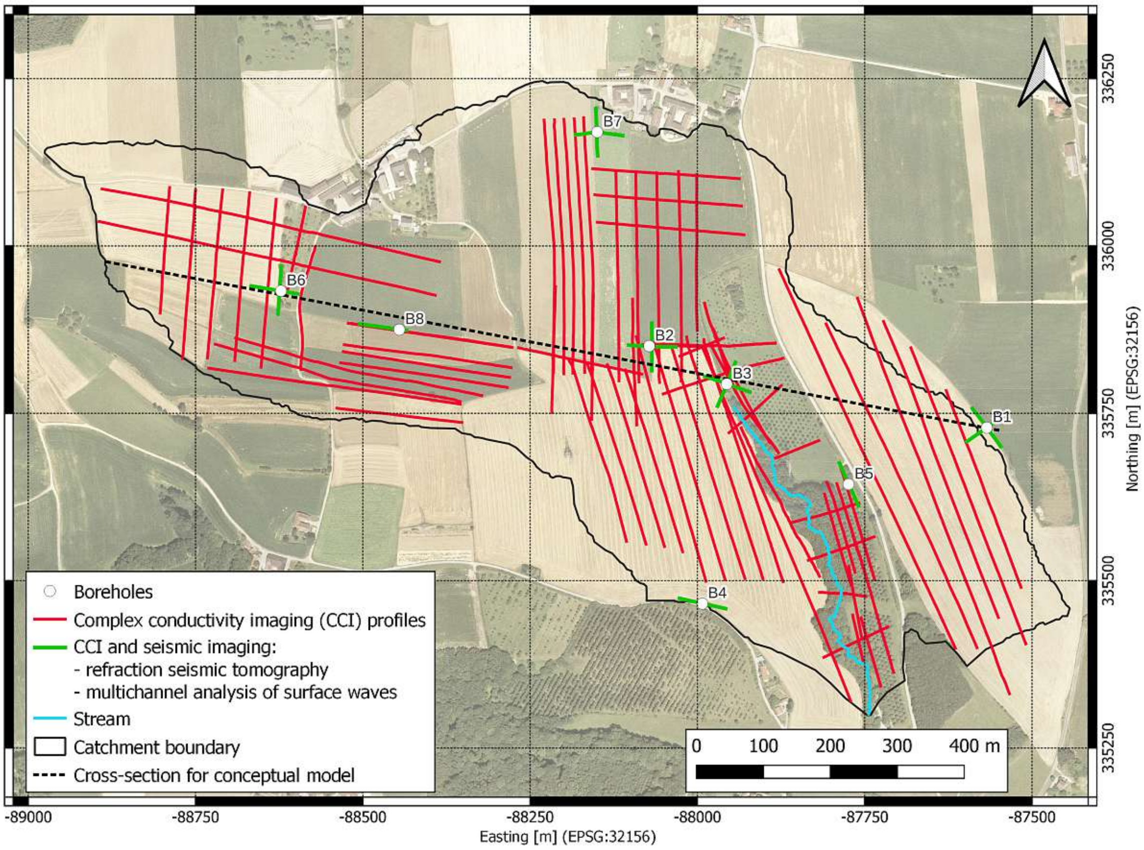

Figure 7.1: General overview of the catchment, location of the complex conductivity imaging (CCI) and seismic imaging profiles and location of boreholes.

The locations of the profiles are identical to the CCI profiles (c.f. Figure 7.1) and the data collection comprised profiles of 48 vertical 30 Hz geophones each, with a spacing of 1 m between each geophone and employing a record length of 1024 ms with 0.5 ms sampling rate. The generation of the seismic wavefield was accomplished with a 5 kg sledgehammer, and shots outside of the receiver spread at -10, -8, -4, -2 and 50, 52, 54, 56 m along the profile and inline at every second geophone starting with geophone 1 were performed with one shot at each location. This geometry facilitated the processing of the data for both RST and MASW.

Processing of the RST data involved signal processing (band-pass filtering, amplitude correction and removal of noisy traces) and the picking of first arrivals of the refracted waves. Inversion was performed with Rayfract^{TM} (Intelligent Resources Inc) to obtain a 2D P-wave velocity field. The surface waves processing entailed combining all shots to generate a single dispersion curve, extraction the first mode of the disperion curve in the dispersion image, and inverting the picked dispersion curve with ParkSEIS (Park Seismic LLC) to obtain a 1D model of the seismic S-wave velocity in

Table 7.1: Drilled depth in each borehole and number of samples analyzed in the laboratory for grain size distribution, total organic carbon, pH and $CaCO_3$.

Borehole	Depth [m]	Laboratory samples
B1	15	7
B2	15	9
B3	8	6
B4	15	8
B5	15	9
B6	15	10
B7	36	7
B8	15	9

the center of the profile.

7.2.3 Ground-truthing through borehole information

To gain information about the soil textural and possible hydrogeologcial situation in the HOAL, eight boreholes (Figure 7.1) were drilled down to a depth of 15 m, with boreholes B3 and B7 being exceptions reaching depths of 8 and 36 m, respectively. Coring was performed in each borehole and the predominant units in the retrieved sediments were sampled for a subsequent laboratory analysis which included grain size distribution based on sieving and sedimentation analysis (ÖNORM L 1061-2) to obtain the volume fractions of sand, silt and clay, and the quantification of total organic carbon (TOC), pH and $CaC0_3$ (with reference to ÖNORM L 1080, ÖNORM L 1083 and ÖNORM L 1084). The number of samples along with the drilled depths are presented in Table 7.1.

7.3 Results and discussion

7.3.1 Boreholes reveal occurrence of artesian aquifer system within lignite sequences

The recovered cores in boreholes B2, B3, B5, B7, and B8 revealed the presence of layers of lignite (Figure 7.2), a low-rank brown coal that forms at the early stage in coal formation. This discovery provides insight into the geological history of the area, as lignite formation is part of a complex process that begins with the accumulation of plant material in swampy areas. Over time, this organic matter partially decomposes to form peat deposits, which are subsequently buried beneath marine sediments due to rising sea levels or land subsidence. The weight of these overlying sediments compresses the peat, and under high temperatures, it gradually transforms into coal, with lignite representing an intermediate stage in this transformation (Závodská and Lesn'y, 2006; Keppeler, 2015).

The lignite unit observed in the boreholes consists of sequences of consolidated and unconsolidated layers in different thicknesses (Figure 7.2). The consolidated layers comprise dry, hard silty/clayey lignite with diminishing fractions of sand, while the unconsolidated layers were highly saturated and featured a wide range of poorly sorted grain sizes with pebbles up to 6 cm. The consolidated layers function as aquitards due to the high clay content (up to 50%), whereas the unconsolidated layers can be classified as aquifers, as evidenced by observed wetness during drilling. Moreover, at borehole B2 one of the many unconsolidated lignite layers corresponds to an confined aquifer, resulting in the formation of an artesian well in B2, with the groundwater level significantly above surface level (~ 1.3 m). This fact forced the reduction of the maximum depth for the drilling of B3 to 8 m. Boreholes B1 and B6 did not reveal any lignite, possibly due to its presence at depths below 15 m. To investigate this hypothesis, borehole B7 was drilled to a substantially larger depth, albeit without continuous core recovery. At approximately 36 m, unconsolidated, saturated, and brownish materials were recovered which were interpreted as one of the unconsolidated lignite aquifers. The core in B4 revealed an earlier stage of lignite formation, characterized by lower compaction and lighter coloration, without the presence of unconsolidated and consolidated layers. The occurrence of lignite was unexpected as the geological prior information indicated siltstones at depth. In general, lignite layers, respectively brown coal have so far only been reported for the Styrian (Bechtel et al., 2002), Vienna (Bechtel et al., 2007) and Alpine Foreland Basin in Upper Austria (Bechtel et al., 2003). Lignite seams do not necessarily need to follow surface topography and their thicknesses can reach from a few dm to tens of meters, thus can be relatively complex, particularly when fracturing is expected (Bechtel et al., 2007; Widera, 2013; Widera, 2016).

To understand the hydrogeological setting in the HOAL, two scenarios could be proposed: (1) the lignite is continuous throughout the catchment and functions as a confining layer without fractures, with smaller aquifer systems within the lignite sequence that are not connected to the overlying sediment system/unconfined aquifer (Figure 7.3a), or (2) the lignite exists as several disconnected lignite seams with varying thickness, potential fractures, and possible recharge through surface water, wherein the lignite may not be continuous throughout the catchment (Figure 7.3b). Evidently, (2) presents a more complex model than (1) and, therefore, as an initial approach to understanding the hydrogeological situation in the HOAL, the conceptual model of scenario (1) was employed for further investigations.

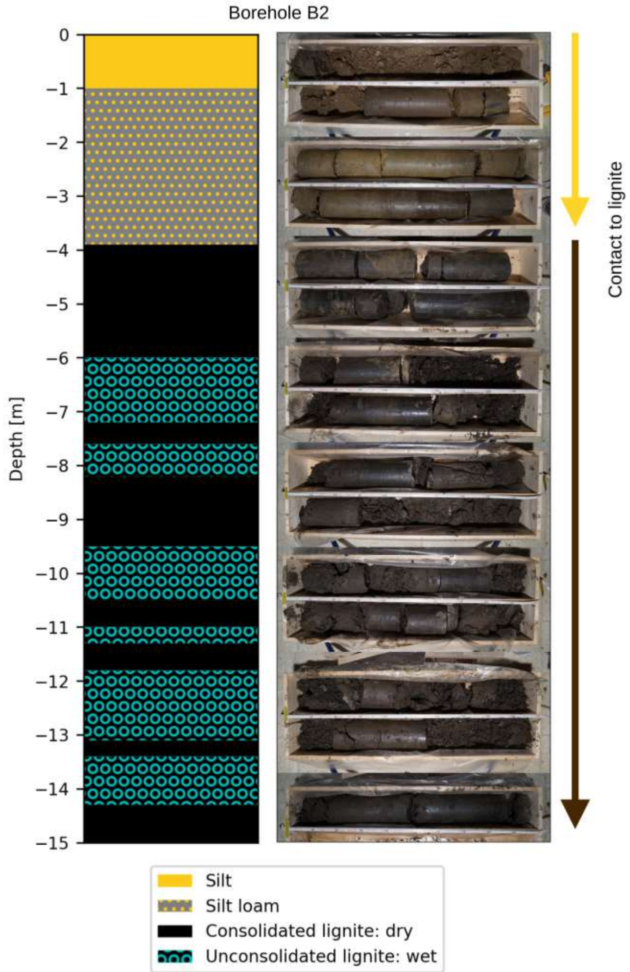

Figure 7.2: Simplified lithological description of borehole B2 and recovered core.

7.3.2 Mapping lignite contact with geophysical imaging

The realization of the aforementioned conceptual model necessitates sufficient contrast in the electrical properties at the depth of the contact to the lignite sequence. If such contrast exists, the extensive CCI mapping could be used to create a map of the lignite elevation and depth for the entire catchment. To evaluate the performance of the applied geophysical imaging methods in this regard, Figure 7.4 presents the imaging results of the CCI, RST, and MASW methods in comparison to the grain size distribution (GSD) and TOC for two selected boreholes. CCI results in terms of the real ($\sigma\,'$) and imaginary ($\sigma,''$) part of the complex conductivity σ^* for B3 demonstrate a gradual increase from roughly 2 to 6.5 m depth with $\sigma\,'$ and $\sigma,''$ values increasing from 40-110 mS/m and 100-400 μS/m, respectively. Below the lignite contact, at 6.5 m depth, $\sigma\,'$ remains constant and $\sigma,''$ decreases slightly to values of $\sim$ 350 μS/m. The change in textural composition for the first three meters, characterized by an increase

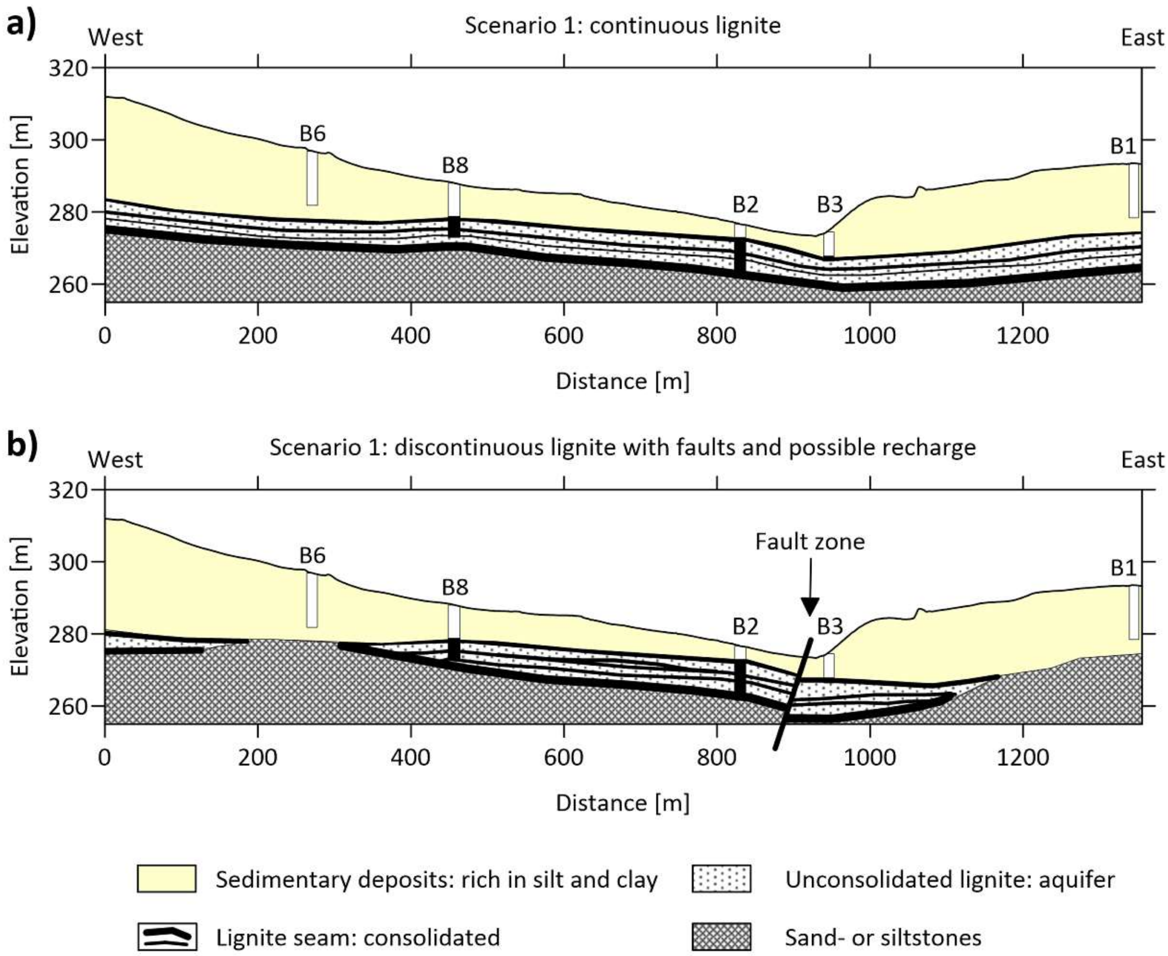

Figure 7.3: Conceptual hydrogeological models for a west-east cross-section in the HOAL (c.f. Figure 7.1) assuming a) a continuous and b) discontinuous lignite sequence.

in sand content (to 10%) and a decrease in clay (from 25 to 10 %), is resolved by both electrical properties, whereas σ' appears to provide slightly more contrast. Similar observations can be made for B5. However, the gradual increase up to the depth of the lignite contact is much more pronounced in σ,″ than σ', with σ'' revealing an increase from 250-625 μS/m in the depth range between 2 and 7 m. In contrast to B3, below the lignite contact (at 6.5 m depth), both electrical properties show a decrease in values, again much more pronounced in σ'' which decreases to a value of 250 μS/m. Nevertheless, for both boreholes σ'' shows a maximum approximately at the depth of the lignite contact, which corresponds to an increase in TOC to 1-2 %. In general, TOC is expected to decrease with depth due diminishing organic input from plant matter, roots exudates, bioturbation and microbial activity (Rumpel and Kögel-Knabner, 2011; Yang et al., 2022). With lignite forming from carbon rich peat layers, the observed increase in TOC can be easily explained and delineation of the

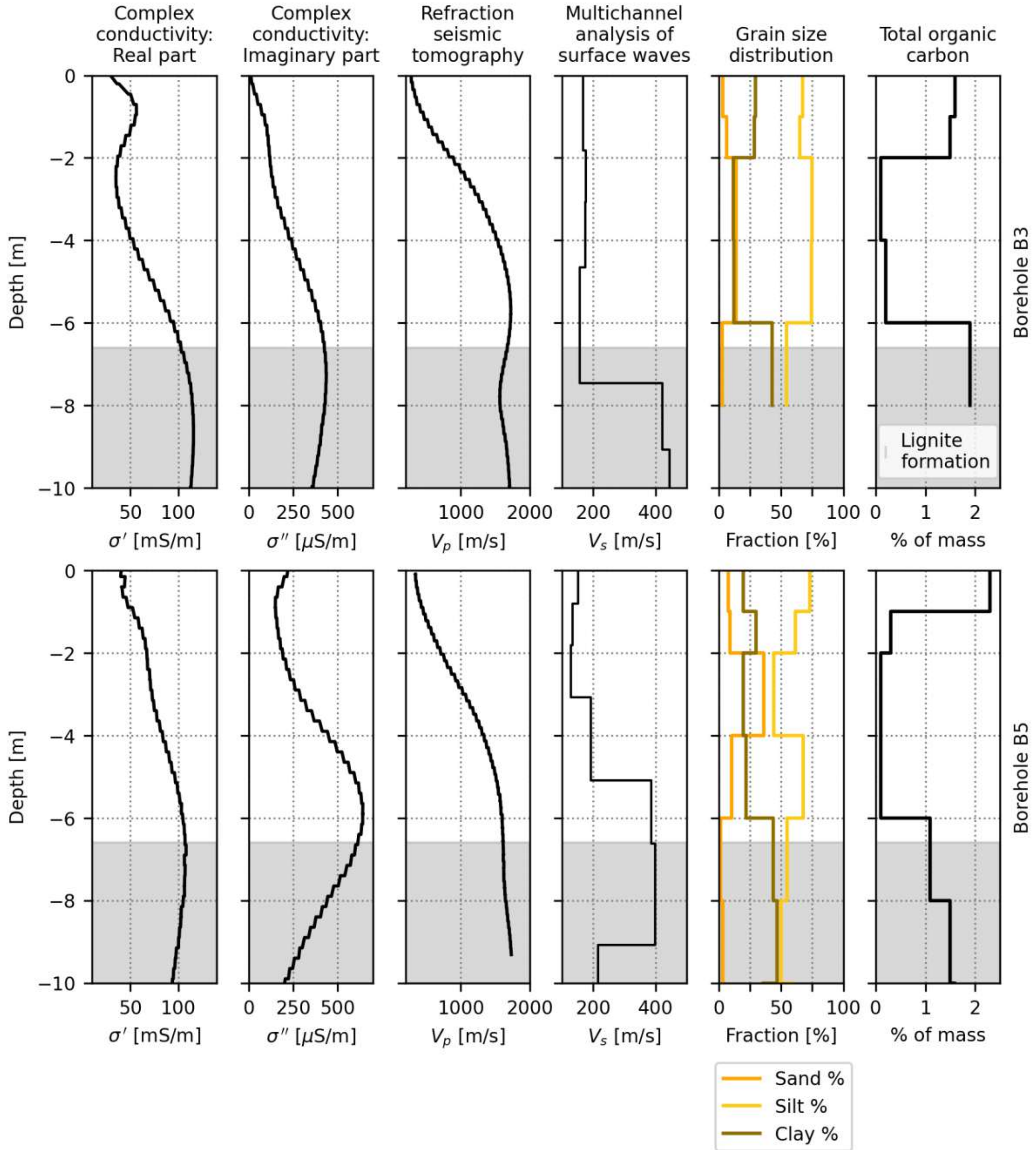

Figure 7.4: Columns 1-4: Geophysical imaging results in terms of the real σ' and imaginary σ'' part of the complex conductivity σ^* and the P- (V_p) and S-wave (V_s) velocity obtained from seismic imaging. Columns 4 and 5: Ground-truth information as grain size distribution (i.e., the volume fractions of sand, silt and clay) and total organic carbon (TOC). The grey box indicates the contact to the lignite sequence.

lignite contact could potentially be realized through mapping of increased TOC values at depth. However, this would require robust petrophysical relationships.

Seismic imaging in terms of RST shows an increase in P-wave velocity down to the lignite contact with V_p values increasing from ~ 500 to 1500 m/s. A plateau (B5) and

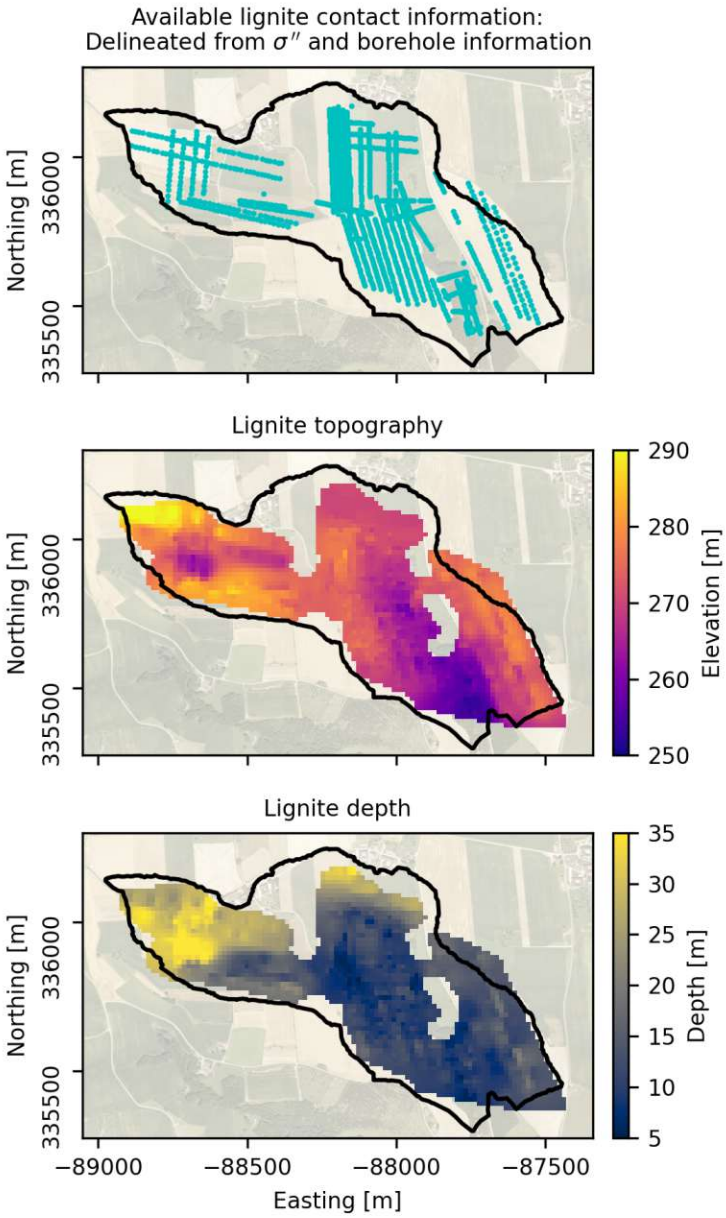

Figure 7.5: Map of the lignite elevation (top) and depth (bottom) based σ'' imaging results for all available profiles in the catchment and incorporating the lignite depth/elevation from borehole information.

maximum value (B2) in V_p can be observed at the approximate depth of the lignite contact, which probably refers to the uppermost consolidated lignite layer, yielding a higher seismic velocity due to compaction of the dry and hard clay. An alternative explanation could be an increase in saturation, as observed in the unconsolidated layers (Milkereit et al., 1986). Moreover, B3 shows a slight decrease in V_p directly below the lignite contact, which, potentially could be correlated with an unconsolidated lignite layer. However, as velocity decreases are notoriously difficult to resolve with RST

(Kearey et al., 2002; Whiteley and Eccleston, 2006; Yari et al., 2021), the interpretation of this anomaly as an unconsolidated layer may be speculative. Furthermore, no such anomaly was observed in the RST results for any other borehole. The results from MASW indicate an increase in S-wave velocity at the depth of the lignite contact from approximately 125 to 400 m/s, consistent to the other discussed methods.

All geophysical methods presented in Figure 7.4 share the characteristic that only the depth to the contact to the lignite can be resolved; however, not the different sequences within it (i.e., consolidated and unconsolidated). Mapping of different layers within the lignite would likely require borehole or borehole-surface measurements not feasible if catchment-scale information is needed. Moreover, all methods show slight discrepancies regarding the estimated depth of the lignite contact, with vertical offsets of ± 1-1.5 m. However, for the realization of an initial hydrogeophysical model this accuracy is sufficient and can be refined with detailed geophysical investigations if necessary.

Given that σ'' revealed the most significant contrast at the lignite contact, this information was used to map lignite depth and elevation throughout the catchment. To achieve this, a semi-supervised approach was developed based on the calculation first derivatives of the σ'' field (sections) to compute the inflection points and, thus, the maxima in their distribution. The obtained depths were visually inspected and reviewed for inconsistencies with neighboring profiles. Moreover, the known lignite depths from boreholes were incorporated.

Maps of lignite depth and elevation, as presented in Figure 7.5, are based on kriging interpolation without direction smoothing and circular searching space. Figure 7.5 demonstrates that, based on the geophysical delineation from the σ'' contrast, the lignite appears to neither follow the surface topography, nor is strictly horizontal. Instead, it shows an undulating topography throughout the catchment, with topographically elevated areas in the western, southwestern and eastern parts, whereas the lowest elevations can be observed in the area surrounding the stream. A significant depression can be observed in the western part of the catchment with elevation gradients of up to 40 m, which may explain why B6 did not reveal lignite in the retrieved cores. The origin of this depression cannot be explained easily. As is refers to well-resolved areas along the CCI profiles and is consistent with neighboring profiles, the possibility of it being an inversion artifact was discounted. Moreover, due to the depth of the observed σ'' anomaly, the likelihood of it being the polarization response due to anthropogenic sources, such as power cables or buried metallic objects, is minimal. To sustain the interpretation of the depression, an evaluation with other potentially deep-reaching geophysical methods, such as transient electromagnetic soundings (TEMs) should be considered (Danielsen et al., 2003; Bücker et al., 2017).

7.3.3 Experimental petrophysical relationships for soil-textural prediction

With the topography of the confining consolidated lignite layer established, the next step towards the realization of the hydrogeophysical model is the quantification of hydraulic conductivity K for the sediments above the lignite layer. To achieve this, either petrophysical relationships, that permit the prediction of K from geophysical parameters or the two-step approach discussed in Chapter 6, which comprises first linking the geophysical parameters to GSD first and then using a PTF to predict K, is required. Given the availability of GSD data at eight boreholes, totaling 82 samples, it was determined that developing site-specific petrophysical relationships would be more appropriate, thus opting for the aforementioned two-step approach rather than rely on upscaling of laboratory-derived relationships, which may not be representative of the soil-physical environment at the study area. To this end, values of the real and imaginary part of the complex conductivity were extracted from the CCI profiles at the depth and location of the borehole samples and correlation analysis using split-sample validation (SSV) was performed. SSV ensures the generalizability of the derived relationships by evaluating the prediction results on unseen data that were not used in the developing of the correlation. For this purpose, the dataset was divided into 80% calibration and 20% validation data. As previously discussed, σ' revealed the most significant sensitivity to soil-textural changes, and, consequently, the following results are only show the correlations with σ'. Similar correlations could be obtained for σ''; however substantially lower R^2 and RMSE values were observed, thus rendering σ' the more suitable predictor variable.

Results of the SSV analysis are presented in Figure 7.6 with each row corresponding to one soil fraction under consideration: column 1 shows linear model fitted to the calibration set, while the validation set presented in column 2 can be used to evaluate the validity of the fitted model. Columns 3 and 4 present the comparison of the sampled and predicted soil fraction for the calibration and validation sets, respectively. As no significant correlation between σ' and the sand fraction could be established, R^2 and RMSE scores are not indicated in Figure 7.6. The plotted linear model is computed as follows:

$$f_{sa} = 100 - (f_{si} + f_c). \tag{7.1}$$

Figure 7.6 demonstrates distinct relationships between σ' and the silt and clay fraction. For silt, a negative correlation (R^2=0.46) can be observed, which is adequately replicated by the validation set. Regarding the prediction performance, comparable RMSE scores (with 7 and 8.5%) can be reached, albeit with a slight overestimation of the intermediate silt range (60-75%). In contrast, a positive relationship of the fraction of clay with increasing σ' can be observed with a comparable R^2 score of 0.45 and similar performance on the validation set. However, for the clay fraction the prediction performance is slightly inferior with RMSE scores of 7.9% for the calibration and 9.4% for the validation set. An increase of σ' with increasing clay content is expected, as for soil textures with an abundance of clay the conduction mechanism shifts from electrolytic conduction to surface conduction along the mineral grain, in the electrical double layer, typically associated with an significant increase in σ' (Ghorbani et al., 2009; Okay et al., 2014).

Figure 7.7 presents the prediction functions derived from the correlation analysis for the different soil fractions, as well as the model parameters of the linear regression models. A comparison with the prediction functions presented in Chapter 6 reveals a similar prediction trends of the obtained relationships. The slopes of the linear models presented in Chapter 6, based on the electrical conductivity (EC) from electromagnetic induction imaging measurements rather than the real part σ' of the complex conductivity, indicate a steeper increases and decreases in the silt and clay prediction, approximately a factor 2 larger than the slopes presented here. Consequently, the cross-over threshold, where the clay fraction exceeds the the silt fraction shifts from approximately 65 mS/m to 120 mS/m. Moreover, this results in a different behavior for the fraction of sand, which now decrease from values of approximately 10-5% for the σ' range under consideration. Nevertheless, the general patterns remain consistent, which permits the application of the recalibrated PTF presented in Chapter 6 to predict saturated hydraulic conductivity.

7.3.4 Progressing towards a hydrogeophysical representation of the HOAL

Considering the decrease in resolution and increase in coarseness of the model discretization of CCI with depth, K_s prediction was performed for nine depth ranges (Table 7.2); smaller depth ranges were used for the shallower depths, with increasingly larger depth ranges for greater depths. The use of 2 m for the first three depth range also represents the many different deployed electrode spacings in the CCI profiles and can be considered as a spatial smoothing filter to average the shallow information from profiles with different lateral resolution. To obtain spatially continuous information, all predicted K_s values in the corresponding depth range were used for the natural neighbor interpolation on a 15x15 m grid, disregarding different elevation values within

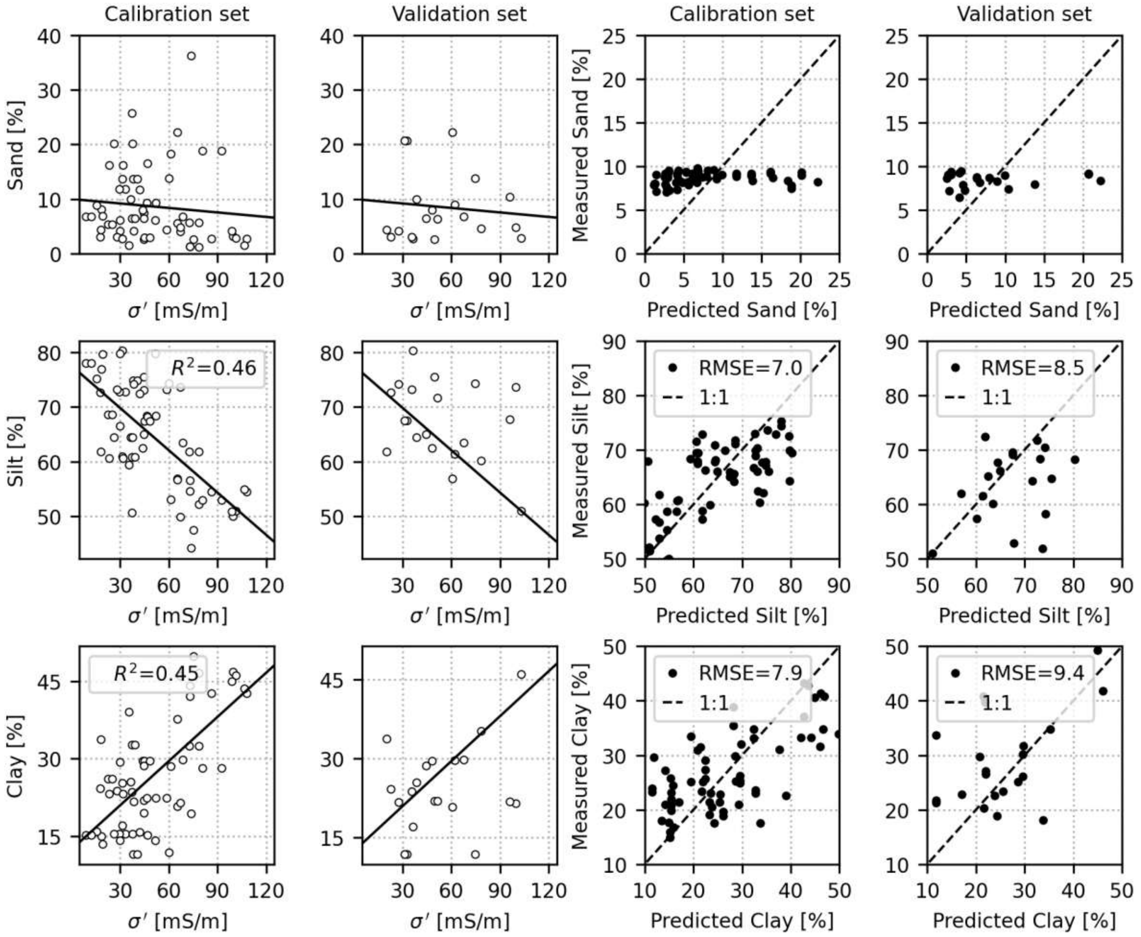

Figure 7.6: Correlation and split-sample validation of the σ' and the different soil volume fractions of sand, silt and clay.

the depth slice. Consequently, the interpolated K_s maps represent an average value of the depth slice.

The K_s maps presented in Figure 7.8 reveal significant variations in the spatial patterns and histograms for the depth ranges under consideration. While shallower depths (between 0-8 m) are associated to K_s values in the range of approximately 10-18 mm/h, with increasing depth, a broadening and shift of the K_s distribution in the histograms towards lower values in the range of 4-12 mm/h can be observed, accompanied by distinct spatial changes. For instance, the hydraulically conductive channels (> 12 mm/h) traversing in west-east direction in the central part of the catchment are less pronounced at greater depths. At these depths, a shift towards large areas of significantly low K_s values (< 4 mm/h) can be observed, particularly for the northern and eastern regions. The comparison of the K_s maps in D_1 and the maps obtained from the EMI survey in Chapter 6, which approximately refer to

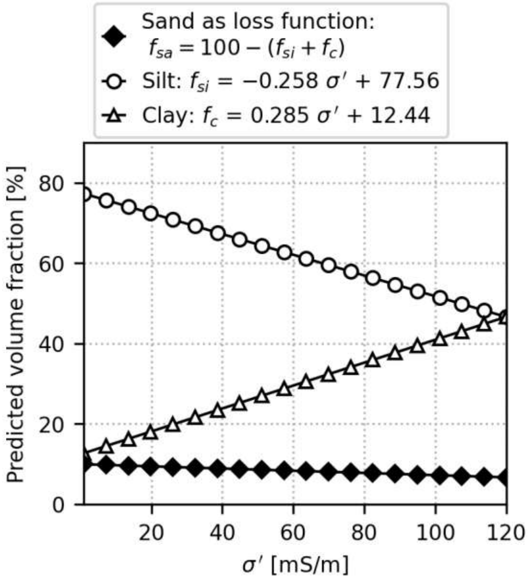

Figure 7.7: Functions to predict the different soil fractions of sand, silt and clay based on their dependence on σ'.

the same depth of investigation, reveals consistent results for depths below 0.5 in the EMI survey. Shallower K_s maps with increased K_s values larger than 30 mm/h in the EMI survey are simply not resolved in the CCI mapping profiles, which are not sensitive to small scale σ' and thus K_s variations in the uppermost subsurface layers. Nevertheless, for depths below 0.5 m consistent spatial patterns and K_s ranges can be observed for both approaches.

Provided the means to predict K_s down to the depth of the lignite sequence, the conceptual model presented in Figure 7.3a can be reevaluated and parameterized. The updated hydrogeophysical model, as illustrated in Figure 7.9, indicates distinct spatial

Table 7.2: Depth ranges used for the prediction of K_s and subsequent interpolation of K_s maps.

Layer	From [m]	To [m]
D_1	0	2
D_2	2	4
D_3	4	8
D_4	8	12
D_5	12	18
D_6	18	24
D_7	24	30
D_8	30	36
D_9	36	45

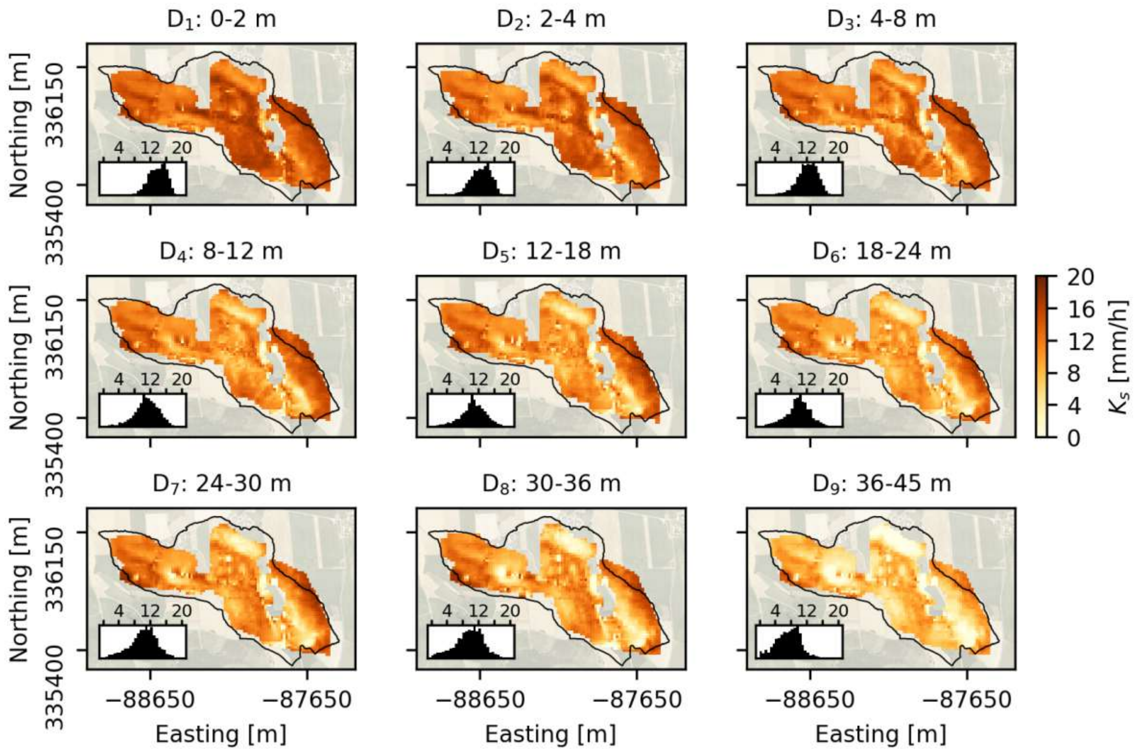

Figure 7.8: Predicted saturated hydraulic conductivity K_s maps and the associated normalized histograms for different depth ranges.

K_s variations along the cross-section characterized by hydraulically conductive areas (K_s between 12-18 mm/h) and hydraulic barriers, where K_s is significantly below 8 mm/h. Notably, such barriers can be observed between boreholes B6 and B8, as well as east of B3. However, further east of B3, there is a gap in both the K_s and lignite contact information, due to the lack of CCI profiles in this particular area (c.f. Figure 7.1), hindering the interpretation of the further extend of such hydraulic barrier. Moreover, Figure 7.9 reveals a minor discrepancy between the lignite contact depth at borehole B2 as obtained from CCI and the borehole information. To investigate this inconsistency, as well as the depression at 200 m along the cross-section, further geophysical investigations are necessary, potentially employing other geophysical methods such as TEM and seismic imaging. The latter, in particular, has demonstrated promising results in delineating the lignite contact, as previously discussed.

As of the present date, there are no comparable field-scale studies that have investigated the quantification of hydraulic conductivity for catchment characterization based on CCI. While previous publications explored the potential of CCI to predict K_s at the field-scale (Hördt et al., 2007; Attwa and Günther, 2013; Maurya et al., 2018), such studies were limited to significantly smaller areas or even single profiles

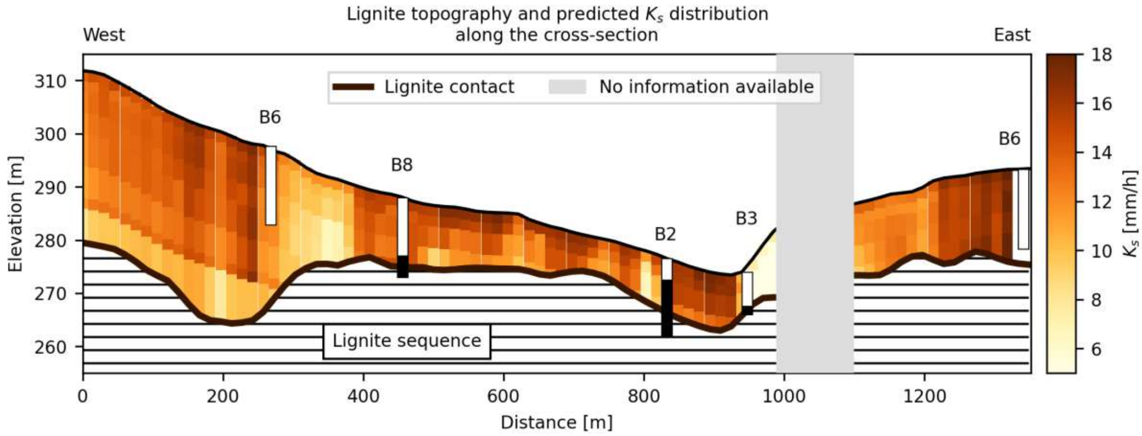

Figure 7.9: Updated hydrogeophysical cross-section incorporating the lignite contact depth and K_s predictions from CCI.

and much smaller depths of investigation. Moreover, the K_s predictions presented in such studies rely on upscaling of laboratory-derived petrophysical relationships, the use of which present challenges such as fitting of specific model parameters or using proxy values for parameters not readily available in field applications (Gallistl et al., 2022; Flores Orozco et al., 2022). In contrast, the multi-step framework outlined herein offers a straightforward and scalable approach to quantify K_s and represents a significant advancement in establishing CCI as a readily applicable tool for hydrogeophysical applications.

7.4 Conclusion

The comprehensive geophysical investigation of the HOAL catchment using large-scale CCI, seismic imaging, along with borehole information has provided valuable insights into the subsurface structure and hydrogeological characteristics of the catchment. The unexpected discovery of lignite layers in the catchment revealed a complex geological history and hydrogeological setting, leading to the development of two conceptual models, whereas only one was considered for the development of a hydrogeophysical model. The conceptual model under consideration features a continuous confining lignite layer with potential artesian aquifer systems. CCI, particularly the imaginary part of complex conductivity, successfully mapped the lignite contact throughout the catchment and seismic imaging was used to evaluated the approach. Site-specific petrophysical relationships linking electrical properties to soil texture were established, enabling catchment-scale prediction of soil textural parameters and consequently spatially-distributed K_s values at various depths above the lignite layer.

This multi-step approach has resulted in a detailed hydrogeophysical model of the HOAL catchment, providing unprecedented insights into its subsurface structure and hydraulic properties at greater depths, when compared to the existing approaches. The methodology developed represents a significant advancement in using CCI for catchment-scale characterization and quantification of hydraulic conductivity, which is crucial for the understanding of run-off processes and the modeling of groundwater recharge and its availability. While some uncertainties remain, particularly regarding the exact depth of the lignite contact in certain areas and the nature of observed depressions in the lignite topography, this study lays a strong foundation for future hydrogeological investigations and modeling efforts in the HOAL catchment. Further geophysical investigations, such as TEM and additional seismic imaging, could help refine the model and address remaining uncertainties.

8 Conclusions and perspectives

8.1 Perspectives for future research activities

8.1.1 Extensions to the deep learning network

8.1.1.1 Incorporation of other geophysical forward models

While Chapter 6 explored the applicability of DL networks (DLNs) in the realm of EMI, its potential extends beyond this specific geophysical method or the forward models presented therein. A more comprehensive approach could involve using a full solution of Maxwell's equations to compute the primary H_P and secondary magnetic fields (H_S) to account for both the in-phase and quadrature phase components (Ward and Hohmann, 1988):

$$\text{in-phase} = \mathrm{Re}(\frac{H_S}{H_P}) \tag{8.1}$$

$$\text{quadrature-phase} = \mathrm{Im}(\frac{H_S}{H_P}). \tag{8.2}$$

The in-phase component is proportionally related to the subsurface magnetic susceptibility χ (Won et al., 1998; Farquharson et al., 2003), while the quadrature-phase component is linked to the subsurface electrical conductivity (McNeill, 1980a). To implement this approach, the n-layered model for forward modeling would need to be extended to include the information the χ and dielectric permittivity in each layer, necessitating adaptations to the training data generation processes.

Recent research by Mendoza Veirana et al., 2024 has revealed a significant correlation between the χ and the cation-exchange-capacity (CEC) and growing evidence suggests that CEC can be estimated from IP measurements (Revil et al., 2021; McLachlan et al., 2024), indicating that IP data could be leveraged for generating training datasets. Incorporating χ into the DLN could expand its applicability to archaeological prospection (De Smedt et al., 2014; Simon et al., 2015; Delefortrie et al., 2018) and potentially resolve interpretation ambiguities in areas where the EMI response is governed by χ rather than the subsurface EC distribution, particularly in situations where the LIN approximation is not valid.

Further modifications to the forward model could include the integration a 3D forward operator, enabling the investigation of subsurface structures with inherent 3D characteristics (Cockett et al., 2015; Guillemoteau and Tronicke, 2016; Peng et al., 2021). This modification would also require improved training data generation approaches to provide the required 3D information needed for the DLN to learn. A potential solution could involve using at least two perpendicular IP profiles and a subsequent interpolation to 3D volume. Alternatively, the use of pseudo-3D information, where the 2D IP profile is extruded in perpendicular direction to build a "3D" model could be investigated. As a final option, synthetic 3D models could be employed, potentially tailored to the study site.

Other potential geophysical methods include the transient electromagnetic method (Danielsen et al., 2003; Christiansen et al., 2006) and seismic imaging based on Rayleigh wave dispersion in the form of multi-channel analysis of surface waves (Park et al., 1999; Xia et al., 1999) or multi-offset phase analysis (Strobbia and Foti, 2006; Barone et al., 2020; Barone et al., 2021). In the case of transient electromagnetic method, the DLN could be adapted to handle time-domain data, learning to map the temporal decay of electromagnetic fields to subsurface 1D EC models. Implementing such an approach would require adequate generation procedures for the training datasets, taking into account the subsurface model parameters (layer ECs and thicknesses) as well as transmitter and receiver characteristics (loop size and shape, current amplitude, waveform and time range of measurements, among others). Such procedures could rely on deep ERT surveys or synthetic models; whereas constructing a training dataset based on field-data specific to the site is preferable. For the surface waves methods, integrating the information from dispersion curves and potentially waveforms could enable the DLN to learn to predict 1D shear-wave velocity models. Considering that such approaches are based on Rayleigh-wave dispersion (Schwab and Knopoff, 1972; Xia et al., 1999), the subsurface models need to be parametrized in terms of the shear-wave velocity, the layer thicknesses and densities as well as Poisson's ratios or P-wave velocities. Moreover, source and receiver array characteristics must be considered.

8.1.1.2 Uncertainty quantification

A major enhancement for the deep learning network (DLN) presented in Chapter 6 would be the quantification of uncertainty associated with it. To fully understand how uncertainty can be represented in DLNs, it is necessary to consider the sources of uncertainty: aleatoric and epistemic uncertainty (Hora, 1996; Hüllermeier and Waegeman, 2021). Aleatoric uncertainty, also referred to as statistical uncertainty, describes the inherent randomness and, thus, the variability in the outcome due to inherently random effects. It captures the uncertainty arising from the natural variability in the input data and cannot be reduced by more observations or improving the model (Kendall and Gal, 2017; Hüllermeier and Waegeman, 2021; Acharya et al., 2024). Conversely, epistemic, or systematic uncertainty, refers to the model's uncertainty about its own predictions and is caused by a lack of knowledge; therefore, it can be reduced by a larger number of observations (Hüllermeier and Waegeman, 2021; Abdar et al., 2021). As such, it represent the model's confidence in its predictions based on the training data it has seen (Kendall and Gal, 2017; Fellaji and Pennerath, 2024; Jürgens et al., 2024). Hence, epistemic uncertainty refers to the uncertainty in model predictions, when encountering data not seen in the training stage, requiring the model to extrapolate beyond its learned knowledge.

As noted by Hüllermeier and Waegeman, 2021; Der Kiureghian and Ditlevsen, 2009 aleatoric and epistemic uncertainty may not be considered as absolute notions, and, in fact, depend on the context and the model. Consequently, changing the context might transform aleatoric into epistemic uncertainty and vice versa (Hüllermeier and Waegeman, 2021). This notion is further supported by the substantial number of publications (> 2500) regarding uncertainty quantification in artificial intelligence between the years 2010 and 2021, as reported in Abdar et al., 2021. As a highly dynamic research field, there is still no consensus on best practices for addressing uncertainty quantification, with various potential solutions being currently discussed including adhoc approaches and approaches embedded in statistical or probabilistic frameworks.

Bayesian neural networks (BNNs) are an extension of standard deep neural networks that incorporate probabilistic principles to capture uncertainty in model parameters and predictions (Goan and Fookes, 2020; Jospin et al., 2022). Unlike traditional neural networks that provide point estimates, BNNs offer probability distributions over output predictions and model weights, enabling better uncertainty quantification both in terms of aleatoric and epistemic uncertainty (Olivier et al., 2021; Jospin et al., 2022). The fundamental concept underlying BNNs is the application of Bayesian inference to neural network training, treating network weights as random variables with prior distributions (Jospin et al., 2022; Charnock et al., 2022). This approach allows for the quantification of epistemic uncertainty through the use of probability distributions over the model parameters, which is particularly useful in scenarios where data is limited or noisy (Woo, 2022; Linander et al., 2023). Aleatoric uncertainty, conversely, can be accounted for quantifying probability distributions for the in- and output, for instance, in terms of normal distributions with a mean and variance (Olivier et al., 2021; Caceres et al., 2021).

Notably, while BNNs appear promising due to sound probabilistic foundation and their ability to quantify both aleatoric and epistemic uncertainty, they are also presented with significant challenges in terms of computational overhead and scalability, which limit their applicability to smaller networks and often come with constraining assumptions (Lampinen and Vehtari, 2001; Sharma and Jennings, 2021; Franchi et al., 2024). Moreover, model selection, including determining the optimal number of nodes, remains an open question for BNNs, as traditional methods for architecture selection may not be directly applicable to BNNs due to their probabilistic nature (Ghosh et al., 2019; Yin and Zhu, 2020).

Deep ensemble (DE) learning has been proposed as an alternative to BNNs offering better computational scalability (Egele et al., 2022; Ganaie et al., 2022), while maintaining the potential to quantify both aleatoric and epistemic uncertainty. DEs involve training multiple neural networks independently and aggregating their predictions. Such ensembles can be constructed by applying different network structures using the same input data, applying identical network structures and input data but using a random initialization for each network in the training process, or by splitting the input data into different subsamples and either training different or the identical network structures and combing the predictions (Egele et al., 2022; Gawlikowski et al., 2023; Mohammed and Kora, 2023). Aleatoric uncertainty can be quantified through the variance in predictions across ensemble members for a given input, while epistemic uncertainty is represented by the disagreement between ensemble members (Lakshminarayanan et al., 2017; Mohammed and Kora, 2023). Other approaches include the decomposition of the predictive variance of DEs to separate the two types of uncertainties (Egele et al., 2022). While originally proposed as a non-Bayesian technique, recent work has shown that DEs can be viewed as an approximate Bayesian method under certain assumptions (Hüllermeier and Waegeman, 2021; Wild et al., 2024).

Both approaches, BNNs and DEs, could be easily implemented for the DLN presented in Chapter 6, as the used deep learning frameworks Tensorflow Martín Abadi et al., 2015; Abadi et al., 2016 and Keras Chollet et al., 2015 provide functionality for both approaches. While DEs are straight-forward to implement, the specific structure of the DLN with three coupled subnets could potentially impede the performance during prediction, as large number of models (3 times the number of models in the ensemble) must be maintained in memory due to the sequential nature of the implementation. Considering this, BNNs might be preferable, despite their challenges with scalability. Since the network dimensions are relatively small compared to DLNs used in natural language processing or pattern recognition in images and videos, scalability or memory limitations during training represent minor concerns. By modifying the training data generation process, uncertainty estimates could be provided and incorporated as prior information during training and prediction within the BNN. Alternatively, ready to use frameworks for uncertainty quantification such as Fortuna (Detommaso et al., 2023), that simplify benchmarking, could be explored.

8.2 Conclusions

All of the research objectives have been successfully addressed by the manuscripts in Chapters 3-6 as well as extended by the study in Chapter 7. The primary findings of the first study relate to significant improvements in data collection within the domain of SIP. The use of standard multicore cables caused substantial distortions in phase readings, even at low frequencies, impeding their applicability for single frequency applications. Conversely, coaxial cables demonstrated superior data quality, even with longer cable lengths than the used electrode spacing. The deployment of coaxial cables not only improved reciprocity in measurements but also simplified field procedures, as approaches that relied on using separate cables for current injection and voltage measurements are no longer necessary. These findings significantly enhanced the applicability of SIP at the field-scale, by potentially facilitating more opportunities to upscale laboratory results to the field-scale without the risk of misinterpreting ambiguous/noisy data.

Secondly, research in this thesis explored the application of EMI and (S)IP for landslide characterization. It was demonstrated that EMI mapping permitted to effectively identified lateral changes in electrical conductivity correlated with geomorphological features, while IP imaging successfully delineated the sliding plane geometry, soil types, and hydrogeological units. Additionally, SIP imaging revealed frequency-dependent polarization effects associated with grain size changes, critical for the understanding of hydrogeological units within the landslide and possible mobilization mechanisms. The combined application of EMI and IP was validated using extensive ground-truth data, demonstrating its suitability for characterizing clay-rich landslides. To date, IP imaging has become an increasingly established method in landslide research, and this thesis has contributed to its advancement.

The third objective focused on obtaining hydraulic properties from geophysical data. Site-specific petrophysical relationships were developed, linking imaginary complex conductivity obtained from IP and the electrical conductivity obtained from EMI to soil volume fractions of (gravel), sand, silt and clay. These relationships allowed for the estimation of textural properties consistent with soil sample measurements, with great care taken to obtain robust and validated relationships. To that end, where possible, split-sample validation analysis of the relationships was performed. Subsequently, a two-step approach was proposed to derive hydraulic conductivity from geophysical data using pedotransfer functions. This approach was validated through a comparison with predictions using laboratory-derived petrophysical relationships, wherein consistent predictions were obtained.

The fourth objective involved the investigation of deep learning techniques as an alternative to standard deterministic inversion of geophysical data. To that end, a deep learning network was developed, evaluated and applied, which permits the rapid and accurate prediction of 1D electrical conductivity depth models from EMI measurements. To emphasize the benefits of using such an approach, the 1D model predictions were used to derive catchment-scale hydraulic conductivity using the aforementioned two-step approach after recalibrating a pedotransfer function developed for the catchment.

In conclusion, the research presented in this thesis has made significant strides in advancing geophysical methods for soil-textural and hydraulic characterization. The comprehensive approach applied in this thesis, combining improved data collection techniques, innovative applications of EMI and IP for landslide analysis, along with the development of site-specific petrophysical relationships, has yielded valuable insights into complex hydrogeological systems. The proposed multi-step framework, incorporating deep learning and recalibrated pedotransfer functions, offers a promising tool for rapid and accurate soil textural and hydraulic characterization. Furthermore, the extensive geophysical investigation of the HOAL catchment has provided a deeper understanding of subsurface structures and their implications for hydrological and hydrogeological processes. These findings not only address the initial research objectives but also pave the way for future applications in non-academic settings, potentially facilitating landslide risk assessment and catchment-scale hydrogeological modeling. The integration of various geophysical methods and the development of robust petrophysical relationships demonstrate the power of interdisciplinary approaches in unraveling complex hydrogeological systems, ultimately contributing to more effective land management and hazard mitigation strategies.

Lists of Abbreviations and Acronyms

AIC	Akaike Information Criterion
BNN	Bayesian Neural Network
CC	Apparent Electrical Conductivity
CCI	Complex Conductivity
CEC	Complex Conductivity Imaging
CNN	Cation Exchange Capacity
CR	Convolutional Neural Network
CRI	Complex Resistivity
CS	Complex Resistivity Imaging
DC	Cumulative Sensitivity
DCA	Direct current
DD	Decay Curve Analysis
DE	Dipole-Dipole
DEM	Deep Ensemble
DL	Digital Elevation Model
DLN	Deep Learning
DPH	Deep Learning Network
ECa	Dynamic Probing Heavy
EC	Electrical Conductivity
EDL	Electrical Double Layer
EM	Electromagnetic
EMI	Electromagnetic Induction
ERT	Electrical Resistivity Tomography
FD	Frequency Domain
FDEM	Frequency-Domain Electromagnetic Induction
FZ	Flysch Zone
IP	Induced Polarization
GSD	Grain Size Distribution
GKZ	Gresten Klippen Zone
HCP	Horizontal Coplanar
HOAL	Hydrological Open Air Laboratory
LIN	Low Induction Number
MASW	Multichannel Analysis of Surface Waves

MG	Multiple Gradient
MGS	Minimum Gradient Support
MICP	Mercury Injection Capillary Pressure Method
MRE	Mean Relative Error
MSE	Mean Squared Error
NCA	Northern Calcareous Alps
NRCS	Natural Resources Conservation Service
PTF	Pedotransfer Function
ReLU	Rectified Linear Unit
RST	Refraction Seismic Tomography
RMSE	Root Mean Square Error
RTK-GNSS	Real Time Kinematic Global Navigation Satellite System
SCF	Sensitivity-Controlled Focusing
SIP	Spectral Induced Polarization
SSC	Sand, Silt, and Clay Volume Fraction
SSV	Split Sample Validation
TEM	Transient Electromagnetic Soundings
TDIP	Time-Domain Induced Polarization
TDR	Time-Domain Reflectrometry
TOC	Total Organic Carbon
VCP	Vertical Coplanar
VG	Van Genuchten (Parameters)

Bibliography

Aal, G. Z. A., L. D. Slater, and E. A. Atekwana (2006). "Induced-polarization measurements on unconsolidated sediments from a site of active hydrocarbon biodegradation". In: *Geophysics* 71.2, H13–H24.

Abadi, M., P. Barham, J. Chen, Z. Chen, A. Davis, J. Dean, M. Devin, S. Ghemawat, G. Irving, M. Isard, et al. (2016). "{TensorFlow}: a system for {Large-Scale} machine learning". In: *12th USENIX symposium on operating systems design and implementation (OSDI 16)*, pp. 265–283.

Abdar, M., F. Pourpanah, S. Hussain, D. Rezazadegan, L. Liu, M. Ghavamzadeh, P. Fieguth, X. Cao, A. Khosravi, U. R. Acharya, et al. (2021). "A review of uncertainty quantification in deep learning: Techniques, applications and challenges". In: *Information fusion* 76, pp. 243–297.

Abdu, H., D. Robinson, M. Seyfried, and S. B. Jones (2008). "Geophysical imaging of watershed subsurface patterns and prediction of soil texture and water holding capacity". In: *Water resources research* 44.4.

Acharya, A., C. Lee, M. D'Alonzo, J. Shamwell, N. R. Ahmed, and R. Russell (2024). "Deep Modeling of Non-Gaussian Aleatoric Uncertainty". In: *arXiv preprint arXiv:2405.20513*.

Achat, D. L., N. Pousse, M. Nicolas, F. Brédoire, and L. Augusto (2016). "Soil properties controlling inorganic phosphorus availability: general results from a national forest network and a global compilation of the literature". In: *Biogeochemistry* 127, pp. 255–272.

Adekola, O. and J. Lamond (2022). "6 - Systems thinking toward climate resilience". In: *Investing in Disaster Risk Reduction for Resilience*. Ed. by A. N. Martins, G. Lizarralde, T. Egbelakin, L. Hobeica, J. M. Mendes, and A. Hobeica. Elsevier, pp. 141–162. ISBN: 978-0-12-818639-8. DOI: https://doi.org/10.1016/B978-0-12-818639-8.00004-1. URL: https://www.sciencedirect.com/science/article/pii/B9780128186398000041.

Aigner, L., P. Högenauer, M. Bücker, and A. Flores Orozco (2021). "A flexible single loop setup for water-borne transient electromagnetic sounding applications". In: *Sensors* 21.19, p. 6624.

Akramkhanov, A., D. Brus, and D. Walvoort (2014). "Geostatistical monitoring of soil salinity in Uzbekistan by repeated EMI surveys". In: *Geoderma* 213, pp. 600–607.

Al Atawneh, D., N. Cartwright, and E. Bertone (2021). "Climate change and its impact on the projected values of groundwater recharge: A review". In: *Journal of Hydrology* 601, p. 126602.

Altdorff, D. and P. Dietrich (2014). "Delineation of areas with different temporal behavior of soil properties at a landslide affected Alpine hillside using time-lapse electromagnetic data". In: *Environmental earth sciences* 72, pp. 1357–1366.

Alvioli, M., M. Melillo, F. Guzzetti, M. Rossi, E. Palazzi, J. von Hardenberg, M. T. Brunetti, and S. Peruccacci (2018). "Implications of climate change on landslide hazard in Central Italy". In: *Science of The Total Environment* 630, pp. 1528–1543.

Amanambu, A. C., O. A. Obarein, J. Mossa, L. Li, S. S. Ayeni, O. Balogun, A. Oyebamiji, and F. U. Ochege (2020). "Groundwater system and climate change: Present status and future considerations". In: *Journal of Hydrology* 589, p. 125163.

Archie, G. E. (1942). "The electrical resistivity log as an aid in determining some reservoir characteristics". In: *Transactions of the AIME* 146.01, pp. 54–62. DOI: 10.2118/942054-g.

Ardali, A., B. Tezkan, and A. Gürer (2018). "On the Salt Water Intrusion into the Durusu Lake, Istanbul: A Joint Central Loop TEM and Multi-Electrode ERT Field Survey". In: *Pure and Applied Geophysics* 175, pp. 3037–3050. DOI: 10.1007/s00024-018-1813-1.

Atekwana, E. A. and L. D. Slater (2009). "Biogeophysics: A new frontier in Earth science research". In: *Reviews of Geophysics* 47.4.

Attwa, M. and T. Günther (2013). "Spectral induced polarization measurements for predicting the hydraulic conductivity in sandy aquifers". In: *Hydrology and Earth System Sciences* 17.10, pp. 4079–4094.

Auken, E., A. V. Christiansen, C. Kirkegaard, G. Fiandaca, C. Schamper, A. A. Behroozmand, A. Binley, E. Nielsen, F. Effersø, N. B. Christensen, et al. (2015). "An overview of a highly versatile forward and stable inverse algorithm for airborne, ground-based and borehole electromagnetic and electric data". In: *Exploration Geophysics* 46.3, pp. 223–235.

Auken, E., L. Pellerin, N. B. Christensen, and K. Sørensen (2006). "A survey of current trends in near-surface electrical and electromagnetic methods". In: *Geophysics* 71.5, G249–G260.

Ausilio, E. and P. Zimmaro (2017). "Landslide characterization using a multidisciplinary approach". In: *Measurement* 104, pp. 294–301.

Balia, R. and A. Viezzoli (2015). "Integrated interpretation of IP and TEM data for salinity monitoring of aquifers and soil in the coastal area of Muravera (Sardinia, Italy)." In: *Bollettino di Geofisica Teorica ed Applicata* 56.1.

Balting, D. F., A. AghaKouchak, G. Lohmann, and M. Ionita (2021). "Northern Hemisphere drought risk in a warming climate". In: *NPJ Climate and Atmospheric Science* 4.1, p. 61.

Ban, N., J. Schmidli, and C. Schär (2015). "Heavy precipitation in a changing climate: Does short-term summer precipitation increase faster?" In: *Geophysical Research Letters* 42.4, pp. 1165–1172.

Banerjee, C., T. Mukherjee, and E. Pasiliao (2019). "An Empirical Study on Generalizations of the ReLU Activation Function". In: *Proceedings of the 2019 ACM Southeast Conference*. ACMSE '19. Kennesaw, GA, USA: Association for Computing Machinery, pp. 164–167. ISBN: 9781450362511. DOI: 10.1145/3299815.3314450. URL: https://doi.org/10.1145/3299815.3314450.

Barone, I., C. Strobbia, and G. Cassiani (2020). "Multimode multi-offset phase analysis of surface waves, a new approach to extend MOPA to higher modes". In: *Geophysical Journal International* 221.3, pp. 1802–1819.

Barone, I., J. Boaga, A. Carrera, A. Flores-Orozco, and G. Cassiani (2021). “Tackling Lateral Variability Using Surface Waves: A Tomography-Like Approach”. In: *Surveys in Geophysics* 42.2, pp. 317–338. DOI: 10.1007/s10712-021-09631-x.

Baumann, S., J. Robl, G. Prasicek, B. Salcher, and M. Keil (2018). “The effects of lithology and base level on topography in the northern alpine foreland”. In: *Geomorphology* 313, pp. 13–26.

Beamish, D. (2011). “Low induction number, ground conductivity meters: A correction procedure in the absence of magnetic effects”. In: *Journal of Applied Geophysics* 75.2, pp. 244–253. ISSN: 0926-9851. DOI: https://doi.org/10.1016/j.jappgeo.2011.07.005. URL: https://www.sciencedirect.com/science/article/pii/S0926985111001492.

Bechtel, A., W. Gruber, R. Sachsenhofer, R. Gratzer, A. Lücke, and W. Püttmann (2003). “Depositional environment of the Late Miocene Hausruck lignite (Alpine Foreland Basin): insights from petrography, organic geochemistry, and stable carbon isotopes”. In: *International Journal of Coal Geology* 53.3, pp. 153–180. ISSN: 0166-5162. DOI: https://doi.org/10.1016/S0166-5162(02)00194-5. URL: https://www.sciencedirect.com/science/article/pii/S0166516202001945.

Bechtel, A., D. Reischenbacher, R. Sachsenhofer, R. Gratzer, and A. Lücke (2007). “Paleogeography and paleoecology of the upper Miocene Zillingdorf lignite deposit (Austria)”. In: *International Journal of Coal Geology* 69.3, pp. 119–143. ISSN: 0166-5162. DOI: https://doi.org/10.1016/j.coal.2006.03.001. URL: https://www.sciencedirect.com/science/article/pii/S0166516206000528.

Bechtel, A., R. Sachsenhofer, I. Kolcon, R. Gratzer, A. Otto, and W. Püttmann (2002). “Organic geochemistry of the Lower Miocene Oberdorf lignite (Styrian Basin, Austria): its relation to petrography, palynology and the palaeoenvironment”. In: *International Journal of Coal Geology* 51.1, pp. 31–57.

Beermann, M. (2011). “Linking corporate climate adaptation strategies with resilience thinking”. In: *Journal of Cleaner Production* 19.8. Critical Perspectives of Sustainable Development Research and Practice, pp. 836–842. ISSN: 0959-6526. DOI: https://doi.org/10.1016/j.jclepro.2010.10.017. URL: https://www.sciencedirect.com/science/article/pii/S095965261000435X.

Bell, R., T. Glade, K. Granica, G. Heiss, P. Leopold, H. Petschko, G. Pomaroli, H. Proske, and J. Schweigl (2013). “Landslide susceptibility maps for spatial planning in lower Austria”. In: *Landslide science and practice*. Springer, pp. 467–472. DOI: 10.1007/978-3-642-31325-7_60.

Bell, R., J.-E. Kruse, A. Garcia, T. Glade, and A. Hördt (2006). “Subsurface investigations of landslides using geophysical methods: geoelectrical applications in the Swabian Alb (Germany)”. In: *Geographica Helvetica* 61.3, pp. 201–208.

Berg, A., J. Sheffield, and P. C. Milly (2017). “Divergent surface and total soil moisture projections under global warming”. In: *Geophysical Research Letters* 44.1, pp. 236–244.

Beucher, A., T. Koganti, B. Iversen, and M. Greve (2020). “Mapping of peat thickness using a multi-receiver electromagnetic induction instrument”. In: *Remote Sensing* 12.15, p. 2458.

Bhandari, B. P. and S. Dhakal (2021). “A multidisciplinary approach of landslide characterization: A case of the Siwalik zone of Nepal Himalaya”. In: *Journal of Asian Earth Sciences: X* 5, p. 100061.

Bichler, A., P. Bobrowsky, M. Best, M. Douma, J. Hunter, T. Calvert, and R. Burns (2004). “Three-dimensional mapping of a landslide using a multi-geophysical approach: the Quesnel Forks landslide”. In: *Landslides* 1.1, pp. 29–40. DOI: 10.1007/s10346-003-0008-7.

Binley, A., S. S. Hubbard, J. A. Huisman, A. Revil, D. A. Robinson, K. Singha, and L. D. Slater (2015). “The emergence of hydrogeophysics for improved understanding of subsurface processes over multiple scales”. In: *Water resources research* 51.6, pp. 3837–3866. DOI: 10.1002/2015wr017016.

Binley, A., J. Keery, L. Slater, W. Barrash, and M. Cardiff (2016). “The hydrogeologic information in cross-borehole complex conductivity data from an unconsolidated conglomeratic sedimentary aquifer”. In: *Geophysics* 81.6, E409–E421. DOI: 10.1190/geo2015-0608.1.

Binley, A. and A. Kemna (2005). “DC Resistivity and Induced Polarization Methods”. In: *Hydrogeophysics*. Ed. by Y. Rubin and S. S. Hubbard. Vol. 50. Springer Netherlands, pp. 129–156. ISBN: 978-1-4020-3102-1. DOI: 10.1007/1-4020-3102-5_5.

Binley, A. and L. Slater (2020). *Resistivity and induced polarization: Theory and applications to the near-surface earth*. Cambridge University Press. ISBN: 9781108492744. DOI: 10.1017/9781108685955.

Binley, A., L. D. Slater, M. Fukes, and G. Cassiani (2005). “Relationship between spectral induced polarization and hydraulic properties of saturated and unsaturated sandstone”. In: *Water resources research* 41.12. DOI: 10.1029/2005wr004202.

Blanchy, G., P. McLachlan, B. Mary, M. Censini, J. Boaga, and G. Cassiani (2024). “Comparison of multi-coil and multi-frequency frequency domain electromagnetic induction instruments”. In: *Frontiers in Soil Science* 4, p. 1239497.

Blanchy, G., S. Saneiyan, J. Boyd, P. McLachlan, and A. Binley (2020). “ResIPy, an intuitive open source software for complex geoelectrical inversion/modeling”. In: *Computers & Geosciences* 137, p. 104423. ISSN: 0098-3004. DOI: 10.1016/j.cageo.2020.104423.

Blaschek, R., A. Hördt, and A. Kemna (2008). “A new sensitivity-controlled focusing regularization scheme for the inversion of induced polarization data based on the minimum gradient support”. In: *Geophysics* 73.2, F45–F54.

Blöschl, G., A. Blaschke, M. Broer, C. Bucher, G. Carr, X. Chen, A. Eder, M. Exner-Kittridge, A. Farnleitner, A. Flores Orozco, et al. (2016). “The hydrological open air laboratory (HOAL) in Petzenkirchen: A hypothesis-driven observatory”. In: *Hydrology and Earth System Sciences* 20.1, pp. 227–255. DOI: 10.5194/hess-20-227-2016.

Blume, T. and H. Van Meerveld (2015). “From hillslope to stream: methods to investigate subsurface connectivity”. In: *Wiley Interdisciplinary Reviews: Water* 2.3, pp. 177–198.

Blyth, E. M., V. K. Arora, D. B. Clark, S. J. Dadson, M. G. De Kauwe, D. M. Lawrence, J. R. Melton, J. Pongratz, R. H. Turton, K. Yoshimura, et al. (2021). “Advances in land surface modelling”. In: *Current Climate Change Reports* 7.2, pp. 45–71.

Boaga, J. (2017). “The use of FDEM in hydrogeophysics: A review”. In: *Journal of Applied Geophysics* 139, pp. 36–46.

Boaga, J., A. Viezzoli, G. Cassiani, G. Deidda, L. Tosi, and S. Silvestri (2020). “Resolving the thickness of peat deposits with contact-less electromagnetic methods: A case study in the Venice coastland”. In: *Science of The Total Environment* 737, p. 139361.

Bogaard, T. A. and R. Greco (2016). “Landslide hydrology: from hydrology to pore pressure”. In: *Wiley Interdisciplinary Reviews: Water* 3.3, pp. 439–459.

Bonsall, J., R. Fry, C. Gaffney, I. Armit, A. Beck, and V. Gaffney (2013). “Assessment of the CMD Mini-Explorer, a New Low-frequency Multi-coil Electromagnetic Device, for Archaeological Investigations”. In: *Archaeological Prospection* 20.3, pp. 219–231. DOI: https://doi.org/10.1002/arp.1458. eprint: https://onlinelibrary.wiley.com/doi/pdf/10.1002/arp.1458. URL: https://onlinelibrary.wiley.com/doi/abs/10.1002/arp.1458.

Börner, F., J. Schopper, and A. Weller (1996a). "Evaluation of transport and storage properties in the soil and groundwater zone from induced polarization measurements1". In: *Geophysical prospecting* 44.4, pp. 583–601. DOI: 10.1111/j.1365-2478.1996.tb00167.x.

Börner, F., J. Schopper, and A. Weller (1996b). "Evaluation of transport and storage properties in the soil and groundwater zone from induced polarization measurements1". In: *Geophysical prospecting* 44.4, pp. 583–601.

Boubaker, S., Z. Liu, Y. Mu, and Y. Zhan (2024). "Carbon dioxide emissions and environmental risks: Long term and short term". In: *Risk Analysis*.

Bouma, J. (1988). "When the mapping is over, then what?" English. In: St. Paul, Minnesota: University of Minnesota, pp. 3–12.

Brevik, E. C., T. E. Fenton, and A. Lazari (2006). "Soil electrical conductivity as a function of soil water content and implications for soil mapping". In: *Precision Agriculture* 7, pp. 393–404.

Brooks, R. H. and A. T. Corey (1966). "Properties of porous media affecting fluid flow". In: *Journal of the irrigation and drainage division* 92.2, pp. 61–88.

Brosten, T. R., F. D. Day-Lewis, G. M. Schultz, G. P. Curtis, and J. W. Lane Jr (2011). "Inversion of multi-frequency electromagnetic induction data for 3D characterization of hydraulic conductivity". In: *Journal of Applied Geophysics* 73.4, pp. 323–335.

Bücker, M., A. Flores Orozco, J. Gallistl, M. Steiner, L. Aigner, J. Hoppenbrock, R. Glebe, W. Morales Barrera, C. Pita de la Paz, C. E. García García, et al. (2021). "Integrated land and water-borne geophysical surveys shed light on the sudden drying of large karst lakes in southern Mexico". In: *Solid Earth* 12.2, pp. 439–461. DOI: 10.5194/se-12-439-2021.

Bücker, M., A. Flores Orozco, S. Undorf, and A. Kemna (2019a). "On the role of stern-and diffuse-layer polarization mechanisms in porous media". In: *Journal of Geophysical Research: Solid Earth* 124.6, pp. 5656–5677. DOI: 10.1029/2019jb017679.

Bücker, M. and A. Hördt (2013). "Long and short narrow pore models for membrane polarization". In: *Geophysics* 78.6, E299–E314.

Bücker, M., S. Lozano García, B. Ortega Guerrero, M. Caballero, L. Pérez, L. Caballero, C. Pita de la Paz, A. Sánchez-Galindo, F. J. Villegas, A. Flores Orozco, et al. (2017). "Geoelectrical and electromagnetic methods applied to paleolimnological studies: Two examples from desiccated lakes in the Basin of Mexico". In: *Boletín de la Sociedad Geológica Mexicana* 69.2, pp. 279–298.

Bücker, M., A. F. Orozco, and A. Kemna (2018). "Electrochemical polarization around metallic particles–Part 1: The role of diffuse-layer and volume-diffusion relaxation". In: *Geophysics* 83.4, E203–E217. DOI: 10.1190/geo2017-0401.1.

Bücker, M., S. Undorf, A. Flores Orozco, and A. Kemna (2019b). "Electrochemical polarization around metallic particles–Part 2: The role of diffuse surface charge". In: *Geophysics* 84.2, E57–E73. DOI: 10.1190/geo2018-0150.1.

Caceres, J., D. Gonzalez, T. Zhou, and E. L. Droguett (2021). "A probabilistic Bayesian recurrent neural network for remaining useful life prognostics considering epistemic and aleatory uncertainties". In: *Structural Control and Health Monitoring* 28.10, e2811. DOI: https://doi.org/10.1002/stc.2811. eprint: https://onlinelibrary.wiley.com/doi/pdf/10.1002/stc.2811. URL: https://onlinelibrary.wiley.com/doi/abs/10.1002/stc.2811.

Callegary, J. B., T. P. Ferré, and R. Groom (2007). "Vertical spatial sensitivity and exploration depth of low-induction-number electromagnetic-induction instruments". In: *Vadose Zone Journal* 6.1, pp. 158–167.

Campbell, R. H. (1975). *Soil slips, debris flows, and rainstorms in the Santa Monica Mountains and vicinity, southern California*. Vol. 851. US Government Printing Office.

Carey, A. M., G. B. Paige, B. J. Carr, W. S. Holbrook, and S. N. Miller (2019). "Characterizing hydrological processes in a semiarid rangeland watershed: A hydrogeophysical approach". In: *Hydrological Processes* 33.5, pp. 759–774.

Carman, P. C. (1939). "Permeability of saturated sands, soils and clays". In: *The Journal of Agricultural Science* 29.2, pp. 262–273.

Caterina, D., T. Hermans, and F. Nguyen (2014). "Case studies of incorporation of prior information in electrical resistivity tomography: comparison of different approaches". In: *Near Surface Geophysics* 12.4, pp. 451–465.

Catt, L. M., L. J. West, and R. A. Clark (2009). "The use of reference models from a priori data to guide 2D inversion of electrical resistivity tomography data". In: *Geophysical prospecting* 57.6, pp. 1035–1048.

Charnock, D. (2005). "Electromagnetic interference coupling between power cables and sensitive circuits". In: *IEEE transactions on power delivery* 20.2, pp. 668–673.

Charnock, T., L. Perreault-Levasseur, and F. Lanusse (2022). "Bayesian neural networks". In: *Artificial Intelligence for High Energy Physics*. World Scientific, pp. 663–713.

Chen, Y. and D. Or (2006). "Geometrical factors and interfacial processes affecting complex dielectric permittivity of partially saturated porous media". In: *Water resources research* 42.6.

Chirico, G. B., H. Medina, and N. Romano (2010). "Functional evaluation of PTF prediction uncertainty: An application at hillslope scale". In: *Geoderma* 155.3-4, pp. 193–202.

Chollet, F. et al. (2015). *Keras*. https://keras.io.

Christensen, N. B. (2022). "Joint inversion of airborne TEM data and surface geoelectrical data. The Egebjerg case". In: *Journal of Applied Geophysics* 196, p. 104511.

Christiansen, A. V., E. Auken, and K. Sørensen (2006). "The transient electromagnetic method". In: *Groundwater geophysics: a tool for hydrogeology*. Springer, pp. 179–225.

Christiansen, A. V., J. B. Pedersen, E. Auken, N. E. Søe, M. K. Holst, and S. M. Kristiansen (2016). "Improved Geoarchaeological Mapping with Electromagnetic Induction Instruments from Dedicated Processing and Inversion". In: *Remote Sensing* 8.12. ISSN: 2072-4292. DOI: 10.3390/rs8121022. URL: https://www.mdpi.com/2072-4292/8/12/1022.

Chuprinko, D. and K. Titov (2017). "Influence of mineral composition on spectral induced polarization in sediments". In: *Geophysical Journal International* 209.1, pp. 186–191.

Cockett, R., S. Kang, L. J. Heagy, A. Pidlisecky, and D. W. Oldenburg (2015). "SimPEG: An open source framework for simulation and gradient based parameter estimation in geophysical applications". In: *Computers & Geosciences* 85, pp. 142–154. ISSN: 0098-3004. DOI: 10.1016/j.cageo.2015.09.015.

Cockx, L., M. Van Meirvenne, U. Vitharana, L. Verbeke, D. Simpson, T. Saey, and F. Van Coillie (2009). "Extracting topsoil information from EM38DD sensor data using a neural network approach". In: *Soil Science Society of America Journal* 73.6, pp. 2051–2058.

Coggon, J. (1984). "New three-point formulas for inductive coupling removal in induced polarization". In: *Geophysics* 49.3, pp. 307–309.

Cole, K. S. and R. H. Cole (1941). "Dispersion and absorption in dielectrics I. Alternating current characteristics". In: *The Journal of chemical physics* 9.4, pp. 341–351. DOI: 10.1063/1.1750906.

Comas, X. and L. Slater (2004). "Low-frequency electrical properties of peat". In: *Water Resources Research* 40.12.

Cook, B. I., J. S. Mankin, and K. J. Anchukaitis (2018). "Climate change and drought: From past to future". In: *Current Climate Change Reports* 4, pp. 164–179.

Corona-Lopez, D. D., S. Sommer, S. A. Rolfe, F. Podd, and B. D. Grieve (2019). "Electrical impedance tomography as a tool for phenotyping plant roots". In: *Plant Methods* 15, pp. 1–15.

Cosby, B., G. Hornberger, R. Clapp, and T. Ginn (1984). "A statistical exploration of the relationships of soil moisture characteristics to the physical properties of soils". In: *Water resources research* 20.6, pp. 682–690.

Cosenza, P., E. Marmet, F. Rejiba, Y. J. Cui, A. Tabbagh, and Y. Charlery (2006). "Correlations between geotechnical and electrical data: A case study at Garchy in France". In: *Journal of Applied Geophysics* 60.3-4, pp. 165–178.

Cruden, D. (Jan. 1996). "Cruden,D.M.,Varnes, D.J.,1996, Landslide Types and Processes, Transportation Research Board, U.S. National Academy of Sciences, Special Report, 247: 36-75". In: *Special Report - National Research Council, Transportation Research Board* 247, pp. 36–57.

Dahlin, T., V. Leroux, and J. Nissen (2002). "Measuring techniques in induced polarisation imaging". In: *Journal of Applied Geophysics* 50.3, pp. 279–298.

Dahlin, T., H. Löfroth, D. Schälin, and P. Suer (2013). "Mapping of quick clay using geoelectrical imaging and CPTU-resistivity". In: *Near Surface Geophysics* 11.6, pp. 659–670.

Dahlin, T. and M. H. Loke (2015). "Negative apparent chargeability in time-domain induced polarisation data". In: *Journal of Applied Geophysics* 123, pp. 322–332.

Dahlin, T. and B. Zhou (2006). "Multiple-gradient array measurements for multichannel 2D resistivity imaging". In: *Near Surface Geophysics* 4.2, pp. 113–123.

Danielsen, J. E., E. Auken, F. Jørgensen, V. Søndergaard, and K. I. Sørensen (2003). "The application of the transient electromagnetic method in hydrogeophysical surveys". In: *Journal of applied geophysics* 53.4, pp. 181–198. DOI: 10.1016/j.jappgeo.2003.08.004.

Darmann, F., I. Schwaighofer, M. Kumpan, T. Weninger, and P. Strauss (2024). "New hydro-pedotransfer functions for Austrian soil mapping applications". In: *Geoderma Regional* 39, e00875.

De Smedt, P., S. Delefortrie, and F. Wyffels (2016). "Identifying and removing micro-drift in ground-based electromagnetic induction data". In: *Journal of Applied Geophysics* 131, pp. 14–22. ISSN: 0926-9851. DOI: https://doi.org/10.1016/j.jappgeo.2016.05.004. URL: https://www.sciencedirect.com/science/article/pii/S0926985116301343.

De Smedt, P., T. Saey, E. Meerschman, J. De Reu, W. De Clercq, and M. Van Meirvenne (2014). "Comparing apparent magnetic susceptibility measurements of a multi-receiver EMI sensor with topsoil and profile magnetic susceptibility data over weak magnetic anomalies". In: *Archaeological Prospection* 21.2, pp. 103–112.

Deidda, G. P., P. Díaz de Alba, C. Fenu, G. Lovicu, and G. Rodriguez (2020). "FDEMtools: a MATLAB package for FDEM data inversion". In: *Numerical Algorithms* 84, pp. 1313–1327.

Delefortrie, S., D. Hanssens, and P. De Smedt (2018). "Low signal-to-noise FDEM in-phase data: Practical potential for magnetic susceptibility modelling". In: *Journal of Applied Geophysics* 152, pp. 17–25.

Der Kiureghian, A. and O. Ditlevsen (2009). "Aleatory or epistemic? Does it matter?" In: *Structural safety* 31.2, pp. 105–112.

Detommaso, G., A. Gasparin, M. Donini, M. Seeger, A. G. Wilson, and C. Archambeau (2023). "Fortuna: A Library for Uncertainty Quantification in Deep Learning". In: *arXiv preprint arXiv:2302.04019*.

Dey, A. and H. F. Morrison (1973). "Electromagnetic coupling in frequency and time-domain induced-polarization surveys over a multilayered earth". In: *Geophysics* 38.2, pp. 380–405.

Di Maio, R., C. De Paola, G. Forte, E. Piegari, M. Pirone, A. Santo, and G. Urciuoli (2020). "An integrated geological, geotechnical and geophysical approach to identify predisposing factors for flowslide occurrence". In: *Engineering Geology* 267, p. 105473. ISSN: 0013-7952. DOI: https://doi.org/10.1016/j.enggeo.2019.105473. URL: https://www.sciencedirect.com/science/article/pii/S001379521931213X.

Do, M.-T. T., L. N. Van, X.-H. Le, G. V. Nguyen, M. Yeon, and G. Lee (2024). "National variability in soil organic carbon stock predictions: Impact of bulk density pedotransfer functions". In: *International Soil and Water Conservation Research*.

Doble, R. C. and R. S. Crosbie (2017). "Current and emerging methods for catchment-scale modelling of recharge and evapotranspiration from shallow groundwater". In: *Hydrogeology journal* 25.1, p. 3.

Doetsch, J., T. Ingeman-Nielsen, A. V. Christiansen, G. Fiandaca, E. Auken, and B. Elberling (2015). "Direct current (DC) resistivity and induced polarization (IP) monitoring of active layer dynamics at high temporal resolution". In: *Cold Regions Science and Technology* 119, pp. 16–28.

Doolittle, J. A. and E. C. Brevik (2014a). "The use of electromagnetic induction techniques in soils studies". In: *Geoderma* 223, pp. 33–45.

Doolittle, J. A. and E. C. Brevik (2014b). "The use of electromagnetic induction techniques in soils studies". In: *Geoderma* 223, pp. 33–45.

Dorugade, A. (2014). "New ridge parameters for ridge regression". In: *Journal of the Association of Arab Universities for Basic and Applied Sciences* 15, pp. 94–99. ISSN: 1815-3852. DOI: https://doi.org/10.1016/j.jaubas.2013.03.005. URL: https://www.sciencedirect.com/science/article/pii/S1815385213000199.

Dragonetti, G., M. Farzamian, A. Basile, F. Monteiro Santos, and A. Coppola (2022). "In situ estimation of soil hydraulic and hydrodispersive properties by inversion of electromagnetic induction measurements and soil hydrological modeling". In: *Hydrology and Earth System Sciences* 26.19, pp. 5119–5136. DOI: 10.5194/hess-26-5119-2022. URL: https://hess.copernicus.org/articles/26/5119/2022/.

Dunn, R. J., L. V. Alexander, M. G. Donat, X. Zhang, M. Bador, N. Herold, T. Lippmann, R. Allan, E. Aguilar, A. A. Barry, et al. (2020). "Development of an updated global land in situ-based data set of temperature and precipitation extremes: HadEX3". In: *Journal of Geophysical Research: Atmospheres* 125.16, e2019JD032263.

Egele, R., R. Maulik, K. Raghavan, B. Lusch, I. Guyon, and P. Balaprakash (2022). "AutoDEUQ: Automated Deep Ensemble with Uncertainty Quantification". In: *2022 26th International Conference on Pattern Recognition (ICPR)*, pp. 1908–1914. DOI: 10.1109/ICPR56361.2022.9956231.

Enemark, T., L. J. Peeters, D. Mallants, and O. Batelaan (2019). "Hydrogeological conceptual model building and testing: A review". In: *Journal of Hydrology* 569, pp. 310–329.

Everett, M. E. (2005). "What do electromagnetic induction responses measure?" In: *The Leading Edge* 24.2, pp. 154–157.

Everett, M. E. (2012). "Theoretical developments in electromagnetic induction geophysics with selected applications in the near surface". In: *Surveys in geophysics* 33, pp. 29–63.

Everett, M. E. (2013). *Near-surface applied geophysics*. Cambridge University Press.

Farquharson, C. G., D. W. Oldenburg, and P. S. Routh (2003). "Simultaneous 1D inversion of loop–loop electromagnetic data for magnetic susceptibility and electrical conductivity". In: *Geophysics* 68.6, pp. 1857–1869.

Federici, P. R., A. Puccinelli, E. Cantarelli, N. Casarosa, G. D. Avanzi, F. Falaschi, R. Giannecchini, A. Pochini, A. Ribolini, M. Bottai, et al. (2007). "Multidisciplinary investigations in evaluating landslide susceptibility—an example in the Serchio River valley (Italy)". In: *Quaternary International* 171, pp. 52–63.

Fellaji, M. and F. Pennerath (2024). "The Epistemic Uncertainty Hole: an issue of Bayesian Neural Networks". In: *arXiv preprint arXiv:2407.01985*.

Fiandaca, G., E. Auken, A. V. Christiansen, and A. Gazoty (2012). "Time-domain-induced polarization: Full-decay forward modeling and 1D laterally constrained inversion of Cole-Cole parameters". In: *Geophysics* 77.3, E213–E225.

Fiandaca, G., L. M. Madsen, and P. K. Maurya (2018). "Reparameterisations of the Cole–Cole model for improved spectral inversion of induced polarization data". In: *Near Surface Geophysics* 16.4, pp. 385–399. DOI: https://doi.org/10.3997/1873-0604.2017065. eprint: https://onlinelibrary.wiley.com/doi/pdf/10.3997/1873-0604.2017065. URL: https://onlinelibrary.wiley.com/doi/abs/10.3997/1873-0604.2017065.

Fiener, P., K. Auerswald, and K. Van Oost (2011). "Spatio-temporal patterns in land use and management affecting surface runoff response of agricultural catchments—A review". In: *Earth-Science Reviews* 106.1-2, pp. 92–104.

Flores Orozco, A., J. Gallistl, M. Steiner, C. Brandstätter, and J. Fellner (2020). "Mapping biogeochemically active zones in landfills with induced polarization imaging: The Heferlbach landfill". In: *Waste Management* 107, pp. 121–132. ISSN: 0956-053X. DOI: 10.1016/j.wasman.2020.04.001.

Flores Orozco, A., L. Aigner, and J. Gallistl (2021). "Investigation of cable effects in spectral induced polarization imaging at the field scale using multicore and coaxial cables". In: *Geophysics* 86.1, E59–E75. DOI: 10.1190/geo2019-0552.1.

Flores Orozco, A., J. Gallistl, M. Bücker, and K. H. Williams (2018a). "Decay curve analysis for data error quantification in time-domain induced polarization imaging". In: *Geophysics* 83.2, E75–E86. DOI: 10.1190/geo2016-0714.1.

Flores Orozco, A., A. Kemna, A. Binley, and G. Cassiani (2019a). "Analysis of time-lapse data error in complex conductivity imaging to alleviate anthropogenic noise for site characterization". In: *Geophysics* 84.2, B181–B193.

Flores Orozco, A., A. Kemna, A. Binley, and G. Cassiani (2019b). "Analysis of time-lapse data error in complex conductivity imaging to alleviate anthropogenic noise for site characterization". In: *Geophysics* 84.2, B181–B193. DOI: 10.1190/geo2017-0755.1.

Flores Orozco, A., M. Bücker, M. Steiner, and J.-P. Malet (2018b). "Complex-conductivity imaging for the understanding of landslide architecture". In: *Engineering Geology* 243, pp. 241–252. ISSN: 0013-7952. DOI: https://doi.org/10.1016/j.enggeo.2018.07.009.

Flores Orozco, A., A. Kemna, C. Oberdörster, L. Zschornack, C. Leven, P. Dietrich, and H. Weiss (2012a). "Delineation of subsurface hydrocarbon contamination at a former hydrogenation plant using spectral induced polarization imaging". In: *Journal of contaminant hydrology* 136, pp. 131–144. DOI: 10.1016/j.jconhyd.2012.06.001.

Flores Orozco, A., A. Kemna, and E. Zimmermann (2012b). "Data error quantification in spectral induced polarization imaging". In: *Geophysics* 77.3, E227–E237. DOI: 10.1190/geo2010-0194.1.

Flores Orozco, A., V. Micić, M. Bücker, J. Gallistl, T. Hofmann, and F. Nguyen (2019c). "Complex-conductivity monitoring to delineate aquifer pore clogging during nanoparticles injection". In: *Geophysical Journal International* 218.3, pp. 1838–1852.

Flores Orozco, A., M. Steiner, T. Katona, N. Roser, C. Moser, M. J. Stumvoll, and T. Glade (2022). "Application of induced polarization imaging across different scales to understand surface and groundwater flow at the Hofermuehle landslide". In: *CATENA* 219, p. 106612. ISSN: 0341-8162. DOI: 10.1016/j.catena.2022.106612.

Flores Orozco, A., M. Velimirovic, T. Tosco, A. Kemna, H. Sapion, N. Klaas, R. Sethi, and L. Bastiaens (2015). "Monitoring the injection of microscale zerovalent iron particles for groundwater remediation by means of complex electrical conductivity imaging". In: *Environmental science & technology* 49.9, pp. 5593–5600. DOI: 10.1021/acs.est.5b00208.

Flores Orozco, A., K. H. Williams, and A. Kemna (2013). "Time-lapse spectral induced polarization imaging of stimulated uranium bioremediation". In: *Near Surface Geophysics* 11.5, pp. 531–544. DOI: 10.3997/1873-0604.2013020.

Flores Orozco, A., K. H. Williams, P. E. Long, S. S. Hubbard, and A. Kemna (2011). "Using complex resistivity imaging to infer biogeochemical processes associated with bioremediation of an uranium-contaminated aquifer". In: *Journal of Geophysical Research: Biogeosciences* 116.G3.

Franchi, G., A. Bursuc, E. Aldea, S. Dubuisson, and I. Bloch (2024). "Encoding the Latent Posterior of Bayesian Neural Networks for Uncertainty Quantification". In: *IEEE Transactions on Pattern Analysis and Machine Intelligence* 46.4, pp. 2027–2040. DOI: 10.1109/TPAMI.2023.3328829.

Fressard, M., O. Maquaire, Y. Thiery, R. Davidson, and C. Lissak (2016). "Multi-method characterisation of an active landslide: Case study in the Pays d'Auge plateau (Normandy, France)". In: *Geomorphology* 270, pp. 22–39.

Gallistl, J., D. Schwindt, J. Birgit, L. Aigner, M. Peresson, and A. Flores Orozco (2022). "Quantification of soil textural and hydraulic properties in a complex conductivity imaging framework: Results from the Wolfsegg slope". In: *Frontiers in Earth Science* 10.

Gallistl, J., M. Weigand, M. Stumvoll, D. Ottowitz, T. Glade, and A. F. Orozco (2018). "Delineation of subsurface variability in clay-rich landslides through spectral induced polarization imaging and electromagnetic methods". In: *Engineering Geology* 245, pp. 292–308. DOI: 10.1016/j.enggeo.2018.09.001.

Gan, L., R. Tang, F. Li, and F. Shen (2024). "A Deep Learning Estimation for Probing Depth of Transient Electromagnetic Observation". In: *Applied Sciences* 14.16. ISSN: 2076-3417. DOI: 10.3390/app14167123. URL: https://www.mdpi.com/2076-3417/14/16/7123.

Ganaie, M. A., M. Hu, A. K. Malik, M. Tanveer, and P. N. Suganthan (2022). "Ensemble deep learning: A review". In: *Engineering Applications of Artificial Intelligence* 115, p. 105151.

Garcia-Tomillo, A., J. M. Mirás-Avalos, J. Dafonte-Dafonte, and A. Paz-González (2017). "Estimating soil organic matter using interpolation methods with a electromagnetic induction sensor and topographic parameters: A case study in a humid region". In: *Precision Agriculture* 18, pp. 882–897.

Gasperikova, E. and H. F. Morrison (2001). “Mapping of induced polarization using natural fields”. In: *Geophysics* 66.1, pp. 137–147.

Gawlikowski, J., C. R. N. Tassi, M. Ali, J. Lee, M. Humt, J. Feng, A. Kruspe, R. Triebel, P. Jung, R. Roscher, et al. (2023). “A survey of uncertainty in deep neural networks”. In: *Artificial Intelligence Review* 56.Suppl 1, pp. 1513–1589.

Gebauer, A., M. Ellinger, V. M. Brito Gomez, and M. Ließ (2020). “Development of pedotransfer functions for water retention in tropical mountain soil landscapes: spotlight on parameter tuning in machine learning”. In: *Soil* 6.1, pp. 215–229.

Georgousis, C., A. Moussouliotis, and C. Babajimopoulos (2009). “Functional evaluation of pedotransfer functions in irrigation scheduling”. In: *Proceedings of the First International Conference on Soft Computing Technology in Civil, Structural and Environmental Engineering*. IKEECONF-2009-012. Aristotle University of Thessaloniki.

Ghorbani, A., P. Cosenza, A. Revil, M. Zamora, M. Schmutz, N. Florsch, and D. Jougnot (2009). “Non-invasive monitoring of water content and textural changes in clay-rocks using spectral induced polarization: A laboratory investigation”. In: *Applied Clay Science* 43.3-4, pp. 493–502.

Ghosh, S., J. Yao, and F. Doshi-Velez (2019). “Model selection in Bayesian neural networks via horseshoe priors”. In: *Journal of Machine Learning Research* 20.182, pp. 1–46.

Glade, T. and R. Dikau (2001). “Landslides at the tertiary escarpments in Rheinhessen, Southwest Germany”. In: *Zeitschrift fur Geomorphologie, Supplementband* 125. Cited by: 17, pp. 65–92. URL: https://www.scopus.com/inward/record.uri?eid=2-s2.0-0034909590&partnerID=40&md5=0ba9868e2dc2a42923aed63bc99aed4b.

Glover, P. W. J. (2015). “11.04 - Geophysical Properties of the Near Surface Earth: Electrical Properties”. In: *Treatise on Geophysics (Second Edition)*. Ed. by G. Schubert. Second Edition. Oxford: Elsevier, pp. 89–137. ISBN: 978-0-444-53803-1. DOI: 10.1016/B978-0-444-53802-4.00189-5.

Goan, E. and C. Fookes (2020). “Bayesian neural networks: An introduction and survey”. In: *Case Studies in Applied Bayesian Data Science: CIRM Jean-Morlet Chair, Fall 2018*, pp. 45–87.

Godio, A. and G. Bottino (2001). “Electrical and electromagnetic investigation for landslide characterisation”. In: *Physics and Chemistry of the Earth, Part C: Solar, Terrestrial & Planetary Science* 26.9, pp. 705–710.

Gómez, A. M., Q. d. J. van Lier, N. E. Silvero, L. Inforsato, M. L. A. de Melo, H. S. Rodríguez-Albarracín, N. A. Rosin, J. T. F. Rosas, R. Rizzo, and J. A. Demattê (2023). “Digital mapping of the soil available water capacity: tool for the resilience of agricultural systems to climate change”. In: *Science of The Total Environment* 882, p. 163572.

Gottschling, P. (2006). “Massenbewegungen”. In: *Geologie der Bundesländer–Niederösterreich, Geologische Bundesanstalt, Wien*, pp. 335–340.

Grandjean, G., J.-C. Gourry, O. Sanchez, A. Bitri, and S. Garambois (2011). “Structural study of the Ballandaz landslide (French Alps) using geophysical imagery”. In: *Journal of Applied Geophysics* 75.3, pp. 531–542.

Grassini, P., L. G. van Bussel, J. Van Wart, J. Wolf, L. Claessens, H. Yang, H. Boogaard, H. de Groot, M. K. van Ittersum, and K. G. Cassman (2015). “How good is good enough? Data requirements for reliable crop yield simulations and yield-gap analysis”. In: *Field Crops Research* 177, pp. 49–63.

Greco, R., P. Marino, and T. A. Bogaard (2023). “Recent advancements of landslide hydrology”. In: *Wiley Interdisciplinary Reviews: Water* 10.6, e1675.

Grunert, P., A. Soliman, S. Coric, R. Scholger, M. Harzhauser, and W. E. Piller (2010). “Stratigraphic re-evaluation of the stratotype for the regional Ottnangian stage (Central Paratethys, middle Burdigalian)”. In: *Newsletters in Stratigraphy* 44.1, p. 1.

Gu, S., S. Jiang, X. Li, N. Zheng, and X. Xia (2023). “Soil salinity simulation based on electromagnetic induction and deep learning”. In: *Soil and Tillage Research* 230, p. 105706. ISSN: 0167-1987. DOI: https://doi.org/10.1016/j.still.2023.105706. URL: https://www.sciencedirect.com/science/article/pii/S0167198723000739.

Guber, A., Y. A. Pachepsky, M. T. Van Genuchten, J. Simunek, D. Jacques, A. Nemes, T. Nicholson, and R. Cady (2009). “Multi-model simulation of water flow in a field soil using pedotransfer functions”. In: *Vadose Zone Journal* 8.1, pp. 1–10.

Guillemoteau, J. and J. Tronicke (2016). “Evaluation of a rapid hybrid spectral-spatial domain 3D forward-modeling approach for loop-loop electromagnetic induction quadrature data acquired in low-induction-number environments”. In: *Geophysics* 81.6, E447–E458.

Günther, T. and T. Martin (2016). “Spectral two-dimensional inversion of frequency-domain induced polarization data from a mining slag heap”. In: *Journal of Applied Geophysics* 135, pp. 436–448.

Guo, R., T. Huang, M. Li, H. Zhang, and Y. C. Eldar (2023). “Physics-Embedded Machine Learning for Electromagnetic Data Imaging: Examining three types of data-driven imaging methods”. In: *IEEE Signal Processing Magazine* 40.2, pp. 18–31. DOI: 10.1109/MSP.2022.3198805.

Gupta, S. and W. Larson (1979). “Estimating soil water retention characteristics from particle size distribution, organic matter percent, and bulk density”. In: *Water resources research* 15.6, pp. 1633–1635.

Gupta, S., P. Lehmann, S. Bonetti, A. Papritz, and D. Or (2021). “Global Prediction of Soil Saturated Hydraulic Conductivity Using Random Forest in a Covariate-Based GeoTransfer Function (CoGTF) Framework”. In: *Journal of Advances in Modeling Earth Systems* 13.4. e2020MS002242 2020MS002242, e2020MS002242. DOI: https://doi.org/10.1029/2020MS002242. eprint: https://agupubs.onlinelibrary.wiley.com/doi/pdf/10.1029/2020MS002242. URL: https://agupubs.onlinelibrary.wiley.com/doi/abs/10.1029/2020MS002242.

Gutmann, E. D. and E. E. Small (2007). “A comparison of land surface model soil hydraulic properties estimated by inverse modeling and pedotransfer functions”. In: *Water Resources Research* 43.5.

Hack, R. (2000). “Geophysics for slope stability”. In: *Surveys in geophysics* 21.4, pp. 423–448.

Hadzick, Z., A. Guber, Y. Pachepsky, and R. Hill (2011). “Pedotransfer functions in soil electrical resistivity estimation”. In: *Geoderma* 164.3-4, pp. 195–202.

Hallof, P. G. (1974). “The IP phase measurement and inductive coupling”. In: *Geophysics* 39.5, pp. 650–665. DOI: 10.1190/1.1440455.

Hanssens, D., S. Delefortrie, J. De Pue, M. Van Meirvenne, and P. De Smedt (2019). “Frequency-Domain Electromagnetic Forward and Sensitivity Modeling: Practical Aspects of Modeling a Magnetic Dipole in a Multilayered Half-Space”. In: *IEEE Geoscience and Remote Sensing Magazine* 7.1, pp. 74–85. DOI: 10.1109/MGRS.2018.2881767.

Haque, U., P. F. Da Silva, G. Devoli, J. Pilz, B. Zhao, A. Khaloua, W. Wilopo, P. Andersen, P. Lu, J. Lee, et al. (2019). “The human cost of global warming: Deadly landslides and their triggers (1995–2014)”. In: *Science of the Total Environment* 682, pp. 673–684.

Harvey, O. R. and C. L. S. Morgan (2009). "Predicting Regional-Scale Soil Variability using a Single Calibrated Apparent Soil Electrical Conductivity Model". In: *Soil Science Society of America Journal* 73.1, pp. 164–169. DOI: https://doi.org/10.2136/sssaj2008.0074. eprint: https://acsess.onlinelibrary.wiley.com/doi/pdf/10.2136/sssaj2008.0074. URL: https://acsess.onlinelibrary.wiley.com/doi/abs/10.2136/sssaj2008.0074.

Heagy, L. J., R. Cockett, S. Kang, G. K. Rosenkjaer, and D. W. Oldenburg (2017). "A framework for simulation and inversion in electromagnetics". In: *Computers & Geosciences* 107, pp. 1–19.

Hebel, C. von, S. Rudolph, A. Mester, J. A. Huisman, P. Kumbhar, H. Vereecken, and J. van der Kruk (2014). "Three-dimensional imaging of subsurface structural patterns using quantitative large-scale multiconfiguration electromagnetic induction data". In: *Water Resources Research* 50.3, pp. 2732–2748.

Heil, K. and U. Schmidhalter (2012). "Characterisation of soil texture variability using the apparent soil electrical conductivity at a highly variable site". In: *Computers Geosciences* 39, pp. 98–110. ISSN: 0098-3004. DOI: https://doi.org/10.1016/j.cageo.2011.06.017. URL: https://www.sciencedirect.com/science/article/pii/S0098300411002214.

Heil, K. and U. Schmidhalter (2015). "Comparison of the EM38 and EM38-MK2 electromagnetic induction-based sensors for spatial soil analysis at field scale". In: *Computers and Electronics in Agriculture* 110, pp. 267–280. ISSN: 0168-1699. DOI: https://doi.org/10.1016/j.compag.2014.11.014. URL: https://www.sciencedirect.com/science/article/pii/S0168169914002968.

Hendrickx, J., B. Borchers, D. Corwin, S. Lesch, A. Hilgendorf, and J. Schlue (2002). "Inversion of soil conductivity profiles from electromagnetic induction measurements: Theory and experimental verification". In: *Soil Science Society of America Journal* 66.3, pp. 673–685.

Herold, R., G. Beisembina, P. Dietrich, and F. Börner (2024). "Experimental investigations on laboratory samples regarding the connection of spectral induced polarization to heterogeneity of hydraulic conductivity". In: *Environmental Earth Sciences* 83.13, p. 389.

Hibert, C., G. Grandjean, A. Bitri, J. Travelletti, and J.-P. Malet (2012). "Characterizing landslides through geophysical data fusion: Example of the La Valette landslide (France)". In: *Engineering Geology* 128, pp. 23–29.

Hinsch, R. (2008). "New insights into the Oligocene to Miocene geological evolution of the Molasse Basin of Austria". In: *Oil Gas-European Magazine* 34.3, pp. 138–143.

Hoerl, A. E. and R. W. Kennard (1970). "Ridge regression: Biased estimation for nonorthogonal problems". In: *Technometrics* 12.1, pp. 55–67.

Holmes, J., J. Chambers, P. Meldrum, P. Wilkinson, J. Boyd, P. Williamson, D. Huntley, K. Sattler, D. Elwood, V. Sivakumar, et al. (2020). "Four-dimensional electrical resistivity tomography for continuous, near-real-time monitoring of a landslide affecting transport infrastructure in British Columbia, Canada". In: *Near Surface Geophysics* 18.Geoelectrical Monitoring, pp. 337–351.

Hora, S. C. (1996). "Aleatory and epistemic uncertainty in probability elicitation with an example from hazardous waste management". In: *Reliability Engineering & System Safety* 54.2-3, pp. 217–223.

Hördt, A., A. Druiventak, R. Blaschek, F. Binot, A. Kemna, P. Kreye, and N. Zisser (2009). "Case histories of hydraulic conductivity estimation with induced polarization at the field scale". In: *Near Surface Geophysics* 7.5-6, pp. 529–545.

Hördt, A., K. Bairlein, A. Bielefeld, M. Bücker, E. Kuhn, S. Nordsiek, and H. Stebner (2016). "The dependence of induced polarization on fluid salinity and pH, studied with an extended model of membrane polarization". In: *Journal of Applied Geophysics* 135, pp. 408–417.

Hördt, A., K. Bairlein, M. Bücker, and H. Stebner (2017). "Geometrical constraints for membrane polarization". In: *Near Surface Geophysics* 15.6, pp. 579–592.

Hördt, A., R. Blaschek, A. Kemna, and N. Zisser (2007). "Hydraulic conductivity estimation from induced polarisation data at the field scale–the Krauthausen case history". In: *Journal of Applied Geophysics* 62.1, pp. 33–46. DOI: 10.1016/j.jappgeo.2006.08.001.

Huang, J., E. Scudiero, W. Clary, D. L. Corwin, and J. Triantafilis (2017). "Time-lapse monitoring of soil water content using electromagnetic conductivity imaging". In: *Soil Use and Management* 33.2, pp. 191–204. DOI: https://doi.org/10.1111/sum.12261. eprint: https://bsssjournals.onlinelibrary.wiley.com/doi/pdf/10.1111/sum.12261. URL: https://bsssjournals.onlinelibrary.wiley.com/doi/abs/10.1111/sum.12261.

Huisman, J. A., E. Zimmermann, O. Esser, F.-H. Haegel, A. Treichel, and H. Vereecken (2016). "Evaluation of a novel correction procedure to remove electrode impedance effects from broadband SIP measurements". In: *Journal of Applied Geophysics* 135, pp. 466–473.

Hüllermeier, E. and W. Waegeman (2021). "Aleatoric and epistemic uncertainty in machine learning: An introduction to concepts and methods". In: *Machine learning* 110.3, pp. 457–506.

Huntley, D., P. Bobrowsky, M. Hendry, R. Macciotta, D. Elwood, K. Sattler, M. Best, J. Chambers, and P. Meldrum (2019). "Application of multi-dimensional electrical resistivity tomography datasets to investigate a very slow-moving landslide near Ashcroft, British Columbia, Canada". In: *Landslides* 16, pp. 1033–1042.

Imhoff, R. O., W. J. van Verseveld, B. van Osnabrugge, and A. H. Weerts (2020). "Scaling Point-Scale (Pedo)transfer Functions to Seamless Large-Domain Parameter Estimates for High-Resolution Distributed Hydrologic Modeling: An Example for the Rhine River". In: *Water Resources Research* 56.4. e2019WR026807 10.1029/2019WR026807, e2019WR026807. DOI: https://doi.org/10.1029/2019WR026807. eprint: https://agupubs.onlinelibrary.wiley.com/doi/pdf/10.1029/2019WR026807. URL: https://agupubs.onlinelibrary.wiley.com/doi/abs/10.1029/2019WR026807.

Ismail Fawaz, H., G. Forestier, J. Weber, L. Idoumghar, and P.-A. Muller (2019). "Deep learning for time series classification: a review". In: *Data mining and knowledge discovery* 33.4, pp. 917–963.

Jana, R. B., B. P. Mohanty, and E. P. Springer (2007). "Multiscale pedotransfer functions for soil water retention". In: *Vadose Zone Journal* 6.4, pp. 868–878.

Jentsch, A. and C. Beierkuhnlein (2008). "Research frontiers in climate change: effects of extreme meteorological events on ecosystems". In: *Comptes Rendus Geoscience* 340.9-10, pp. 621–628.

Jian, J., A. Shiklomanov, W. D. Shuster, and R. D. Stewart (2021). "Predicting near-saturated hydraulic conductivity in urban soils". In: *Journal of Hydrology* 595, p. 126051.

Jiang, Z.-Y., X.-Y. Li, H.-W. Wu, X. Xiao, H.-Y. Chen, and J.-Q. Wei (2016). "Using electromagnetic induction method to reveal dynamics of soil water and salt during continual rainfall events". In: *biosystems engineering* 152, pp. 3–13.

Johnson, D. L., J. Koplik, and L. M. Schwartz (1986). "New pore-size parameter characterizing transport in porous media". In: *Physical review letters* 57.20, p. 2564.

Jongmans, D. and S. Garambois (2007). "Geophysical investigation of landslides: a review". In: *Bulletin de la Société géologique de France* 178.2, pp. 101–112. DOI: 10.2113/gssgfbull.178.2.101.

Jorda, H., M. Bechtold, N. Jarvis, and J. Koestel (2015). "Using boosted regression trees to explore key factors controlling saturated and near-saturated hydraulic conductivity". In: *European Journal of Soil Science* 66.4, pp. 744–756.

Jospin, L. V., H. Laga, F. Boussaid, W. Buntine, and M. Bennamoun (2022). "Hands-on Bayesian neural networks—A tutorial for deep learning users". In: *IEEE Computational Intelligence Magazine* 17.2, pp. 29–48.

Jost, W. (1952). "Diffusion in solids, liquids, gases". In: *Zeitschrift für Physikalische Chemie* 201.1-2, pp. 319–320.

Jougnot, D., A. Ghorbani, A. Revil, P. Leroy, and P. Cosenza (2010). "Spectral induced polarization of partially saturated clay-rocks: A mechanistic approach". In: *Geophysical Journal International* 180.1, pp. 210–224.

Jürgens, M., N. Meinert, V. Bengs, E. Hüllermeier, and W. Waegeman (2024). "Is Epistemic Uncertainty Faithfully Represented by Evidential Deep Learning Methods?" In: *arXiv preprint arXiv:2402.09056*.

Kaminsky, A. (2001). *Zondtem1d*. zond software corporation.

Katona, T., B. S. Gilfedder, S. Frei, M. Bücker, and A. Flores Orozco (2021). "High-resolution induced polarization imaging of biogeochemical carbon-turnover hot spots in a peatland". In: *Biogeosciences Discussions*, pp. 1–44. DOI: 10.5194/bg-18-4039-2021.

Katona, T., A. Flores-Orozco, L. Aigner, and C. Benold (2024). "Graphite Content Identification with Laboratory and Field Spectral Induced Polarization Measurements". In: *Applied Sciences* 14.10, p. 3955.

Katz, A. and A. Thompson (1987). "Prediction of rock electrical conductivity from mercury injection measurements". In: *Journal of Geophysical Research: Solid Earth* 92.B1, pp. 599–607.

Kearey, P., M. Brooks, and I. Hill (2002). *An introduction to geophysical exploration*. Vol. 4. John Wiley & Sons.

Keller, G. V. and F. C. Frischknecht (1966). *Electrical methods in geophysical prospecting*. Pergamon Press.

Kemna, A. (2000). "Tomographic inversion of complex resistivity - Theory and application". PhD thesis. Ruhr-Universität Bochum.

Kemna, A., A. Binley, G. Cassiani, E. Niederleithinger, A. Revil, L. Slater, K. H. Williams, A. F. Orozco, F.-H. Haegel, A. Hördt, et al. (2012). "An overview of the spectral induced polarization method for near-surface applications". In: *Near Surface Geophysics* 10.6, pp. 453–468. DOI: 10.3997/1873-0604.2012027.

Kemna, A., A. Binley, A. Ramirez, and W. Daily (2000). "Complex resistivity tomography for environmental applications". In: *Chemical Engineering Journal* 77.1-2, pp. 11–18. DOI: 10.1016/S1385-8947(99)00135-7.

Kemna, A., A. Binley, and L. Slater (2004). "Crosshole IP imaging for engineering and environmental applications". In: *Geophysics* 69.1, pp. 97–107. DOI: 10.1190/1.1649379.

Kemna, A., J. Vanderborght, B. Kulessa, and H. Vereecken (2002). "Imaging and characterisation of subsurface solute transport using electrical resistivity tomography (ERT) and equivalent transport models". In: *Journal of hydrology* 267.3-4, pp. 125–146.

Kendall, A. and Y. Gal (2017). "What uncertainties do we need in bayesian deep learning for computer vision?" In: *Advances in neural information processing systems* 30.

Keppeler, J. G. (2015). "Coals, Lignite, and Peat". In: *Mechanical Engineers' Handbook, Volume 4: Energy and Power* 4, p. 703.

Klose, T., J. Guillemoteau, F.-X. Simon, and J. Tronicke (Aug. 2018). "Toward subsurface magnetic permeability imaging with electromagnetic induction sensors: Sensitivity computation and reconstruction of measured data". In: *Geophysics* 83.5, E335–E345. DOI: 10.1190/geo2017-0827.1. eprint: https://pubs.geoscienceworld.org/seg/geophysics/article-pdf/83/5/E335/4521179/geo-2017-0827.1.pdf. URL: https://doi.org/10.1190/geo2017-0827.1.

Klose, T., J. Guillemoteau, G. Vignoli, and J. Tronicke (2022). "Laterally constrained inversion (LCI) of multi-configuration EMI data with tunable sharpness". In: *Journal of Applied Geophysics* 196, p. 104519. ISSN: 0926-9851. DOI: https://doi.org/10.1016/j.jappgeo.2021.104519. URL: https://www.sciencedirect.com/science/article/pii/S0926985121002676.

Koch, K., A. Kemna, J. Irving, and K. Holliger (2011). "Impact of changes in grain size and pore space on the hydraulic conductivity and spectral induced polarization response of sand". In: *Hydrology and Earth System Sciences* 15.6, pp. 1785–1794.

Kohavi, R. (1995). "A study of cross-validation and bootstrap for accuracy estimation and model selection". In: *Morgan Kaufman Publishing*.

Konapala, G., A. K. Mishra, Y. Wada, and M. E. Mann (2020). "Climate change will affect global water availability through compounding changes in seasonal precipitation and evaporation". In: *Nature communications* 11.1, p. 3044.

Kreith, D., P. Leroy, and M. Bücker (2024). "A new semi-analytic model for Stern-layer polarization in pore throats". In: *Geophysical Journal International* 239.3, pp. 1910–1927.

Krenmayr, H. and W. Schnabel (2006). "Geologische Karte Oberösterreich 1:200.000". In: *Geologische Karte Oberösterreich 1:200.000*. Geological Survey of Austria.

Kušnirák, D., I. Dostál, R. Putiška, and A. Mojzeš (2016). "Complex geophysical investigation of the Kapušany landslide (Eastern Slovakia)". In: *Contributions to Geophysics and Geodesy* 46.2, pp. 111–124.

LaBrecque, D. and W. Daily (2008). "Assessment of measurement errors for galvanic-resistivity electrodes of different composition". In: *Geophysics* 73.2, F55–F64.

LaBrecque, D. J., M. Miletto, W. Daily, A. Ramirez, and E. Owen (1996). "The effects of noise on Occam's inversion of resistivity tomography data". In: *Geophysics* 61.2, pp. 538–548. DOI: 10.1190/1.1443980.

LaBrecque, D. J. and S. H. Ward (1990). "Two-dimensional cross-borehole resistivity model fitting". In: *Geotechnical and environmental geophysics* 1, pp. 51–57.

Lakshminarayanan, B., A. Pritzel, and C. Blundell (2017). "Simple and scalable predictive uncertainty estimation using deep ensembles". In: *Advances in neural information processing systems* 30.

Lampinen, J. and A. Vehtari (2001). "Bayesian approach for neural networks—review and case studies". In: *Neural Networks* 14.3, pp. 257–274. ISSN: 0893-6080. DOI: https://doi.org/10.1016/S0893-6080(00)00098-8. URL: https://www.sciencedirect.com/science/article/pii/S0893608000000988.

Lankston, R. W. (1990). "High-resolution refraction seismic data acquisition and interpretation". In: *Geotechnical an Environmental Geophysics: Volume I: Review and Tutorial*. Society of Exploration Geophysicists, pp. 45–74.

Lapenna, V., P. Lorenzo, A. Perrone, S. Piscitelli, F. Sdao, and E. Rizzo (2003). "High-resolution geoelectrical tomographies in the study of Giarrossa landslide (southern Italy)". In: *Bulletin of Engineering Geology and the Environment* 62.3, pp. 259–268. DOI: 10.1007/s10064-002-0184-z.

Lebourg, T., S. Binet, E. Tric, H. Jomard, and S. El Bedoui (2005). "Geophysical survey to estimate the 3D sliding surface and the 4D evolution of the water pressure on part of a deep seated landslide". In: *Terra Nova* 17.5, pp. 399–406.

Lehmann, P., F. Gambazzi, B. Suski, L. Baron, A. Askarinejad, S. M. Springman, K. Holliger, and D. Or (2013). "Evolution of soil wetting patterns preceding a hydrologically induced landslide inferred from electrical resistivity survey and point measurements of volumetric water content and pore water pressure". In: *Water Resources Research* 49.12, pp. 7992–8004.

Lehmann, P., O. Merlin, P. Gentine, and D. Or (2018). "Soil texture effects on surface resistance to bare-soil evaporation". In: *Geophysical Research Letters* 45.19, pp. 10–398.

Lehmann, P., J. von Ruette, and D. Or (2019). "Deforestation effects on rainfall-induced shallow landslides: Remote sensing and physically-based modelling". In: *Water Resources Research* 55.11, pp. 9962–9976.

Leroy, P. and A. Revil (2004). "A triple-layer model of the surface electrochemical properties of clay minerals". In: *Journal of Colloid and interface Science* 270.2, pp. 371–380.

Leroy, P., A. Revil, A. Kemna, P. Cosenza, and A. Ghorbani (2008). "Complex conductivity of water-saturated packs of glass beads". In: *Journal of colloid and interface science* 321.1, pp. 103–117. DOI: 10.1016/j.jcis.2007.12.031.

Leroy, P. and A. Revil (2009). "A mechanistic model for the spectral induced polarization of clay materials". In: *Journal of Geophysical Research: solid earth* 114.B10. DOI: 10.1029/2008jb006114.

Lesch, S. M., D. J. Strauss, and J. D. Rhoades (1995). "Spatial prediction of soil salinity using electromagnetic induction techniques: 2. An efficient spatial sampling algorithm suitable for multiple linear regression model identification and estimation". In: *Water resources research* 31.2, pp. 387–398.

Lesmes, D. P. and K. M. Frye (2001). "Influence of pore fluid chemistry on the complex conductivity and induced polarization responses of Berea sandstone". In: *Journal of Geophysical Research: Solid Earth* 106.B3, pp. 4079–4090. DOI: 10.1029/2000jb900392.

Lesmes, D. P. and F. D. Morgan (2001). "Dielectric spectroscopy of sedimentary rocks". In: *Journal of Geophysical Research: Solid Earth* 106.B7, pp. 13329–13346. DOI: 10.1029/2000jb900402.

Leucci, G., F. Greco, L. De Giorgi, and R. Mauceri (2007). "Three-dimensional image of seismic refraction tomography and electrical resistivity tomography survey in the castle of Occhiola (Sicily, Italy)". In: *Journal of Archaeological science* 34.2, pp. 233–242.

Lévy, L., B. Gibert, F. Sigmundsson, Ó. G. Flóvenz, G. Hersir, P. Briole, and P. Pezard (2018). "The role of smectites in the electrical conductivity of active hydrothermal systems: electrical properties of core samples from Krafla volcano, Iceland". In: *Geophysical Journal International* 215.3, pp. 1558–1582.

Li, J., Y. Liu, C. Yin, X. Ren, and Y. Su (2020a). "Fast imaging of time-domain airborne EM data using deep learning technology". In: *GEOPHYSICS* 85.5, E163–E170. DOI: 10.1190/geo2019-0015.1. URL: https://doi.org/10.1190/geo2019-0015.1.

Li, P., Y. Zha, Y. Zhang, C.-H. Michael Tso, S. Attinger, L. Samaniego, and J. Peng (2024a). "Deep Learning Integrating Scale Conversion and Pedo-Transfer Function to Avoid Potential Errors in Cross-Scale Transfer". In: *Water Resources Research* 60.3. e2023WR035543 2023WR035543, e2023WR035543. DOI: https://doi.org/10.1029/2023WR035543. eprint: https://agupubs.onlinelibrary.wiley.com/doi/pdf/10.1029/2023WR035543. URL: https://agupubs.onlinelibrary.wiley.com/doi/abs/10.1029/2023WR035543.

Li, R., X. Hu, D. Xu, Y. Liu, and N. Yu (2020b). "Characterizing the 3D hydrogeological structure of a debris landslide using the transient electromagnetic method". In: *Journal of Applied Geophysics* 175, p. 103991.

Li, S., W. Song, L. Fang, Y. Chen, P. Ghamisi, and J. A. Benediktsson (2019). "Deep learning for hyperspectral image classification: An overview". In: *IEEE Transactions on Geoscience and Remote Sensing* 57.9, pp. 6690–6709.

Li, X., H. Wang, S. Qin, L. Lin, X. Wang, and W. Cornelis (2024b). "Evaluating ensemble learning in developing pedotransfer functions to predict soil hydraulic properties". In: *Journal of Hydrology* 640, p. 131658.

Lilly, A., A. Nemes, W. Rawls, and Y. A. Pachepsky (2008). "Probabilistic approach to the identification of input variables to estimate hydraulic conductivity". In: *Soil Science Society of America Journal* 72.1, pp. 16–24.

Lim, H., H. Yang, K. W. Chun, and H. T. Choi (2020). "Development of Pedo-Transfer Functions for the Saturated Hydraulic Conductivity of Forest Soil in South Korea Considering Forest Stand and Site Characteristics". In: *Water* 12.8. ISSN: 2073-4441. DOI: 10.3390/w12082217. URL: https://www.mdpi.com/2073-4441/12/8/2217.

Lin, Q., S. Steger, M. Pittore, J. Zhang, L. Wang, T. Jiang, and Y. Wang (2022). "Evaluation of potential changes in landslide susceptibility and landslide occurrence frequency in China under climate change". In: *Science of the total environment* 850, p. 158049.

Lin, Q., Y. Wang, T. Glade, J. Zhang, and Y. Zhang (2020). "Assessing the spatiotemporal impact of climate change on event rainfall characteristics influencing landslide occurrences based on multiple GCM projections in China". In: *Climatic Change* 162, pp. 761–779.

Linander, H., O. Balabanov, H. Yang, and B. Mehlig (2023). "Looking at the posterior: accuracy and uncertainty of neural-network predictions". In: *Machine Learning: Science and Technology* 4.4, p. 045032.

Loke, M., J. Chambers, and R. Ogilvy (2006). "Inversion of 2D spectral induced polarization imaging data". In: *Geophysical Prospecting* 54.3, pp. 287–301.

Lubczynski, M., M. Leblanc, and O. Batelaan (2024). "Remote sensing and hydrogeophysics give a new impetus to integrated hydrological models: A review". In: *Journal of Hydrology*, p. 130901.

Lui, S., T. Kuramochi, S. Smit, M. Roelfsema, A. Hsu, A. Weinfurter, S. Chan, T. Hale, H. Fekete, K. Lütkehermöller, et al. (2021). "Correcting course: the emission reduction potential of international cooperative initiatives". In: *Climate Policy* 21.2, pp. 232–250.

Lysdahl, A., A. A. Pfaffhuber, H. Anschütz, K. Kåsin, and S. Bazin (2017). "Helicopter electromagnetic scanning as a first step in regional quick clay mapping". In: *Landslides in Sensitive Clays: From Research to Implementation*, pp. 443–452.

Madsen, L. M., G. Fiandaca, and E. Auken (2020). "3-D time-domain spectral inversion of resistivity and full-decay induced polarization data—full solution of Poisson's equation and modelling of the current waveform". In: *Geophysical Journal International* 223.3, pp. 2101–2116.

Maierhofer, T., C. Hauck, C. Hilbich, A. Kemna, and A. Flores Orozco (2022). "Spectral induced polarization imaging to investigate an ice-rich mountain permafrost site in Switzerland".

In: *The Cryosphere* 16.5, pp. 1903–1925. DOI: 10.5194/tc-16-1903-2022.

Maierhofer, T., A. Flores Orozco, N. Roser, J. K. Limbrock, C. Hilbich, C. Moser, A. Kemna, E. Drigo, U. Morra di Cella, and C. Hauck (2024). "Spectral induced polarization imaging to monitor seasonal and annual dynamics of frozen ground at a mountain permafrost site in the Italian Alps". In: *The Cryosphere* 18.7, pp. 3383–3414.

Malet, J.-P., D. Laigle, A. Remaıtre, and O. Maquaire (2005). "Triggering conditions and mobility of debris flows associated to complex earthflows". In: *Geomorphology* 66.1-4, pp. 215–235.

Manchado, A. M.-T., J. A. Ballesteros-Cánovas, S. Allen, and M. Stoffel (2022). "Deforestation controls landslide susceptibility in Far-Western Nepal". In: *Catena* 219, p. 106627.

Marciniak, A., S. Kowalczyk, T. Gontar, B. Owoc, A. Nawrot, B. Luks, J. Cader, and M. Majdański (2021). "Integrated geophysical imaging of a mountain landslide–a case study from the Outer Carpathians, Poland". In: *Journal of Applied Geophysics* 191, p. 104364.

Marescot, L., R. Monnet, and D. Chapellier (2008). "Resistivity and induced polarization surveys for slope instability studies in the Swiss Alps". In: *Engineering Geology* 98.1-2, pp. 18–28. DOI: 10.1016/j.enggeo.2008.01.010.

Markert, A., K. Bohne, M. Facklam, and G. Wessolek (2017). "Pedotransfer functions of soil thermal conductivity for the textural classes sand, silt, and loam". In: *Soil Science Society of America Journal* 81.6, pp. 1315–1327.

Marshall, D. J. and T. R. Madden (1959). "Induced polarization, a study of its causes". In: *Geophysics* 24.4, pp. 790–816. DOI: 10.1190/1.1438659.

Martin, T. and T. Günther (2013). "Complex resistivity tomography (CRT) for fungus detection on standing oak trees". In: *European Journal of Forest Research* 132, pp. 765–776.

Martin, T., T. Günther, A. F. Orozco, and T. Dahlin (2020). "Evaluation of spectral induced polarization field measurements in time and frequency domain". In: *Journal of Applied Geophysics* 180, p. 104141. DOI: 10.1016/j.jappgeo.2020.104141.

Martín Abadi, Ashish Agarwal, Paul Barham, Eugene Brevdo, Zhifeng Chen, Craig Citro, Greg S. Corrado, Andy Davis, Jeffrey Dean, Matthieu Devin, Sanjay Ghemawat, Ian Goodfellow, Andrew Harp, Geoffrey Irving, Michael Isard, Y. Jia, Rafal Jozefowicz, Lukasz Kaiser, Manjunath Kudlur, Josh Levenberg, Dandelion Mané, Rajat Monga, Sherry Moore, Derek Murray, Chris Olah, Mike Schuster, Jonathon Shlens, Benoit Steiner, Ilya Sutskever, Kunal Talwar, Paul Tucker, Vincent Vanhoucke, Vijay Vasudevan, Fernanda Viégas, Oriol Vinyals, Pete Warden, Martin Wattenberg, Martin Wicke, Yuan Yu, and Xiaoqiang Zheng (2015). *TensorFlow: Large-Scale Machine Learning on Heterogeneous Systems*. Software available from tensorflow.org. URL: https://www.tensorflow.org/.

Martinez, G., K. Vanderlinden, J. V. Giráldez, A. J. Espejo, and J. L. Muriel (2010). "Field-scale soil moisture pattern mapping using electromagnetic induction". In: *Vadose Zone Journal* 9.4, pp. 871–881.

Martínez-Moreno, F. J., F. A. Monteiro-Santos, I. Bernardo, M. Farzamian, C. Nascimento, J. Fernandes, B. Casal, and J. Ribeiro (2017). "Identifying seawater intrusion in coastal areas by means of 1D and quasi-2D joint inversion of TDEM and VES data". In: *Journal of Hydrology* 552, pp. 609–619.

Martini, E., U. Werban, S. Zacharias, M. Pohle, P. Dietrich, and U. Wollschläger (2017a). "Repeated electromagnetic induction measurements for mapping soil moisture at the field scale: Validation with data from a wireless soil moisture monitoring network". In: *Hydrology and Earth System Sciences* 21.1, pp. 495–513.

Martini, E., U. Werban, S. Zacharias, M. Pohle, P. Dietrich, and U. Wollschläger (2017b). "Repeated electromagnetic induction measurements for mapping soil moisture at the field scale: Validation with data from a wireless soil moisture monitoring network". In: *Hydrology and Earth System Sciences* 21.1, pp. 495–513.

Mauritsch, H. J., W. Seiberl, R. Arndt, A. Römer, K. Schneiderbauer, and G. P. Sendlhofer (2000). "Geophysical investigations of large landslides in the Carnic Region of southern Austria". In: *Engineering Geology* 56.3-4, pp. 373–388.

Maurya, P. K., N. Balbarini, I. Møller, V. Rønde, A. V. Christiansen, P. L. Bjerg, E. Auken, and G. Fiandaca (Jan. 2018). "Subsurface imaging of water electrical conductivity, hydraulic permeability and lithology at contaminated sites by induced polarization". In: *Geophysical Journal International* 213.2, pp. 770–785. ISSN: 0956-540X. DOI: 10.1093/gji/ggy018. eprint: https://academic.oup.com/gji/article-pdf/213/2/770/24139587/ggy018.pdf. URL: https://doi.org/10.1093/gji/ggy018.

McBratney, A. B., B. Minasny, S. R. Cattle, and R. W. Vervoort (2002). "From pedotransfer functions to soil inference systems". In: *Geoderma* 109.1-2, pp. 41–73.

McBratney, A. B., B. Minasny, and G. Tranter (2011). "Necessary meta-data for pedotransfer functions". In: *Geoderma* 160.3-4, pp. 627–629.

McLachlan, P., G. Blanchy, and A. Binley (2021a). "EMagPy: Open-source standalone software for processing, forward modeling and inversion of electromagnetic induction data". In: *Computers & Geosciences* 146, p. 104561.

McLachlan, P., G. Blanchy, J. Chambers, J. Sorensen, S. Uhlemann, P. Wilkinson, and A. Binley (2021b). "The application of electromagnetic induction methods to reveal the hydrogeological structure of a riparian wetland". In: *Water Resources Research* 57.6, e2020WR029221.

McLachlan, P. J., V. Karloukovski, and A. Binley (2024). "Field-based estimation of cation exchange capacity using induced polarization methods". In: *Earth Surface Processes and Landforms*.

McNeill, J. (1980a). *Electrical Conductivity of Soil and Rocks. Technical Note TN-5*. Geonics Ltd. Missiauga, Canada.

McNeill, J. (1980b). *Electromagnetic Terrain Conductivity Measurements at Low Induction Numbers. Technical Note TN-6*. Geonics Ltd. Missiauga, Canada.

Meier, P., T. Kalscheuer, J. E. Podgorski, L. Kgotlhang, A. G. Green, S. Greenhalgh, L. Rabenstein, J. Doetsch, W. Kinzelbach, E. Auken, et al. (2014). "Hydrogeophysical investigations in the western and north-central Okavango Delta (Botswana) based on helicopter and ground-based transient electromagnetic data and electrical resistance tomography". In: *Geophysics* 79.5, B201–B211.

Mendoza Veirana, G. M., H. Grison, J. Verhegge, W. Cornelis, and P. De Smedt (2024). "Exploring the link between cation exchange capacity and magnetic susceptibility". In: *EGUsphere[preprint]* 2024, pp. 1–17.

Mensah, C., Y. Katanda, M. Krishnapillai, M. Cheema, and L. Galagedara (Aug. 2023). "Estimation of soil water content using electromagnetic induction sensors under different land uses". In: *Environmental Research Communications* 5.8, p. 085002. DOI: 10.1088/2515-7620/acebbd. URL: https://dx.doi.org/10.1088/2515-7620/acebbd.

Merritt, A., J. Chambers, W. Murphy, P. Wilkinson, L. West, D. Gunn, P. Meldrum, M. Kirkham, and N. Dixon (2014). "3D ground model development for an active landslide in Lias mudrocks using geophysical, remote sensing and geotechnical methods". In: *Landslides* 11, pp. 537–550.

Mester, A., J. van der Kruk, E. Zimmermann, and H. Vereecken (2011). "Quantitative two-layer conductivity inversion of multi-configuration electromagnetic induction measurements". In: *Vadose Zone Journal* 10.4, pp. 1319–1330.

Milkereit, B., H. Stümpel, and W. Rabbel (1986). "Shear-wave reflection profiling for near-surface lignite exploration". In: *Geophysical prospecting* 34.6, pp. 845–855.

Minasny, B. and E. Perfect (2004). "Solute adsorption and transport parameters". In: *Developments in Soil Science* 30, pp. 195–224.

Minasny, B., A. B. McBratney, and K. L. Bristow (1999). "Comparison of different approaches to the development of pedotransfer functions for water-retention curves". In: *Geoderma* 93.3-4, pp. 225–253.

Minasny, B. and A. B. McBratney (2002). "The Neuro-m Method for Fitting Neural Network Parametric Pedotransfer Functions". In: *Soil Science Society of America Journal* 66.2, pp. 352–361. DOI: https://doi.org/10.2136/sssaj2002.3520. eprint: https://acsess.onlinelibrary.wiley.com/doi/pdf/10.2136/sssaj2002.3520. URL: https://acsess.onlinelibrary.wiley.com/doi/abs/10.2136/sssaj2002.3520.

Minsley, B. J. (2011). "A trans-dimensional Bayesian Markov chain Monte Carlo algorithm for model assessment using frequency-domain electromagnetic data". In: *Geophysical Journal International* 187.1, pp. 252–272.

Moeys, J., M. Larsbo, L. Bergström, C. D. Brown, Y. Coquet, and N. Jarvis (2012). "Functional test of pedotransfer functions to predict water flow and solute transport with the dual-permeability model MACRO". In: *Hydrology and Earth System Sciences* 16.7, pp. 2069–2083.

Moghadas, D. (2020). "One-dimensional deep learning inversion of electromagnetic induction data using convolutional neural network". In: *Geophysical Journal International* 222.1, pp. 247–259.

Moghadas, D., K. Z. Jadoon, and M. F. McCabe (2017). "Spatiotemporal monitoring of soil water content profiles in an irrigated field using probabilistic inversion of time-lapse EMI data". In: *Advances in Water Resources* 110, pp. 238–248.

Mohammadi Foumani, N., L. Miller, C. W. Tan, G. I. Webb, G. Forestier, and M. Salehi (2024). "Deep learning for time series classification and extrinsic regression: A current survey". In: *ACM Computing Surveys* 56.9, pp. 1–45.

Mohammed, A. and R. Kora (2023). "A comprehensive review on ensemble deep learning: Opportunities and challenges". In: *Journal of King Saud University-Computer and Information Sciences* 35.2, pp. 757–774.

Morelli, G. and D. J. LaBrecque (1996). "Robust scheme for ERT inverse modeling". In: *9th EEGS Symposium on the Application of Geophysics to Engineering and Environmental Problems*. European Association of Geoscientists & Engineers, cp–205.

Mualem, Y. and S. Friedman (1991). "Theoretical prediction of electrical conductivity in saturated and unsaturated soil". In: *Water Resources Research* 27.10, pp. 2771–2777.

Mualem, Y. (1976). "A new model for predicting the hydraulic conductivity of unsaturated porous media". In: *Water resources research* 12.3, pp. 513–522.

Myers, K. J. and P. B. Wignall (1987). "Understanding Jurassic organic-rich mudrocks—new concepts using gamma-ray spectrometry and palaeoecology: examples from the Kimmeridge Clay of Dorset and the Jet Rock of Yorkshire". In: *Marine clastic sedimentology: Concepts and case studies*, pp. 172–189.

Nakazato, H. and N. Konishi (2005). "Subsurface structure exploration of wide landslide area by Aerial electromagnetic exploration". In: *Landslides* 2, pp. 165–169.

Nasta, P., B. Szabó, and N. Romano (2021). "Evaluation of pedotransfer functions for predicting soil hydraulic properties: A voyage from regional to field scales across Europe". In: *Journal of Hydrology: Regional Studies* 37, p. 100903.

Neira-Albornoz, A., M. Martínez-Parga-Méndez, M. González, and A. Spitz (2024). "Understanding requirements, limitations and applicability of QSAR and PTF models for predicting sorption of pollutants on soils: a systematic review". In: *Frontiers in Environmental Science* 12, p. 1379283.

Nemes, A. (2015). "Why do they keep rejecting my manuscript—do's and don'ts and new horizons in pedotransfer studies". In: *Agrokémia és talajtan* 64.2, pp. 361–371.

Nemes, A., E. Czinege, and C. Farkas (2010). "Use of simulation modeling and pedotransfer functions to evaluate different irrigation scheduling scenarios in a heterogeneous field". In: *Proceedings of the 19th World Congress of Soil Science, Soil Solutions for a Changing World, Brisbane, Australia*, pp. 1–6.

Nemes, A., W. J. Rawls, and Y. A. Pachepsky (2006). "Use of the nonparametric nearest neighbor approach to estimate soil hydraulic properties". In: *Soil Science Society of America Journal* 70.2, pp. 327–336.

Nemes, A., M. Schaap, and J. Wösten (2003). "Functional evaluation of pedotransfer functions derived from different scales of data collection". In: *Soil Science Society of America Journal* 67.4, pp. 1093–1102.

Niu, Q. (2023). "Revisiting the diffuse layer polarization of a spherical grain in electrolytes with numerical solutions of Nernst-Planck-Poisson equations". In: *Journal of Geophysical Research: Solid Earth* 128.8, e2022JB025934.

Ntarlagiannis, D., J. Robinson, P. Soupios, and L. Slater (2016). "Field-scale electrical geophysics over an olive oil mill waste deposition site: Evaluating the information content of resistivity versus induced polarization (IP) images for delineating the spatial extent of organic contamination". In: *Journal of Applied Geophysics* 135, pp. 418–426.

Ntarlagiannis, D., K. H. Williams, L. Slater, and S. Hubbard (2005). "Low-frequency electrical response to microbial induced sulfide precipitation". In: *Journal of Geophysical Research: Biogeosciences* 110.G2.

Okay, G., P. Leroy, A. Ghorbani, P. Cosenza, C. Camerlynck, J. Cabrera, N. Florsch, and A. Revil (2014). "Spectral induced polarization of clay-sand mixtures: Experiments and modeling". In: *Geophysics* 79.6, E353–E375.

Oldenburg, D. W. and Y. Li (1994). "Inversion of induced polarization data". In: *Geophysics* 59.9, pp. 1327–1341.

Olivier, A., M. D. Shields, and L. Graham-Brady (2021). "Bayesian neural networks for uncertainty quantification in data-driven materials modeling". In: *Computer methods in applied mechanics and engineering* 386, p. 114079.

Olsson, P.-I., G. Fiandaca, P. K. Maurya, T. Dahlin, and E. Auken (2019). "Effect of current pulse duration in recovering quantitative induced polarization models from time-domain full-response and integral chargeability data". In: *Geophysical Journal International* 218.3, pp. 1739–1747.

Overgaard, J., D. Rosbjerg, and M. Butts (2006). "Land-surface modelling in hydrological perspective–a review". In: *Biogeosciences* 3.2, pp. 229–241.

Pachepsky, Y. A. and W. Rawls (2003). “Soil structure and pedotransfer functions”. In: *European Journal of Soil Science* 54.3, pp. 443–452.

Pachepsky, Y. A., W. Rawls, and H. Lin (2006). “Hydropedology and pedotransfer functions”. In: *Geoderma* 131.3-4, pp. 308–316.

Papalexiou, S. M. and A. Montanari (2019). “Global and regional increase of precipitation extremes under global warming”. In: *Water Resources Research* 55.6, pp. 4901–4914.

Pape, H., L. Riepe, and J. R. Schopper (1987). “Theory of self-similar network structures in sedimentary and igneous rocks and their investigation with microscopical and physical methods”. In: *Journal of Microscopy* 148.2, pp. 121–147.

Parasnis, D. S. (2012). *Principles of applied geophysics*. Springer Science & Business Media.

Park, C. B., R. D. Miller, and J. Xia (1999). “Multichannel analysis of surface waves”. In: *Geophysics* 64.3, pp. 800–808. DOI: 10.1190/1.1444590.

Patil, N. G. and S. K. Singh (2016). “Pedotransfer functions for estimating soil hydraulic properties: A review”. In: *Pedosphere* 26.4, pp. 417–430.

Pavlin, L., B. Széles, P. Strauss, A. P. Blaschke, and G. Blöschl (2020). “Event and seasonal hydrologic connectivity patterns in an agricultural headwater catchment”. In: *Hydrology and Earth System Sciences Discussions* 2020, pp. 1–34.

Paz, M. C., M. Farzamian, A. M. Paz, N. L. Castanheira, M. C. Gonçalves, and F. Monteiro Santos (2020). “Assessing soil salinity dynamics using time-lapse electromagnetic conductivity imaging”. In: *SOIL* 6.2, pp. 499–511. DOI: 10.5194/soil-6-499-2020. URL: https://soil.copernicus.org/articles/6/499/2020/.

Paz, M. C., N. L. Castanheira, A. M. Paz, M. C. Gonçalves, F. Monteiro Santos, and M. Farzamian (2024). “Comparison of Electromagnetic Induction and Electrical Resistivity Tomography in Assessing Soil Salinity: Insights from Four Plots with Distinct Soil Salinity Levels”. In: *Land* 13.3, p. 295.

Pazzi, V., S. Morelli, and R. Fanti (2019). “A review of the advantages and limitations of geophysical investigations in landslide studies”. In: *International Journal of Geophysics* 2019. DOI: 10.1155/2019/2983087.

Pelton, W. H., S. Ward, P. Hallof, W. Sill, and P. H. Nelson (1978). “Mineral discrimination and removal of inductive coupling with multifrequency IP”. In: *Geophysics* 43.3, pp. 588–609. DOI: 10.1190/1.1440839.

Peng, P., L. Liu, T. A. Arkhangelskaya, A. Y. Mady, M. Dyck, F. Zvomuya, and H. He (2024). “Random forest approach to estimate soil thermal diffusivity: Evaluation and comparison with traditional pedotransfer functions”. In: *Soil and Tillage Research* 244, p. 106233.

Peng, R., B. Han, Y. Liu, and X. Hu (2021). “EM3DANI: A Julia package for fully anisotropic 3D forward modeling of electromagnetic data”. In: *GEOPHYSICS* 86.5, F49–F60. DOI: 10.1190/geo2020-0489.1. eprint: https://doi.org/10.1190/geo2020-0489.1. URL: https://doi.org/10.1190/geo2020-0489.1.

Perrone, A., F. Canora, G. Calamita, J. Bellanova, V. Serlenga, S. Panebianco, N. Tragni, S. Piscitelli, L. Vignola, A. Doglioni, et al. (2021). “A multidisciplinary approach for landslide residual risk assessment: the Pomarico landslide (Basilicata Region, Southern Italy) case study”. In: *Landslides* 18, pp. 353–365.

Perrone, A., V. Lapenna, and S. Piscitelli (2014). “Electrical resistivity tomography technique for landslide investigation: A review”. In: *Earth-Science Reviews* 135, pp. 65–82. DOI: 10.1016/j.earscirev.2014.04.002.

Petley, D. N. (2010). “On the impact of climate change and population growth on the occurrence of fatal landslides in South, East and SE Asia”. In: *Quarterly Journal of Engineering Geology and Hydrogeology* 43.4, pp. 487–496.

Petley, D., F. Mantovani, M. Bulmer, and A. Zannoni (2005). “The use of surface monitoring data for the interpretation of landslide movement patterns”. In: *Geomorphology* 66.1-4, pp. 133–147.

Petschko, H., A. Brenning, R. Bell, J. Goetz, and T. Glade (2014). “Assessing the quality of landslide susceptibility maps–case study Lower Austria”. In: *Natural hazards and earth system sciences* 14.1, pp. 95–118.

Picarelli, L., S. Lacasse, and K. K. S. Ho (2021). “The Impact of Climate Change on Landslide Hazard and Risk”. In: *Understanding and Reducing Landslide Disaster Risk: Volume 1 Sendai Landslide Partnerships and Kyoto Landslide Commitment*. Ed. by K. Sassa, M. Mikoš, S. Sassa, P. T. Bobrowsky, K. Takara, and K. Dang. Cham: Springer International Publishing, pp. 131–141. ISBN: 978-3-030-60196-6. DOI: 10.1007/978-3-030-60196-6_6. URL: https://doi.org/10.1007/978-3-030-60196-6_6.

Picciafuoco, T., R. Morbidelli, A. Flammini, C. Saltalippi, C. Corradini, P. Strauss, and G. Blöschl (2019a). “A Pedotransfer Function for Field-Scale Saturated Hydraulic Conductivity of a Small Watershed”. In: *Vadose Zone Journal* 18.1, p. 190018. DOI: https://doi.org/10.2136/vzj2019.02.0018. eprint: https://acsess.onlinelibrary.wiley.com/doi/pdf/10.2136/vzj2019.02.0018. URL: https://acsess.onlinelibrary.wiley.com/doi/abs/10.2136/vzj2019.02.0018.

Picciafuoco, T., R. Morbidelli, A. Flammini, C. Saltalippi, C. Corradini, P. Strauss, and G. Blöschl (2019b). “On the estimation of spatially representative plot scale saturated hydraulic conductivity in an agricultural setting”. In: *Journal of hydrology* 570, pp. 106–117.

Portniaguine, O. and M. S. Zhdanov (1999). “Focusing geophysical inversion images”. In: *Geophysics* 64.3, pp. 874–887.

Price, W., A. Potter, T. K. Thomson, G. Smith, A. Hazen, and R. Beardsley (1911). “Discussion on dams on sand foundations”. In: *Transactions of the American Society of Civil Engineers* 73.3, pp. 190–208.

Pringle, M., N. Romano, B. Minasny, G. B. Chirico, and R. Lark (2007). “Spatial evaluation of pedotransfer functions using wavelet analysis”. In: *Journal of Hydrology* 333.2-4, pp. 182–198.

Puhlmann, H. and K. von Wilpert (2012). “Pedotransfer functions for water retention and unsaturated hydraulic conductivity of forest soils”. In: *Journal of Plant Nutrition and Soil Science* 175.2, pp. 221–235. DOI: https://doi.org/10.1002/jpln.201100139. eprint: https://onlinelibrary.wiley.com/doi/pdf/10.1002/jpln.201100139. URL: https://onlinelibrary.wiley.com/doi/abs/10.1002/jpln.201100139.

Puzyrev, V. (May 2019). “Deep learning electromagnetic inversion with convolutional neural networks”. In: *Geophysical Journal International* 218.2, pp. 817–832. ISSN: 0956-540X. DOI: 10.1093/gji/ggz204. eprint: https://academic.oup.com/gji/article-pdf/218/2/817/28693772/ggz204.pdf. URL: https://doi.org/10.1093/gji/ggz204.

Radic, T. (2016). “New modular multi-channel field equipment for SIP measurements up to 20 kHz”. In: *Near Surface Geoscience 2016-22nd European Meeting of Environmental and Engineering Geophysics*. Vol. 2016. 1. European Association of Geoscientists & Engineers, cp–495.

Rawls, W. J., D. L. Brakensiek, and K. Saxtonn (1982). “Estimation of soil water properties”. In: *Transactions of the ASAE* 25.5, pp. 1316–1320.

Reinecke, R., H. Müller Schmied, T. Trautmann, L. S. Andersen, P. Burek, M. Flörke, S. N. Gosling, M. Grillakis, N. Hanasaki, A. Koutroulis, et al. (2021). "Uncertainty of simulated groundwater recharge at different global warming levels: a global-scale multi-model ensemble study". In: *Hydrology and Earth System Sciences* 25.2, pp. 787–810.

Ren, D., L. M. Leslie, and Q. Duan (2012). "Landslides caused deforestation". In: *Deforestation around the World* 95, p. 123.

Revil, A. (2012). "Spectral induced polarization of shaly sands: Influence of the electrical double layer". In: *Water Resources Research* 48.2. DOI: 10.1029/2011wr011260.

Revil, A. and N. Florsch (2010). "Determination of permeability from spectral induced polarization in granular media". In: *Geophysical Journal International* 181.3, pp. 1480–1498. DOI: 10.1111/j.1365-246x.2010.04573.x.

Revil, A. and P. Glover (1997). "Theory of ionic-surface electrical conduction in porous media". In: *Physical review B* 55.3, p. 1757.

Revil, A., M. Schmutz, F. Abdulsamad, A. Balde, C. Beck, A. Ghorbani, and S. Hubbard (2021). "Field-scale estimation of soil properties from spectral induced polarization tomography". In: *Geoderma* 403, p. 115380. DOI: 10.1016/j.geoderma.2021.115380.

Revil, A., A. S. Ahmed, A. Coperey, L. Ravanel, R. Sharma, and N. Panwar (2020). "Induced polarization as a tool to characterize shallow landslides". In: *Journal of Hydrology* 589, p. 125369. ISSN: 0022-1694. DOI: 10.1016/j.jhydrol.2020.125369.

Revil, A., A. Coperey, Z. Shao, N. Florsch, I. L. Fabricius, Y. Deng, J. R. Delsman, P. S. Pauw, M. Karaoulis, P. G. B. de Louw, E. S. van Baaren, W. Dabekaussen, A. Menkovic, and J. L. Gunnink (2017). "Complex conductivity of soils. COMPLEX CONDUCTIVITY OF SOILS". In: *Water Resources Research* 53, pp. 7121–7147. ISSN: 0043-1397. DOI: 10.1002/2017wr020655.

Revil, A. and P. W. J. Glover (1998). "Nature of surface electrical conductivity in natural sands, sandstones, and clays". In: *Geophysical Research Letters* 25.5, pp. 691–694. DOI: https://doi.org/10.1029/98GL00296. eprint: https://agupubs.onlinelibrary.wiley.com/doi/pdf/10.1029/98GL00296. URL: https://agupubs.onlinelibrary.wiley.com/doi/abs/10.1029/98GL00296.

Revil, A., E. Atekwana, C. Zhang, A. Jardani, and S. Smith (2012a). "A new model for the spectral induced polarization signature of bacterial growth in porous media". In: *Water Resources Research* 48.9.

Revil, A., M. Karaoulis, T. Johnson, and A. Kemna (2012b). "Some low-frequency electrical methods for subsurface characterization and monitoring in hydrogeology". In: *Hydrogeology Journal* 20.4, p. 617.

Revil, A., A. Binley, L. Mejus, and P. Kessouri (2015a). "Predicting permeability from the characteristic relaxation time and intrinsic formation factor of complex conductivity spectra". In: *Water Resources Research* 51.8, pp. 6672–6700. DOI: 10.1002/2015wr017074.

Revil, A., N. Florsch, and D. Mao (2015b). "Induced polarization response of porous media with metallic particles–Part 1: A theory for disseminated semiconductors". In: *Geophysics* 80.5, pp. D525–D538. DOI: 10.1190/geo2014-0577.1.

Revil, A., P. Kessouri, and C. Torres-Verdín (2014). "Electrical conductivity, induced polarization, and permeability of the Fontainebleau sandstone". In: *Geophysics* 79.5, pp. D301–D318.

Revil, A., K. Koch, and K. Holliger (2012c). "Is it the grain size or the characteristic pore size that controls the induced polarization relaxation time of clean sands and sandstones?" In: *Water Resources Research* 48.5. DOI: https://doi.org/10.1029/2011WR011561. eprint: https://agupubs.onlinelibrary.wiley.com/doi/pdf/10.1029/2011WR011561. URL: https://agupubs.onlinelibrary.wiley.com/doi/abs/10.1029/2011WR011561.

Robinet, J., C. von Hebel, G. Govers, J. van der Kruk, J. P. Minella, A. Schlesner, Y. Ameijeiras-Mariño, and J. Vanderborght (2018). "Spatial variability of soil water content and soil electrical conductivity across scales derived from Electromagnetic Induction and Time Domain Reflectometry". In: *Geoderma* 314, pp. 160–174. ISSN: 0016-7061. DOI: https://doi.org/10.1016/j.geoderma.2017.10.045. URL: https://www.sciencedirect.com/science/article/pii/S0016706117307875.

Robinson, D., I. Lebron, B. Kocar, K. Phan, M. Sampson, N. Crook, and S. Fendorf (2009). "Time-lapse geophysical imaging of soil moisture dynamics in tropical deltaic soils: An aid to interpreting hydrological and geochemical processes". In: *Water Resources Research* 45.4.

Robinson, D. A., H. Abdu, I. Lebron, and S. B. Jones (2012). "Imaging of hill-slope soil moisture wetting patterns in a semi-arid oak savanna catchment using time-lapse electromagnetic induction". In: *Journal of Hydrology* 416-417, pp. 39–49. ISSN: 0022-1694. DOI: https://doi.org/10.1016/j.jhydrol.2011.11.034. URL: https://www.sciencedirect.com/science/article/pii/S0022169411008195.

Robinson, J., L. Slater, A. Weller, K. Keating, T. Robinson, C. Rose, and B. Parker (2018). "On permeability prediction from complex conductivity measurements using polarization magnitude and relaxation time". In: *Water Resources Research* 54.5, pp. 3436–3452.

Rogers, N. W. and M. J. Selby (1980). "Mechanisms of shallow translational landsliding during summer rainstorms: North Island, New Zealand". In: *Geografiska Annaler: Series A, Physical Geography* 62.1-2, pp. 11–21. DOI: 10.1080/04353676.1980.11879995. eprint: https://doi.org/10.1080/04353676.1980.11879995. URL: https://doi.org/10.1080/04353676.1980.11879995.

Rögl, F. (1997). "Palaeogeographic considerations for Mediterranean and Paratethys seaways (Oligocene to Miocene)". In: *Annalen des Naturhistorischen Museums in Wien. Serie A für Mineralogie und Petrographie, Geologie und Paläontologie, Anthropologie und Prähistorie*, pp. 279–310.

Routh, P. S. and D. W. Oldenburg (2001). "Electromagnetic coupling in frequency-domain induced polarization data: A method for removal". In: *Geophysical Journal International* 145.1, pp. 59–76.

Rücker, C., T. Günther, and F. M. Wagner (2017). "pyGIMLi: An open-source library for modelling and inversion in geophysics". In: *Computers & Geosciences* 109, pp. 106–123. DOI: 10.1016/j.cageo.2017.07.011.

Rumpel, C. and I. Kögel-Knabner (2011). "Deep soil organic matter—a key but poorly understood component of terrestrial C cycle". In: *Plant and soil* 338, pp. 143–158.

Rupp, C., M. Linner, and G. Mandl (2011). "Geologie der Österreichischen Bundeslander. Erläuterungen zur Geologischen Karte von Oberösterreich 1: 200.000. Geologische Bundesanstalt". In.

Ruttner, A. and W. Schnabel (1988). "Blatt 71 Ybbsitz". In: *Geologische Karte der Republik Österreich 1:50.000.* Geological Survey of Austria.

Samyn, K., J. Travelletti, A. Bitri, G. Grandjean, and J.-P. Malet (2012). "Characterization of a landslide geometry using 3D seismic refraction traveltime tomography: The La Valette landslide case history". In: *Journal of Applied Geophysics* 86, pp. 120–132. DOI: 10.1016/j.jappgeo.2012.07.014.

Sass, O., R. Bell, and T. Glade (2008). "Comparison of GPR, 2D-resistivity and traditional techniques for the subsurface exploration of the Öschingen landslide, Swabian Alb (Germany)". In: *Geomorphology* 93.1. Challenges in Geomorphological Methods and Techniques, pp. 89–103. ISSN: 0169-555X. DOI: https:

//doi.org/10.1016/j.geomorph.2006.12.019. URL: https://www.sciencedirect.com/science/article/pii/S0169555X07001572.

Sastry, R. G., S. K. Mondal, and A. K. Pachauri (2012). "Combined Gravity and Electrical Imaging in Landslide Investigations at Narayan Bagar, Garhwal, Himalaya, India". In: *Symposium on the Application of Geophysics to Engineering and Environmental Problems 2012*. Environmental Engineering Geophysical Society, pp. 401–410. DOI: 10.4133/1.4721834. eprint: https://library.seg.org/doi/pdf/10.4133/1.4721834. URL: https://library.seg.org/doi/abs/10.4133/1.4721834.

Scanlon, B. R., J. G. Paine, and R. S. Goldsmith (1999). "Evaluation of Electromagnetic Induction as a Reconnaissance Technique to Characterize Unsaturated Flow in an Arid Setting". In: *Groundwater* 37.2, pp. 296–304. DOI: https://doi.org/10.1111/j.1745-6584.1999.tb00987.x. eprint: https://ngwa.onlinelibrary.wiley.com/doi/pdf/10.1111/j.1745-6584.1999.tb00987.x. URL: https://ngwa.onlinelibrary.wiley.com/doi/abs/10.1111/j.1745-6584.1999.tb00987.x.

Schaap, M. G., F. J. Leij, and M. T. Van Genuchten (2001). "Rosetta: A computer program for estimating soil hydraulic parameters with hierarchical pedotransfer functions". In: *Journal of hydrology* 251.3-4, pp. 163–176.

Schmäck, J., L. Weihermüller, A. Klotzsche, C. von Hebel, S. Pätzold, G. Welp, and H. Vereecken (2022). "Large-scale detection and quantification of harmful soil compaction in a post-mining landscape using multi-configuration electromagnetic induction". In: *Soil Use and Management* 38.1, pp. 212–228.

Schnabel, W., H. Krenmayr, G. Mandl, A. Nowotny, R. Roetzel, and S. Scharbert (2002). "Geologische Karte Niederösterreich 1:200.000". In: *Geologische Karte Niederösterreich 1:200.000*. Geological Survey of Austria.

Schnyder, J., A. Ruffell, J.-F. Deconinck, and F. Baudin (2006). "Conjunctive use of spectral gamma-ray logs and clay mineralogy in defining late Jurassic–early Cretaceous palaeoclimate change (Dorset, UK)". In: *Palaeogeography, Palaeoclimatology, Palaeoecology* 229.4, pp. 303–320.

Schultz, G. and C. Ruppel (2005). "Inversion of inductive electromagnetic data in highly conductive terrains". In: *GEOPHYSICS* 70.1, G16–G28. DOI: 10.1190/1.1852775. eprint: https://doi.org/10.1190/1.1852775. URL: https://doi.org/10.1190/1.1852775.

Schwab, F. and L. Knopoff (1972). "Fast surface wave and free mode computations". In: *Methods in computational physics: Advances in research and applications*. Vol. 11. Elsevier, pp. 87–180.

Schwarz, G. (1962). "A theory of the low-frequency dielectric dispersion of colloidal particles in electrolyte solution1, 2". In: *The Journal of Physical Chemistry* 66.12, pp. 2636–2642. DOI: 10.1021/j100818a067.

Searchinger, T. D., S. Wirsenius, T. Beringer, and P. Dumas (2018). "Assessing the efficiency of changes in land use for mitigating climate change". In: *Nature* 564.7735, pp. 249–253.

Seigel, H., M. Nabighian, D. S. Parasnis, and K. Vozoff (2007). "The early history of the induced polarization method". In: *The Leading Edge* 26.3, pp. 312–321.

Serson, P. (1973). "Instrumentation for induction studies on land". In: *Physics of the Earth and Planetary Interiors* 7.3, pp. 313–322.

Shanahan, P. W., A. Binley, W. R. Whalley, and C. W. Watts (2015). "The use of electromagnetic induction to monitor changes in soil moisture profiles beneath different wheat genotypes". In: *Soil Science Society of America Journal* 79.2, pp. 459–466.

Sharma, H. and E. Jennings (2021). "Bayesian neural networks at scale: a performance analysis and pruning study". In: *The Journal of Supercomputing* 77.4, pp. 3811–3839.

Shen, C., J. Niu, and K. Fang (2014). "Quantifying the effects of data integration algorithms on the outcomes of a subsurface–land surface processes model". In: *Environmental Modelling & Software* 59, pp. 146–161.

Shrestha, A. and A. Mahmood (2019). "Review of deep learning algorithms and architectures". In: *IEEE access* 7, pp. 53040–53065.

Sidle, R. C., R. Greco, and T. Bogaard (2019). *Overview of landslide hydrology*.

Simon, F.-X., A. Sarris, J. Thiesson, and A. Tabbagh (2015). "Mapping of quadrature magnetic susceptibility/magnetic viscosity of soils by using multi-frequency EMI". In: *Journal of Applied Geophysics* 120, pp. 36–47.

Singh, V. K., K. C. Panda, A. Sagar, N. Al-Ansari, H.-F. Duan, P. K. Paramaguru, D. K. Vishwakarma, A. Kumar, D. Kumar, P. Kashyap, et al. (2022). "Novel Genetic Algorithm (GA) based hybrid machine learning-pedotransfer Function (ML-PTF) for prediction of spatial pattern of saturated hydraulic conductivity". In: *Engineering Applications of Computational Fluid Mechanics* 16.1, pp. 1082–1099.

Sirles, P., K. Haramy, R. D. Andrew, and R. W. Surdahl (2013). "Seismic and Electrical 3D Imaging to Aid in Landslide Remediation Design, East Fork Landslide, Wolf Creek Pass, Colorado". In: *GeoChallenges: Rising to the Geotechnical Challenges of Colorado*. American Society of Civil Engineers, pp. 76–89. DOI: 10.1061/9780784412633.0005. eprint: https://ascelibrary.org/doi/pdf/10.1061/9780784412633.0005. URL: https://ascelibrary.org/doi/abs/10.1061/9780784412633.0005.

Slater, L. and D. Glaser (2003). "Controls on induced polarization in sandy unconsolidated sediments and application to aquifer characterization". In: *Geophysics* 68.5, pp. 1547–1558. DOI: 10.1190/1.1620628.

Slater, L. (2007). "Near surface electrical characterization of hydraulic conductivity: From petrophysical properties to aquifer geometries–A review". In: *Surveys in Geophysics* 28.2, pp. 169–197. DOI: 10.1007/s10712-007-9022-y.

Slater, L., W. Barrash, J. Montrey, and A. Binley (2014). "Electrical-hydraulic relationships observed for unconsolidated sediments in the presence of a cobble framework". In: *Water Resources Research* 50.7, pp. 5721–5742.

Slater, L., A. Binley, W. Daily, and R. Johnson (2000). "Cross-hole electrical imaging of a controlled saline tracer injection". In: *Journal of applied geophysics* 44.2-3, pp. 85–102. DOI: 10.1016/s0926-9851(00)00002-1.

Slater, L. and D. P. Lesmes (2002a). "Electrical-hydraulic relationships observed for unconsolidated sediments". In: *Water resources research* 38.10, pp. 31–1. DOI: 10.1029/2001wr001075.

Slater, L., D. Ntarlagiannis, Y. R. Personna, and S. Hubbard (2007). "Pore-scale spectral induced polarization signatures associated with FeS biomineral transformations". In: *Geophysical Research Letters* 34.21.

Slater, L., D. Ntarlagiannis, and D. Wishart (2006). "On the relationship between induced polarization and surface area in metal-sand and clay-sand mixtures". In: *GEOPHYSICS* 71.2, A1–A5. DOI: 10.1190/1.2187707. eprint: https://doi.org/10.1190/1.2187707. URL: https://doi.org/10.1190/1.2187707.

Slater, L. D. and D. Lesmes (2002b). "IP interpretation in environmental investigations". In: *Geophysics* 67.1, pp. 77–88. DOI: 10.1190/1.1451353.

Slater, L. D. and A. Reeve (2002). "Investigating peatland stratigraphy and hydrogeology using integrated electrical geophysics". In: *Geophysics* 67.2, pp. 365–378.

Snee, R. D. (1977). "Validation of Regression Models: Methods and Examples". In: *Technometrics* 19.4, pp. 415–428. DOI: 10.1080/00401706.1977.10489581. eprint: https://www.tandfonline.com/doi/pdf/10.1080/00401706.1977.10489581. URL: https://www.tandfonline.com/doi/abs/10.1080/00401706.1977.10489581.

Sobie, S. R. (2020). "Future changes in precipitation-caused landslide frequency in British Columbia". In: *Climatic Change* 162.2, pp. 465–484.

Sobieraj, J., H. Elsenbeer, and R. Vertessy (2001). "Pedotransfer functions for estimating saturated hydraulic conductivity: implications for modeling storm flow generation". In: *Journal of Hydrology* 251.3-4, pp. 202–220.

Soto, J., J. P. Galve, J. A. Palenzuela, J. M. Azañón, J. Tamay, and C. Irigaray (2017). "A multi-method approach for the characterization of landslides in an intramontane basin in the Andes (Loja, Ecuador)". In: *Landslides* 14, pp. 1929–1947.

Spies, B. (1996). "Electrical and electromagnetic borehole measurements: A review". In: *Surveys in Geophysics* 17, pp. 517–556.

Steiner, M. and A. F. Orozco (2023). "formikoj: A flexible library for data management and processing in geophysics—Application for seismic refraction data". In: *Computers & Geosciences* 176, p. 105339.

Steiner, M., F. M. Wagner, T. Maierhofer, W. Schöner, and A. Flores Orozco (2021). "Improved estimation of ice and water contents in Alpine permafrost through constrained petrophysical joint inversion: The Hoher Sonnblick case study". In: *Geophysics* 86.5, pp. 1–84. DOI: 10.1190/geo2020-0592.1.

Strobbia, C. and S. Foti (2006). "Multi-offset phase analysis of surface wave data (MOPA)". In: *Journal of Applied Geophysics* 59.4, pp. 300–313. ISSN: 0926-9851. DOI: https://doi.org/10.1016/j.jappgeo.2005.10.009. URL: https://www.sciencedirect.com/science/article/pii/S0926985105000959.

Stumvoll, M., E. Canli, A. Engels, B. Thiebes, B. Groiss, T. Glade, J. Schweigl, and M. Bertagnoli (2020). "The "Salcher" landslide observatory–experimental long-term monitoring in the Flysch Zone of Lower Austria". In: *Bulletin of Engineering Geology and the Environment* 79.4, pp. 1831–1848.

Supper, R., D. Ottowitz, B. Jochum, J.-H. Kim, A. Römer, I. Baron, S. Pfeiler, M. Lovisolo, S. Gruber, and F. Vecchiotti (2014). "Geoelectrical monitoring: an innovative method to supplement landslide surveillance and early warning". In: *Near Surface Geophysics* 12.1, pp. 133–150. DOI: 10.3997/1873-0604.2013060.

Szabó, B., M. Weynants, and T. K. Weber (2021). "Updated European hydraulic pedotransfer functions with communicated uncertainties in the predicted variables (euptfv2)". In: *Geoscientific Model Development* 14.1, pp. 151–175.

Tabari, H. (2020). "Climate change impact on flood and extreme precipitation increases with water availability". In: *Scientific reports* 10.1, p. 13768.

Taboga, A. (2011). "Developement of Integrated High-Resolution Geophysical, Photogrammetric and GPS Surveying Applied to Landslides in the South Wales Coalfield". PhD thesis. Cardiff University, United Kingdom.

Tanner, J. and D. Hughes (2015). "Surface water–groundwater interactions in catchment scale water resources assessments—understanding and hypothesis testing with a hydrological model". In: *Hydrological Sciences Journal* 60.11, pp. 1880–1895.

Tarasov, A. and K. Titov (2007). "Relaxation time distribution from time domain induced polarization measurements". In: *Geophysical Journal International* 170.1, pp. 31–43.

Tarnawski, V., P. Coppa, W. Leong, M. McCombie, and G. Bovesecchi (2020). "On modelling the thermal conductivity of soils using normalized-multi-variable pedotransfer functions". In: *International Journal of Thermal Sciences* 156, p. 106493.

Tazifor, M., E. Zimmermann, J. A. Huisman, M. Dick, A. Mester, and S. Van Waasen (2022). "Model-Based Correction of Temperature-Dependent Measurement Errors in Frequency Domain Electromagnetic Induction (FDEMI) Systems". In: *Sensors* 22.10. ISSN: 1424-8220. DOI: 10.3390/s22103882. URL: https://www.mdpi.com/1424-8220/22/10/3882.

Telford, W. M., L. P. Geldart, and R. E. Sheriff (1990). *Applied geophysics*. Cambridge university press.

Tieleman, T. and G. Hinton (2012). "Lecture 6.5-rmsprop, coursera: Neural networks for machine learning". In: *University of Toronto, Technical Report* 6.

Titov, K., V. Komarov, V. Tarasov, and A. Levitski (2002). "Theoretical and experimental study of time domain-induced polarization in water-saturated sands". In: *Journal of Applied Geophysics* 50.4, pp. 417–433. ISSN: 0926-9851. DOI: https://doi.org/10.1016/S0926-9851(02)00168-4. URL: https://www.sciencedirect.com/science/article/pii/S0926985102001684.

Titov, K., A. Tarasov, Y. Ilyin, N. Seleznev, and A. Boyd (Mar. 2010). "Relationships between induced polarization relaxation time and hydraulic properties of sandstone". In: *Geophysical Journal International* 180.3, pp. 1095–1106. ISSN: 0956-540X. DOI: 10.1111/j.1365-246X.2009.04465.x. eprint: https://academic.oup.com/gji/article-pdf/180/3/1095/5886950/180-3-1095.pdf. URL: https://doi.org/10.1111/j.1365-246X.2009.04465.x.

Tóth, B., M. Weynants, A. Nemes, A. Makó, G. Bilas, and G. Tóth (2015). "New generation of hydraulic pedotransfer functions for Europe". In: *European journal of soil science* 66.1, pp. 226–238.

Triantafilis, J. and S. Lesch (2005). "Mapping clay content variation using electromagnetic induction techniques". In: *Computers and Electronics in Agriculture* 46.1. Applications of Apparent Soil Electrical Conductivity in Precision Agriculture, pp. 203–237. ISSN: 0168-1699. DOI: https://doi.org/10.1016/j.compag.2004.11.006. URL: https://www.sciencedirect.com/science/article/pii/S0168169904001310.

Triantafilis, J. and F. Monteiro Santos (2013). "Electromagnetic conductivity imaging (EMCI) of soil using a DUALEM-421 and inversion modelling software (EM4Soil)". In: *Geoderma* 211-212, pp. 28–38. ISSN: 0016-7061. DOI: https://doi.org/10.1016/j.geoderma.2013.06.001. URL: https://www.sciencedirect.com/science/article/pii/S0016706113002000.

Twarakavi, N. K., J. Šimnek, and M. Schaap (2009). "Development of pedotransfer functions for estimation of soil hydraulic parameters using support vector machines". In: *Soil Science Society of America Journal* 73.5, pp. 1443–1452.

Uhlemann, S., S. Hagedorn, B. Dashwood, H. Maurer, D. Gunn, T. Dijkstra, and J. Chambers (2016). "Landslide characterization using P- and S-wave seismic refraction tomography–The importance of elastic moduli". In: *Journal of Applied Geophysics* 134, pp. 64–76. ISSN: 0926-9851. DOI: 10.1016/j.jappgeo.2016.08.014.

Uhlemann, S., C. Ulrich, M. Newcomer, P. Fiske, J. Kim, and J. Pope (2022). "3D hydrogeophysical characterization of managed aquifer recharge basins". In: *Frontiers in Earth Science* 10, p. 942737.

Van Asch, T. W., J. Buma, and L. Van Beek (1999). “A view on some hydrological triggering systems in landslides”. In: *Geomorphology* 30.1-2, pp. 25–32.

van Genuchten, M. T. (1980). “A closed-form equation for predicting the hydraulic conductivity of unsaturated soils”. In: *Soil science society of America journal* 44.5, pp. 892–898. DOI: 10.2136/sssaj1980.03615995004400050002x.

van Leeuwen, C., M. Schmutz, and L. de Rességuier (2024). “The contribution of near surface geophysics to measure soil related terroir factors in viticulture: A review”. In: *Geoderma* 449, p. 116983. ISSN: 0016-7061. DOI: https://doi.org/10.1016/j.geoderma.2024.116983. URL: https://www.sciencedirect.com/science/article/pii/S001670612400212X.

Van Looy, K., J. Bouma, M. Herbst, J. Koestel, B. Minasny, U. Mishra, C. Montzka, A. Nemes, Y. A. Pachepsky, J. Padarian, et al. (2017a). “Pedotransfer functions in Earth system science: Challenges and perspectives”. In: *Reviews of Geophysics* 55.4, pp. 1199–1256.

Van Looy, K., J. Bouma, M. Herbst, J. Koestel, B. Minasny, U. Mishra, C. Montzka, A. Nemes, Y. A. Pachepsky, J. Padarian, M. G. Schaap, B. Tóth, A. Verhoef, J. Vanderborght, M. J. van der Ploeg, L. Weihermüller, S. Zacharias, Y. Zhang, and H. Vereecken (2017b). “Pedotransfer Functions in Earth System Science: Challenges and Perspectives”. In: *Reviews of Geophysics* 55.4, pp. 1199–1256. DOI: https://doi.org/10.1002/2017RG000581. eprint: https://agupubs.onlinelibrary.wiley.com/doi/pdf/10.1002/2017RG000581. URL: https://agupubs.onlinelibrary.wiley.com/doi/abs/10.1002/2017RG000581.

Van Voorhis, G., P. Nelson, and T. Drake (1973). “Complex resistivity spectra of porphyry copper mineralization”. In: *Geophysics* 38.1, pp. 49–60.

Vereecken, H., J. Diels, J. Van Orshoven, J. Feyen, and J. Bouma (1992). “Functional evaluation of pedotransfer functions for the estimation of soil hydraulic properties”. In: *Soil Science Society of America Journal* 56.5, pp. 1371–1378.

Vereecken, H., M. Weynants, M. Javaux, Y. Pachepsky, M. Schaap, and M. T. Van Genuchten (2010). “Using pedotransfer functions to estimate the van Genuchten–Mualem soil hydraulic properties: A review”. In: *Vadose Zone Journal* 9.4, pp. 795–820.

Vervoort, R. and Y. Annen (2006). “Palaeochannels in Northern New South Wales: Inversion of electromagnetic induction data to infer hydrologically relevant stratigraphy”. In: *Soil Research* 44.1, pp. 35–45.

Vinegar, H. and M. Waxman (1984). “Induced polarization of shaly sands”. In: *Geophysics* 49.8, pp. 1267–1287. DOI: 10.1190/1.1441755.

Visconti, F. and J. M. de Paz (2021). “Sensitivity of soil electromagnetic induction measurements to salinity, water content, clay, organic matter and bulk density”. In: *Precision Agriculture* 22.5, pp. 1559–1577.

Wainwright, H. M., A. Flores Orozco, M. Bücker, B. Dafflon, J. Chen, S. S. Hubbard, and K. H. Williams (2016). “Hierarchical Bayesian method for mapping biogeochemical hot spots using induced polarization imaging”. In: *Water Resources Research* 52.1, pp. 533–551. DOI: https://doi.org/10.1002/2015WR017763. eprint: https://agupubs.onlinelibrary.wiley.com/doi/pdf/10.1002/2015WR017763. URL: https://agupubs.onlinelibrary.wiley.com/doi/abs/10.1002/2015WR017763.

Wait, J. R. and T. P. Gruszka (1986). “On electromagnetic coupling “removal” from induced polarization surveys”. In: *Geoexploration* 24.1, pp. 21–27.

Ward, S. H. (1988). “The resistivity and induced polarization methods”. In: *Symposium on the Application of Geophysics to Engineering and Environmental Problems 1988*. Society of Exploration Geophysicists, pp. 109–250. DOI: 10.1190/1.9781560802785.ch6.

Ward, S. H. and G. W. Hohmann (1988). “Electromagnetic theory for geophysical applications”. In: *Electromagnetic methods in applied geophysics: Volume 1, theory.*

Ward, S. H. (1990). “6. Resistivity and Induced Polarization Methods”. In: *Geotechnical and Environmental Geophysics: Volume I, Review and Tutorial.* Society of Exploration Geophysicists, pp. 147–190. DOI: 10.1190/1.9781560802785.ch6. eprint: https://library.seg.org/doi/pdf/10.1190/1.9781560802785.ch6. URL: https://library.seg.org/doi/abs/10.1190/1.9781560802785.ch6.

Waseem, M., F. Kachholz, W. Klehr, and J. Traenckner (2020). “Suitability of a coupled hydrologic and hydraulic model to simulate surface water and groundwater hydrology in a typical North-Eastern Germany lowland catchment”. In: *Applied sciences* 10.4, p. 1281.

Watlet, A., O. Kaufmann, A. Triantafyllou, A. Poulain, J. E. Chambers, P. I. Meldrum, P. B. Wilkinson, V. Hallet, Y. Quinif, M. Van Ruymbeke, et al. (2018). “Imaging groundwater infiltration dynamics in the karst vadose zone with long-term ERT monitoring”. In: *Hydrology and Earth System Sciences* 22.2, pp. 1563–1592.

Waxman, M. H. and L. Smits (1968). “Electrical conductivities in oil-bearing shaly sands”. In: *Society of Petroleum Engineers Journal* 8.02, pp. 107–122. DOI: 10.2118/1863-a.

Weber, L. (1997). “Exzerpt (Basiskarte Geologie) aus der Metallogenetischen Karte von Österreich 1:500 000”. In: *Flächendeckende Beschreibung der Geologie von Österreich 1:500 000 im Vektorformat.* Geological Survey of Austria.

Weber, T. K. D., L. Weihermüller, A. Nemes, M. Bechtold, A. Degré, E. Diamantopoulos, S. Fatichi, V. Filipović, S. Gupta, T. L. Hohenbrink, et al. (2024). “Hydro-pedotransfer functions: a roadmap for future development”. In: *Hydrology and Earth System Sciences* 28.14, pp. 3391–3433.

Weigand, M. and A. Kemna (2016). “Relationship between Cole–Cole model parameters and spectral decomposition parameters derived from SIP data”. In: *Geophysical Journal International* 205.3, pp. 1414–1419. DOI: 10.1093/gji/ggw099.

Weigand, M. and A. Kemna (2019). “Imaging and functional characterization of crop root systems using spectroscopic electrical impedance measurements”. In: *Plant and Soil* 435, pp. 201–224.

Weigand, M., A. F. Orozco, and A. Kemna (2017). “Reconstruction quality of SIP parameters in multi-frequency complex resistivity imaging”. In: *Near Surface Geophysics* 15.2, pp. 187–199. ISSN: 1873-0604. DOI: https://doi.org/10.3997/1873-0604.2016050. URL: https://www.earthdoc.org/content/journals/10.3997/1873-0604.2016050.

Weiskopf, S. R., M. A. Rubenstein, L. G. Crozier, S. Gaichas, R. Griffis, J. E. Halofsky, K. J. Hyde, T. L. Morelli, J. T. Morisette, R. C. Muñoz, et al. (2020). “Climate change effects on biodiversity, ecosystems, ecosystem services, and natural resource management in the United States”. In: *Science of the Total Environment* 733, p. 137782.

Weller, A. and L. Slater (2012). “Salinity dependence of complex conductivity of unconsolidated and consolidated materials: Comparisons with electrical double layer models”. In: *Geophysics* 77.5, pp. D185–D198.

Weller, A. and L. Slater (2019). “Permeability estimation from induced polarization: An evaluation of geophysical length scales using an effective hydraulic radius concept”. In: *Near surface geophysics* 17.6, pp. 581–594.

Weller, A., L. Slater, A. Binley, S. Nordsiek, and S. Xu (2015). "Permeability prediction based on induced polarization: Insights from measurements on sandstone and unconsolidated samples spanning a wide permeability range". In: *Geophysics* 80.2, pp. D161–D173. DOI: 10.1190/geo2014-0368.1.

Weller, A., L. Slater, and S. Nordsiek (2013). "On the relationship between induced polarization and surface conductivity: Implications for petrophysical interpretation of electrical measurements". In: *Geophysics* 78.5, pp. D315–D325. DOI: 10.1190/geo2013-0076.1.

Weller, A., L. Slater, S. Nordsiek, and D. Ntarlagiannis (2010). "On the estimation of specific surface per unit pore volume from induced polarization: A robust empirical relation fits multiple data sets". In: *GEOPHYSICS* 75.4, WA105–WA112. DOI: 10.1190/1.3471577. eprint: https://doi.org/10.1190/1.3471577. URL: https://doi.org/10.1190/1.3471577.

Weller, U., M. Zipprich, M. Sommer, W. Z. Castell, and M. Wehrhan (2007). "Mapping Clay Content across Boundaries at the Landscape Scale with Electromagnetic Induction". In: *Soil Science Society of America Journal* 71.6, pp. 1740–1747. DOI: https://doi.org/10.2136/sssaj2006.0177. eprint: https://acsess.onlinelibrary.wiley.com/doi/pdf/10.2136/sssaj2006.0177. URL: https://acsess.onlinelibrary.wiley.com/doi/abs/10.2136/sssaj2006.0177.

Wessely, G., I. Draxler, G. Gangl, P. Gottschling, M. Heinrich, T. Hofmann, W. Lenhardt, A. Matura, R. Pavuza, H. Peresson, and R. Sauer (2006). *Geologische der österreichischen Bundesländer - Niederösterreich*. Tech. rep. Geological Survey of Austria.

Weynants, M., L. Montanarella, G. Toth, A. Arnoldussen, M. Anaya Romero, G. Bilas, T. Borresen, W. Cornelis, J. Daroussin, M. D. C. Gonçalves, et al. (2013). "European hydropedological data inventory (EU-HYDI)". In: *EUR Scientific and Technical Research Series*.

Whiteley, J. S., A. Watlet, J. M. Kendall, and J. E. Chambers (2021). "Brief communication: The role of geophysical imaging in local landslide early warning systems". In: *Natural Hazards and Earth System Sciences Discussions* 2021, pp. 1–13.

Whiteley, J., J. Chambers, S. Uhlemann, P. B. Wilkinson, and J. Kendall (2019). "Geophysical monitoring of moisture-induced landslides: a review". In: *Reviews of Geophysics* 57.1, pp. 106–145. DOI: 10.1029/2018rg000603.

Whiteley, R. J. and P. J. Eccleston (2006). "Comparison of shallow seismic refraction interpretation methods for regolith mapping". In: *Exploration Geophysics* 37.4, pp. 340–347.

Widera, M. (2013). "Changes of the lignite seam architecture—A case study from Polish lignite deposits". In: *International Journal of Coal Geology* 114, pp. 60–73.

Widera, M. (2016). "Genetic classification of Polish lignite deposits: A review". In: *International Journal of Coal Geology* 158, pp. 107–118.

Wild, V. D., S. Ghalebikesabi, D. Sejdinovic, and J. Knoblauch (2024). "A rigorous link between deep ensembles and (variational) Bayesian methods". In: *Advances in Neural Information Processing Systems* 36.

Williams, K. H., A. Kemna, M. J. Wilkins, J. Druhan, E. Arntzen, A. L. N'Guessan, P. E. Long, S. S. Hubbard, and J. F. Banfield (2009). "Geophysical monitoring of coupled microbial and geochemical processes during stimulated subsurface bioremediation". In: *Environmental science & technology* 43.17, pp. 6717–6723. DOI: 10.1021/es900855j.

Williams, K. H., D. Ntarlagiannis, L. D. Slater, A. Dohnalkova, S. S. Hubbard, and J. F. Banfield (2005). "Geophysical imaging of stimulated microbial biomineralization". In: *Environmental science & technology* 39.19, pp. 7592–7600. DOI: 10.1021/es0504035.

Wolf, L. and A. Flores Orozco (2024). "Design, Development and Application of a Modular Electromagnetic Induction (EMI) Sensor for Near-Surface Geophysical Surveys". In: *Sensors* 24.13. ISSN: 1424-8220. DOI: 10.3390/s24134159. URL: https://www.mdpi.com/1424-8220/24/13/4159.

Won, I., D. Keiswetter, and E. Novikova (1998). "Electromagnetic induction spectroscopy". In: *11th EEGS Symposium on the Application of Geophysics to Engineering and Environmental Problems*. European Association of Geoscientists & Engineers, cp–203.

Wong, J. (1979). "An electrochemical model of the induced-polarization phenomenon in disseminated sulfide ores". In: *Geophysics* 44.7, pp. 1245–1265. DOI: 10.1190/1.1441005.

Woo, J. O. (2022). "Analytic mutual information in bayesian neural networks". In: *2022 IEEE International Symposium on Information Theory (ISIT)*. IEEE, pp. 300–305.

Wösten, J. (1997). "Pedotransfer functions to evaluate soil quality". In: *Developments in Soil Science*. Vol. 25. Elsevier, pp. 221–245.

Wu, S., Q. Huang, and L. Zhao (Nov. 2022a). "A deep learning-based network for the simulation of airborne electromagnetic responses". In: *Geophysical Journal International* 233.1, pp. 253–263. ISSN: 0956-540X. DOI: 10.1093/gji/ggac463. eprint: https://academic.oup.com/gji/article-pdf/233/1/253/48352361/ggac463.pdf. URL: https://doi.org/10.1093/gji/ggac463.

Wu, S., Q. Huang, and L. Zhao (July 2024). "Physics-guided deep learning-based inversion for airborne electromagnetic data". In: *Geophysical Journal International* 238.3, pp. 1774–1789. ISSN: 1365-246X. DOI: 10.1093/gji/ggae244. eprint: https://academic.oup.com/gji/article-pdf/238/3/1774/58713027/ggae244.pdf. URL: https://doi.org/10.1093/gji/ggae244.

Wu, X., G. Xue, Y. Zhao, P. lv, Z. Zhou, and J. Shi (2022b). "A Deep Learning Estimation of the Earth Resistivity Model for the Airborne Transient Electromagnetic Observation". In: *Journal of Geophysical Research: Solid Earth* 127.3. e2021JB023185 2021JB023185, e2021JB023185. DOI: https://doi.org/10.1029/2021JB023185. eprint: https://agupubs.onlinelibrary.wiley.com/doi/pdf/10.1029/2021JB023185. URL: https://agupubs.onlinelibrary.wiley.com/doi/abs/10.1029/2021JB023185.

Xia, J., R. D. Miller, and C. B. Park (1999). "Estimation of near-surface shear-wave velocity by inversion of Rayleigh waves". In: *Geophysics* 64.3, pp. 691–700.

Ya, Y., L. Dongdong, S. Dongli, N. Jie, F. Yuanhang, and Y. Shimei (2024). "Integrating calibrated PTFs and modified OpenKarHydro framework to map the responses of ecohydrological processes to climate change across the Loess Plateau". In: *Catena* 246, p. 108391.

Yang, S., Y. Dong, X. Song, H. Wu, X. Zhao, J. Yang, S. Chen, J. Smith, and G.-L. Zhang (2022). "Vertical distribution and influencing factors of deep soil organic carbon in a typical subtropical agricultural watershed". In: *Agriculture, Ecosystems Environment* 339, p. 108141. ISSN: 0167-8809. DOI: https://doi.org/10.1016/j.agee.2022.108141. URL: https://www.sciencedirect.com/science/article/pii/S0167880922002900.

Yao, R., J. Yang, D. Wu, W. Xie, P. Gao, and W. Jin (2016). "Digital mapping of soil salinity and crop yield across a coastal agricultural landscape using repeated electromagnetic induction (EMI) surveys". In: *PloS one* 11.5, e0153377.

Yari, M., M. Nabi-Bidhendi, R. Ghanati, and Z.-H. Shomali (2021). "Hidden layer imaging using joint inversion of P-wave traveltime and electrical resistivity data". In: *Near Surface Geophysics* 19.3, pp. 297–313.

Yin, T. and H.-P. Zhu (2020). "An efficient algorithm for architecture design of Bayesian neural network in structural model updating". In: *Computer-Aided Civil and Infrastructure Engineering* 35.4, pp. 354–372.

Závodská, L. and J. Lesn'y (2006). "Recent development in lignite investigation". In: *HEJ Manuscript*, pp. 1418–7108.

Zhang, Y., M. Person, and C. W. Gable (2007). "Representative hydraulic conductivity of hydrogeologic units: Insights from an experimental stratigraphy". In: *Journal of Hydrology* 339.1, pp. 65–78. ISSN: 0022-1694. DOI: https://doi.org/10.1016/j.jhydrol.2007.03.007. URL: https://www.sciencedirect.com/science/article/pii/S0022169407001849.

Zhang, Y. and M. G. Schaap (2017). "Weighted recalibration of the Rosetta pedotransfer model with improved estimates of hydraulic parameter distributions and summary statistics (Rosetta3)". In: *Journal of Hydrology* 547, pp. 39–53.

Zhang, Y. and M. G. Schaap (2019). "Estimation of saturated hydraulic conductivity with pedotransfer functions: A review". In: *Journal of Hydrology* 575, pp. 1011–1030.

Zhao, X., J. Wang, D. Zhao, N. Li, E. Zare, and J. Triantafilis (2019). "Digital regolith mapping of clay across the Ashley irrigation area using electromagnetic induction data and inversion modelling". In: *Geoderma* 346, pp. 18–29. ISSN: 0016-7061. DOI: https://doi.org/10.1016/j.geoderma.2019.01.033. URL: https://www.sciencedirect.com/science/article/pii/S0016706118320639.

Zhao, Y., E. Zimmermann, J. Huisman, A. Treichel, B. Wolters, S. Van Waasen, and A. Kemna (2013). "Broadband EIT borehole measurements with high phase accuracy using numerical corrections of electromagnetic coupling effects". In: *Measurement Science and Technology* 24.8, p. 085005.

Zhao, Y., E. Zimmermann, J. Huisman, A. Treichel, B. Wolters, S. van Waasen, and A. Kemna (2014). "Phase correction of electromagnetic coupling effects in cross-borehole EIT measurements". In: *Measurement science and technology* 26.1, p. 015801.

Zhdanov, M. S. (2023). "Introduction to inversion theory". In: *Advanced Methods of Joint Inversion and Fusion of Multiphysics Data*. Springer, pp. 3–12.

Zimmermann, E., J. Huisman, A. Mester, and S. Van Waasen (2019). "Correction of phase errors due to leakage currents in wideband EIT field measurements on soil and sediments". In: *Measurement Science and Technology* 30.8, p. 084002.

Zimmermann, E., A. Kemna, J. Berwix, W. Glaas, and H. Vereecken (July 2008). "EIT measurement system with high phase accuracy for the imaging of spectral induced polarization properties of soils and sediments". In: *Measurement Science and Technology* 19.9, p. 094010. DOI: 10.1088/0957-0233/19/9/094010. URL: https://dx.doi.org/10.1088/0957-0233/19/9/094010.